UNIVERSITI TEKNOLOGI MARA

JmechE

Journal of mechanical engineering

Special Issue 2023 : Vol. SI 12

Sustainability in Advanced Materials & Manufacturing

ISSN : 1823 - 5514

e-ISSN : 2550 - 164x

jmeche.uitm.edu.my

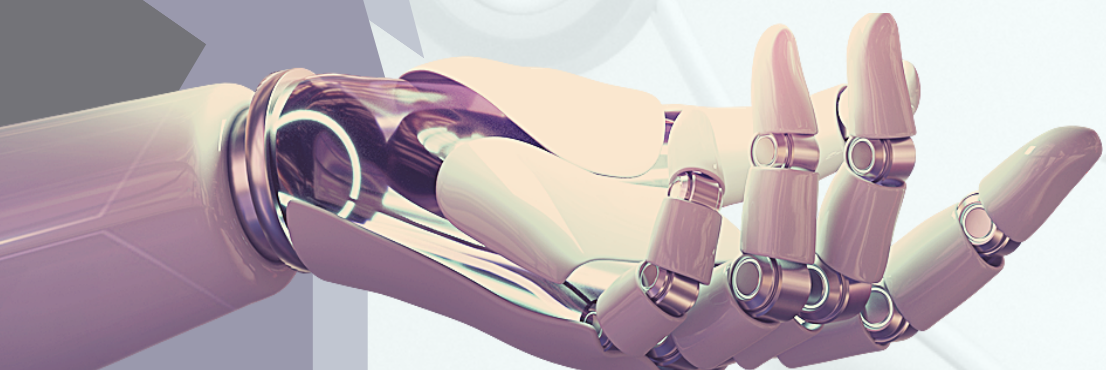

JOURNAL OF MECHANICAL ENGINEERING

Journal of Mechanical Engineering (ISSN 1823-5514, e-ISSN 2550-164X) is published by Penerbit UiTM (UiTM Press), Universiti Teknologi MARA, 40450 Shah Alam, Selangor, Malaysia.

JOURNAL OF
MECHANICAL ENGINEERING
An International Journal

Special Issue
Sustainability in Advanced Materials and Manufacturing

Vol SI 12	15 Nov 2023	ISSN 1823-5514	eISSN 2550-164X

1	Experimental Determination of High-Acceleration Shock Characteristics of Industrial Marine Fenders *David, N. V.[*], Adelin Khairina, M. S., and Vipin Gopan* [*]https://orcid.org/0000-0003-4128-5850	1
2	The Effect of Cobalt Alloy Nanocrystalline Coating on Tensile Properties and Surface Performance of Mild Steel *Mohd Zakuan Zabri, Nik Rozlin Nik Masdek[*], and Koay Mei Hyie* [*]https://orcid.org/00009-0004-8355-622X	21
3	Mechanical Properties of Rice Husk-Recycled Polypropylene Composite *Umar Iqqbal Al-Biruni Mohd Adnan, Freddawati Rashiddy Wong[*], Mohamad Firhan Morni, Abdul Hakim Abdullah, Amirul Abd Rashid, Soon Kong Yong* [*]https://orcid.org/0000-0001-8960-2064	45
4	The Influence of Cutting Parameter under Sustainable Machining Approaches on Surface Roughness of AISI 4340 *Ahsana Aqilah Ahmad, Jaharah A. Ghani[*], and Che Hassan Che Haron* [*]https://orcid.org/0000-0002-0777-5437	63
5	Unravelling Tool Edge Trajectory Patterns: Implications on Surface Roughness in End Milling Process *Fatiha Naziera Yusof, Mohd Fauzi Ismail[*], and Rizal Mohamed Noor* [*]https://orcid.org/0000-0002-3422-0664	81
6	Effects of Printing Parameters on the Mechanical Strength of Thermoplastics 3D Printed Specimens *Mohammad Azeeb Mazlan, Muhammad Fadil Mustar, Abdul Halim Abdullah[*], Noor Ayuni Che Zakaria, Natiara Mohamad Hashim, and Azizah Intan Pangesty* [*]https://orcid.org/0000-0002-8377-329X	101

7	Characterization of Rubber Degradation in a Brake Wheel Cylinder Under Cyclic Loading *Abdul Hakim Abdullah*[*]*, Muhammad Fakhruddin Abd Wahid , Noorazizi Mohd Samsuddin, Zainoor Hailmee Solihin, and Nor Fazli Adull Manan* [*]https://orcid.org/0000-0002-1062-0997	119
8	Effectiveness of RFID Smart Library Management System *Maizatul Mazni Suhaimi, Zulkifli Mohamed, and Nurul Syuhadah Khusaini*[*] [*]https://orcid.org/0000-0001-5715-9766	133
9	Structural Performance of Ti6Al4V Tibial Tray in Total Knee Arthroplasty (TKA) by Functionally Graded Lattice Structures using Numerical Analysis *Nurasyrani Rabuan, Mohd Shahriman Adenan*[*]*, Yupiter HP Manurung, Mohd Afzan Mohd Anuar, and Solehuddin Shuib* [*]https://orcid.org/0000-0002-1016-8136	153
10	Improved Mechanical Properties of Basalt and Glass Fibre Reinforced Polymer Composite by Incorporating Nano Silica *Mohamad Asrofi Muslim, Aidah Jumahat*[*]*, Shahrul Azam Abdullah, Fauziah Md Yusof, M.Z. Zahari, Mochamad Chalid, Mohd Azrul Jaafar, and Raymond Siew Teng Loy* [*]https://orcid.org/0000-0002-7994-122X	173
11	Numerical Analysis of Threaded Pin Fins Heat Sink by Natural Convection *Muhammad Firdaus Hamidan, Rosnadiah Bahsan*[*]*, Alhassan Salami Tijani, Irnie Azlin Zakaria, and Sajith Thottathil Abdulrahman* [*]https://orcid.org/0009-0007-0886-040X	185
12	Design Parameters Optimization in CNC Machining Based on Taguchi, ANOVA, and Screening Method *Armansyah*[*]*, Lilik Zulaihah, Siti Rohana Nasution, Gary Geraldus Sinaga, Juri Saedon, and Agus Sudianto* [*]https://orcid.org/0000-0001-9535-727X	209
13	Physical Properties of Graphene *Mohd Rafal Sahudin, Muhammed Zourob, Muhammad Haziq Noor Akashah, Rozina Abdul Rani, and Siti Rabizah Makhsin*[*] [*]https://orcid.org/0000-0002-3458-9592	225
14	The Densification of Hydroxyapatite from Eggshell Waste at Different Sintering Temperature *Natasha Ahmad Nawawi*[*]*, Nur Natrah Auni Ahmad, Nurul Hidayah Imaniah Noor Hamdan, and Le Thi Bang* https://orcid.org/0000-0002-1985-5522	269

Experimental Determination of High-Acceleration Shock Characteristics of Industrial Marine Fenders

David, N. V.[*]*, Adelin Khairina, M. S.*
School of Mechanical Engineering, College of Engineering,
Universiti Teknologi MARA, 40450 Shah Alam, Selangor, MALAYSIA
[*]*davidfkm@uitm.edu.my*

Vipin Gopan
Department of Mechanical Engineering,
St. Thomas College of Engineering and Technology,
689521 Chengannur, Kerala, INDIA

ABSTRACT

Engineering systems are often subject to complex loading mechanisms including accelerated mechanical shock during transportation, handling, and operations. Shock can be understood as a drastic, irregular change in acceleration experienced by an object due to impact at a very short period. This paper presents a preliminary study of the crashworthiness properties of in-service industrial marine fenders (or bumpers) intended for shock energy absorption. The peak accelerations (G_{peak}) of the test specimens are experimentally measured and compared to theoretical estimations. The energy absorptions and impact forces of the test specimens are calculated using analytical formulations. The effects of introducing tubular through-holes in the specimens on the resulting peak accelerations and thereby the shock energy absorbing capacities are also investigated. Test specimens of thicknesses ranging between 10 mm and 30 mm are subjected to half-sine shock waves between 50G and 70G, which are generated by dropping a 5-kg payload from different heights ranging from 150 mm to 280 mm onto a padded shock seat for a pulse duration between 5 and 8 ms. The analytically determined G_{peak} agrees well with the experimental values. It is found that the through-holes specimens with lower G_{peak}, resisted smaller impact forces and absorbed up to 12% lesser energy per unit mass than their solid counterparts.

ISSN 1823-5514, eISSN 2550-164X

https://doi.org/10.24191/jmeche.v12i1.24635

Received for review: 2023-07-26
Accepted for publication: 2023-10-18
Published: 2023-11-15

Keywords: *Mechanical Shock; Crashworthiness; Marine Fender; Energy Absorption; Half-Sine Wave; Impact Force*

Introduction

Shock is an incident of rapid high acceleration that may come in the form of impact and cause structural damage to the components exposed to it. Efficient energy absorption by materials and components can protect them from sudden shock at peak acceleration, i.e. G_{peak} (e.g., [1]-[3]). Crashworthiness properties of a material system such as a marine fender (see Figure 1a) are essential for product designing and life cycle analysis [4]. High shock impacts induce microcracks that can grow and propagate resulting in major fracture of the material system and industrial components (e.g., [5]-[8]). Industries pertinent to crashworthy component applications therefore routinely employ measures to lessen the post-impact damages. Mechanical shock testing experiments are designed to evaluate the capability of crashworthy components to absorb impact energy at high shock accelerations by dropping them from a certain height and measuring the resulting G_{peak}. This usually involves prior determination of the shock pulse durations and heights as the input parameters for the test (e.g., [9]-[10]). The G_{peak} and velocity change experienced by the test specimens are measured using an accelerometer and used to theoretically determine the impact force and maximum energy absorption of the specimens. G_{peak} can also be analytically calculated. In this case, the principle of conservation of energy is normally invoked to relate test parameters including drop height, h, and pulse duration, dt, to the impact force and energy absorption of the specimens (e.g., [11]-[12]). The following expression for G_{peak} is derived based on the assumption that the test system is conservative and there is no rebound of the mass during the impact (see Appendix A for derivation):

$$G_{peak} = \frac{\pi\sqrt{gh}}{dt\sqrt{2}} \tag{1}$$

The impact force, F, can be determined from the velocity change, dv, specimen mass, m, and dt as follows:

$$F = m\left(\frac{dv}{dt}\right) \tag{2}$$

Potential energy, U, of the mass at a height h from where the mass is dropped is assumed to be fully transformed to kinetic energy, T, just as it impacts the programmer at its peak velocity (see Figure 1b). Using this assumption, the maximum specific energy absorption of the specimens, SEA,

can be determined from the maximum velocity, v_{max}, and dt as follows (see Appendix A for derivation):

$$\text{SEA} = \frac{1}{2}\left(\frac{G_{peak} \times dt}{2\pi}\right)^2 \tag{3}$$

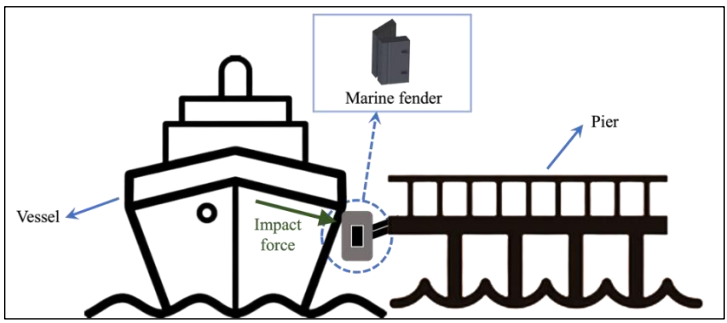

Figure 1a: Illustration of a crashworthy marine fender application: A vessel berthing at a pier and the impact force direction on the marine fender

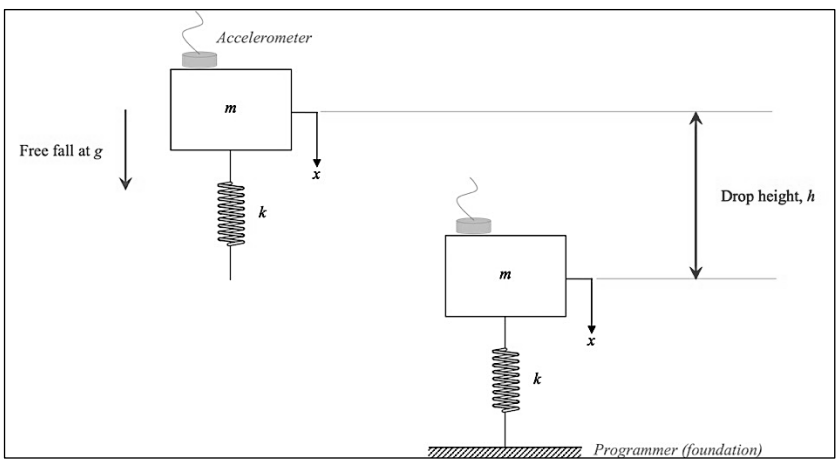

Figure 1b: Schematic modeling of a test specimen; (a) during free fall, and (b) upon impact on programmer to simulate the mechanical shock experienced by the specimen

The crashworthy properties of a marine fender including its G_{peak}, and the related F and SEA are dependent on a variety of factors including the type

and make of the fender, vessel tonnage, berthing mechanism and impact velocity, dynamic factors, and the geometrical setup of the fender installation at the docking terminal [13]. Various types of fenders for different kinds of loading applications have been studied (e.g., [14]-[16]). Marine fenders are used between 10 and 40 years in general. The physical, thermal, and mechanical properties of marine fenders particularly those made of rubber change over time from their first commercial usage due to repeated impacts and aging due to environmental conditions (e.g., seawater absorption, corrosion, UV radiation). The changes in these properties in turn affect the crashworthiness performance of the fenders in later years as reported in major marine industry standards and guidelines (e.g., [17]-[18]). However, the changes in the crashworthiness of in-service marine fenders because of prior impact and aging are not generally investigated. The present study is novel in this aspect.

In this study, the crashworthiness of an industrial marine fender block of the element type is experimentally determined. The as-is test specimen is then modified by introducing tubular through-holes to investigate the combined effects of reduced mass and geometrical change on their G_{peak} levels and thereby the shock energy absorbing capacities. This modification is intended to simulate the effects of high acceleration shock experienced by the fenders and other material systems in real-world applications (e.g., [19]-[22]). The results are further analyzed using the above theoretical formulations to determine the impact forces and SEA of the original and modified specimens.

Methods

Specimen preparation

The test specimens for the purpose of this study are sampled from an industrial-grade rubber fender (or, bumper) contributed by Malaysia Marine and Heavy Engineering Sdn. Bhd. in its pre-used condition. This marine bumper (MB) block, which is an element fender type intended for berthing oil and gas vessels, is cut into the required test dimensions using a horizontal band saw. The solid MB specimens (MB-S) have a common width of 100 mm and a length of 150 mm but differ by their thicknesses, i.e. 10 mm, 20 mm, and 30 mm which are labeled as MB1-S, MB2-S, and MB3-S, respectively. The benefit of introducing hollow sections in a solid fender on its energy absorption capability is described in [15]. The test specimens in the present study are therefore further varied by adding hollow sections of 5-mm diameter through holes, which are drilled using the ERLO TSR-32 column drilling machine. This set of specimens is labeled as MB-H. The placements of the symmetrical hollow sections are indicated in Figure 2. The specimens are shown in Figure 3 and their respective masses are listed in Table 1. It is to be noted that specimen MB2-H is heavier than MB2-S. This implies density changes within

this specimen that could have occurred during the operational service of the MB block.

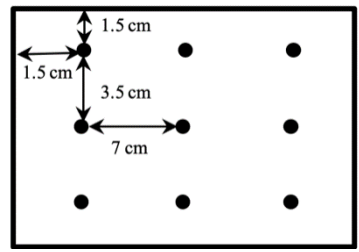

Figure 2: The positions of hollow sections in specimens MB-H

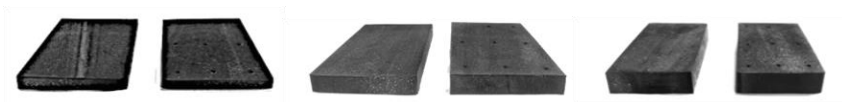

Figure 3: The array of test specimens
(*Can be viewed in 3D at https://xr.plus/yad*)

Table 1: Masses of the marine bumper specimens

Specimen ID	MB1-S	MB1-H	MB2-S	MB2-H	MB3-S	MB3-H
Mass (kg)	0.226	0.184	0.387	0.406	0.590	0.568

Experimental procedure

Trial rounds of mechanical shock testing are first conducted on pilot specimens to identify the input parameters, i.e. the combinations of height (h) and pulse duration (dt), that would provide a range of desired peak acceleration, G_{peak}, levels, i.e. 50G, 60G, and 70G. These levels correspond to the berthing energies that are normally encountered by industrial marine fenders intended for oil and gas vessels [17]. The identified input parameters are listed in Table 2.

The specimens for both pilot and actual test rounds are subjected to half-sine shock waves, which are generated by dropping a 5-kg payload onto a padded shock seat in an ASLI SS-5 high acceleration mechanical shock tester based on the MIL-STD 810 standard (Method 516, Procedure 1) [23] (see Figure 4). Specimens for the actual test rounds are subjected to three drops each at the identified input parameters.

The experimentally measured peak accelerations (G_{peakEx}), dv, and dt for each specimen for all the three drops are logged. The average G_{peakEx} values are compared to analytical peak accelerations, G_{peakAn}, that are determined

using Equation 1. The impact forces and energy absorptions of the specimens are then determined from Equations 2 and 3, respectively.

Table 2: Input parameters identified for each test specimen

Desired G_{peak}		Specimens					
		MB 1 (t = 10 mm)		MB 2 (t = 20 mm)		MB 3 (t = 30 mm)	
G	m/s^2	H (mm)	dt (ms)	h (mm)	dt (ms)	h (mm)	dt (ms)
50	490.5	170	8	150	8	160	7
60	588.6	220	6	180	6	200	6
70	686.7	280	6	240	5	240	5

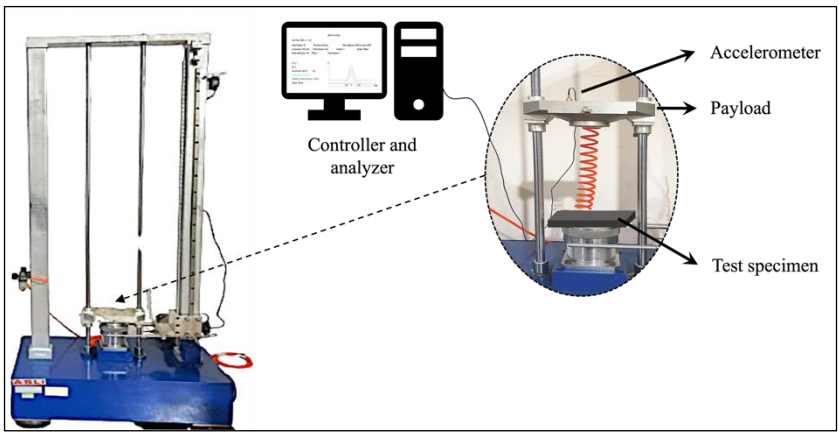

Figure 4: Experimental setup of the mechanical shock tester

Results and Discussions

Validation of input parameters

The input parameters listed in Table 2 need to be validated in producing the desired accelerations on the specimens. Table 3 lists the output G_{peakEx} values for all the specimens in response to the respective input parameters during the trial rounds. The median G_{peakEx} values at each desired acceleration are shown in Figure 5. The standard deviations of G_{peakEx} at the desired accelerations of 50G, 60G, and 70G are 40.7 m/s^2, 35.3 m/s^{2,} and 16.8 m/s^2, respectively. This represents a variation of not more than 8% from the intended input accelerations onto the specimens.

Table 3: Trial round experimental peak accelerations (G_{peakEx}) in response to the input parameters listed in Table 2

Desired G_{peak}		G_{peakEx} (output)					
G	m/s^2	MB1-S	MB1-H	MB2-S	MB2-H	MB3-S	MB3-H
50	490.5	527.3	516.9	581.2	470.4	504.7	473.8
60	588.6	644.5	611.6	590.4	543.4	565.1	594.5
70	686.7	720.4	711.4	674.3	697.0	694.3	685.3

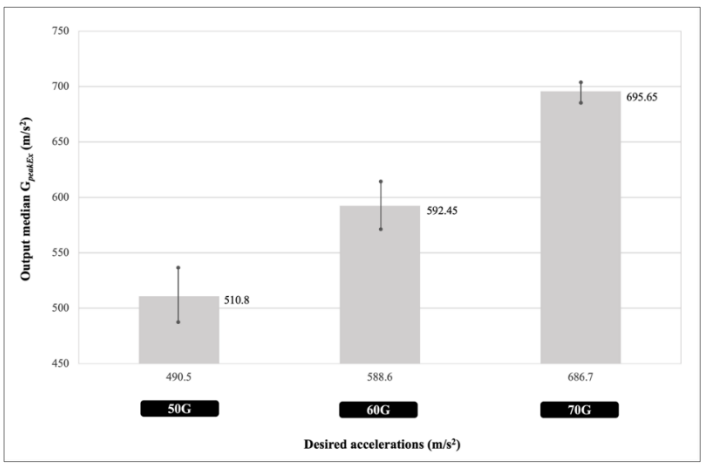

Figure 5: Median G_{peakEx} values (indicated at top right corner of each bar) at the desired accelerations of 50G, 60G, and 70G

Experimental and analytical shock acceleration responses

The shock acceleration responses of the specimens at 50G, 60G, and 70G inputs during the actual drop tests, i.e. G_{peakEx}, are shown in Figures 6, 7, and 8 for specimens MB-1, MB-2, and MB-3, respectively. These figures also include the corresponding values of G_{peakAn}. The correlation strength between G_{peakEx} and G_{peakAn} is indicated by the R^2 values.

The R^2 values, which lie between 0.9848 and 1, signify a strong correlation between G_{peakEx} and G_{peakAn}. This indicates that the analytically determined shock accelerations agree well with that of the experimental values. The analytical expression in Equation 1 can therefore be reliably employed to predict the acceleration response of the marine fender specimens. Figures 5, 6, and 7 also show that the peak accelerations are generally greater for the solid specimens than the hollow ones. This observation is further examined in the next two sections.

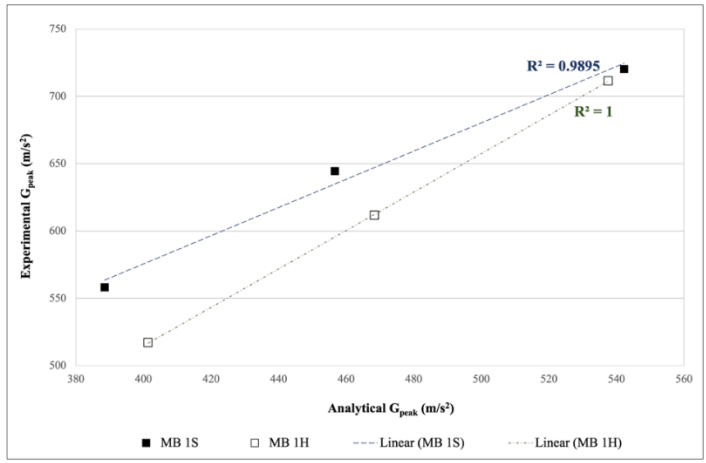

Figure 6: Experimental and analytical shock acceleration responses of specimen MB-1 (t = 10 mm)

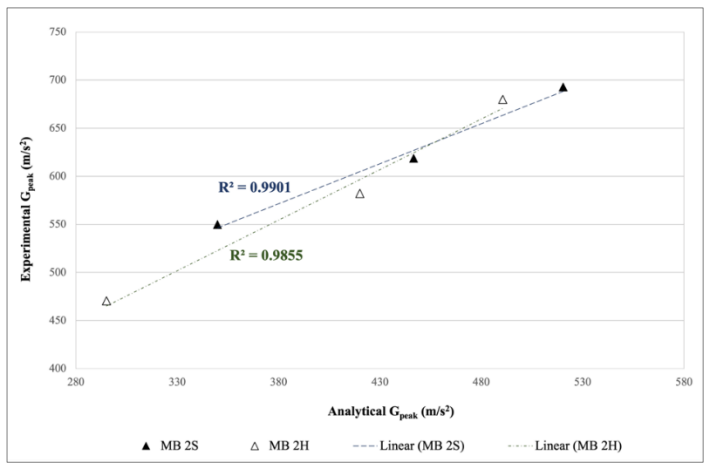

Figure 7: Experimental and analytical shock acceleration responses of specimen MB-2 (t = 20 mm)

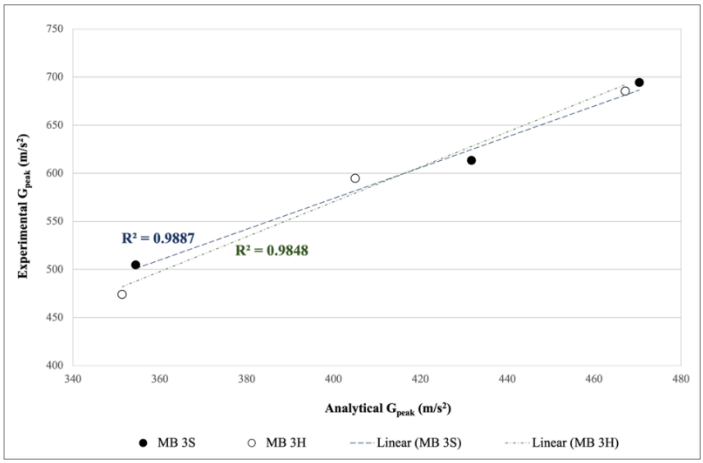

Figure 8: Experimental and analytical shock acceleration responses of specimen MB-3 (t = 30 mm)

Effect of specimen thickness on shock response

The experimentally measured shock responses of the specimens are analyzed based on the effect of their thickness on the resulting peak accelerations. Figures 9, 10, and 11 show the G_{peakEx} values for increasing specimen thicknesses at constant input accelerations of 50G, 60G, and 70G, respectively. It is observed that the G_{peakEx} values decreased for thicker specimens. Since the density and lateral dimensions of all specimens are comparable, thicknesses therefore correspond linearly to specimen masses. This illustrates the effect of increased thickness in lowering the peak acceleration experienced by the specimen. Besides, the pulse durations, dt, are shorter for thicker specimens and at higher input accelerations. Hence the influence of thickness (i.e., mass) on dt and G_{peakEx}, which in turn affects the ensuing impact force and energy absorption capacity of the specimens. These aspects will be discussed in the next two sections.

The effect of reduced mass of the hollow-sectioned specimens of similar thickness on is G_{peakEx} also evident in Figures 9, 10, and 11. G_{peakEx} of the hollow specimens are on average 5% lower than that of the solid specimens for a given thickness and at a given input acceleration. The tubular hollow section thus affected the deformation and energy-absorbing mechanism of the MB specimens. Similar findings for polymeric material systems were reported in [21] and [24]. The effects of the profile and size of through holes on the shock characteristics of MB specimens will be treated in a separate study.

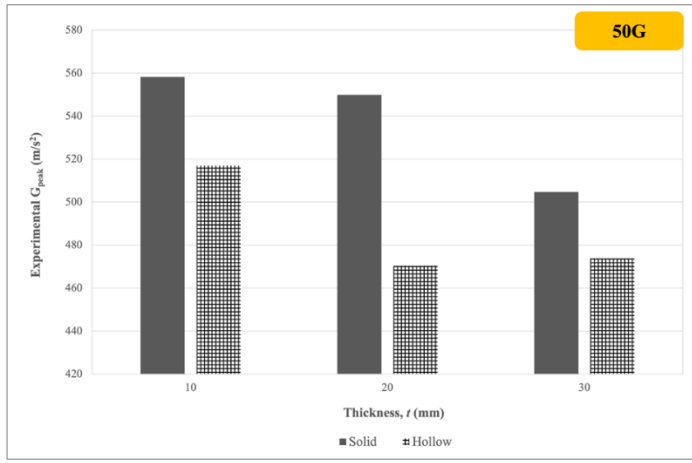

Figure 9: Experimental shock acceleration responses as a function of specimen thickness at 50G input

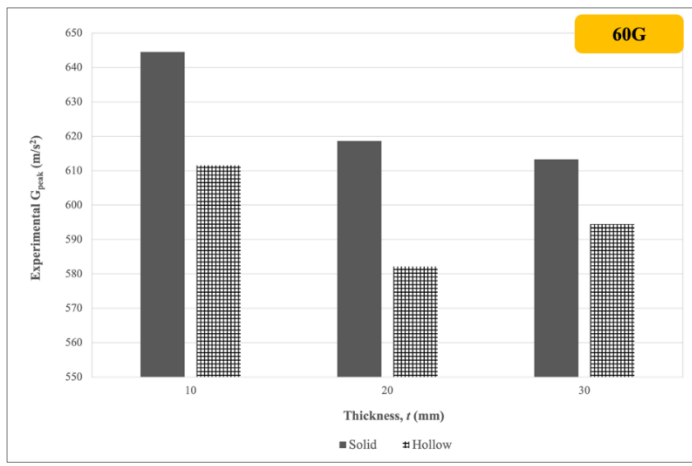

Figure 10: Experimental shock acceleration responses as a function of specimen thickness at 60G input

Effect of velocity change and pulse duration on impact force

Figures 12, 13, and 14 show the analytically determined impact forces at 50G, 60G, and 70G for specimens MB-1, MB-2, and MB-3, in order. The impact forces are calculated using Equation 2 and the experimentally measured velocity change, *dv*, and pulse duration, *dt*. Impact force here is defined as the

force that delivers the shock in a relatively short period of time (i.e., *dt*) when the specimen and the programmer get in contact (see Figure 1b).

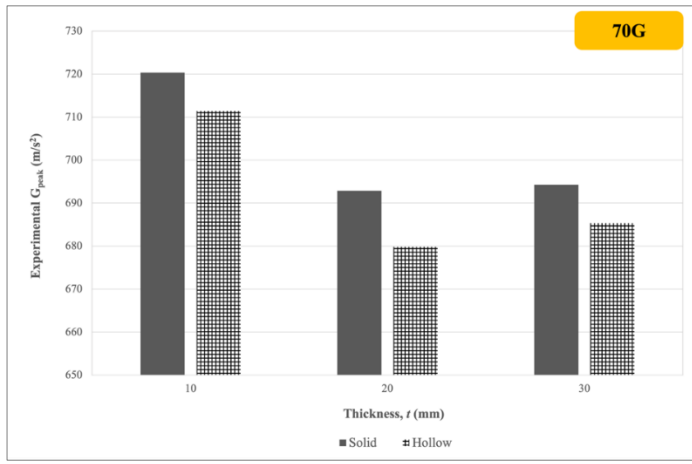

Figure 11: Experimental shock acceleration responses as a function of specimen thickness at 70G input

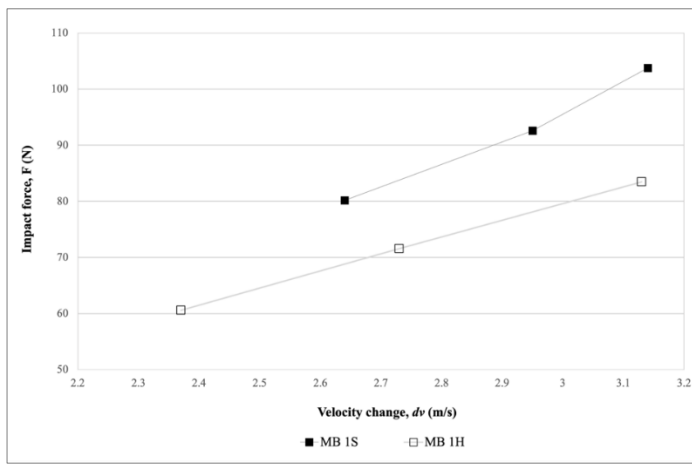

Figure 12: Impact force of specimen MB-1 (t = 10 mm) at 50G, 60G, and 70G

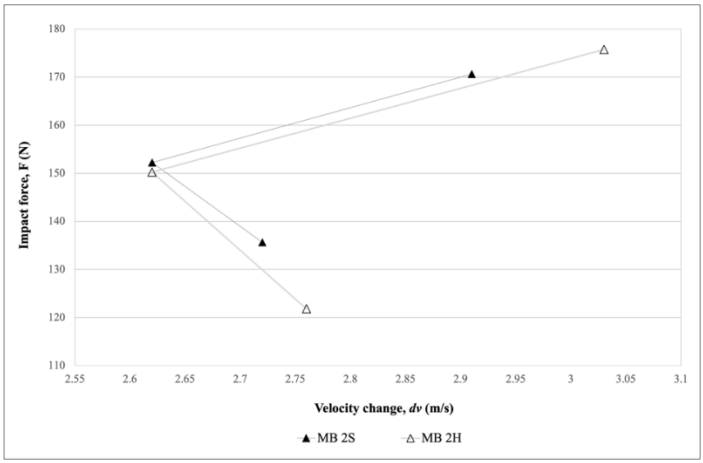

Figure 13: Impact force of specimen MB-2 (t = 20 mm) at 50G, 60G, and 70G

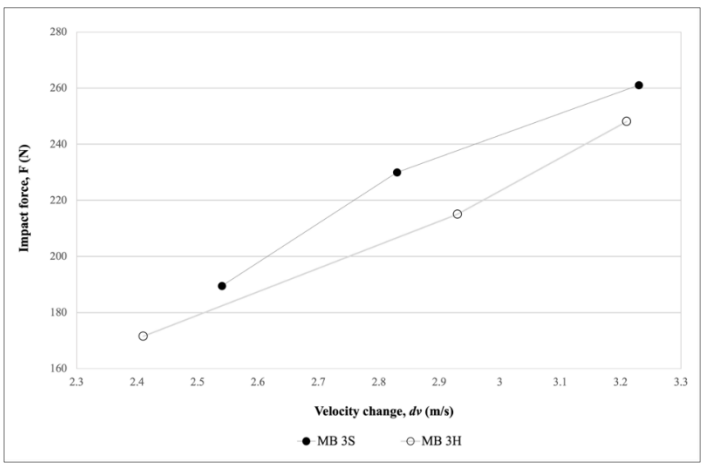

Figure 14: Impact force of specimen MB-3 (t = 30 mm) at 50G, 60G, and 70G

Specimens MB-1 and MB-3 exhibit a linear relationship between dv and the resulting impact force as per Equation 2. However, specimen MB-2, which has a non-uniform mass distribution (see section "Specimen Preparation"), showed a greater inverse dependency on *dt* than its linear relationship with *dv*. In general, impact forces are higher for the solid specimens compared to the hollow specimens. Solid specimens resisted greater

impact forces compared to the hollow specimens as thickness increases from MB-1 to MB-3, which indicates the overriding influence of mass on impact force.

Specific energy absorption

The energy absorbed per unit mass, i.e. specific energy absorption (*SEA*), of the specimens, is determined using Equation 3 and listed in Table 4. The *SEA* of specimens MB-1H and MB-3H are smaller than their solid counterparts by, in order, 11% and 1% on average. Specimen MB-2H, however, has a 6% greater *SEA* than MB-2S. This finding is consistent with that made in section "Effect of specimen thickness on shock response" on the effect of increasing thickness (and thereby, mass) on G_{peak} of MB-2.

Table 4: Specific energy absorption of the marine bumper specimens

Input	Specific energy absorption (J/kg)					
G	MB1-S	MB1-H	MB2-S	MB2-H	MB3-S	MB3-H
50	0.218	0.175	0.231	0.237	0.202	0.181
60	0.273	0.233	0.215	0.215	0.251	0.268
70	0.307	0.305	0.265	0.287	0.325	0.321

The shorter pulse durations for thicker specimens and at higher input accelerations, i.e. greater G_{peakEx} (see section "Experimental and analytical shock acceleration responses"), have an intricate consequence on their *SEA*. Clearly, from Equation 3, larger G_{peakEx} and shorter *dt* will have a leveling net effect on *SEA*. The specimens however registered an average reduction of 30.3% in dt (see Table 2) and a 36.2% increment in median G_{peakEx} (see Figure 5) when the input acceleration is increased from 50G to 70G. This substantiates the higher *SEA* of the specimens at larger input accelerations as can be seen in Table 4. The solid specimens absorbed up to 12% more energy per unit mass than their hollow counterparts. Comparable observations are made in [25]-[27] for a variety of material systems.

Conclusion

The crashworthiness characteristics of an industrial marine fender block are experimentally studied. The as-is test specimen is modified by introducing tubular through-holes to simulate the effects of high acceleration shock experienced by the fender in the real world. Test specimens of 10 mm, 20 mm, and 30 mm thicknesses are subjected to half-sine shock waves for a pulse duration between 5 and 8 ms at desired input accelerations of 50G, 60G, and 70G. Input parameters including drop height and pulse duration (*dt*) that would provide the desired accelerations are identified and validated by correlating the

measured peak acceleration (G_{peakEx}) levels to the theoretically estimated peak acceleration (G_{peakAn}) values. The coefficients of correlation, which lie between 0.9848 and 1, indicate that the analytically determined shock accelerations agree well with that of the experimental values. The combined effects of reduced mass and geometrical change on the G_{peakEx} of the hollow specimens are measured. The specific energy absorption and impact force values of the specimens are then analytically determined. It is found that the through-holes specimens have lower G_{peak} levels, resist smaller impact forces, and absorb up to 12% lesser energy per unit mass than their solid counterparts. This preliminary study also indicates that the impact force of the 20-mm specimen with a non-uniform mass distribution has a greater inverse dependency on dt than its linear relationship with velocity change, dv. Further study will be conducted to investigate the effects of pre-straining and mass distribution on G_{peak}.

Contributions of Authors

The authors confirm the equal contribution in each part of this work. All authors reviewed and approved the final version of this work. David worked on the experimental and data analysis parts alongside with Adelin. Vipin contributed equally on the manuscript drafting and copyreading parts.

Funding

This work received no specific research grant from any funding agency.

Conflict of Interests

All authors declare that they have no conflicts of interest with any party.

Acknowledgment

The authors thank the School of Mechanical Engineering, College of Engineering, Universiti Teknologi MARA, Shah Alam, Malaysia and the Department of Mechanical Engineering, St. Thomas College of Engineering and Technology, Kerala, India for the technical and administrative supports. Malaysia Marine and Heavy Engineering Sdn. Bhd. is thanked for the contribution of the as-is industrial marine fender specimen.

References

[1] X. Guo, J. Deng, and Z. Cao, "Study on the propagation characteristics of pressure wave generated by mechanical shock in leaking pipelines," *Process Safety and Environmental Protection*, vol. 164, pp. 706–714, 2022.

[2] A. M. Asyraf and A. Yulfian, "Rectangular honeycomb structure as absorber structure for road crashed barrier application," *AIP Conference Proceedings*, vol. 2643, no. 1, p. 050068, 2023. https://doi.org/10.1063/5.0110748

[3] V. David and M. Azlan, "Moisture Absorption Properties and Shock Cushioning Characteristics of Bio-Based Polyurethane Foam Composites," *Journal of Mechanical Engineering*, vol. SI 5, no. 2, pp. 157-168, 2018.

[4] Z. Zhang, Z. Xu, X. Shao, Y. Li, and B. Li, "Damage boundary of piezoresistive pressure sensor under shock environment," *Acta Astronautica*, vol. 192, pp. 328–340, 2022. https://doi.org/10.1016/j.actaastro.2021.12.040

[5] D. F. Ledezma-Ramírez, P. E. Tapia-González, M. J. Brennan, and P. J. Paupitz Gonçalves, "An experimental investigation into the shock response of a compact wire rope isolator in its axial direction," *Engineering Structures*, vol. 262, p. 114317, 2022. https://doi.org/10.1016/j.engstruct.2022.114317

[6] F. Mannacio, A. Barbato, F. di Marzo, M. Gaiotti, C. M. Rizzo, and M. Venturini, "Shock effects of underwater explosion on naval ship foundations: Validation of numerical models by dedicated tests," *Ocean Engineering*, vol. 253, p. 111290, 2022. https://doi.org/10.1016/j.oceaneng.2022.111290

[7] Q. Yu, H. Zhang, R. Yang, Z. Cai, and K. Liu, "Experimental and numerical study on the effect of electrohydraulic shock wave on concrete fracturing," *Journal of Petroleum Science and Engineering*, vol. 215, p. 110685, 2022. https://doi.org/10.1016/j.petrol.2022.110685

[8] W. Salman et al., "A high-efficiency energy regenerative shock absorber using helical gears for powering low-wattage electrical device of electric vehicles," *Energy*, vol. 159, pp. 361–372, 2018. https://doi.org/10.1016/j.energy.2018.06.152

[9] W. Li et al., "Magnetorheological semi-active shock mitigation control. Part I: Numerical analysis and preliminary tests," *Journal of Intelligent Material Systems and Structures*, vol. 34, no. 16, pp. 1885-1901, 2023. https://doi.org/10.1177/1045389X221151071

[10] I. Muhammad Zahid, I. Asif Israr, and A. Tanveer, "Semi active control of sinusoidal shock waveform on drop test machine (DTM) using non-

linear dynamic model of hybrid wave generator (HWG) consisting of rubber and electromagnet," *Review of Scientific Instruments*, vol. 94, p. 035005, 2023. https://doi.org/10.1063/5.0124138

[11] M. Spielbauer, P. Berg, J. Soellner, J. Peters, F. Schaeufl, C. Rosenmüller, O. Bohlen, and A. Jossen, "Experimental investigation of the failure mechanism of 18650 lithium-ion batteries due to shock and drop," *Journal of Energy Storage*, vol. 43, p. 103213, 2022. https://doi.org/10.1016/j.est.2021.103213

[12] F. Lei, X. Lv, J. Fang, Q. Li, and G. Sun, "Nondeterministic multi-objective and multi-case discrete optimization of functionally-graded front-bumper structures for pedestrian protection," *Thin-Walled Structures*, vol. 167, p. 106921, 2021. https://doi.org/10.1016/j.tws.2020.106921

[13] Z., Jiang, and M., Gu, "Optimization of a fender structure for the crashworthiness design," *Materials & Design*, vol. 31, no. 3, pp. 1085–1095, 2010. https://doi.org/10.1016/j.matdes.2009.09.047

[14] H. Kawakami, "The use of marine fenders as energy absorbing damper units in mooring systems," in Bratteland, E. (eds) Advances in Berthing and Mooring of Ships and Offshore Structures. NATO ASI Series, vol. 146. Springer, Dordrecht, 1988. https://doi.org/10.1007/978-94-009-1407-0_33

[15] J., Tuleja, K., Kędzierska, M., Sowa, and P. Galor, "Evaluation of the possibility of increasing the energy absorption efficiency of fender devices using the example of cylindrical fenders with additional structural elements applied," *Energies*, vol. 16, no. 3, p. 1165, 2023. https://doi.org/10.3390/en16031165

[16] P. H., Mott and C.M., Roland, "Aging of Natural Rubber in Air and Seawater," *Rubber Chemistry and Technology*, vol. 74, no. 1, pp. 79–88, 2001. https://doi.org/10.5254/1.3547641

[17] Guidelines for design and testing of rubber fender systems (June 2019), Coastal Development Institute of Technology, Japan, 2019. https://www.cdit.or.jp/english/tech/FenderDesignTestGuideline.pdf

[18] R., Iversen, A., Roubos, and P., Mirihagalla, "PIANC Working Group 211: Reliability based design of marine fenders – No more abnormal berthing factor," *American Society of Civil Engineers*, vol. 1, pp. 1435 – 443, 2022. https://doi.org/10.1061/9780784484395.044

[19] H. Taghavifar, A. Modarres Motlagh, A. Mardani, A. Hassanpour, A. Haji Hosseinloo, and C. Wei, "The induced shock and impact force as affected by the obstacle geometric factors during tire-obstacle collision dynamics," *Measurement*, vol. 84, pp. 47–55, 2016. https://doi.org/10.1016/j.measurement.2016.02.003

[20] Y. Liu, T. A. Schaedler, and X. Chen, "Dynamic energy absorption characteristics of hollow microlattice structures," *Mechanics of*

Materials, vol. 77, pp. 1–13, 2014. https://doi.org/10.1016/j.mechmat.2014.06.008

[21] M.A. Mahamood, N. Mohamad, A.R. Jeeffeerie, A.H. Mohd Zain, M.I. Shueb, and H.E. Ab Maulod., "Correlation of open cell structure with properties of green rubber foam from epoxidised natural rubber/reclaimed rubber glove," *Journal of Mechanical Engineering*, vol. SI 1, no. 1, pp. 113-122, 2016.

[22] S. G. Gomez, A. Irigoyen, S. Gonzalez, K. Estala-Rodriguez, E. Shafirovich, Md Sahid Hassan, S. Zaman, and Y. Lin., "Fabrication and characterization of hollow polysiloxane microsphere polymer matrix composites with improved energy absorption," *Journal of Composites Science*, vol. 7, no. 3, pp. 1-18, 2023. https://doi.org/10.3390/jcs7030098

[23] Military Specification (MIL)-STD-810G Test Method 516 (Shock Test), Environmental Engineering Considerations and Laboratory Tests, US Department of Defense, 2008.

[24] K. Szklarek, M. Kotełko, and M. Ferdynus, "Crashworthiness performance of thin-walled hollow and foam-filled prismatic frusta – FEM parametric studies – Part 1," *Thin-Walled Structures*, vol. 181, p. 110046, 2022. https://doi.org/10.1016/j.tws.2022.110046

[25] B. Jiang, X. Chen, J. Yu, Y. Zhao, Z. Xie, and H. Tan, "Energy-absorbing properties of thin-walled square tubes filled with hollow spheres," *Thin-Walled Structures*, vol. 180, p. 109765, 2022. https://doi.org/10.1016/j.tws.2022.109765

[26] A. Sadighi, A. Eyvazian, M. Asgari, and A. M. Hamouda, "A novel axially half corrugated thin-walled tube for energy absorption under axial loading," *Thin-Walled Structures*, vol. 145, p. 106418, 2019. https://doi.org/10.1016/j.tws.2019.106418

[27] J. Li, C. Tian, W. Hong, S. Duan, Y. Zhang, W. Wu, G. Hu, R. Xia, "Shock responses of nanoporous gold subjected to dynamic loadings: Energy absorption," *International Journal of Mechanical Sciences*, vol. 192, p. 106191, 2021. https://doi.org/10.1016/j.ijmecsci.2020.106191

APPENDIX A

Derivation of an expression for peak acceleration, G_{peak}, during shock impact.

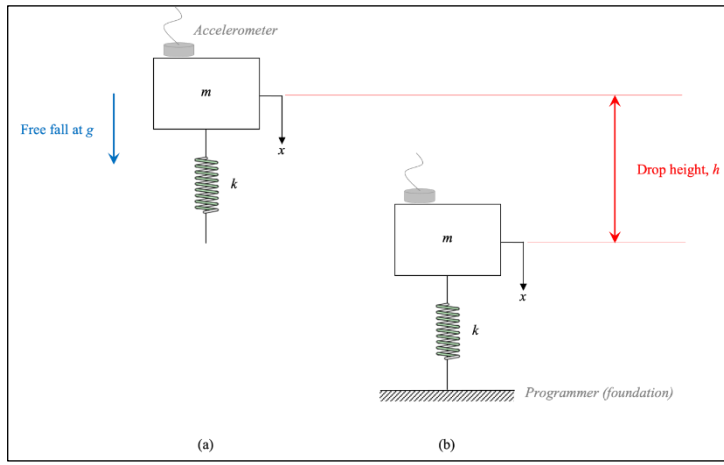

Figure A1: (a) Test specimen during free fall, and (b) test specimen during impact

Free body diagram (at impact)

Note: Static displacement force, $k\Delta$, where Δ is the displacement of the spring from the static equilibrium position (SEP) prior to motion of the system, is balanced by the weight of the mass, mg, i.e $k\Delta = mg$.

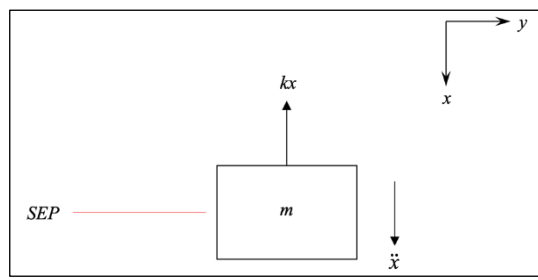

Figure A1: Free body diagram

Equation of motion

Using the Newton's Second Law of Motion:

$$+\downarrow \Sigma F = ma$$

$$\Rightarrow w - k(\Delta + x) = ma \quad : \quad a = \ddot{x}$$

Since $k\Delta = w = mg$,

$$\Rightarrow -kx = m\ddot{x}$$

$$\therefore m\ddot{x} + kx = 0 \tag{1}$$

By applying the definition of natural frequency, $\omega_n = \sqrt{\frac{k}{m}}$ in Equation 1,

$$\therefore \ddot{x} + \omega_n^2 x = 0 \tag{2}$$

Assuming a solution to Equation 2 in the following form:

$$x(t) = A\sin(\omega_n t + \varphi) \tag{3}$$

where A is the amplitude of oscillation and φ is the phase shift between input (impulse force) and output (resulting displacement).

The peak velocity, $\dot{x}_{max}$, and peak acceleration, $\ddot{x}_{max}$, can be obtained from Equation 3 as follows:

$$\dot{x}_{max} = A\omega_n \tag{4}$$

$$\ddot{x}_{max} = A\omega_n^2 \tag{5}$$

Using Equations 4 in 5, the expression of peak acceleration can be rewritten as:

$$\ddot{x}_{max} \equiv G_{peak} = \dot{x}_{max}\omega_n \tag{6}$$

This concludes the basic derivation of an expression for the peak acceleration experienced by the test sample during a shock testing in terms of its peak velocity. The principle of conservation of energy will be invoked next to relate this expression to the test parameters including drop height, h, and pulse duration, dt.

The potential energy, U, of the mass at a height h from where the weight is dropped is assumed to be fully transformed to kinetic energy, T, just as it impacts the programmer at its peak velocity, $\dot{x}_{\max} \equiv v$. In this case,

$$\Rightarrow U = T$$
$$\Rightarrow mgh = \frac{1}{2} mv^2 \tag{7}$$

Rearranging Equation 7 for the peak velocity gives;

$$\therefore v \equiv \dot{x}_{\max} = \sqrt{2gh} \tag{8}$$

Substituting Equation 8 and $\omega_n = \frac{2\pi}{dt}$ where dt is the pulse duration of the impact into Equation 6 yields the final expression of G_{peak} as follows:

$$\therefore G_{\text{peak}} = \frac{\pi\sqrt{gh}}{dt\sqrt{2}} \tag{9}$$

It is to be noted that this expression is subject to the assumption that the system is conservative and there is no rebound of the impactor mass (not the test specimen) during the impact.

Derivation of an expression for specific energy absorption, *SEA*, of the test specimen

Potential energy, U, of the mass at a height h from where the mass is dropped is assumed to be fully transformed to kinetic energy, T, just as it impacts the programmer at its peak velocity (see Figure A1b). Using this assumption, the maximum specific energy absorption of the specimens, SEA, can be determined from the maximum velocity, v_{max}, from Equations 8 and 9 as follows:

$$\Rightarrow T_{max} = \frac{1}{2} m v_{max}^2 \tag{10}$$

$$\Rightarrow SEA = \frac{T_{max}}{m} \tag{11}$$

Substituting v_{max} from Equation 8 into Equation 10 gives:

$$\Rightarrow SEA = \frac{1}{2}(2gh) \tag{12}$$

Substituting gh from Equation 9 into Equation 12 yields:

$$\therefore SEA = \frac{1}{2}\left(\frac{G_{peak} \times dt}{2\pi}\right)^2$$

The Effect of Cobalt Alloy Nanocrystalline Coating on Tensile Properties and Surface Performance of Mild Steel

*Mohd Zakuan Zabri, Nik Rozlin Nik Masdek**
School of Mechanical Engineering, College of Engineering,
Universiti Teknologi MARA, 40450 Shah Alam, Selangor, MALAYSIA
**nikrozlin@uitm.edu.my*

Koay Mei Hyie
Centre for Mechanical Studies, Universiti Teknologi MARA,
Pulau Pinang Branch, Permatang Pauh Campus, 13500 Pulau Pinang,
MALAYSIA

ABSTRACT

Coatings are frequently used to enhance the mechanical and physical characteristics of mild steel by protecting mild steel surfaces against corrosion. Corrosion might attack surface without proper coating method which may lead to structural failures and increase maintenance cost. The main objective of this study is to investigate the effect of CoNiFe nanocrystalline coating on surface roughness, hardness, and tensile performance of mild steel substrate. Different parameters were introduced, such as current, pH, deposition times and heat treatment to analyse surface roughness, hardness, and tensile strength of CoNiFe nanocrystalline coating. The lowest surface roughness of 2.14 µm was recorded by CoNiFe nanocrystalline coating with 30 minutes deposition time at pH 3, I: 3 A and heat treated, while the highest recorded surface roughness of 4.233 µm was detected on uncoated mild steel. The highest improvement of microhardness was observed on CoNiFe nanocrystalline coating with 45 minutes deposition time at pH 3, I: 1.5 A and heat treated (393.6 Hv) as compared to the uncoated mild steel (171.44 Hv). Tensile performance of CoNiFe nanocrystalline coating with 45 minutes deposition time at pH 3, I: 1.5 A and heat treated was the highest with yield stress and ultimate tensile stress of 472.35 MPa and 559.11 MPa, respectively. The lowest tensile performance was recorded by uncoated mild steel with yield stress and ultimate tensile stress of 149.40 MPa and 186.78 MPa, respectively.

ISSN 1823-5514, eISSN 2550-164X
Received for review: 2023-08-30
Accepted for publication: 2023-10-18
Published: 2023-11-15

https://doi.org/10.24191/jmeche.v12i1.24636

CoNiFe nanocrystalline coating has considerably improved the mild steel surface roughness, hardness and tensile strength which indicate superior mechanical properties for future engineering application.

Keywords: *CoNiFe; Deposition Time; Tensile; Surface Properties; Hardness*

Introduction

Surface coatings have been applied in several engineering applications to cordon and increases the lifespan of components exposed to corrosive environment [1]. In order to build, operate and protect electronics, machinery, construction and structural systems in harsh environments, nanoparticle alloy coatings with excellent mechanical and corrosion resistance are needed [2]. According to statistics, the annual maintenance cost for corrosion alone is estimated to cost millions of dollars, making it necessary to provide assistance and preventive measures to mitigate the consequences of erosion [3].

According to a study, uncoated metal surface cannot match the corrosion resistance and polarization resistance of nanocomposite coatings surface [4]. Therefore, adding a layer would significantly improve the strength and wear of mild steel. Electrodeposition technique is the best and most straightforward way of embedding nanocrystalline materials coating onto metal surfaces. In electrodeposition, an electric current is passed through a chemical solution to create an ionic solution, which allows the counter electrode's to be transferred to the working electrode's surface and form a coating. Electrodeposited coatings enhance the life cycle of the components used for various applications, besides being cost-effective, faster speed of deposition rate, and ease of control over the nanocoating fabrication process [5]. Popular electrodeposition materials such as Ni-P, Ni-W, Ni-P-W, Ag/Pd, Cu/Ag, Co/Ni, Co/Ag, and Zn-Ni are among the metals that have been extensively explored [6]-[8]. Co, Ni and Fe nanoparticles trio combination is chosen due to the existing excellent performance of each individual nanoparticles. Variable processing parameters such as electrolyte pH, temperature, deposition time, current density, and electrolyte composition govern the coatings' characteristics and performance during the electrodeposition process [9].

CoNiFe is being used for several applications. Yang et al. [10] in his research work on both air thermal stability and solar selectivity of CoNiFe oxide coating fabricated by facile sol-gel method and fast spraying process discovered that by optimizing the ratio of three transition metal nitrates, annealing temperature, and the number of spraying layers, the Solar Selective Absorber Coatings (SSACs) with solar absorptance of 0.93 and vertical emittance of 0.11 were obtained which is good for solar absorber indication. Barati Darband et al. [11] in their study highlighted the usage of CoNiFe alloy

as effective and stable electrocatalyst. In this research, self-made Ni-Fe-Co electrode was developed using electrodeposition method. The fabricated electrocatalyst exhibited excellent properties for the evolution of hydrogen and oxygen.

Chaudhary et al. [12] developed ternary Fe-Co-Ni alloy system in search of the next generation rotating electrical machine which possesses high curie temperature, mechanically strong and magnetic soft magnet. The authors discovered that Co-lean alloys exhibited good combination of magnetic, mechanical, and electrical properties but low Curie temperatures. Ledwig et al. [13] in their research of electrodeposited Ni-Co-Fe nanocrystalline coating on copper plate determined the properties required for good-quality MEMS components. Ledwig et al. [13] concluded that Ni-Fe-Co coatings exhibit soft magnetic properties with coercivity below 23 Oe, besides discovering that the corrosion resistance of Ni-Co-Fe coatings is satisfactory with notation that the higher Fe content leads to the deterioration of the corrosion resistance. Ledwig et al. [13] suggested that Ni-Fe-Co coating could be a promising material for MEMS application.

Heat treatment technique is an additional approach for enhancing the performance of the coating. The heating and cooling processes change the composition and structure of metals and alloys [14]. Depending on the materials used and the desired outcomes, various heat treatment processes, such as annealing, tempering, normalizing, and hardening, can increase a material's strength. Heat treatment enhances the strength, flexibility, and toughness of metals and alloys. Arias et al. [15] evaluated the effect of heat treatment on tribological properties of Ni-B coatings on low carbon steel. According to the finding, the hardness and Young Modulus of Ni-B coatings were improved, and the value recorded was 1.6 times higher compared to untreated coatings after implementing heat treatment process, due to grain refinement process during heating.

The tensile test, which involves applying a controlled tension to a specimen until failure, is a crucial and common engineering test used for all metallic materials. It provides information about the material's yield strength, elongation at break, ultimate tensile strength, Young's modulus, and other properties [16]. Strain rate, or the rate at which the specimen under test deforms, is a critical tensile test variable that is controlled within specified limits based on the type of test being done.

This paper will assess the surface roughness and hardness, besides conducting tensile test to determine the impact of the Cobalt-Nickel-Iron (CoNiFe) nanocrystalline coating on the tensile performance of coated mild steel, and evaluate the impact of deposition time, varying current and additional heat treatment process on the strength and hardness of coating. It is expected that both yield and ultimate tensile strength of the mild steel substrate will improve with the application of CoNiFe nanocrystalline coating. This may be due to the fact that hard coating could suppress the initiation of cracks; as

such, higher stress is needed for crack initiating. During the crack propagation period, the hard coating cracked at a relative higher velocity, which led to the cracking of the ductile substrate and elongation reduction [17]. It is also expected that both surface roughness and microhardness of the mild steel substrate will improve with the application of CoNiFe nanocrystalline coating.

Methodology

Sample preparation

Material used for this study was uncoated mild steel substrate. Mild steel plates with 2 mm thickness were subsequently cut into the dimensions of 100 mm x 16 mm using a water jet machine, before further cutting them into dog bone forms with size that adheres to ASTM E466 standard as illustrated in Figures 1a and b. In order to promote uniformity and comparability throughout the studies, the sizes of the samples are kept fixed using water jet cutting machine with the data obtained from CATIA format drawing file (.dxf) for precision cutting process. The usage of water jet cutter also ensures that the cutting process leaves no noticeable flaws in the finished products, which could hinder testing results.

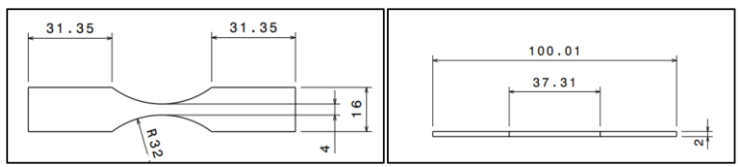

(a) (b)

Figure 1: Dimension of dog bone; (a) front view; and (b) top view

Bath preparation and electroplating process

In this study, mild steel samples were coated with CoNiFe nanocrystalline coating. Current, electrolyte pH and deposition times were among the manipulated variables tested throughout electrodeposition process.

The solution was prepared through the mixture of several sulphate-based powders such as Cobalt sulphate ($CoSO_4$), Nickel sulphate ($NiSO_4$), Iron sulphate ($FeSO_4$) and ascorbic acid (C_6 H_8 O_6). The remaining two powders coming from Boric acid (H_3 BO_3) and saccharin (C_7 H_4 NO_3 S) were added as pH buffer and grain refinement agent respectively. Table 1 shows the chemical composition used to produce an electrolyte for the coating process. The electrolyte solution was created by mixing the ingredients and heating them to 50±3°C, which was maintained throughout the electrodeposition process. A magnetic stirrer was used to swirl the electrolyte

mixture to ensure that a homogenous mixture was obtained. In addition, the solution pH was carefully observed, where potassium hydroxide (KOH) solution was added until pH 3 was reached before starting the electrodeposition process.

Table 1: Chemical composition of electrolyte solution

Compound	No. of moles
Cobalt Sulphate ($CoSO_4$)	0.050
Nickel Sulphate ($NiSO_4$)	0.133
Iron (II) Sulphate ($FeSO_4$)	0.020
Boric Acid ($H_3\ BO_3$)	0.267
Ascorbic Acid ($C_6\ H_8\ O_6$)	0.067
Saccharine($C_7\ H_5\ NO_3\ S$)	0.007

Electroplating is a well-known method of depositing metal coatings onto a substrate. The principle behind the electroplating process works by the reaction of metal ions in an acidic electrolyte which comprises a mixture of soluble Co, Ni, and Fe ions inside the similar bath container. For a normal soluble anode, the reaction of metal ions formed is as follows:

$$Co + 2e^- = Co^{2+} \quad (1)$$
$$Ni + 2e^- = Ni^{2+} \quad (2)$$
$$Fe + 2e^- = Fe^{2+} \quad (3)$$

When an insoluble anode (platinum mesh plate) is introduced, oxygen evolves:

$$2H_2O + 4e^- = O_2 + 4H^+ \quad (4)$$

At the cathode, the main reaction is Co, Ni, and Fe deposition, as described by Equations (1), (2), and (3). Hydrogen evolution takes place as a secondary reaction at the cathode surface:

$$2H^+ + 2e^- = H_2 \quad (5)$$

If the electrolyte/electrode movement is limited due to the reduction of metal Ion quantity in the bath, the secondary reaction in Equation (5) reduces current efficiency and local pH, which can result in deposit porosity due to hydrogen gas bubbles sticking to the coating surface [18]. Figure 2 depicts a schematic diagram of the electrodeposition process setup.

Throughout electrodeposition process, mild steel samples were linked to the cathode, while the platinum plate was attached to anode. The current used during electroplating was set to 1.5A and 3.0 A, while the pH used was 3 and 5, respectively. Deposition time of 15, 30, and 45 minutes was used

throughout the electrodeposition process. It is critical to monitor the temperature of the electrolyte solution during the electroplating process. Overheating the solution may result in changes of its composition and a decrease in the quality of the coating material deposited on the substrate. Table 2 summarizes the parameters involved in the electrodeposition process.

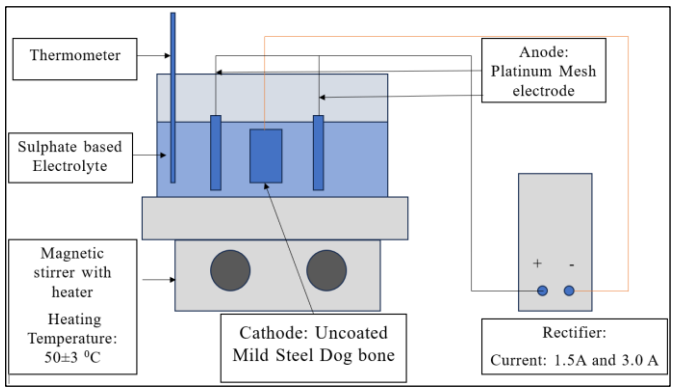

Figure 2: Schematic diagram of the setup for the electrodeposition process

Table 2: Summary of parameters involved in the electrodeposition process

Parameters	Control setting
Arrangement of electrode	Anode: Platinum wire mesh Cathode: Mild steel substate (Dog bone shape)
Temperature	50±3 °C
Electrolyte pH	3 and 5
Current used	1.5 and 3.0 A
Deposition time	15, 30, and 45 minutes

Heat treatment process

The CoNiFe nanocrystalline coated mild steel samples received heat treatment after electrodeposition process. The CoNiFe nanocrystalline coated samples were subjected to a heat treatment procedure that entails immersing them for two hours soaking time at a continuous temperature of 300 °C in a furnace. Following heat treatment, the samples were slowly cooled using a normalizing technique. This approach was chosen because it offers a moderate and steady cooling rate, which reduces the possibility of residual stresses and crack formation. The coating's mechanical and structural qualities were determined after the heat treatment procedure.

Characterization and testing

All samples were carried out for surface roughness, Vickers microhardness and tensile test. The samples were categorized as presented in Table 3. The surface roughness of the CoNiFe nanocrystalline coating on the mild steel sample was investigated using a 3D surface metrology machine. The coating's surface roughness was influenced by the pH, current, deposition time and heat treatment process. Selecting a number of locations on the coated mild steel surfaces allows the average value of the surface roughness profile, *R* to be calculated. The outcome from surface roughness measurement is to find the lowest possible surface roughness value for the determination of the best coating samples.

Table 3: Summary of samples involved for this study

Type of samples	Parameters
CoNiFe nanocrystalline coating - no heat treatment process	15-, 30- and 45-minutes deposition time at fixed pH 3; I:1.5 A
CoNiFe nanocrystalline coating -with heat treatment process	15-, 30- and 45-minutes deposition time at fixed pH 3; I:1.5 A
CoNiFe nanocrystalline coating -with different pH solution	30-minutes deposition time, at pH 5; I:1.5 A
CoNiFe nanocrystalline coating - with different current setting	30-minutes deposition time, at pH 3; I:3.0 A
uncoated mild steel	Uncoated mild steel-reference sample for comparison

The Vickers microhardness tester machine, MITUTOYO MVK-H1, was used to conduct microhardness testing as to evaluate the hardness of the CoNiFe nanocrystalline coating of the uncoated mild steel. With a 10 N load, the specimen's surface was indented. An average of five measurements was taken at various locations of the central portion of each specimen's surface to obtain the final microhardness values. The target of Vickers microhardness test is to determine the best hardness coating through the highest microhardness values obtained at the end of measurement.

Tensile tests were carried out to ascertain the mechanical characteristics of the base metal and CoNiFe nanocrystalline coating. The servohydraulic Instron 8801 test apparatus, which is capable of applying axial forces of up to 100 kN, was used for the testing. Specimens were 2 mm thick and had a gauge length of 37.31 mm. Tensile tests were conducted at constant loading rate of 0.5 mm/min until failure. The highest yield strength and ultimate tensile test obtained from tensile test will be the utmost priority for the determination of best coating condition.

Results and Discussion

Surface roughness

The outcomes of the surface roughness measurement are covered in this section. In the following sub-section, the impact of surface roughness at various deposition time, heat treatment and electrodeposition parameters such as current and pH are being explored.

The effect of surface roughness of CoNiFe nanocrystalline coating at different deposition time

Figure 3 displays the surface roughness data obtained for mild steel coated with different CoNiFe nanocrystalline deposition time. The surface roughness value decreases as the deposition time increases from 15 minutes to 45 minutes. Reduction of surface roughness value indicates a sign of improvement through the introduction of CoNiFe nanocrystalline coating onto the surface of uncoated mild steel. The highest surface roughness result obtained for uncoated mild steel was 4.233 µm, while mild steel coated for 45 minutes CoNiFe nanocrystalline coating recorded the lowest surface roughness of 2.354 µm. Mild steel samples coated for 15 and 30 minutes recorded the surface roughness of 3.737 µm and 2.667 µm, respectively. From the results, it can be deduced that the surface roughness is affected by the duration of deposition time, due to void formation and oxidation process that might take place on the surface material [19].

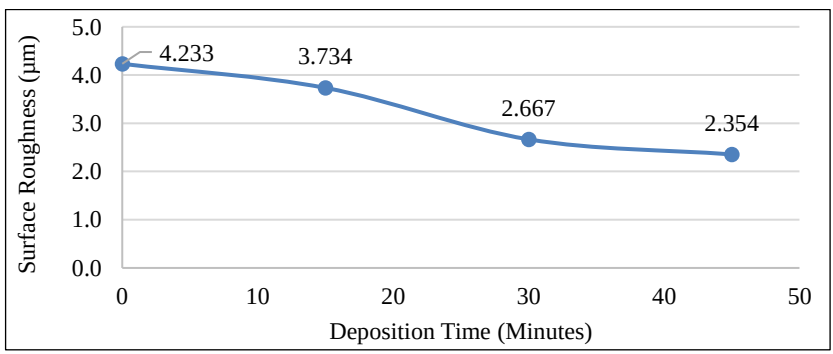

Figure 3: Comparison of CoNiFe nanocrystalline surface roughness electrodeposited at different deposition time

The presence of oxidation and corrosion initially produces an increase in the surface roughness of uncoated mild steel. Exposure to moisture, air, or severe circumstances without a protective coating lead to higher susceptibility of oxidation and corrosion on the uncoated mild steel. Iron oxide (rust) can form on the surface as a result of oxidation, increasing the surface roughness

value. However, the smoothing effect was established as the surface roughness of CoNiFe nanocrystalline coating reached the lowest after 45 minutes deposition time. Coating is a common method of giving surfaces a smoother, more uniform appearance [20]. Surface roughness can be reduced by filling up or bridging microscopic surface flaws using these coatings. Furthermore, coatings can improve the overall surface smoothness by concealing flaws and voids, besides providing a more polished surface.

The effect of surface roughness of CoNiFe nanocrystalline coating with or without heat treatment process

Figure 4 shows the comparison of CoNiFe nanocrystalline coating surface roughness for both CoNiFe electrodeposited coating and CoNiFe electrodeposited coating with heat treatment. CoNiFe nanocrystalline coatings for both electrodeposited samples and heat treatment samples were compared for 15, 30 and 45 minutes. The surface roughness of CoNiFe nanocrystalline coating for both electrodeposited samples and heat treatment samples showed similar decreasing pattern. The highest surface roughness recorded for both CoNiFe nanocrystalline coating process at 15 minutes deposition time was 3.740 µm and 3.590 µm, respectively. Meanwhile, the lowest surface roughness obtained from both samples with and without heat treatment process at 45 minutes deposition time was 2.350 µm and 1.820 µm respectively.

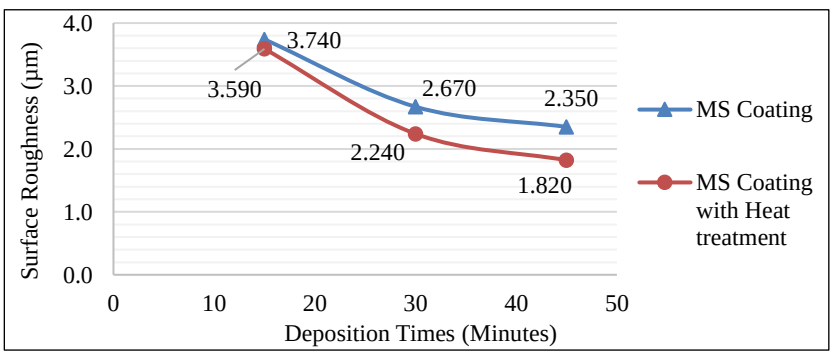

Figure 4: Surface roughness comparison for CoNiFe nanocrystalline coating with and without heat treatment process

Heat treatment was assumed to have increased the particle compactness and density of CoNiFe nanocrystalline coating. The levelling and smoothing impact of heat treatment on the coating confirms this trend. Throughout the heat treatment, the CoNiFe nanocrystalline coating is subjected to controlled heating and cooling cycles. Heat treatment process promotes the redistribution and relaxation of tensions within the coating, improving adhesion and

reducing surface defects. The heat treatment process also improves the flow and levelling of the coating material, resulting in a smoother surface with decreased surface roughness value [21]. The linear decrease in surface roughness is observed as heat treatment process allows the coating material to reflow and rearrange, minimizing surface voids and inconsistencies. The regulated heat application causes structural changes in the coating, resulting in a more uniform surface texture. Furthermore, the decrease in surface roughness is also attributed to the creation of early clusters with smaller particle sizes and dense populations as nucleation density increases [22].

The effect of surface roughness of CoNiFe nanocrystalline coating with varying coating parameters at constant deposition time (current, pH, and heat treatment process)

The surface roughness obtained for mild steel coated with 30 minutes deposition times at various pH and current is shown in Figure 5. Based on the findings, it is worth noting that the surface roughness value increased as the pH value increased. The surface roughness of mild steel CoNiFe nanocrystalline coating with 30 minutes deposition time (pH: 5 and current of 1.5 A) was higher than that of coated mild steel with 30 minutes deposition time (pH: 3 and current of 1.5 A).

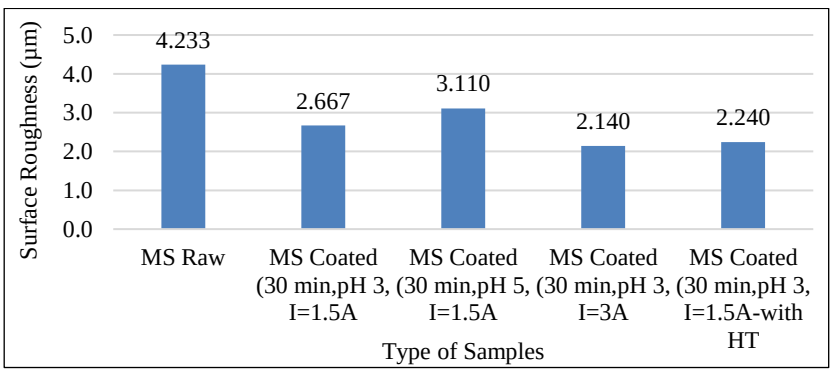

Figure 5: Surface roughness comparison of CoNiFe nanocrystalline coated for 30 minutes with different parameters

At the same current setting, less coating material was deposited onto the surface since higher electrolyte pH value (pH=5) contributes to a lower deposition rate. As a result, the coating thickness might be reduced, and surface roughness may not be filled or levelled out effectively which leads to higher surface roughness. Resali et al. [23] discovered that the effect of phase formation on particle size was insignificant. However, as the pH increased, the nucleation of crystallites resulted in the formation of coalesced particles.

Hence, the particle tended to aggregate and produced larger particles, while void formation was discovered in samples prepared at higher bath pH.

It is also worth noting that as the applied current increased from 1.5 A to 3.0 A, the surface roughness decreased. The decrease in surface roughness might be due to a higher current applied during electrodeposition process, which results in a faster deposition rate. A thicker and more uniform coating occurred on the mild steel surface due to the faster deposition rate [24]. The faster deposition process was able to aid in the filling of surface imperfections and the reduction of surface roughness. The addition of heat treatment process on the CoNiFe nanocrystalline coating also effectively reduced the surface roughness compared to the other 30 minutes CoNiFe nanocrystalline coating. Similar improvement of surface roughness was discovered by Bejaxhin et al. [25]. They observed an increase in hardness value due to the heat treatment effect. They also claimed that 41% improvement in surface roughness was obtained by the effect of heat treatment as well as the specific machining conditions.

Microhardness test

In the following subsection, the microhardness impacts of CoNiFe nanocrystalline coating at various deposition durations, heat treatment processes, and parameters such as current and pH are discussed.

The effect of CoNiFe nanocrystalline microhardness at different deposition times

Figure 6 depicts the change in hardness qualities as a function of deposition time at 15 minutes, 30 minutes, and 45 minutes for each sample. Mild steel has a rapid increase in hardness from 171.44 HV (uncoated mild steel sample) to 245.36 HV (15 minutes deposition times), and a sustained increasing pattern of 252.56 HV and 267.46 HV for coating times of 30 minutes and 45 minutes, respectively.

The steady increase in hardness from uncoated mild steel to mild steel with 45 minutes deposition time may be attributed to the changes in the phase structure, effect of porosity, solid hardening mechanism and particle size of the nanocrystalline deposit [26]. Longer deposition time also enables more CoNiFe nanocrystalline coating to be deposited on the mild steel substrate, resulting in a thicker covering which makes the surface of the coating harder [23]. As particle size decreases, the microstructure becomes denser with particle barriers and grain boundaries [24]. During electrodeposition process, metal ions from the electrolyte may reduce and deposit onto the substrate, resulting in metal grains. Longer deposition time give grains more time to develop and mature. Smaller grains have a higher dislocation density, which contributes to the high microhardness value. Dislocations are crystal structural imperfections that limit dislocation mobility while also strengthening the material.

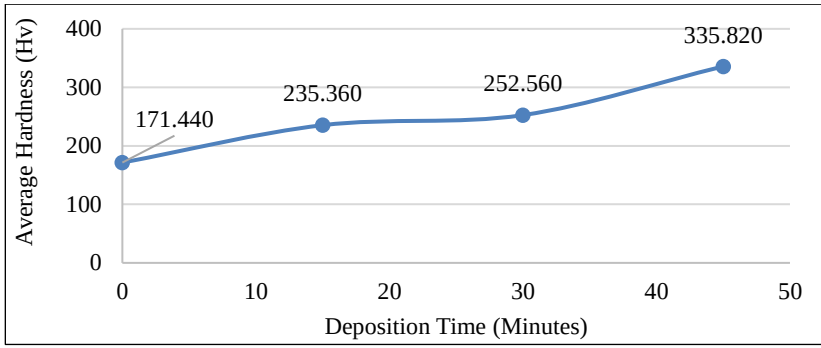

Figure 6: Vickers microhardness test for CoNiFe nanocrystalline coating at different deposition time

The effect of CoNiFe nanocrystalline microhardness with or without heat treatment process

The microhardness of CoNiFe nanocrystalline coated surfaces with and without heat treatment is shown in Figure 7. The results were plotted, and both CoNiFe nanocrystalline coating with and without heat treatment process exhibited an increase in microhardness. It can be seen that CoNiFe nanocrystalline coating with additional heat treatment process had a higher hardness as compared to CoNiFe nanocrystalline coating without heat treatment process.

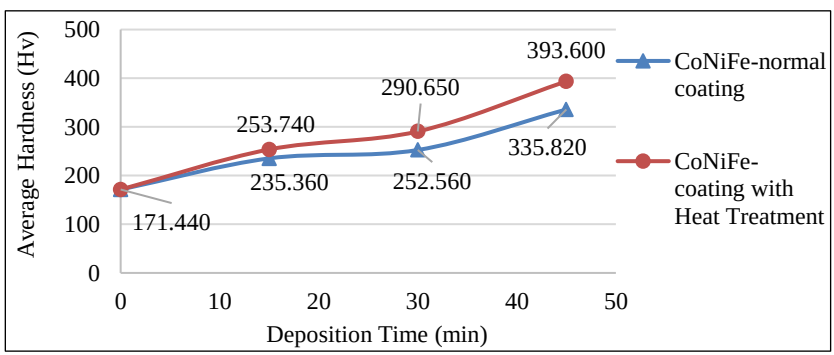

Figure 7: Vickers hardness test comparison for CoNiFe nanocrystalline coating at different deposition time (with or without heat treatment process)

The microhardness value for CoNiFe nanocrystalline coating with heat treatment process was 393.6 HV (45 minutes deposition time) and the lowest average microhardness CoNiFe nanocrystalline coating with heat treatment

process was 253.74 HV (15 minutes deposition time). In comparison, the highest microhardness value for CoNiFe nanocrystalline coating without heat treatment was 335.82 HV for the same deposition duration (45 minutes deposition time) and the lowest microhardness CoNiFe nanocrystalline coating without heat treatment process was 235.36 HV (15 minutes deposition time).

The data clearly showed that CoNiFe nanocrystalline coating with heat treatment process surpassed the hardness performance of CoNiFe nanocrystalline coating without heat treatment process. Heat treatment produces grain development and coarsening in the coating and substrate, enhancing their mechanical properties. As grain size grows, the number of grain boundaries per unit volume reduces, and the remaining grain boundaries become more resistant to dislocation movement. Particle barriers also restrict dislocation motion and contribute to the formation of a more complex layer in the microstructure [27]. Furthermore, the homogeneous particle distribution, compact and dense microstructure, as well as higher temperature resulted in CoNiFe nanocrystalline coating with a much better microhardness [28]. Overall, the application of CoNiFe nanocrystalline coating with and without heat treatment process improves the hardness performance of uncoated mild steel substrate.

The effect of CoNiFe nanocrystalline microhardness when varying coating parameters at constant deposition time (current, pH, and heat treatment process)

The average value of microhardness obtained for mild steel using the same deposition time and various pH and current value is shown in Figure 8. It can be seen that the microhardness value decreased as the pH value for the constant 30 minutes deposition time increased from pH 3 to 5. The microhardness of mild steel CoNiFe nanocrystalline coating with 30 minutes deposition time (pH: 5 and current of 1.5 A) was lower than that of coated mild steel with 30 minutes deposition time (pH: 3 and current of 1.5 A). The decreasing pattern of microhardness from 252.56 HV to 212.36 HV may be related to changes in coating structure and properties as the pH shifts from 3 to 5. At pH 3, the electrodeposition reaction kinetics may be more favourable, resulting in a more dense and compact coating.

It is well known that the performance of material hardness is usually in excellent form if its particle size is smaller. However, at pH 5, the electrodeposition process may be less effective and form bigger particle size, resulting in a thinner layer with agglomeration and void formation that may happen in the microstructure [23]. These structural changes may result in a decrease of microhardness at pH 5. It is also worth noticing that the microhardness value improved as the applied current increased from 1.5 A to 3.0 A. The rising trend in average microhardness is caused by a larger current delivered during the electrodeposition process, which results in a faster

deposition rate and may promote the nucleation and growth of smaller grains [24].

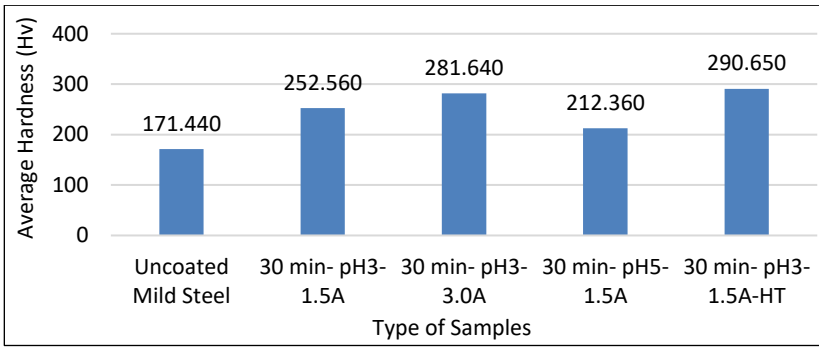

Figure 8: Vickers hardness test comparison for CoNiFe nanocrystalline coating fixed at 30 minutes deposition time (varies pH, current and heat treatment)

Smaller grains have higher dislocation density, which limits dislocation movement and increases microhardness [27]. Improved grain refining at a current intensity of 3 A versus 1.5 A may result in higher microhardness values. The addition of the heat treatment process raises the microhardness compared to sample coated for 30 minutes deposition time. The synergistic effect between nanoparticles introduction and microstructural features on coating microhardness results in higher values of CoNiFe nanocrystalline coating coated for 30 minutes deposition time with additional heat treatment process as compared to their standard counterpart, with a progressive hardness increase of up to 290.65 HV. Addition of heat treatment given to as-deposited CoNiFe nanocrystalline effectively strengthens coatings hardness. The findings were also reported by Pedrizzetti et al. [29] who discovered the synergistic effect between nanoparticles introduction and microstructural features on coating microhardness which resulted in higher hardness values for nanocomposites compared to their standard counterpart, with a progressive hardness increase of up to heat treatment at 400 °C.

Tensile performance

This section discusses the tensile performance at various deposition time, additional heat treatment process, and various electrodeposition parameters such as current and pH.

Tensile performance of CoNiFe nanocrystalline at different deposition time

The stress-strain curves of all specimens are shown in Figure 9. The ultimate tensile strength of coated mild steel was seen to be higher than uncoated mild steel, as shown in Table 4.

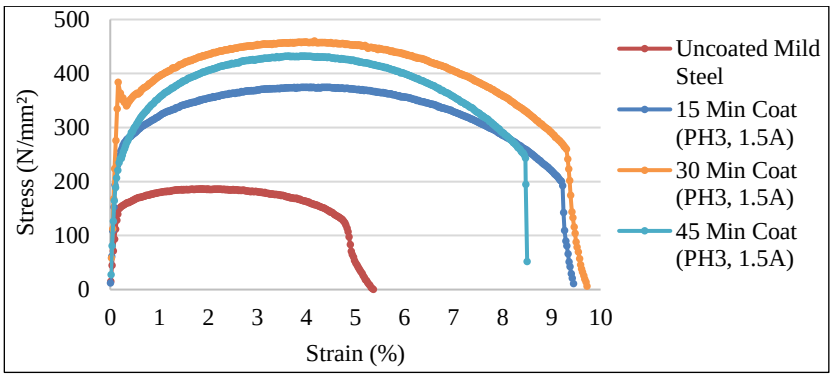

Figure 9: Stress-strain curves of CoNiFe nanocrystalline coating applied at different deposition time

Table 4: The yield stress and ultimate strength of uncoated and CoNiFe nanocrystalline coated specimens at different deposition time

Specimen	Yield stress σ_y, MPa	Ultimate Tensile strength σ_u, MPa
Uncoated	149.400	186.780
15 min	267.310	375.920
30 min	384.060	460.380
45 min	243.830	432.670

Uncoated mild steel, mild steel coated for 15 minutes, 30 minutes, and 45 minutes have ultimate tensile strengths of 186.780 MPa, 375.920 MPa, 460.380 MPa, and 432.670 MPa, respectively. The fact that CoNiFe nanocrystalline coated mild steel had a greater ultimate tensile strength than uncoated mild steel suggests that the coating implementation improved the mechanical properties of mild steel substrate [30]. The uncoated mild steel appeared to have gained strength as a result of the coating, allowing them to withstand greater quantities of stress before failure [31]. However, the ultimate tensile strength of 30 minutes was greater than that of 45 minutes. This scenario may be explained by factors such as coating quality and possibly due to the material experiencing transformations or alterations that modify its mechanical properties.

The coating's quality may also have an effect on its final tensile strength. Uniformity, adherence, presents of voids, agglomeration and abnormalities on the coating layer can all have a significant impact on the mechanical properties of CoNiFe nanocrystalline coated surfaces [32]. Furthermore, the yield stress for uncoated, 15 minutes, 30 minutes, and 45 minutes CoNiFe nanocrystalline coating was 149.400 MPa, 267.310 MPa, 384.060 MPa, and 243.830 MPa, respectively which showed similar increasing pattern as the ultimate tensile strength measurement.

Tensile performance of CoNiFe nanocrystalline with and without heat treatment process

Figure 10 shows the ultimate tensile strength values of CoNiFe nanocrystalline coating samples subjected to different heat treatment durations compared to CoNiFe nanocrystalline samples. The ultimate tensile strength values for CoNiFe nanocrystalline coating with heat treatment varied according to the deposition time, as shown in Table 5 where the values were 407.330 MPa at 15 minutes, 467.670 MPa at 30 minutes, and 559.110 MPa at 45 minutes. In contrast, recorded ultimate tensile stress for as-coated CoNiFe nanocrystalline samples was 375.920 at 15 minutes, 460.380 MPa at 30 minutes, and 432.67 0 MPa at 45 minutes which were significantly lower as compared to the heat-treated coatings.

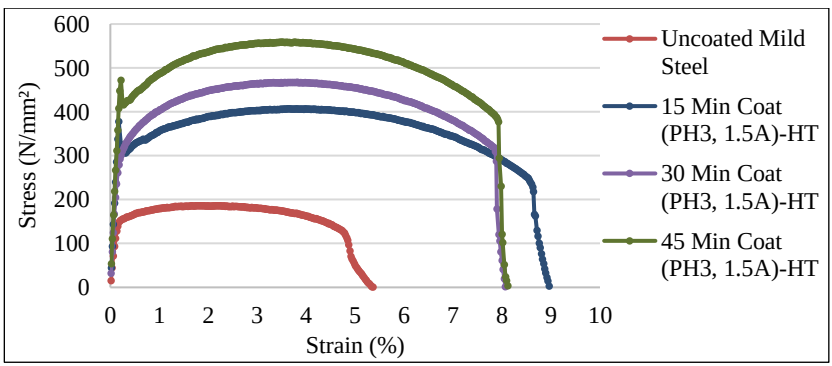

Figure 10: Stress-strain curves of CoNiFe nanocrystalline coating applied at different deposition time with heat treatment process

According to the results, heat treatment has a significant impact on the ultimate tensile strength of CoNiFe nanocrystalline coated materials and affects the material's microstructure, resulting in variations in strength. These observations could be linked to the formation of soft ferrite during the cooling process [33]. The ultimate tensile strength of CoNiFe nanocrystalline coated was much higher after the coating underwent heat treatment of minimal

deposition time and additional heat treatment process enhanced with mechanical strength which were represented by the higher ultimate tensile strength and yield stress compared to uncoated sample. The continuous trend of ultimate tensile strength after 30 and 45 minutes CoNiFe nanocrystalline coating with heat treatment could be attributed to other microstructural changes, such as precipitation hardening or grain refinement, which contributed to higher mechanical strength [34].

Table 5: The yield stress and ultimate strength of CoNiFe coated specimens with heat treatment process

Specimen	Yield stress σ_y, MPa	Ultimate strength σ_u, MPa
15 min	378.350	407.330
30 min	301.200	467.670
45 min	472.350	559.110

Despite the fact that additional heat treatment process increased the ultimate tensile strength of CoNiFe nanocrystalline coating, the resulting yield strength did not follow the same increment pattern. The yield stress of CoNiFe nanocrystalline coating coated for 45 minutes deposition time was found to be the highest (472.350 MPa) whereas 30 minutes coating sample showed the lowest yield stress (301.200 MPa). During heat treatment procedure, changes in the microstructure of the CoNiFe nanocrystalline coating may occur, possibly contributing to a slight decline in yield stress for the 30 minutes coating sample. Surprisingly, the yield stress increased dramatically after 45 minutes of heat treatment (472.350 MPa).

Tensile performance of CoNiFe nanocrystalline when varying coating parameters at constant deposition time (current, pH, heat treatment process)

Figure 11 depicts the tensile test data which demonstrate the ultimate tensile strength of mild steel when coated under various conditions. According to Table 6, the ultimate tensile strength of CoNiFe nanocrystalline coating greatly increased when the current intensity was increased at a constant pH (520.590 MPa). The result demonstrated that the tensile properties of the CoNiFe nanocrystalline coating were determined by the current adjustment factor in the electrodeposition process. The rise in the ultimate tensile strength was attributed to different strengthening mechanisms, such as solid solution and precipitation strengthening [23]. The strongly adhesive CoNiFe nanocrystalline covering might effectively suppress the failure of the mild steel substrate at early stages. PJ Teng et al. also discovered that the coating layer significantly improved the tensile resistance of the substrate and concluded that the tensile properties of their coated specimens increased due to the increase in current densities throughout electrodeposition process [35].

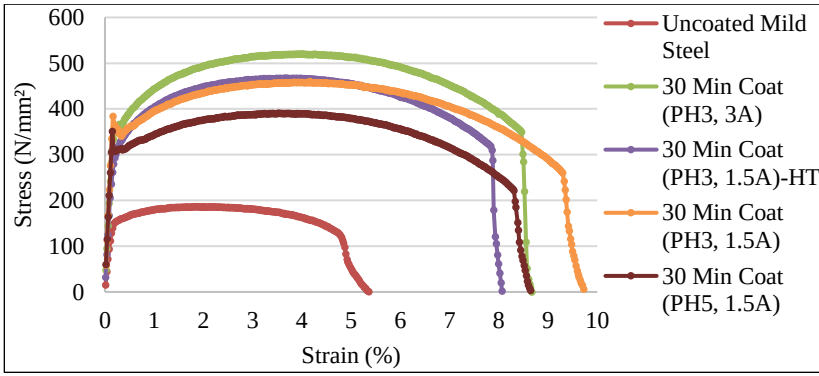

Figure 11: Stress-strain curves of CoNiFe nanocrystalline coating applied at 30 minutes deposition time with various parameter setup (different pH, current and heat treatment)

Table 6: The yield stress and ultimate strength of heat treated CoNiFe coated specimens

Specimen	Yield stress σy, MPa	Ultimate strength σu, MPa
Uncoated	149.40	186.78
30 min (pH=3, I=1.5 A)-HT	301.21	467.71
30 min (pH=3, I=1.5 A)	384.06	460.38
30 min (pH=3, I=3 A)	348.19	520.59
30 min (pH=5, I=1.5 A)	351.23	390.99

However, when the pH of the electrolyte was increased to 5 with constant current intensity of 1.5 A, the ultimate tensile strength slightly reduced to 390.99 MPa. This demonstrated that, as compared to the effects of current intensity, a higher pH value has a lesser effect on ultimate tensile stress. These data suggested that the intensity of the current and the pH level during the coating process could have a significant impact on the ultimate tensile stress of CoNiFe nanocrystalline coating. This finding was similar to M. Stamenovic et al. who reported that alkaline solutions at higher pH value caused a decrease on the tensile properties. During the treatment of the samples, they coated the inner surfaces and went deeper into the samples through micro-cracks and other surface damages which existed after fabrication and shrinkage of the material. On the other hand, the composite material was strengthened during treatment of samples with acids (lower pH) and increment in tensile properties was obtained [36].

Conclusions

It is concluded that surface roughness, Vickers hardness and tensile enhancement are experienced throughout the introduction of CoNiFe nanocrystalline coating. The highest improvement for surface roughness, microhardness and tensile performance was recorded by CoNiFe nanocrystalline coating at 45 minutes deposition time with pH 3, I:1.5 A and heat treated (surface roughness: 1.82 µm; microhardness: 393.6 Hv; YS: 472.35 MPa; UTS: 186.78 MPa) as compared to reference uncoated mild steel (surface roughness:4.233 µm; microhardness: 171.44 Hv; YS: 149.40 MPa; UTS: 186.78 MPa). It is shown that both surface roughness and hardness obtained are 2.3 times better than the reference uncoated mild steel. Both yield strength and ultimate tensile strength values show a direct improvement of 3.16 and 3 times compared to uncoated mild steel samples. The introduction of higher current setting boosts up both yield strength (348.19 MPa) and ultimate tensile strength (520.59 MPa). CoNiFe nanocrystalline coating successfully serves as a protective layer and performance booster in which it protects the underlying mild steel from external forces that can cause failure of low strength purpose.

Contributions of Authors

The authors confirm the equal contribution in each part of this work. All authors reviewed and approved the final version of this work.

Funding

This work was supported by the "Lestari Grant" [600-RMC/MyRA 5/3/LESTARI] and College of Engineering, Universiti Teknologi MARA (UiTM) Shah Alam.

Conflict of Interests

All authors declare that they have no conflicts of interest.

Acknowledgment

The author would like to thank Universiti Teknologi MARA (UiTM) under Lestari Grant [600-RMC/MyRA 5/3/LESTARI] and College of Engineering,

Universiti Teknologi MARA (UiTM) Shah Alam on the financial supports given.

References

[1] M.Z. Zabri , N.R.N. Masdek, and K.M. Hyie, "A brief review of co-ni-fe nanocrystalline coatings: properties and their applications," *Current Topics in Electrochemistry*, vol. 24, pp. 85-99, 2022.

[2] Md. Nor, M.S., Z. Salleh, N.R. Nik Masdek, M.H. Koay, and S. Kushairi, "Effects of Deposition Time on Surface Properties of Co-Ni-Fe Alloy Synthesised on Hex Bolts," *International Journal of Engineering and Advanced Technology*, vol. 9, no. 1, pp. 5780-5785, 2019. https://doi.org/10.35940/ijeat.a3062.109119

[3] G.H. Koch, M.P. Brongers, N.G. Thompson, Y.P. Virmani, and J.H. Payer, 2002, Corrosion cost and preventive strategies in the United States. United States. Federal Highway Administration.

[4] L. Benea, P.L. Bonora, A. Borello, and S. Martelli, "Wear corrosion properties of nano-structured SiC–nickel composite coatings obtained by electroplating," *Wear*, vol. 249, no. 10-11, pp. 995-1003, 2001. https://doi.org/10.1016/s0043-1648(01)00844-4

[5] Z. Lin, L. Xu, X. Li, L. Wang, W. Guo, C. Wu, and Y. Yang, "Corrosion resistance of composite coating used for fastener protection," *Anti-Corrosion Methods and Materials*, vol. 66, no. 5, pp. 595-602, 2019. https://doi.org/10.1108/ACMM-03-2019-2095

[6] D.H. Abdeen, M. El Hachach, M. Koc, and M.A. Atieh, "A review on the corrosion behaviour of nanocoatings on metallic substrates," *Materials*, vol 12, no. 2, p. 210, 2019. https://doi.org/10.3390/coatings9100689

[7] H.-h. Zhou, Z.-w. Liao, C.-x. Fang, H.-x. Li, F. Bin, X. Song, G.-f. Cao, and Y.-f. Kuang, "Pulse electroplating of Ni-WP coating and its anti-corrosion performance," *Transactions of Nonferrous Metals Society of China*, vol. 28, no. 1, pp. 88-95, 2018. https://doi.org/10.1016/S1003-6326(18)64641-2

[8] A.B. Radwan, K. Ali, R. Shakoor, H. Mohammed, T. Alsalama, R. Kahraman, M.M. Yusuf, A.M. Abdullah, M.F. Montemor, and M. Helal, "Properties enhancement of Ni-P electrodeposited coatings by the incorporation of nanoscale Y2O3 particles," *Applied Surface Science*, vol. 457, pp. 956-967, 2018. https://doi.org/10.1016/j.apsusc.2018.06.241

[9] S. Gao, Y. Liu, and X. Kou, "Effect of electrolyte pH and deposition time on the microstructure and magnetic properties of electrodeposited Fe2CoSn Heusler alloy," *International Journal of Electrochemical Science*, vol. 10, pp. 8727-8737, 2015

[10] Z. Yang, S. Tan, J. Yang, Y. Li, X. Yang, and J. Deng, "Study on the solar selectivity and air thermal stability of cobalt–nickel–iron oxide coating fabricated by spraying method," *Optical Materials*, vol. 111, p. 110573, 2021. https://doi.org/10.1016/j.optmat.2020.110573

[11] G. Barati Darband, M. Aliofkhazraei, and A.S. Rouhaghdam, "Facile electrodeposition of ternary Ni-Fe-Co alloy nanostructure as a binder free, cost-effective and durable electrocatalyst for high-performance overall water splitting," *Journal of Colloid and Interface Science*, vol. 547, pp. 407-420, 2019. https://doi.org/10.1016/j.jcis.2019.03.098

[12] V. Chaudhary, L.P. Tan, V.K. Sharma, and R. Ramanujan, "Accelerated study of magnetic Fe-Co-Ni alloys through compositionally graded spark plasma sintered samples," *Journal of Alloys and Compounds*, vol. 869, p. 159318, 2021. https://doi.org/10.1016/j.jallcom.2021.159318

[13] P. Ledwig, M. Kac, A. Kopia, J. Falkus, and B. Dubiel, "Microstructure and properties of electrodeposited nanocrystalline Ni-Co-Fe coatings," *Materials*, vol. 14, no. 14, p. 3886, 2021. https://doi.org/10.3390/ma14143886

[14] M. Haizad, N. Rozlin, C. Mardziah, and S. Ramesh. "Characterization and corrosion behavior of heat-treated electrodeposited cobalt alloy coating," *AIP Conference Proceedings*, vol 2643, no. 1, p. 050031, 2023. https://doi.org/10.1063/5.0110851

[15] S. Arias, J.G. Castaño, E. Correa, F. Echeverría, and M. Gómez, "Effect of heat treatment on tribological properties of Ni-B coatings on low carbon steel: wear maps and wear mechanisms," *Journal of Tribology*, vol. 141, no. 9, p. 091601, 2019. https://doi.org/10.1115/1.4043906.

[16] F. Baciu, A. Rusu-Casandra, and Ș.-D. Pastramă, "Low strain rate testing of tensile properties of steel," *Materials Today: Proceedings*, vol. 32, no. 2, pp. 128-132, 2020. https://doi.org/10.1016/j.matpr.2020.03.469

[17] Z. Zhang, J. Chen, G. He, and G. Yang, "Fatigue and mechanical behavior of ti-6al-4v alloy with crn and tin coating deposited by magnetic filtered cathodic vacuum arc process," *Coatings*, vol. 9, no. 10, p. 689, 2019. https://doi.org/10.3390/coatings9100689.

[18] A. Karimzadeh, M. Aliofkhazraei, and F.C. Walsh, "A review of electrodeposited Ni-Co alloy and composite coatings: Microstructure, properties and applications," *Surface and Coatings Technology*, vol. 372, pp. 463-498, 2019. https://doi.org/10.1016/j.surfcoat.2019.04.079

[19] N.R.N. Masdek, M.S.H. Mansor, Z. Salleh, and K.M. Hyie. "Synthesizing the nanocrytalline cobalt-iron coating through the electrodeposition process with different time deposition" *IOP Conference Series: Materials Science and Engineering*, vol. 328, no. 1, p. 012002, 2018. https://doi.org/10.1088/1757-899x/328/1/012002

[20] J.R. McNeil, L. Wei, G.A. Al-Jumaily, S. Shakir, and J.K. Mclver, "Surface smoothing effects of thin film deposition?," *Applied Optics*, vol. 24, no. 4, pp. 480-485, 1985. https://doi.org/10.1364/ao.24.000480

[21] L. Gurleyen, U. Ayata, B. Esteves, and N. Cakicier, "Effects of heat treatment on the adhesion strength, pendulum hardness, surface roughness, color and glossiness of Scots pine laminated parquet with two different types of UV varnish application," *Maderas Ciencia y tecnología*, vol. 19, no. 2, pp. 213-224, 2017. https://doi.org/10.4067/s0718-221x2017005000019

[22] S. Lee, and M. So, "Effects of deposition temperature and pressure of the surface roughness and the grain size of polycrystalline Si1− xGex films," *Journal of Materials Science*, vol. 35, pp. 4789-4794, 2000. https://doi.org/10.1023/A:1004868627888.

[23] N.A. Resali, K.M. Hyie, W.N.R. Abdullah, M. Ghani, and A. Kalam. "The effect of bath pH on the phase formation of ternary Co-Ni-Fe nano-coatings," *Applied Mechanics and Materials*, vol. 39, pp. 9-13, 2013. https://doi.org/10.4028/www.scientific.net/amm.391.9

[24] E. Saraloğlu Güler, İ. Karakaya, and E. Konca, "Effects of current density, coating thickness, temperature, pH and particle concentration on internal stress during Ni–MoS2 electrocodeposition," *Surface Engineering*, vol. 30, no. 2, pp. 109-114, 2014. https://doi.org/10.1179/1743294413y.0000000223

[25] Bovas Herbert Bejaxhin, A., G. Balamurugan, S. Sivagami, K. Ramkumar, V. Vijayan, and S. Rajkumar, "Tribological behavior and analysis on surface roughness of CNC milled dual heat treated Al6061 composites," *Advances in Materials Science and Engineering*, vol. 2021, pp. 1-14, 2021. https://doi.org/10.1155/2021/3844194

[26] K.M. Hyie, M.Z. Zabri, N.R.N. Roseley, and N.R.N.M. Masdek, "Effect of deposition time on wear and corrosion performance of Co–Ni–Fe alloy coated mild steel," *Journal of Materials Research*, vol. 31, no. 13, pp. 1848-1856, 2016. .https://doi.org/10.1557/jmr.2016.32

[27] B. Yoo, S. Hernandez, D.-Y. Park, and N. Myung, "Electrodeposition of FeCoNi thin films for magnetic-MEMS devices," *Electrochimica Acta*, vol. 51, no. 28, pp. 6346-6352, 2006. https://doi.org/10.1016/j.electacta.2006.04.020

[28] K. Mei Hyie, Z. Salleh, C. Mardziah, N.M. Masdek, N. Rozlin, and N. Azrina Resali, "Corrosion behavior of heat treated nanocrystalline co-ni-fe coating on stainless steel," *Journal of Mechanical Engineering*, vol. 5, pp. 1823-5514, 2018.

[29] G. Pedrizzetti, L. Paglia, V. Genova, M. Conti, L. Baiamonte, and F. Marra, "The effect of composition and heat treatment on microhardness of ni-p and ni-p-nanozro2 coatings," *Chemical Engineering Transactions*, vol. 100, pp. 433-438, 2023. https://doi.org/10.3303/CET23100073

[30] Y.Yu, S. Tang, Z. Wang, and J. Hu, "Effects of coating contents on the interfacial reaction and tensile properties of Al2O3 coated-Al18B4O33w/Al–Mg matrix composites," *Materials Characterization*,

vol. 107, pp. 327-333, 2015. https://doi.org/10.1016/j.matchar.2015.07.029

[31] N.A. Siddiqui, E.L. Li, M.-L. Sham, B.Z. Tang, S.L. Gao, E. Mäder, and J.-K. Kim, "Tensile strength of glass fibres with carbon nanotube–epoxy nanocomposite coating: effects of CNT morphology and dispersion state," *Composites Part A: Applied Science and Manufacturing*, vol. 41, no. 4, pp. 539-548. 2010. https://doi.org/10.1016/j.compositesa.2009.12.011

[32] A.W.-Y. Tan, W. Sun, A. Bhowmik, J.Y. Lek, I. Marinescu, F. Li, N.W. Khun, Z. Dong, and E. Liu, "Effect of coating thickness on microstructure, mechanical properties and fracture behaviour of cold sprayed Ti6Al4V coatings on Ti6Al4V substrates," *Surface and Coatings Technology*, vol. 349, pp. 303-317, 2018. https://doi.org/10.1016/j.surfcoat.2018.05.060

[33] A.M. Abaas, A.A. Ramadhan, and F.H. Hasan. "Study the effect of cooling medium on the torsion resistance and hardness of medium carbon steel," *IOP Conference Series: Materials Science and Engineering*, vol. 405, no. 1, p. 012005, 2018. https://doi.org/10.1088/1757-899x/405/1/012005

[34] T. Yin, X. Li, W. Cao, and K. Xia, "Effects of thermal treatment on tensile strength of Laurentian granite using Brazilian test," *Rock Mechanics and Rock Engineering*, vol. 48, pp. 2213-2223, 2015. https://doi.org/10.1007/s00603-015-0712-3

[35] P.-J. Teng, C.-H. Lin, and S.-W. Mao, "Deposition of nickel-tungsten-phosphorus coatings on pure copper in a saline water environment," *International Journal of Electrochemical Science*, vol. 16, no. 2, p. 21025, 2021. https://doi.org/10.20964/2021.02.06

[36] M. Stamenović, S. Putić, M. Rakin, B. Medjo, and D. Čikara, "Effect of alkaline and acidic solutions on the tensile properties of glass–polyester pipes," *Materials & Design*, vol. 32, no. 4, pp. 2456-2461, 2011. https://doi.org/10.1016/j.matdes.2010.11.023

Mechanical Properties of Rice Husk-Recycled Polypropylene Composite

Umar Iqqbal Al-Biruni Mohd Adnan, Freddawati Rashiddy Wong, Mohamad Firhan Morni, Abdul Hakim Abdullah, Amirul Abd Rashid*
School of Mechanical Engineering, College of Engineering,
Universiti Teknologi MARA, 40450 Shah Alam, Selangor, MALAYSIA
**freddawati@uitm.edu.my*

Soon Kong Yong
Soil Assessment and Remediation Research Group,
Faculty of Applied Sciences, Universiti Teknologi MARA,
40450 Shah Alam, Selangor, MALAYSIA

ABSTRACT

The growing amount of plastic and food waste has become a serious problem around the worldwide. As a byproduct of milling rice, rice husk is an agricultural waste that is produced in bulk quantities. Rice husk has been used as filler in polymer composites in a variety of ways. However, there have only been a few reports of using rice husk as reinforcement in composites made of recycled polypropylene. The limited interfacial reaction between natural fibre and polymer is the fundamental issue in natural fibre-based composites. This prompted the development of sustainable composite manufactured from recycled polypropylene(rPP) and rice husk (RH). Thus, we investigated the intermolecular adhesion between rPP–RH composite with maleic anhydride grafted polypropylene (MAPP) as a coupling agent. Varied compositions of RH in the range of 10–40 wt% with 4 wt% of MAPP were fabricated. The rPP, RH and MAPP were blended and executed in injection moulding. The mechanical properties will be analysed through differential scanning calorimetry, rheology, tensile, flexural, impact and hardness tests. The result shows RH agglomeration and limited dispersion in the composite cause a reduction of up to 40% for tensile strength compared to neat rPP. Despite this, it demonstrates improvements in tensile modulus, flexural modulus, impact, and hardness. It is evidence of a good intermolecular between rPP matrix and RH. In conclusion, the ideal RH loading for composites occurs at a filler

ISSN 1823-5514, eISSN 2550-164X

https://doi.org/10.24191/jmeche.v12i1.24637

Received for review: 2023-09-19
Accepted for publication: 2023-10-18
Published: 2023-11-15

content of 40% and has acceptable mechanical properties for various composite applications.

Keywords: *Recycled Polypropylene; Rice Husk; Rice Husk Reinforced Recycled Polypropylene Composite; Polymer Composite; Mechanical Properties*

Introduction

Water pollution, air pollution, and climate change all negatively affect people and the environment. Scheduled wastes recorded in 2019 exceeded 4.0 million tonnes, according to Malaysia's Department of Statistics [1]. The power plants, metal refineries, chemical industries, and electrical and electronics industries each contributed 57.1% (2.3 million tonnes) of the total scheduled waste [2]. Although this is not a new concern, it remains the world's most significant issue and one of the leading causes of diseases and mortality in people. Environmental pollution impacts the lives of animals and the ecological system's balance. The increase of plastic waste in landfills and the ocean is becoming the most common threat that has been discovered. It harms the environment because plastics will take decades to decompose. It becomes hazardous to humans, animals, and marine life. Therefore, this issue has a bad impact on the food chain, resulting in poisonous food being consumed by humans such as causing digestive issues.

Waste management is critical for the long-term sustainability of the environment. Several programs have been implemented to prevent this problem such as beach clean-up, which intercepts plastic before it reaches the ocean. Recently, there have been new initiatives in separating, cleaning and recycling waste contained in recyclable materials. The most popular program was Coca-Cola, the world’s first bottle made from ocean plastic waste that was recovered from the Mediterranean Sea [3]. Thus, the idea of developing composite with the combination of recycled plastics with agricultural waste has big potential for a sustainable environment. Common processing methods that have been used for natural fibre-reinforced thermoplastic composites are compression moulding, injection moulding, and extrusion [3]-[10].

Rice is the most important crop and produces rice husk as a by-product. The annual output of rice husks is large but most are burned by the peasants. The main components of the rice are identical to those found in wood, including cellulose, hemicellulose, lignin, and silica [4]. Therefore, rice husk may be a potential substitute for alternative wood in wood-plastic composite because of the high amount of cellulose in the rice husk. Meanwhile, the exterior surface of the rice husk has a plethora of organised conical protrusions. It is a combination of lignin and silica that generates a natural protective coating in the form of silicon fibre membranes.

The challenging process of polymerization with fibres is its incompatibility with non-polar matrices. The RH (filler) particles tend to aggregate when combined with a non–polar polymer rPP (matrix), which limits the stress transmission from matrix to filler [11]. Weak interfacial adhesion due to fibre-matrix incompatibility reduces composite impact strength, tensile strength and tensile elongation at break [6]. The mechanical properties of biocomposites are dependent on strong compatibility between the dispersed phase filler and the continuous phase matrix. Modifying the surface of the RH fibre is necessary to increase RH compatibility with non-polar polymers. The compatibility of RH fibre–polymer composite is achieved by using surface treatment processes such as mercerization, ozonolysis, plasma, electron beam irradiation, and coupling agents [12]. Coupling agents have gained significant attention in the production of biocomposite materials due to their ability to improve matrix interfacial adhesion in natural fibre-reinforced polymer composite systems. Simultaneously, the chemical treatment is also preferable to use because its uses simple technology, inexpensive and effective in the modification of the interface between natural fibre and the polymeric matrix. Common chemicals used in the chemical treatment are silane, sodium hydroxide (NaOH), methylene diphenyl diisocyanate (MDI), and MAPP [4]-[5], [13].

Recently, MAPP has been used in producing excellent filler-matrix bridge effects. It was also discovered that rice husk's O–H group and MAPP's maleic anhydride group can esterify each other [13]-[14]. The bi-functional chemical structures of interface MAPP can consume hydrophilic groups (such as O–H groups) on the fibre surface and introduce hydrophobic groups (such as C–H groups in PP) to the fibre surface which results in the higher interface compatibility between hydrophilic fibre and hydrophobic PP, thus make them stronger interactions at the fibre/rPP composites interface [14]. This reduced the moisture absorption of the composite and improved the tensile and flexural strengths [15]. Furthermore, the lower impact properties of the fibre/polymer matrix composite are beyond the point of the improved interaction of the fibre/polymer matrix interface rPP.

This research intends to explore the utilization of MAPP as a coupling agent to improve the surface interaction between RH fibre and rPP matrix composite, and to improve the mechanical, rheological, and thermal properties. This research is focused on various weight percentages of rPP:RH ratios, which are 100:0, 90:10, 80:20, 70:30, and 60:40. This research will promote the circular economy, natural fibre-based composite as an alternative automotive parts, and gain environmental benefits. Simultaneously, this research also adheres well to the sustainable development goal (SDG).

Methodology

The experimentation process for this project starts with the collecting, cleaning, drying, and crushing of material for the feedstock. Following that, the composite was mixed to evaluate five different composition ratios with reinforcement fibre. Rheology and DSC analyses were carried out to comprehend the behaviour of the material before moving on to the injection moulding process. The sample was prepared via injection moulding to analyse the mechanical measurement. Tensile, flexural, impact and hardness tests will be conducted to study the mechanical properties. Thus, the findings of all these tests are revealed and discussed.

Feedstock preparation

Recycled polypropylene with a density of 0.893 g/cm^3 [16] is used to calculate the composition weight of the composite. The recycled polypropylene was collected from a recycling centre in Subang Bestari, Shah Alam, and granulated into pellets before being used as a matrix. The rice husk fibre was supplied by Persatuan Peladang Kebangsaaan (KPK) in Sungai Besar, Selangor, as a reinforcing fibre. Rice husks were blended until they were in the size range of 20−100 mm, then dried in the oven for 3 hours at 105 °C to remove any moisture content [16]. MAPP was purchased from Sigma Aldrich Sdn. Bhd. MAPP weight of 4% remained consistent across the research [13]. Table 1 shows the weight composition ratio of RH, rPP, and MAPP as coupling agents that had been used in the composites.

Table 1: The weight of rice husk (RH), recycled polypropylene (rPP), and MAPP for each composition of composite

Composition ratio	Density (g/cm^3)	Weight (g)		MAPP (g)
		rPP	RH	
rPP/10RH	0.834	345.6	40	14.4
rPP/20RH	0.782	307.2	80	12.8
rPP/30RH	0.737	268.8	120	11.2
rPP/40RH	0.696	230.4	160	9.6

Mixing process

The VT Sigma Blade mixer machine was used to mix the materials at a temperature range of 170−190 °C. The materials were slowly added to the mixing chamber for 20 min, then the mixing was continued for 40 min at a rotation rate range of 30−50 rpm. Then, the mixed composite was taken out from the mixer and allowed to cool to room temperature before being fed into a granulator.

Differential scanning calorimeter (DSC) analysis

Two samples for neat rPP and rPP/40RH composite were examined using the DSC Melter Toledo machine. The material was scanned from 0 to 500 °C at a heating rate of 10 °C/min with a weight of 9.6 mg and under a nitrogen atmosphere. This DSC analysis data is useful in evaluating the permissible temperature range to be considered in the injection moulding process.

Rheology measurement

The rheological characteristics of rPP and rPP/40RH, such as shear stress, shear viscosity, and the flow behaviour index, *n*, are determined using a capillary rheometer machine (model Capillary Bohlin). The feedstock flowability data were created using the Rosand Capillary Rheometer FlowMaster software. The shear rate of the machine was fixed at a range of 10 to 10000 s^{-1}, pressure at 0.1 MPa, diameter capillary die was 1 mm and length-to-diameter (L/D) of 10 was used for this test. This analysis determines the three temperatures with different variances of 165, 175 and 185 °C in order to find the optimal temperature for injection moulding.

Injection moulding process

The injection moulding process was conducted using a compact injection moulding machine (model Boy 22A). The temperatures for the feed zone, trans zone, metering, and nozzle zones are adjusted to 170, 180, 190 and 200 °C, respectively, based on optimum temperatures obtained from the rheology measurement. The injection moulding process parameters that had been used are shown in Table 2. The mould was designed according to the standard sample size for the tensile and flexural tests following ASTM 412-D and ASTM D790 standards, respectively.

Table 2: Injection moulding process parameters

Sample	Volume (mm^3)	Injection pressure (bar)	Holding time (min)
ASTM 412-D	17-19	60	3
ASTM D790	23	65	3

Mechanical measurement

The mechanical properties of fibre-reinforced polymers are determined using tensile, flexural, impact, and hardness tests. A Shimadzu Universal Testing Machine (UTM) (model AG-IC) equipped with a 50 kN load cell was used in this research to perform tensile and flexural tests according to ASTM D412-D and ASTM D790 standards. The crosshead speed was 5 mm/min. The flexural test was span at 50 mm and a crosshead speed of 5 mm/min. Meanwhile, the impact test was performed using a Notched Izod Impact Test Machine following an ASTM D256 standard. The type of weight R1 (2.71) with 0.453

kg was used to perform this test. Next, the sample size of 125×125×2 mm^3 was prepared for the hardness test using the Rockwell Hardness Tester (model INSTRON A654R). Meanwhile, the sample for the impact and hardness tests was modified from a flexural sample produced from the injection moulding process. For each test, five samples were tested for each composition.

Results and Discussion

Differential scanning calorimeter (DSC) analysis

Thermal phase transitions of rice husk (RH) fibre, neat recycled polypropylene (rPP) and rPP/40RH were studied using differential scanning calorimeters (DSC). Figure 1 illustrates the endothermic reactions of rPP and rPP/40RH. The result shows that rPP had a well-defined melt transition at 164.26 °C and the phase transformation occurred between 130−174 °C. The rPP/40RH composite melting behaviour was very similar to that of neat rPP, which melted at 165 °C and underwent phase transformations between 135 and 177 °C. If the temperature increases more, composite materials may degrade. At temperatures between 318−471 °C and 353−495 °C, respectively, the breakdown of rPP to rPP/40RH started to end. However, compared to neat rPP, modified composites showed greater degradation temperatures (both onset and endset). Because filler was added to the composites, there were mechanical interlocking and nucleating effects [17]. The outcome also showed that the decomposition peak for rPP and rPP/40RH happened around 440 and 454.2 °C, respectively. It has the same results as those reported in the previous works, where an endothermic peak at 448 °C may be related to the depolymerization of polypropylene with the production of propylene [18]. The data also showed that for rPP, there was another peak at 226.24 °C, which could be caused by impurities in the recycled material collection. As a result, the information acquired was utilised to choose the ideal temperature, which was above 165 °C when the material started to melt, and the data were used to determine the temperature for rheological study.

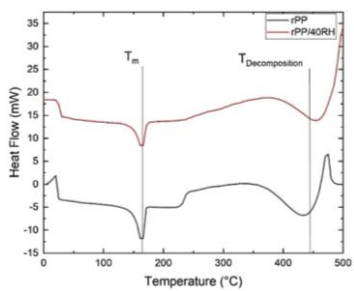

Figure 1: DSC analysis of neat rPP and rPP/40RH composite

Rheological properties

The melt viscosity of recycled polymer blends was evaluated to learn more about the interaction of the polymers in the blend and how compatibilizers affect it. This study was conducted to find the feedstock's stability during the injection moulding process [19]. A feedstock's flow behaviour is preferably pseudoplastic, which means that as the shear rate increases, the viscosity drops. The value of *n* for a pseudoplastic flow must be less than 1. The lower the value of viscosity, the better the flowability of the feedstock. Figures 2a and 2b illustrate the relationship between shear viscosity and shear rate. The data indicated that at 165 °C, the neat rPP and rPP/40RH had the lowest shear viscosity compared to the value of shear rate at 175 and 185 °C. According to recent research, the shear viscosity increased as the temperature value decreased [20]. In this case, the temperature of 165 °C for rPP and rPP/40RH may have been triggered by physical or equipment errors that affect the results of shear rate and shear viscosity. Shear viscosity comparisons between rPP and rPP/40RH indicated that the composite required higher temperatures than rPP, and this may cause the amount of fibre in the composite. The graph showed that the data series for viscosity and shear rate ranged from 0 to 500 Pa.s and 0 to 10000 s^{-1}, respectively. The results indicated that both composite materials had compressive strengths of less than 1000 Pa.s, considering that the materials were acceptable for injection moulding [21].

In this study, the shear sensitivity index *(n)* characteristics can also be evaluated. Previous studies have demonstrated that the optimal *n* value in the pseudoplastic flow phase is in the range of 0.5 to 0.7 [19]. The explanation is because the feedstock viscosity changes with the shear rate more quickly with a smaller *n* value, indicating how a high *n* value may lead to process instability and make it harder to control the sample quality. Table 3 presents the *n* value obtained from the slope of Figures 2a and 2b. The result showed that the lowest *n* value was obtained at 165 °C, while the value *n* in the range of 0.5−0.7 was obtained at 175 °C and 185 °C. Both compositions showed pseudoplastic behaviour at all temperatures. This suggests that as the shearing force increases, molecules that are typically out of alignment start to align their axes in the direction of flow [20]. With less internal resistance, the materials can shear more quickly under each succeeding shearing stress based on this orientation. As a result, the ideal temperature to set during injection moulding is above 175 °C. This information is necessary to keep in the injection moulding stage because it involves the flow of molten feedstock into the mould cavity. Pseudoplastic flow behaviour is the preferred one when using injection moulding [17]. The equation is a Power Law equation that may be used to determine this rheological behaviour (1) where ŋ, K, γ and n are viscosity, coefficient, shear rate and shear sensitivity index, respectively.

$$ŋ = K\gamma^{n-1} \quad (1)$$

Table 3: Flow behaviour index, *n*

Feedstock	Temperature (°C)	Flow Behaviour Index, *n*
rPP	165	0.01
	175	0.6
	185	0.7
rPP/40RH	165	0.01
	175	0.5
	185	0.5

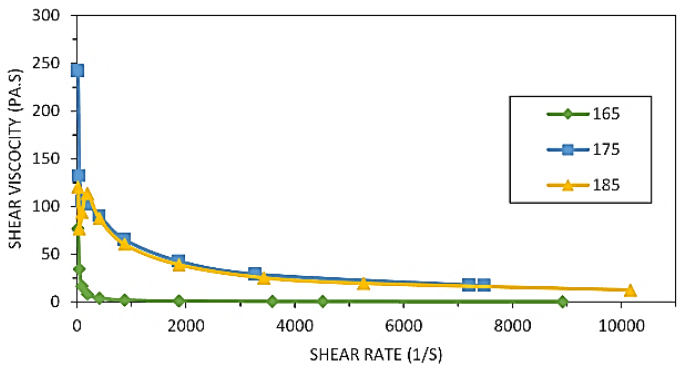

(a)

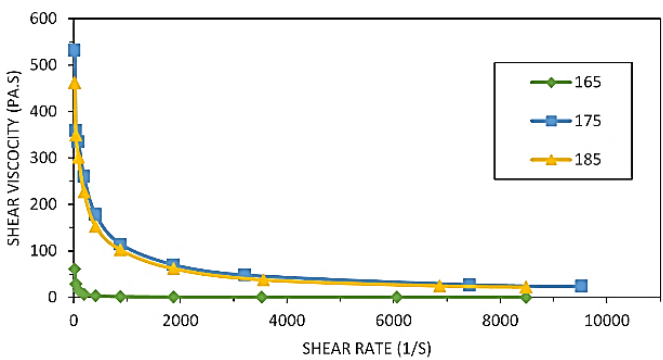

(b)

Figure 2: a) Correlation between shear viscosity and a shear rate of rPP, and b) correlation between shear viscosity and a shear rate of rPP/40RH

Mechanical properties

Tensile properties

A tensile test was conducted on the injection moulded rPP/RH composite to determine its mechanical properties. The tensile tests studied the significant properties of tensile strength, tensile modulus and tensile elongation. The tensile strength, tensile modulus, and tensile elongation of neat rPP and rPP reinforced with varying amounts of fibre loading are shown in Figure 3. It can be seen that the addition of fibre and MAPP to the rPP matrix reduced the tensile strength of the material by 22 to 44% compared to the neat rPP. The same result was also recorded, where the tensile strength of neat polypropylene and recycled polypropylene matrix declined when the rice husk filler percentage exceeded 5% [16]. Due to the small size of the filler particles, there was a large interfacial surface between the polar filler and the apolar matrix [22]. The lack of chemical bonding between the rPP and RH, as well as poor RH dispersion over the rPP matrix due to the substantial differences in surface energy of the rPP and RH fillers, was the potential reason for the reduction of tensile strength when compared to neat rPP. Furthermore, insufficient dispersion caused filler agglomeration, as well as a reduction in tensile characteristics, which may be due to low homogeneity during the mixing process that contributes to this reduction in the MAPP bridge effect between the filler and matrix. Agglomerates' presence can lead to flaws and extra voids between the and the matrix polymer, which lowers the tensile strength. However, according to a previous report, the hydroxyl groups in RH reacted with the anhydride groups in MAPP through an esterification process, which may help to increase the interfacial adhesion between the filler and matrix [13]. The tensile strength increased gradually to the maximum value as the amount of RH fibre was increased to the maximum fibre loading of 40%, as shown by the results in Figure 3a. The results indicated an excellent bridge effect between the filler and matrix, fibre dispersion and fibre−matrix adhesion. Thus, it improved the stress transfer efficiency of the rPP/RH composite. However, the tensile modulus of the rPP−RH composite improved by 33 to 46% compared to neat rPP. The increase in tensile modulus with an addition of RH in the loading of rPP matrix was due to the RH's ability to impart more stiffness to the matrix [23]. This is a typical behaviour when the hard filler is added to softer polymer matrices. Natural fibres have a higher elastic modulus than pure rPP, resulting in increased composite stiffness [12]. Due to this, adding these fillers tends to significantly improve the stiffness of its composites. Figure 3b illustrates the tensile elongation of the composite, which indicates its flexibility of the composite. The results demonstrated a decrease in tensile elongation with the increase in fibre percentage. It can be seen that fibre reinforcement composite with MAPP had a lesser tensile elongation than neat rPP. This occurred as a result of the coupling agent function in igniting the interaction between the filler surfaces and rPP that caused the composite to stiffen. The coupling agent's impact on this property was not immediately

apparent in this study. These results also indicated that MAPP decreases the flexibility and elasticity of materials, which is consistent with earlier research [24].

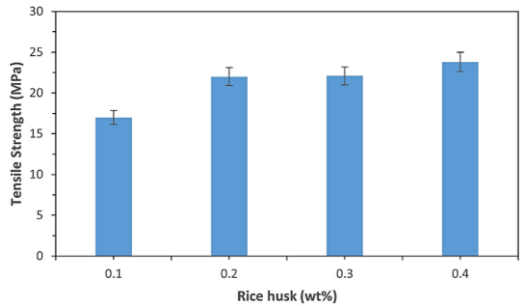

(a)

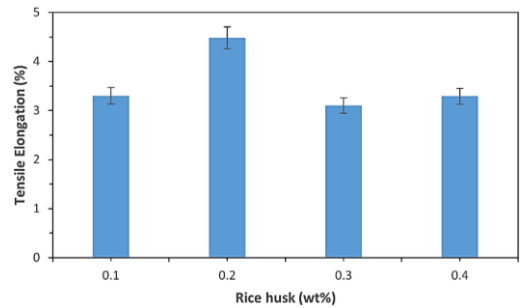

(b)

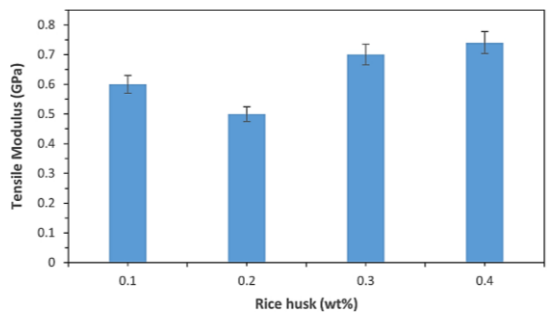

(c)

Figure 3: Tensile properties of rPP/RH composite with different percentage of rice husk fibre; a) tensile strength, b) tensile elongation at break, and c) tensile modulus

Flexural properties

The flexural analysis found that the matrix fillers have excellent interfacial bonding in the composite. Figure 4 shows the flexural strength and modulus of rice husk-reinforced polypropylene composites. In comparison to neat rPP, the data showed that 40 wt% fibre has the maximum flexural strength and flexural modulus. This could be attributable to the introduction of filler and coupling agent, which increases due to an improvement in the filler and matrix boundary region. This is further proven by the fact that flexural strength improves when MAPP is added to neat rPP [15]. The same outcome was observed in the earlier investigation, where adding more fibre and MAPP as a coupling agent has been shown to improve flexural modulus by 73% from neat PP [7]. Interestingly, the modulus of composites with coupling agents at high filler loading was much better than that of the composite without coupling agents. The rising pattern could be brought on by the fact that rice husk is much stiffer than rPP. A crystalline layer can develop around the fibres when coupling agents are present because surface crystallisation takes precedence over bulk crystallisation [15]. Crystallite can enhance the polymer matrix's contribution to the composite modulus since they have a greater modulus than amorphous areas.

Impact

Rapid crack propagation via the material causes impact failures [25]. The rate of fracture growth is inversely proportional to the material's impact resistance. To be deemed as impact resistant, a polymer must be able to absorb the majority of the impact energy and limit the rate of crack development. The Izod impact test was used to determine the amount of impact energy required to crack or fail the surface. Figure 5 demonstrates that rPP and rPP reinforced with fibre had similar results at 20, 30, and 40%; however, 10 wt% fibre resulted in low absorbance as compared with neat PP. According to the previous study, the addition of rice husks resulted in a reduction of impact strength because the husks reduced energy absorption ability which led to the increase of fibre breakage and more residual stress in the composite [13]. The addition of MAPP to the fibre-matrix composite structure made it more brittle, and the husks limited the free motion of matrix chains. The matrix dampened the force during loading since there was greater matrix movement between the husks. However, adding rice husks led to a similar impact strength of 1.8 kJ/mm^2. This finding suggests that the MAPP may have improved the interaction between rice husk fibre and matrix.

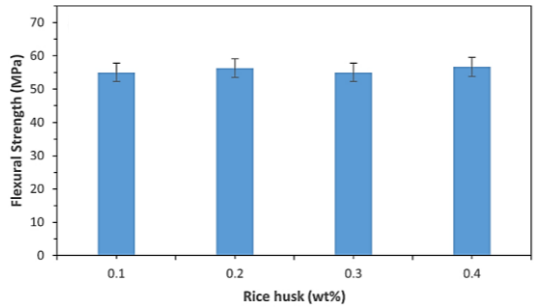

(a)

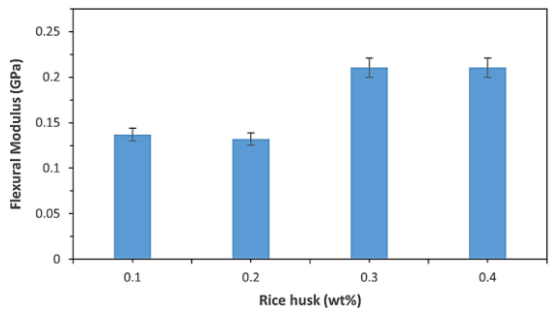

(b)

Figure 4: Flexural properties of rPP/RH composite with different percentages of rice husk fibre; a) flexural strength, and b) flexural modulus

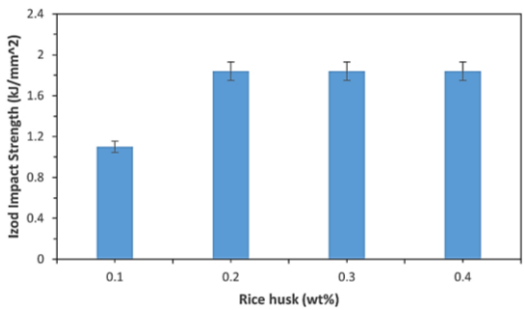

Figure 5: Impact of rPP/RH composite with different percentages of rice husk fibre

Hardness

Figure 6 illustrates the hardness strength with neat rPP and different fibre loading. The optimum hardness was obtained at 40% fibre load. In comparison

to neat rPP, the composite can improve by up to 16%. This improvement in the composite can be attributed to the high interfacial adhesion of the rPP−RH and MAPP composite, as well as the RH material's molecular-level dispersion in the matrix, which results in an improvement in how effectively stress is transferred from the matrix to the filler phase [23]. Additionally, when a material becomes more resistant to deformation, its hardness improves. This occurs when additional filler is introduced, making the composite harder and the substance tougher [26]. Better resistance to plastic deformation in the filler's transverse direction is provided by the filler layer.

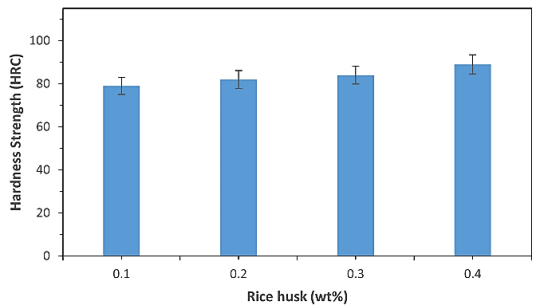

Figure 6: Hardness of rPP/RH composite with different percentage of rice husk fibre

Conclusion

Different rice husk weight ratios have been successfully made and used to characterise the effects of rice husk (RH) as a reinforcement filler on the properties of recycled polypropylene (rPP) matrix with maleic anhydride grafted polypropylene (MAPP) as coupling agents. The determination of the rheology temperature range is set at 165, 175 and 185 °C. Thus, the data indicate that the feedstock has the best flow mouldability at temperatures between 175 and 185 °C, where the *n* value obtained is in the range of 0.5−0.7, which exhibits pseudoplastic behaviour. Therefore, the result demonstrates a decrease in tensile strength and tensile elongation in the composite. However, the finding indicates that tensile modulus, flexural strength, flexural modulus, impact strength, and hardness strength have all improved. In this experiment, the tensile strength and tensile elongation show a decline of 22 to 44% and 33 to 46%, respectively, compared to neat rPP, which shows that the composite lacks chemical bonding and dispersion. According to the flexural study, the best outcome occurs at a fibre loading of 40% weight when a good polymer matrix contributes to the matrix. In addition, when the ratio of RH reinforcement is added to the rPP−RH matrix, the hardness data show an

improvement of 3−16% in contact that absorbs high energy impact. Therefore, a composite that incorporates 40% rice husk fibre and MAPP demonstrates greater results among the composites. In conclusion, rice husks and maleic anhydride polypropylene have successfully proven to have better properties of polymer-based nanocomposites and other composite applications as coupling agents.

Contributions of Authors

The authors confirm the equal contribution in each part of this work. All authors reviewed and approved the final version of this work.

Funding

This work received no specific grant from any funding agency.

Conflict of Interests

One of the authors, Freddawati Rashiddy Wong, is an assistant managing editor of the Journal of Mechanical Engineering (JMechE). The author has no other conflict of interest to note.

Acknowledgement

The author would like to thank the Heat Treatment Lab, Composite Lab, Advance Materials Lab, Concrete Lab, Polymer Lab and Workshop of the College of Engineering, UiTM Shah Alam, for their technical help in completing this research.

References

[1] Jabatan Perangkaan Malaysia, “Department of Statistic Malaysia eStatistic,” Department of Statistics Malaysia.com. https://www.dosm.gov.my/v1/index.php (accessed Jul. 01, 2022).
[2] C. W. Macosko, Rheology: Principles, Measurements, and Applications, 1st Ed., New York: Wiley−VCH, pp. 1−568, 1994.
[3] B. Maldonado-García, A. K. Pal, M. Misra, S. Gregori, and A. K. Mohanty, “Sustainable 3D printed composites from recycled ocean

plastics and pyrolyzed soy-hulls: optimization of printing parameters, performance studies and prototypes development," *Composites Part C: Open Access*, vol. 6, no. 10, pp. 1−17, 2021. doi: 10.1016/j.jcomc.2021.100197.

[4] J. Sun, Y. Pang, J. Zhao, R. Xia, Y. Li, and Y. Liu, "Improvement of rice husk/ high-density polyethylene bio−composites interfacial properties by silane coupling agent and compatibilizer complementary modification," *Multidisciplinary Digital Publications Institute*, vol. 11, no. 12, pp. 1–13, 2019. doi: 10.3390/polym11121928.

[5] C. H. Tsou, W.H. Yao, C.S. Wu, W.S. Hung, J.C. Chen, J. Guo, S. Yuan, E. Wen, R.Y. Wang, M.C. Sunn, and S.C. Liu, "Preparation and characterization of renewable composites from polylactide and rice husk for 3D printing applications," *Journal Polymer Research*, vol. 26, no. 9, pp. 1−10, 2019. doi: 10.1007/s10965-019-1882-6.

[6] C. O. Umerah, D. Kodali, S. Head, S. Jeelani, and V. K. Rangari, "Synthesis of carbon from waste coconutshell and their application as filler in bioplast polymer filaments for 3D printing," *Composite Part B Engineering*, vol. 202, no. 2, pp. 1−9, 2020. doi: 10.1016/j.compositesb.2020.108428.

[7] M. A. Morales, A. Maranon, C. Hernandez, and A. Porras, "Development and characterization of a 3D printed cocoa bean shell filled recycled polypropylene for sustainable composites," *Multidisciplinary Digital Publications Institute*, vol. 13, no. 18, pp. 1−17, 2021. doi: 10.3390/polym13183162.

[8] K. L. Pickering and D. B. Stoof, "Sustainable composite fused deposition modelling filament using post-consumer recycled polypropylene," *Journal Composite Science*, vol. 1, no. 2, pp. 1−12, 2017. doi: 10.3390/jcs1020017.

[9] C. S. Wu, S. S. Wang, D. Y. Wu, and W. L. Shih, "Novel composite 3D-printed filament made from fish scale-derived hydroxyapatite, eggshell and polylactic acid via a fused fabrication approach," *Additive Manufacturing*, vol. 46, no. 2, pp. 1−12, 2021. doi: 10.1016/j.addma.2021.102169.

[10] C. S. Wu, H. T. Liao, and Y. X. Cai, "Characterisation, biodegradability and application of palm fibre-reinforced polyhydroxyalkanoate composites," *Polymer Degradation Stability*, vol. 140, no. 1, pp. 55−63, 2017. doi: 10.1016/j.polymdegradstab.2017.04.016.

[11] R. Arjmandi, A. Hassan, K. Majeed, and Z. Zakaria, "Rice husk filled polymer composites," *International Journal of Polymer Science*, vol. 15, no. 10, pp. 1−33, 2015. doi: 10.1155/2015/501471.

[12] O. E. Ezenkwa, A. Hassan, and S. A. Samsudin, "Tensile and impact properties of rice husk filled ethylene-acrylic ester maleic anhydride compatibilized polypropylene composites," *Chemical Engineering*

Transactions, vol. 83, no. 2, pp. 511−516, 2021. doi: 10.3303/CET2183086.

[13] U. Huner, "Effect of chemical treatment and maleic anhydride grafted polypropylene coupling agent on rice husk and rice husk reinforced composite," *Material Express*, vol. 7, no. 2, pp. 134–144, 2017. doi: 10.1166/mex.2017.1359.

[14] W. Song, W. Wei, X. Li, and S. Zhang, "Utilization of polypropylene film as an adhesive to prepare formaldehyde-free, weather-resistant plywoodlike composites: process optimization, performance evaluation, and interface modification," *BioResources*, vol. 12, no. 1, pp. 228–254, 2016. doi: 10.15376/biores.12.1.228-254.

[15] N. Raghu, A. Kale, S. Chauhan, and P. K. Aggarwal, "Rice husk reinforced polypropylene composites: mechanical, morphological and thermal properties," *Journal of the Indian Academy Wood Science*, vol. 15, no. 1, pp. 96−104, 2018. doi: 10.1007/s13196-018-0212-7.

[16] M. A. Morales, C. L. Atencio Martinez, A. Maranon, C. Hernandez, V. Michaud, and A. Porras, "Development and characterization of rice husk and recycled polypropylene composite filaments for 3D printing," *Multidisciplinary Digital Publications Institute*, vol. 13, no. 7, pp. 1−17, 2021. doi: 10.3390/polym13071067.

[17] V. Kumar, M. S. Saini, B. K. Kanungo, and S. Sinha, "Study of thermal properties of rice husk polypropylene composites," *Advances Composites Letters*, vol. 22, no. 6, pp. 125−130, 2013. doi: 10.1177/096369351302200601.

[18] B. Mukhiddinov, L. Tilavova, and S. Juraev. (2 June 2021). Development of compositions from waste of polypropylene and polyethylene terephthalate and research of their technological and thermal properties. Presented at International Scientific Conference [Online]. Available: https://doi.org/10.1051/e3sconf/202126405005.

[19] N.H.M. Nor, F. Morni; and M.H. Ismail, "Thermal and flow analysis of stainless 2 steel and alumina feedstock used for 3 2C-process injection moulding," *Journal Mechanical Engineering*, vol. 21, no.1, pp. 1−18, 2021. doi: 10.1590/S1516- 14392009000300014.

[20] R. W. Goodwin, J. W., and Hughes, "Rheology for Chemists: An Introduction," 2nd Ed. :Royal Society of Chemistry, 2008, Accessed: Apr. 16, 2022. [Online]. Available: https://doi.org/10.1039/9781847551832

[21] A. P. Marzuki, F. M. Salleh, M. N. S. Rosli, I. Tharazi, A. H. Abdullah, and N. H. A. Halim, "Rheological, mechanical and physical properties of poly-lactic acid/ hydroxyapatites composites prepared by an injection moulding process," *Journal Mechanical Engineering*, vol. 19, no. 2, pp. 17−39, 2022.

[22] S. M. L. Rosa, E. F. Santos, C. A. Ferreira, and S. M. B. Nachtigalt, "Studies on the properties of rice-husk-filled-polypropylene composites

- effect of maleated polypropylene," *Material Research*, vol. 12, no. 3, pp. 333−338, 2009. doi: 10.1590/S1516-14392009000300014.
[23] I. Ahmad, D. R. Abu Bakar, S. N. Mokhilas, and A. Ramli, "Recycled polyethylene terephthalate for rice husk/ polyester composites," *ASEAN Journal on Science Technology for Development*, vol. 22, no. 4, pp. 345, 2017. doi: 10.29037/ajstd.170.
[24] M. Awang, "Study the effects of an addition of titanium dioxide on the mechanical and thermal properties of polypropylene-rice husk green composites," *Materials Research Express*, vol. 2, no. 3 pp. 1−15, 2017. doi: 10.1088/2053-1591/ab1173.
[25] R. S. Chen, S. Ahmad, and S. Gan, "Rice husk bio-filler reinforced polymer blends of recycled high-density polyethylene/ polyethylene terephthalate - threedimensional stability under water immersion and mechanical performance," *Polymer Composite*, vol. 39, no. 8, pp. 2695–2704, 2018. doi: 10.1002/pc.24260.
[26] S. Subramonian, A. Ali, M. Amran, L. D. Sivakumar, S. Salleh, and A. Rajaizam, "Effect of fiber loading on the mechanical properties of bagasse fiber-reinforced polypropylene composites," *Advance Mechanical Engineering*, vol. 8, no. 8, pp. 1–5, 2016. doi: 10.1177/1687814016664258.

The Influence of Cutting Parameter under Sustainable Machining Approaches on Surface Roughness of AISI 4340

*Ahsana Aqilah Ahmad[1,2], Jaharah A. Ghani[*2], Che Hassan Che Haron[2]*

[1]School of Mechanical Engineering, College of Engineering,
Universiti Teknologi MARA, 40450 Shah Alam, Selangor, MALAYSIA
[2]Department of Mechanical and Manufacturing Engineering,
Faculty of Engineering and Built Environment,
Universiti Kebangsaan Malaysia, 43600 Bangi, Selangor, MALAYSIA
** jaharahaghani@ukm.edu.my*

ABSTRACT

This study presents the result of surface roughness (SR) during milling AISI 4340 under sustainable machining techniques of minimum quantity lubrication (MQL) and cryogenic using liquid nitrogen (LN_2). Along with MQL, Treated Recycled Cooking Oil (TRCO) using waste Palm Oil is used to promote a greener cutting condition. Taguchi L9 orthogonal array and ANOVA are used to investigate the effect of cutting parameters (cutting speed, feed rate, depth of cut and width of cut) on the measured output value. Statically, in both conditions results show that cutting speed and feed rate are the parameters that affect the surface roughness. ANOVA analysis for MQL cutting found that feed rate contributed 87.39% of the output value. While in the cryogenic condition, cutting speed is the main factor that affects the SR value, representing 54.83%. At a lower cutting speed, the SR yield during MQL is lower compared to cryogenic conditions. At a higher cutting speed, the SR value in the cryogenic condition is better than that in MQL condition. However, when the feed rate increases, the SR value is almost similar in both conditions. This finding shows that using this experimental condition with TRCO can improve the SR value even at a higher cutting speed.

Keywords: *Treated Recycle Cooking Oil (TRCO); Minimum Quantity Lubrication (MQL); Cryogenic (LN_2); Sustainable Machining; Taguchi*

ISSN 1823-5514, eISSN 2550-164X

https://doi.org/10.24191/jmeche.v12i1.24638

Received for review: 2023-09-25
Accepted for publication: 2023-10-18
Published: 2023-11-15

Introduction

Removing heat from the cutting region during machining is important because excessive heat is associated with many quality problems in the metal cutting operation. The heat that is generated at primary and secondary shear zones is transferred to the cutting tool and weakens its mechanical bonding, leading to changes in the cutting tool geometry. The blunt tool accelerates tool wear, thus affecting the surface roughness (SR) of the finished part and its final dimensional accuracy [1]. Moreover, the heat that is generated above the material's recrystallisation temperature may lead to surface microstructure alteration. These occurrences are associated with various surface quality problems such as poor SR, white layer formation, microstructure distortion and residual stresses [2]. These problems are common in the automotive and aerospace industries, and they reduce parts' functionality and increase the rejection rate of finished parts [3]. A common way to improve the surface quality is to apply a lubricant/coolant during machining. However, the excessive use of cutting fluid poses a problem to machining sustainability, especially given current global issues.

In line with this situation, dry cutting, minimum quantity lubrication (MQL) and cryogenic coolant have been extensively studied by researchers to limit the usage of cutting fluid and thus eliminate the problems associated with the usage of MWF. Dry cutting uses no MWF, thus eliminating any related costs. However, dry cutting is associated with a high value for both thermal and mechanical loading, thus being more prone to damaging the work surface when compared with the situation in which cutting fluid is used [4]. MQL is a method of delivering cutting fluid to the cutting edge by mixing a minute amount of cutting fluid with pressurised air to form a mist of cutting fluid, which is then sprayed to the cutting region by a nozzle. The fluid consumption of MQL varies from 0.2 to 500 ml/hour as opposed to that of flood coolant at 30,000 to 60,000 ml/hour [5]. As soon as the mist from the MQL encounters the hot surface of the cutting zone, the heat is carried away by the vaporisation and cools down the cutting process, thus leaving the oil particles on the tool surface. These oil particles act as a tribofilm that reduces the friction at the tool–chip interface, resulting in better SR and longer tool life [6]. Still, the effectiveness of MQL also heavily depends on the quality of the supplied oil mist to the cutting zone. In cryogenic machining, the cutting edge is cooled down by cryogenic gas or liquid such as liquid nitrogen (LN_2) and carbon dioxide (CO_2). These gases are known to be environmentally friendly and do not harm humans. Cryogenic cooling effectively reduces the cutting temperature, thus improving the surface integrity of the machined part. However, a proper delivery system of cryogenic coolant to the cutting edge is crucial because excessive exposure of the workpiece and the cutting tool to this cryogenic temperature may lead to work tool hardening, which increases

energy consumption during cutting. Furthermore, cryogenic coolant does not provide better lubrication than the cutting oil.

Research by [7] revealed a relation between tool wear, cutting temperature and tool vibration with the workpiece SR and tool life. When cutting under MQL condition, the heat is effectively carried away by the chips via the pressurised air of the MQL system. The cutting vibration and tool wear are reduced because the oil provides an ample lubrication barrier that reduces the friction at the cutting tool–workpiece interface. As the result, the SR improved by 89% while tool life prolonged by 267% when compared with dry cutting. The result is also consistent with that of Rahim et al. [8], who found that the application of MQL reduced the cutting temperature by 10% to 30% when compared with dry cutting. The effective coolant/lubrication is supported by the chip produced in the experiment. Thinner chips were produced, indicating a lower cutting temperature and less chip–workpiece friction during the cutting process by using the MQL method. Based on Taguchi analysis during AISI 4140 MQL machining, the SR of the work material is mainly contributed by the feed rate. This finding is consistent with that of Abidin et al. [9], who also found that feed rate is the effective parameter that determines the quality of the product surface of AISI 4140. Increasing the feed rate value will yield a poorer surface finish because of higher vibration during the cutting process [10]. Other researchers found out that the MQL method is not effective when applied at higher cutting speeds. Kedare et al. [11] investigated the effect of cutting under MQL and flood conditions for different cutting speeds and depths of cut. The SR values are lower than those of the flooding method at all cutting speeds (160–300 m/min). However, the value does not vary considerably when the cutting speed and depth of cut increase. A similar result was obtained by [12] when cutting AISI 4140 in MQL, flood and dry conditions. At a higher cutting speed, the influence of coolant/lubricant is reduced because of the lack of oil mist penetration in the cutting region. At a higher cutting speed, the tool–chip is in a fully elastic condition and prevents the oil from penetrating the cutting region. At a lower cutting speed, the tool–chip is in a partially elastic condition, thus enabling the cutting fluid to enter the gap between the chip–tool interface by the capillary action to form a thin lubricant film that reduces friction [13].

Different types of cutting oil used during machining with MQL also contribute to the outcome of the machining process. Werda et al. [14] conducted an experiment to explore the effect of cutting oil on the SR of the work material. Vegetable-based cutting oil yields lower SR compared with alcohol-base cutting oil during dry cutting. This better result is due to the complex structure of fatty acids in the vegetable oil, thus providing high oxidation stability, which is important during high-temperature machining to help maintain the oil properties throughout the process [15]-[16]. Similarly, these scholars found that using palm oil as a cutting fluid improves machinability in terms of SR, cutting force and tool life when compared with

other types of vegetable oil-based cutting fluid. In Malaysia, most industrial and domestic frying oil is palm fruit-based. Estimations suggest that 50,000 MT of used frying oils, both vegetable oils and animal fats are disposed of yearly in Malaysia without treatment [17].

This study focuses on the effect of MQL and cryogenic conditions on SR when machining AISI 4340. Treated recycled cooking oil (TRCO) is proposed as the MQL cutting fluid due to its availability in Malaysia; in addition, it is more suitable than fresh palm oil for human consumption. In addition, biodiesel based on renewable energy of used cooking oil has become one of the initiatives in automotive industries to lessen the carbon footprint and attain a greener transportation system. Thus, this work also plays a small part in creating a more sustainable industry by utilising TRCO in the product life cycle when machining the metal parts.

Methodology

Material, cutting tools and TRCO

This experiment uses a block of pre-hardened AISI 4340 high-strength low-alloy steel with dimensions of 178 × 102 × 52 mm and an average hardness of 32HRC. AISI 4340 alloy steel is widely used in the automotive and aircraft industries to produce structural components due to its excellent toughness and strength properties. A PVD (TiAlN/AlCrN) multilayer coated carbide indexable end mill is used to machine the metal surface.

In this experiment, TRCO is used to replace the conventionally used cutting fluid. The TRCO is treated and purchased from Universiti Teknikal Malaysia as an effort towards a sustainable machining environment. The initial stage of producing TRCO is started by collecting used cooking oil (UCO) from a franchise restaurant. For the treatment process, the acquired UCO is filtered to remove all the visible residues and particles. Then, with every 50 g of UCO, 10 wt.% of palm kernel activated carbon (PKAC) is added to the UCO. PKAC is a by-product of palm oil processing; palm oil is easily available in Malaysia and Indonesia, and it is known to have excellent absorbent properties due to its higher surface area. PKAC is usually used to neutralise chemical substances and odour from wastewater [34]. The size of the powder PKAC is between 250 - 297 microns in diameter. The mixture of UCO–PKAC is then heated between 100 to 110 °C for 80 minutes to ensure that all water content is removed from the mixture. The oil sample solution is then filtered to remove excess PKAC powder. The properties of TRCO are presented in Table 1 while Table 2 lists the details of the experiment condition.

Table 1: Properties of TRCO before and after treatment [18]

Properties	Before treatment	After treatment
Density at 25 °C (g/ml)	0.9284	0.9294
Viscosity at 40 °C (cSt)	45.658	31.91
Peroxide value (mEq O2/kg)	16	14
Free fatty acid, FFA (%)	0.38	0.3666
Acid value (mgKOH/g)	1.456	1.122

Table 2: Experimental conditions

Machine Tool	:	Vertical milling (DMG-ECO) 8000 RPM spindle speed
Work specimen	:	AISI 4340 HSLA Steel (C=0.37%, Si=0.33%, Mn=0.80%, P=0.014%, S=0.002%, Cr=1.70%, Mo=0.22%, Ni=1.33%, Fe= Balance)
Cutting Tool Insert		
Cutting insert	:	PVD multicoated TiAlN/AlCrN grade ACP200
Tool holder	:	32 mm diameter, 5 indexable inserts (WEX 2032E)
Tool geometry	:	Rake angle=28°, clearance angle=11°, thickness=3.58 mm
Process Parameters		
Cutting speed, *Vc*	:	300, 350, 400 m/min
Feed rate, *fz*	:	0.15, 0.2, 0.3 mm/tooth
Axial DOC, a_p	:	0.5, 0.6, 0.7 mm
Radial DOC, a_e	:	0.3, 0.5, 0.7 mm
MQL Supply	:	Air: 8.0 bar, lubricant: 60 ml/hr, 2 external nozzles, nozzle distance, *d*=25 mm, elevation angle=60°, cutting fluid= TRCO
Cryogenic Supply	:	LN_2, pressure= 2 MPa, flow rate=1.159×10^{-3} m^3/s, elevation angle=45°

Experimental procedure

This metal's block is downmilled using a straight-line surface machining strategy on a DMG-ECO, vertical milling machine with 8000 RPM spindle speed capacity. PVD (TiAlN/AlCrN) multilayer coated carbide end mill insert is fixed to a 32 mm diameter tool holder manufactured by Sumitomo. The tool holder consists of five indexable cutting inserts, but only one insert is utilised to avoid tooltip runout during wear measurement. The experiment is conducted under MQL with a mixture of compressed air and TRCO as the cutting fluid at a rate of 60 ml/hr via two nozzles. For comparison, the experiment is repeated under cryogenic condition by using LN_2. To avoid excessive cooling, only one nozzle supplying LN_2 is used during the experiment. Table 2 lists the details of the experiment condition. The average surface roughness (*Ra*) measurement is taken according to ISO 4288 (2) 1996. For each tested parameter, the SR value was taken three times at three different locations along the feed direction of the workpiece by using a Mitutoyo portable SR tester. The stylus movement of the portable SR tester is set at 5.6 mm at an evaluation

distance of 4 mm and a cut-off value (λc) of 0.8 mm. Figure 1a illustrates experimental setup for cutting under MQL condition using 2 nozzles. While Figure 1b illustrates the experimental setup for cryogenic cutting and the LN_2 flow during machining process.

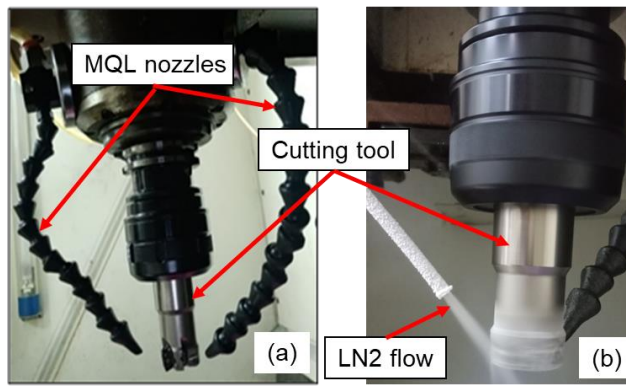

Figure 1: Experimental setup for; (a) MQL, and (b) cryogenic

Design of experiment and machining parameters

In this work, Minitab v18.1 software is used to design, plot, and analyse the data. Taguchi method is used for the design of experiment (DOE) by calculating a signal-to-noise (S/N) ratio to determine the variability of the parameter in the process. A higher S/N ratio is desired because it indicates the optimal level for the process parameters [19]. The output of the experiment is to determine the best parameter combination for minimising SR; thus, the-smaller-the-better S/N ratio is used for the calculation. Four input parameters, namely, cutting speed (Vc), feed rate (fz), depth of cut (a_p) and width of cut (a_e), at three levels of values are selected for this experiment (Table 2). Hence, according to the Taguchi approach, L9 (3^4) orthogonal array is the suitable number of experiments to facilitate four cutting parameters and three levels of the parameter's value [20]. Later, ANOVA analysis is performed to determine the percentage of influence of each parameter to the measured response. Table 3 outlines the nine experiments conducted in this study and the SR obtained for both cutting conditions.

Table 3: L9 orthogonal array of the experiment and SR result for MQL and cryogenic condition

Exp. no.	Cutting speed Vc	Feed rate, fz	Axial a_p	Radial a_e	Surface Roughness MQL	Cryogenic
1	300	0.15	0.5	0.3	0.134	0.165
2	300	0.2	0.6	0.5	0.178	0.20
3	300	0.3	0.7	0.7	0.209	0.235
4	350	0.15	0.6	0.7	0.141	0.149
5	350	0.2	0.7	0.3	0.174	0.142
6	350	0.3	0.5	0.5	0.182	0.176
7	400	0.15	0.7	0.5	0.129	0.135
8	400	0.2	0.5	0.7	0.166	0.16
9	400	0.3	0.6	0.3	0.179	0.161

Results and Discussion

Figure 2a illustrates that the highest S/N ratio indicates the optimum level for obtaining the best combination of the response. With the use of 'the smaller, the better' principle for S/N ratio calculation, the optimal factor combination for minimising SR Ra for MQL is a cutting speed of 400 m/min, feed rate of 0.15 mm/tooth, depth of cut of 0.5 mm and width of cut of 0.3 mm. The main effect plot graph in Figure 2 indicates that feed rate and cutting speed are the main parameters that affect the output value of SR, whereas DOC and WOC are the parameters that have the least effect. For comparison, the experiments were repeated under cryogenic condition to investigate the effect of cutting parameters on SR in different cutting conditions. Based on the S/N ratio from the main effect plot of Figure 2b, the optimum parameters for obtaining the lowest SR in the cryogenic condition is similar to those in the MQL condition. The feed rate and cutting speed are the parameters that heavily influence the surface quality of the machined surface. Theoretically, cutting under cryogenic condition will produce a finer SR in comparison to that under dry and wet conditions [21]. When compared to other cutting conditions, LN_2 offers lubrication at the cutting zone, thus reducing tool's sticking and wear and eventually producing a better surface roughness. When it comes to MQL, previous studies reveal that MQL machining produces finer SR at a lower cutting speed compared with cryogenic cooling [22]–[25]. The good surface finish during MQL cutting is due to the cutting oil effectively reducing the friction at the cutting zone. However, at a higher cutting speed, Kaynak [23] reported lower cutting force when cutting Inconel 718 under cryogenic condition, hence producing better SR. Thus, this work aims to investigate the SR value when machining AISI 4340 in both cutting conditions.

Based on Figure 2, the main effect plot for both cutting conditions revealed that feed rate and cutting speed are the most influential parameters that affect the value of SR. However, it does not indicate the significant factors and percentage of influence of each parameter to the measured response. The ANOVA results for both cutting conditions are shown in Tables 3 and 4. A lower *p*-value from the ANOVA's table represents a higher impact of that input factor on the measured output [26]. The contribution value, on the other hand, reflects the percentage of influence of each parameter on the measured response. Table 4 shows that the *p*-value for the feed rate and cutting speed is the lowest for SR in MQL machining, with contribution factors of 87.39% and 6.70%, respectively; radial DOC has the least impact (3.18%) on SR, which agrees with the finding by [27]-[28]. When cutting in cryogenic conditions (Table 5), cutting speed and feed rate have the lowest *p*-value and greatly affect the output value by 54.83% and 32.45%, respectively. Both outcomes from Tables 4 and 5 support the result obtained from the S/N ratio. Thus, the value of the feed rate and cutting speed should be optimised to achieve the lowest SR in MQL and cryogenic conditions.

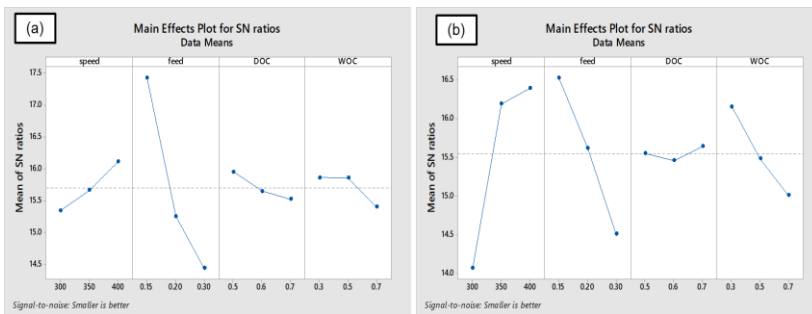

Figure 2 Main effect plot for SR in; (a) MQL condition, and (b) cryogenic conditions

Table 4: ANOVA SR under MQL condition

Source	DF	Seq SS	Contribution	Adj SS	Adj MS	*P*-Value	*F*-Value
Vc	2	0.000368	6.70%	0.00037	0.00018	0.29	2.45
fz	2	0.004806	87.39%	0.00481	0.00240	0.03	31.99
ae	2	0.000175	3.18%	0.00018	0.00009	0.46	1.16
Error	2	0.000150	2.73%	0.00015	0.00008		
Total	8	0.005500	100.00%				

Table 5: ANOVA SR under cryogenic condition

Source	DF	Seq SS	Contribution	Adj SS	Adj MS	*P*-Value	*F*-Value
Vc	2	0.004283	54.83%	0.00428	0.00214	0.005	187.12
fz	2	0.002538	32.48%	0.00254	0.00127	0.009	110.86
ae	2	0.000968	12.39%	0.00097	0.00049	0.023	42.30
Error	2	0.000023	0.29%	0.00002	0.00001		
Total	8	0.007812	100.00%				

The experimental result revealed that the SR value ranges from 0.134 to 0.235 µm for both cutting conditions (refer Table 3). These values are less than the 0.5 µm value that is usually produced by manual polishing. The lowest SR is attained during machining under MQL, whereas the highest SR is obtained during machining under cryogenic condition. Both occur at the lowest cutting speed. Figure 3 shows that MQL works better at a lower cutting speed during machining AISI 4340. As the cutting speed progresses, the SR value during cryogenic cooling improves slightly. However, the results are closely similar to the SR value for MQL. The highest improvement of SR is observed in experiment 5 with 18.4% SR reduction. Therefore, this experimental process and the utilisation of TRCO can produce a good surface finish similar to the cryogenic condition even at a higher cutting speed and feed rate.

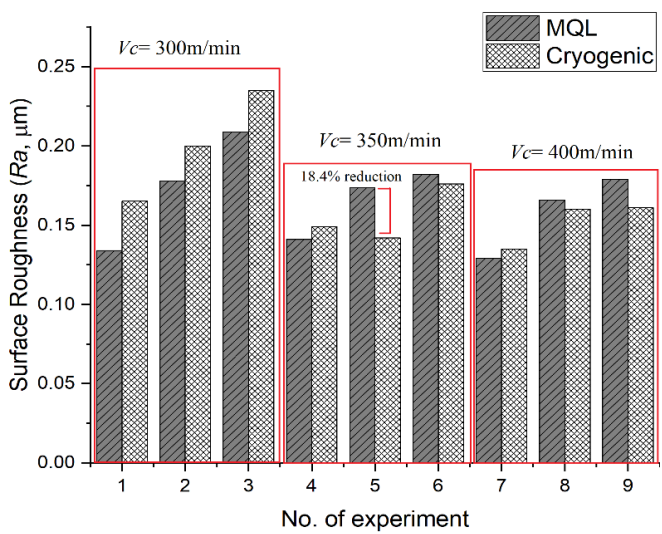

Figure 3: SR experimental results for various cutting parameters when cutting under MQL and cryogenic conditions

Previous researchers found that cutting in cryogenic conditions is more effective in high velocity while MQL is at low speed [29]. However, the findings of this study found that when the cutting speed is increased to 350 and 400 m/min, MQL-TRCO cutting can produce a surface roughness that is almost the same as machining in cryogenic conditions. This may occur because the use of plant-based lubricants for MQL-TRCO machining has a stable fatty acid structure to withstand increasing cutting temperatures [15]-[16].

Figure 4 depicts that the increasing value of feed rate from 0.15–0.3 mm/tooth will directly increase the SR value for both cutting conditions. The main effect plot (Figure 2) also indicates that the increasing value of WOC and DOC can be detrimental to SR because increasing these parameters will lead to a higher material removal rate, which will increase the vibration, thus affecting the SR [10], [30]-[31]. At a lower cutting speed of 300 m/min (Figure 4a), the SR value under the MQL condition is lower than that under the cryogenic condition at all feed rates. At a lower cutting speed, the tool–chip is partially elastic, thus enabling the cutting fluid to enter the gap between the chip–tool interface through capillary action to form a thin lubricant film that reduces friction [13]. Furthermore, the presence of TRCO at the cutting zone limits the contact area between tool and workpiece; hence, thinner chips are produced [12]. A higher SR under cryogenic cooling at a cutting speed of 300 m/min is probably a result of work hardening due to the excessive cooling at the cutting region at a lower cutting speed. According to Thakur et al. [32], the effect of work hardening is less at a high cutting speed compared with that at a lower cutting speed. Figure 4b shows that the SR value for MQL cutting is more sensitive to the variation of feed rate at a higher cutting speed. As the cutting speed varies from 300–400 m/min, the SR value under the cryogenic condition improves, although it becomes less noticeable at the feed rate increases. Figure 5 shows that increasing the cutting speed can help improve SR. The figure shows that the increasing value of cutting speed from 300–400 m/min yields finer SR at both feed rate values. This condition occurs because, at a higher cutting speed, the built-up temperature at the tool tip eases plastic deformation during shearing due to thermal softening of the workpiece. Similar results were obtained by other studies [33]-[34]. The SR value under cryogenic condition is more sensitive to variations in the cutting speed compared with that under MQL conditions.

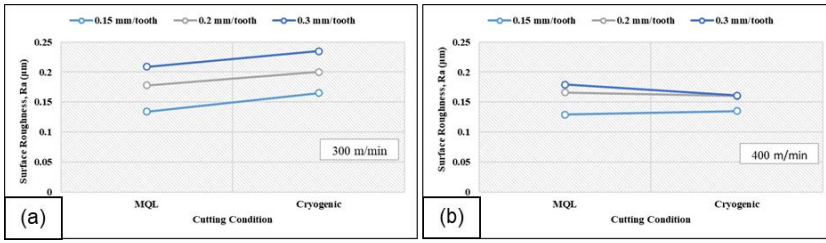

Figure 4: Effect of cooling/lubricating on SR at different feed rates with constant cutting speed; (a) 300 m/min, and (b) 400 m/min

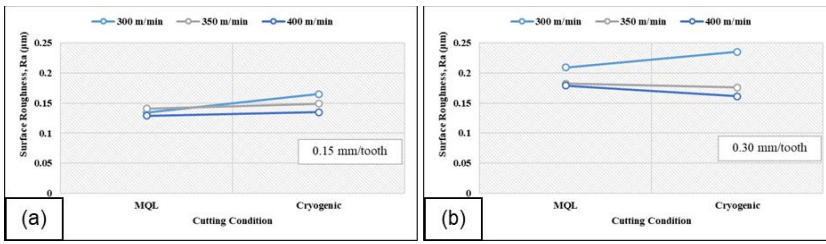

Figure 5: Effect of cooling/lubricating on SR at different cutting speeds with constant feed rate; (a) 0.15 mm/tooth, and (b) 0.3 mm/tooth

On top of that, the value of surface roughness can affect the tool life of the cutting tool. Figure 6 shows the average flank wear (*Vbavg*) of the cutting tool when machining in MQL and cryogenic condition for experiment 8. The figure also displays the value of surface roughness at six stages of tool wear rate starting from *Vbavg* at 0.096 mm until 0.3 mm before the tool fail at 37.04 min and 40.64 min for MQL and cryogenic, respectively. At the *Vbavg* value between 0.15 mm and 0.10 mm, the wear rate for cryogenic cutting can be seen rapidly built-up compared to MQL cutting and the value of SR during cryogenic cutting is higher than MQL cutting. It is probably due to the heat has not yet accumulated at the cutting zone; thus, the lubricating action of the cutting oil is shown to be effective. However, as the tool wear is progressing at the value of *Vbavg* >0.15 mm, the wear rate can be seen rapidly progressed in MQL condition while slowly progressed in cryogenic condition. The cryogenic substance effectively removed the heat, while the effectiveness of the cutting oil to lubricate depreciate as the cutting temperature increased [35]. Thus, resulting rapid tool wear and subsequently increasing the SR value. Finally at the critical wear point of *Vbavg* = 0.25 mm, the wear value is rapidly grown for both cutting but in a slowly trend as compared to MQL. It owns to the fact in the cryogenic conditions, the accumulate heat is effectively removed and prevented the thermal softening of the tool thus slowing the disintegration

of tool's coating material [36]. The harden tool and effective heat control prevent tool chipping, thereby reducing the sliding-sticking zone which associated to the increased value of SR and cutting force [37].

Figure 7 depicts the progressive tool wear in both cutting condition. The MQL cutting produces flank wear that extends to the rake face by 0.781 mm as compare to cryogenic cutting by 0.412 mm. It shows that the cryogenic cutting reduces the contact between the cutting tool and the workpiece resulting reduction of friction and finer SR. However, the improvement of tool life in MQL cutting when compared to cryogenic cutting is only 10%. It maybe contributes by the effectiveness of TRCO during the MQL cutting that capable to retain it lubrication property even at higher cutting temperature.

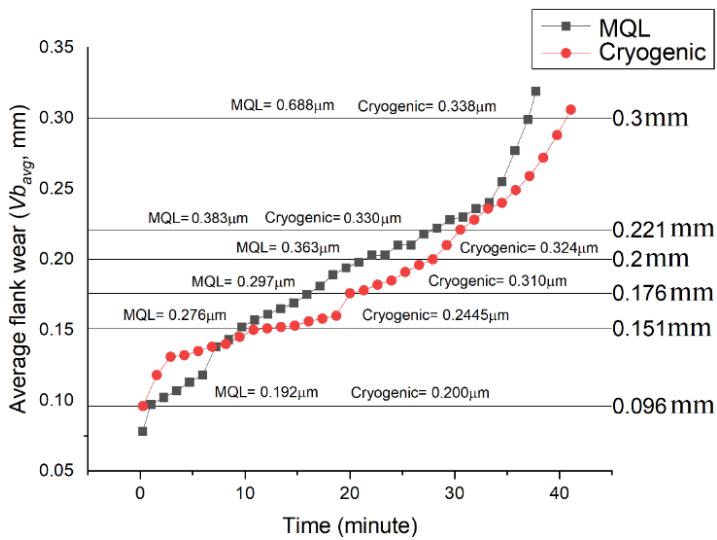

Figure 6: Comparison of average flank wear when cutting AISI 4340 in MQL and cryogenic conditions using experiment 8 for *Vc*= 400 m/min, *fz*= 0.2 mm/tooth, DOC= 0.5 mm and WOC= 0.7 mm

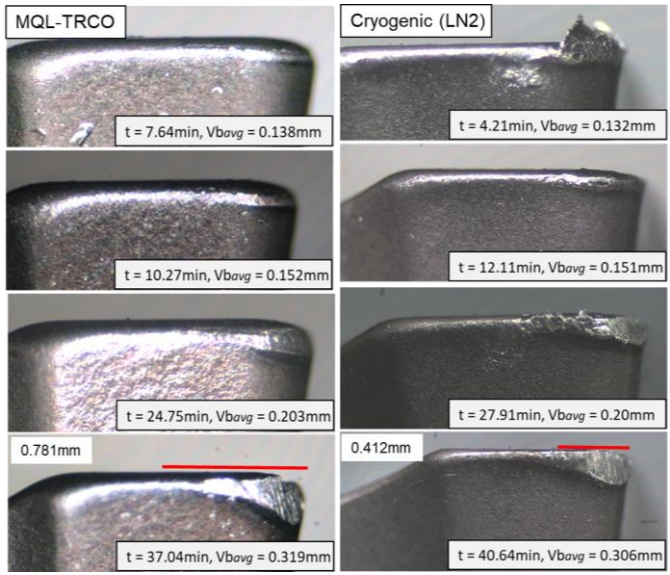

Figure 7: Progressive tool wear of AISI 4340 when cutting in MQL and cryogenic condition using experiment 8 for *Vc*= 400 m/min, *fz*= 0.2 mm/tooth, DOC= 0.5 mm and WOC= 0.7 mm

Conclusion

Cryogenic coolant is a medium that can effectively improve SR at a higher cutting speed, whereas MQL is more effective at improving SR at a lower cutting speed. This work proved that the use of TRCO during MQL cutting enables MQL to produce an SR value that is comparable to that of cryogenic cutting at a higher cutting speed. Based on the results, the following conclusions can be made:

i. The experimental parameters and setup can produce a surface finish of less than 0.5 µm;
ii. TRCO has the potential to be used as a sustainable cutting fluid;
iii. The lowest feed rate and highest cutting speed are the best combination for minimising SR under both cutting conditions;
iv. During MQL cutting statistical analysis showed that an 87.39% feed rate, a 6.70% cutting speed and 3.18% width depth of cut had the greatest effects on the SR;
v. For cryogenic cutting, a cutting speed of 54.83%, feed rate of 32.489% and 12% width depth of cut had the greatest effects on SR.

vi. Cryogenic cutting reduces the contact between the cutting tool and the workpiece as compared to MQL cutting
vii. This work conforms that MQL lack in cooling abilities while cryogenic substance is weak at providing lubrication between the tool and workpiece. Therefore, to overcome these problems, a combination between MQL and cryogenic techniques can be further explored to improve lubrication and cooling effects of a milling process.

Contributions of Authors

The authors confirm the equal contribution in each part of this work. All authors reviewed and approved the final version of this work.

Funding

This work was supported by Malaysian government for research under grant number: FRGS/1/2019/TK03/UKM/01/2

Conflict of Interests

One of the authors, Ahsana Aqilah Ahmad, is an assistant managing editor of the Journal of Mechanical Engineering (JMechE). The author has no other conflict of interest to note.

Acknowledgment

The authors would like to extend their appreciation to the Malaysian government for funding this research under grant number: FRGS/1/2019/TK03/UKM/01/2. Special thanks go to the Department of Mechanical and Manufacturing Engineering, Universiti Kebangsaan Malaysia and College of Engineering, UiTM for the lab, machining facilities, and publication funding.

References

[1] E. Dimla, "Development of an Innovative Tool Wear Monitoring System for Zero-Defect Manufacturing," *International Journal of Mechanical Engineering Robotic Research*, vol. 7, no. 2, pp. 305–312, 2016, doi:

10.18178/ijmerr.7.3.305-312.

[2] N. A. Raof, J. A. Ghani, and C. H. C. Haron, "Machining-induced grain refinement of AISI 4340 alloy steel under dry and cryogenic conditions," *Journal of Materials Research and Technology*, vol. 8, no. 5, pp. 4347–4353, 2019, doi: 10.1016/j.jmrt.2019.07.045.

[3] G. Guerrini, F. Lerra, and A. Fortunato, "The effect of radial infeed on surface integrity in dry generating gear grinding for industrial production of automotive transmission gears," *Journal of Manufacturing Processes*, vol. 45, pp. 234–241, 2019, doi: 10.1016/j.jmapro.2019.07.006.

[4] J. C. C. Pereira, P. C. M. Rodrigues, and A. M. Abrão, "The surface integrity of AISI 1010 and AISI 4340 steels subjected to face milling," *Journal of The Brazilian Society of Mechanical Sciences and Engineering*, vol. 39, no. 10, pp. 4069–4080, 2017, doi: 10.1007/s40430-017-0870-1.

[5] N. Boubekri, V. Shaikh, and P. R. Foster, "A technology enabler for green machining: minimum quantity lubrication (MQL)," *Journal of Manufacturing Technology Management*, vol. 21, no. 5, pp. 556–566, 2010, doi: 10.1108/17410381011046968.

[6] Y. S. Liao and H. M. Lin, "Mechanism of minimum quantity lubrication in high-speed milling of hardened steel," *International Journal of Machines and Tools Manufacture*, vol. 47, no. 11, pp. 1660–1666, 2007, doi: 10.1016/j.ijmachtools.2007.01.007.

[7] O. Özbek and H. Saruhan, "The effect of vibration and cutting zonetemperature on surface roughness and tool wear ineco-friendly MQL turning of AISI D2," *Journal of Materials Research and Technology*, vol. 9, no. 3, pp. 2762–2772, 2020, doi: 10.1016/j.jmrt.2020.01.010.

[8] E. A. Rahim, M. R. Ibrahim, A. A. Rahim, S. Aziz, and Z. Mohid, "Experimental investigation of minimum quantity lubrication (MQL) as a sustainable cooling technique," *Procedia CIRP*, vol. 26, pp. 351-354, 2015, doi: 10.1016/j.procir.2014.07.029.

[9] A. Sahinoğlu and E. Ulas, "An investigation of cutting parameters effect on sound level, surface roughness, and power consumption during machining of hardened AISI 4140," *Mechanics & Industry*, vol. 21, no. 5, 2020, doi: 10.1051/meca/2020068.

[10] H. Gürbüz and Y. Emre Gönülaçar, "Optimization and evaluation of dry and minimum quantity lubricating methods on machinability of AISI 4140 using Taguchi design and ANOVA," *Proceedings of the Institution of Mechanical Engineers, Part C: Journal of Mechanical Engineering Science*, vol. 235, no. 7, pp. 1211-1227, 2020, doi: 10.1177/0954406220939609.

[11] S. B. Kedare, D. R. Borse, and P. T. Shahane, "Effect of Minimum Quantity Lubrication (MQL) on Surface Roughness of Mild Steel of 15HRC on Universal Milling Machine," *Procedia Materials Science*, vol. 6, pp. 150–153, 2014, doi: 10.1016/j.mspro.2014.07.018.

[12] M. Hadad and B. Sadeghi, "Minimum quantity lubrication-MQL turning of AISI 4140 steel alloy," *Journal of Cleaner Production*, vol. 54, pp. 332–343, 2013, doi: 10.1016/j.jclepro.2013.05.011.

[13] N. Ranjan Dhar, S. Islam, and M. Kamruzzaman, "Effect of Minimum Quantity Lubrication (MQL) on Tool Wear, Surface Roughness and Dimensional Deviation in Turning AISI-4340 Steel," *Journal of Materials Processing* Technology, vol. 172, no. 2, pp. 299-304, 2007, https://doi.org/10.1016/j.jmatprotec.2005.09.022.

[14] S. Werda, A. Duchosal, G. Le Quilliec, A. Morandeau, and R. Leroy, "Minimum Quantity Lubrication: Influence of the Oil Nature on Surface Integrity," *Procedia CIRP*, vol. 45, pp. 287–290, Jan. 2016, doi: 10.1016/j.procir.2016.02.330.

[15] S. Shankar, T. Mohanraj, and K. Ponappa, "Influence of vegetable based cutting fluids on cutting force and vibration signature during milling of aluminium metal matrix composites," *Jurnal Tribologi*, vol. 12, no. 12, pp. 1–17, 2017.

[16] S. A. Lawal, I. A. Choudhury, and Y. Nukman, "Evaluation of vegetable and mineral oil-in-water emulsion cutting fluids in turning AISI 4340 steel with coated carbide tools," *Journal of Cleaner Production*, vol. 66, pp. 610–618, 2014, doi: 10.1016/j.jclepro.2013.11.066.

[17] L. Soh Kheang, C. Yuen May, C. Sit Foon, and M. A. Ngan, "Recovery and Conversion of Palm Olein-Derived Used Frying Oil to Methyl Esters for Biodiesel," 2006. Accessed: Apr. 18, 2019. [Online]. Available: http://palmoilis.mpob.gov.my/publications/joprv18june-loh.pdf.

[18] A. A. Ahmad, J. A. Ghani, and C. H. C. Haron, "Potential of Bio-Metal Cutting Fluid from Treated Recycled Cooking Oil for Metal Cutting Fluid Application," *Journal of Mechanical Engineering*, vol. 19, no. 1, pp. 83–97, 2022, doi: 10.24191/jmeche.v19i1.19688.

[19] M. Sarikaya and A. Güllü, "Taguchi design and response surface methodology based analysis of machining parameters in CNC turning under MQL," *Journal of Cleaner Production*, vol. 65, pp. 604–616, 2014, doi: 10.1016/j.jclepro.2013.08.040.

[20] S. S. Muhamad, J. A. Ghani, and C. H. C. Haron, "Investigation of cutting forces in end milling of AISI 4340 under dry and cryogenic conditions," *Jurnal Tribologi*, vol. 23, pp. 125–136, 2019.

[21] S. Ravi and P. Gurusamy, "Experimental investigation to study the performance of cryogenic cooling in end milling of AISI P20 steel," *Materials Today: Proceedings*, vol. 37, pp. 2170–2173, 2021, doi: 10.1016/j.matpr.2020.07.640.

[22] Y. Sun, B. Huang, D. A. Puleo, and I. S. Jawahir, "Enhanced machinability of Ti-5553 alloy from cryogenic machining: Comparison with MQL and flood-cooled machining and modeling," *Procedia CIRP*, vol. 31, pp. 477–482, 2015. doi: 10.1016/j.procir.2015.03.099.

[23] Y. Kaynak, "Evaluation of machining performance in cryogenic

machining of Inconel 718 and comparison with dry and MQL machining," *The International Journal of Advanced Manufacturing Technology*, vol. 72, no. 5–8, pp. 919–933, 2014. doi: 10.1007/s00170-014-5683-0.

[24] M. Jamil, A. M. Khan, N. He, L. Li, A. Iqbal, and M. Mia, "Evaluation of machinability and economic performance in cryogenic-assisted hard turning of α-β titanium: A step towards sustainable manufacturing," *Machining Science and Technology*, vol. 23, no. 6, pp. 1022–1046, 2019. doi: 10.1080/10910344.2019.1652312.

[25] Ç. V. Yildirim, T. Kivak, M. Sarikaya, and Ş. Şirin, "Evaluation of tool wear, surface roughness/topography and chip morphology when machining of Ni-based alloy 625 under MQL, cryogenic cooling and CryoMQL," *Journal of Materials Research and Technology*, vol. 9, no. 2, pp. 2079–2092, 2020. doi: 10.1016/j.jmrt.2019.12.069.

[26] A. Qasim, S. Nisar, A. Shah, M. S. Khalid, and M. A. Sheikh, "Optimization of process parameters for machining of AISI-1045 steel using Taguchi design and ANOVA," *Simulation Modelling Practice and Theory*, vol. 59, pp. 36–51, 2015. doi: 10.1016/j.simpat.2015.08.004.

[27] S. R. Das, A. Kumar, D. Dhupal, and S. K. Mohapatra, "Optimization of Surface Roughness in Hard Turning of AISI 4340 Steel using Coated Carbide Inserts," *International Journal of Information and Computation Technology*, vol. 3, no. 9, pp. 871-880, 2013.

[28] S. R. Das, A. Panda, and D. Dhupal, "Experimental investigation of surface roughness, flank wear, chip morphology and cost estimation during machining of hardened AISI 4340 steel with coated carbide insert," *Mechanics of Advanced Materials and Modern Processes*, vol. 3, no. 1, p. 9, 2017. doi: 10.1186/s40759-017-0025-1.

[29] A. A. Ahmad, J. A. Ghani, and C. H. C. Haron, "Green lubrication technique for sustainable machining of AISI 4340 alloy steel," *Jurnal Tribologi*, vol. 28, 2020, pp. 1–19, 2021.

[30] M. M. de Aguiar, A. E. Diniz, and R. Pederiva, "Correlating surface roughness, tool wear and tool vibration in the milling process of hardened steel using long slender tools," *International Journal of Machine Tools and Manufacture*, vol. 68, pp. 1–10, 2013. doi: 10.1016/j.ijmachtools.2013.01.002.

[31] H. Hassanpour, M. H. Sadeghi, A. Rasti, and S. Shajari, "Investigation of surface roughness, microhardness and white layer thickness in hard milling of AISI 4340 using minimum quantity lubrication," *Journal of Cleaner Production*, vol. 120, pp. 124–134, 2016. doi: 10.1016/j.jclepro.2015.12.091.

[32] D. G. Thakur, B. Ramamoorthy, and L. Vijayaraghavan, "Effect of cutting parameters on the degree of work hardening and tool life during high-speed machining of Inconel 718," *The International Journal of Advanced Manufacturing Technology*, vol. 59, no. 5–8, pp. 483–489,

2012. doi: 10.1007/s00170-011-3529-6.

[33] H. Sohrabpoor, S. P. Khanghah, and R. Teimouri, "Investigation of lubricant condition and machining parameters while turning of AISI 4340," *The International Journal of Advanced Manufacturing Technolgy*, vol. 76, no. 9–12, pp. 2099–2116, 2015. doi: 10.1007/s00170-014-6395-1.

[34] S. S. Sarnobat and H. K. Raval, "Experimental investigation and analysis of the influence of tool edge geometry and work piece hardness on surface residual stresses, surface roughness and work-hardening in hard turning of AISI D2 steel," *Measurement*, vol. 131, pp. 235–260, 2019. doi: 10.1016/j.measurement.2018.08.048.

[35] D. Mark Benjamin, V. N. Sabarish, M. V. Hariharan, and D. Samuel Raj, "On the benefits of sub-zero air supplemented minimum quantity lubrication systems: An experimental and mechanistic investigation on end milling of Ti-6-Al-4-V alloy," *Tribology International*, vol. 119, pp. 464–473, 2018. doi: 10.1016/j.triboint.2017.11.021.

[36] S. Sheik Muhamad, J. A. Ghani, C. H. Che Haron, and H. Yazid, "Wear mechanism of a coated carbide tool in cryogenic machining of AISI 4340," *Industrial Lubrication and Tribology*, vol. 72, no. 4, pp. 509–514, 2019. doi: 10.1108/ilt-07-2019-0291.

[37] C. Courbon, F. Pusavec, F. Dumont, J. Rech, and J. Kopac, "Tribological behaviour of Ti6Al4V and Inconel718 under dry and cryogenic conditions - Application to the context of machining with carbide tools," *Tribology International*, vol. 66, pp. 72–82, 2013. doi: 10.1016/j.triboint.2013.04.010.

Unravelling Tool Edge Trajectory Patterns: Implications on Surface Roughness in End Milling Process

Fatiha Naziera Yusof, Mohd Fauzi Ismail[*]
School of Mechanical Engineering, College of Engineering,
Universiti Teknologi MARA, 40450 Shah Alam, Selangor, MALAYSIA
[*]*mohdfauzi305@uitm.edu.my*

Rizal Mohamed Noor
School of Mechanical Engineering, Universiti Teknologi MARA,
Pulau Pinang Branch, Permatang Pauh Campus, Pulau Pinang, MALAYSIA

ABSTRACT

This study examines the effect of end milling on surface roughness in modern manufacturing. Mathematical equations simulate and analyse the tool edge trajectory of a two-flute end mill during end milling. The results are refined using MATLAB and watershed segmentation. An aluminium alloy flat bar is end-milled using a CNC milling machine for the experimental phase. Optical 3D surface measurements provide roughness data for analysis. The study shows that higher spindle speeds produce smoother surfaces with improved surface quality. The correlation matrix analysis highlights the significance of spindle speed in shaping surface roughness, and tool trajectories are associated with softer surfaces at elevated speeds for the spindle speed ranging between 1000 to 3500 rpm. The study offers valuable insights into the complex relationship between tool edge trajectories and surface roughness.

Keywords: *Machining Processes; End Milling; Surface Roughness; Tool Edge Trajectory; CNC Milling*

Introduction

Machining processes are always in high demand in the aerospace, automotive, medical, and naval industries. Since the beginning of the industrial era, machining processes have played a fundamental role in

ISSN 1823-5514, eISSN 2550-164X
Received for review: 2023-09-01
Accepted for publication: 2023-10-18
Published: 2023-11-15

https://doi.org/10.24191/jmeche.v12i1.24639

shaping modern manufacturing, enabling the production of parts with precise surface quality and geometric accuracy. Conventional machining, in combination with computer numerical control (CNC), enhances versatility and increases the dependency of many industries on the technology [1].

At the heart of machining techniques, milling is a prominent cutting procedure. It involves primary motion generated by the rotation of the milling head and auxiliary motion driven by the workpiece moving perpendicular to the cutter axis, an essential feature for creating complex parts. End milling stands out and is acclaimed for efficient material removal with maintained surface quality, enabling diverse configurations using milling cutters [2].

Over several decades, a substantial body of theoretical and experimental research has been dedicated to understanding machined products' surface profiles and roughness. Experimental approaches, including those involving Artificial Neural Networks (ANN) [3]-[5], Design of Experiment (DoE) [6], Response Surface Method (RSM) [7]-[8], gene expression programming method [9], and linear regression analysis [10], aim to correlate machining parameters with surface roughness parameters such as *Ra* (arithmetical mean of the absolute surface heights). However, these approaches often do not consider the physical aspects of the tool-work interaction during the formation of surface texture.

The geometrical transfer from the tool to the work surface is one of the many factors contributing to creating the work surface texture and, consequently, its surface roughness. Ideally, this geometrical transfer creates the work surface texture and affects surface roughness. The work surface condition becomes predictable when the tool has a known perfect shape.

Simulation is a computational method used to create models that simulate the formation of the machined surface profile, enabling the visualisation and evaluation of surface texture and roughness [11]. Simulation allows observing potential outcomes, reducing expensive experimental work's material and effort requirements. While it cannot guarantee precise results, it approximates actual outcomes. Simulation has a long history in machining, and its use in predicting surface roughness has yielded remarkable results. Several research reports focus on 3D surface topography modelling for the geometrical transcription of the tool during face milling [12]-[13] and ball-end milling [14]-[16]. Most of this research focuses on tools with prominent geometric characteristics of tool cutting tips; none addresses the flat-end milling tool.

This research's primary objective is to comprehensively analyse a two-flute end mill's tool edge trajectory pattern during end milling processes. This study introduces a mathematical model to simulate the trajectory of a tool's edge as it interacts with the workpiece surface during end milling. This is achieved by developing a mathematical model and investigating the impact of varying spindle speeds on both simulated and experimental surface lay

patterns. Furthermore, the study aims to establish a connection between these surface lay patterns and workpiece roughness parameters.

Methodology

Simulation process

The study employs a systematic simulation process meticulously designed to predict and analyse the intricate tool edge trajectory pattern generated by two-flute end mills during the end milling process, providing valuable insights into surface roughness. The simulation process consists of four stages as follows.

Governing equation

The initial stage revolves around formulating a foundational mathematical equation that precisely captures the complex trajectory of the end mill cutting tool edges during end milling. This equation harmoniously integrates critical variables encompassing the cutting tool's radius (R), spindle speed (W), and feed rate (f). Derived from Equation (1) and Equation (2), this equation is the foundation for the following stages, offering a dependable representation of the tool's path on the machined surface. Equation (1) estimates the location of the tool edge of the first flute on the x-y plane, while Equation (2) estimates the position of the tool edge of the second flute at the time t for a 2-flute end mill cutting tool.

$$x(t) = - R\cos(2W\pi t) + (ft) \quad (1)$$
$$y(t) = R\sin(2W\pi t)$$

$$x(t) = - R\cos(2W\pi t - \pi) + (ft) \quad (2)$$
$$y(t) = R\sin(2W\pi t - \pi)$$

Tool edge trajectory plot

This research prepares graphs or plots depicting the tool edge trajectory of a 2-flute end mill under various machining conditions. MATLAB R2017 is utilised to transform these plots into grayscale images, and a meticulous calibration process ensues to ensure accurate alignment and scaling. This careful calibration accurately depicts the tool's movement across the machined surface. A grayscale image processing approach compares these image plots with surface topography characterised by hills and valleys. This study applies a similar approach to the tool edge trajectory plots, where darker trajectory lines signify valleys, while the brighter background represents hills. Subsequently, the plot images are resized to a consistent area dimension and converted into grayscale surfaces, where the z-axis corresponds to the grayscale values. To ensure precise characterisation and

quantification, the x and y axes of these grayscale images/surfaces depicting the tool's trajectory are correctly calibrated. The cropping of the plots is achieved by utilising a specialised algorithm known as SurfSuite, which is part of a Surface Analysis System. It is important to note that SurfSuite is a specialised MATLAB tool developed with a user-friendly Graphical User Interface (GUI) tailored to enhance the precision and reliability of the simulation tasks at hand.

Extracting pattern fragments

The tool edge trajectory of the 2-flute end mill tool in some time *t* results in fragmented patterns with the trajectory curves as the boundaries. Watershed segmentation in MATLAB R2017 is employed to partition the grayscale image of the tool edge trajectory plot and isolate each fragmented pattern into distinct regions or segments with the trajectory curves as their boundaries, thereby providing detailed information about each segment, including its size measured in pixel units. Each segment is uniquely color-coded to represent its surface area. When analysing the tool edge trajectory pattern, variations in curvature and intersections result in segments of varying sizes. Varying spindle speeds (*W*) under different cutting conditions leads to discrepancies in the number and size of these segmented areas. This study's primary focus is on the analysis of these segmented areas. For each surface or cutting condition, various statistical metrics related to the segmented regions, such as the count of segmented regions, standard deviation, and average size, are utilised to characterise the trajectory pattern. These statistical measures help identify and analyse the differences between different sets of machining conditions.

Quantification

In the final stage, the segmented plot is subjected to quantification and statistical analysis. This step uses Microsoft Excel 2019 to extract statistical quantity from the segmented plot. Parameters of interest include the number and area size of segments.

Transition to experimental phase: application and measurement

The machining process involves using the DMG MORI DMU 50, a 5-axis universal CNC milling machine, to mill flat bars made of aluminium alloy, specifically the 6061 alloy, based on the parameters detailed in Table 1. Utilising a 12 mm TiAIN-coated HRC48 carbide endmill, the samples undergo systematic machining along a designated cutting path, encompassing spindle speeds ranging from 1000 rpm to 4000 rpm. Table 2 provides a comprehensive overview of the cutting tool, including detailed specifications and characteristics. The experimental work unfolds in two distinct stages: fabrication and surface roughness measurement.

Fabrication

The flat bars used in the study have specific dimensions, measuring 152.4 x 88.9 x 12.7 mm, as shown in Figure 1. The initial stage involves setting up the CNC milling machine, developing a program using computer-aided manufacturing (CAM) software, and executing the milling process under the defined parameters. Two specimens are prepared, each subjected to varying spindle speed ranges. To minimise the presence of burrs, the machining process is repeated thrice for each speed range. A total of 7 distinct end milling patterns are meticulously produced, with the feed rate remaining constant at 2000 mm/min to ensure a consistent travel length of 88.9 mm. Tables 3 and 4 provide detailed information on the workpiece's chemical, mechanical, and physical properties.

Table 1: End milling parameters for the experimental phase

Parameters	Samples						
	1	2	3	4	5	6	7
Spindle speed (x1000 rpm)	1.0	1.5	2	2.5	3.0	3.5	4.0
Feed rate (mm/min)	2000						
Depth of cut (mm)	0.2						
Tool path strategy	A unidirectional linear cutting trajectory						
Machining tool	A 12 mm diameter two-flute cutting tool						

Table 2: HRC48 carbide end mill specifications and end milling parameters

HRC48 carbide end mill	
Number of flutes	2
Helical	Helix 35 degree
Diameter	12 mm
Cutting length	30 mm
Length	75 mm

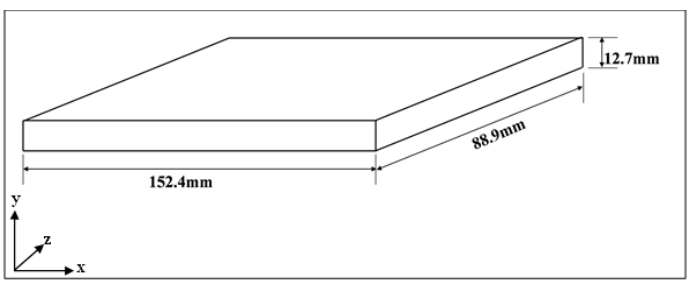

Figure 1: Schematic diagram of the workpiece

Surface roughness measurement

An optical 3D surface measurement device, Alicona Infinite Focus Microscope (IFM), is employed to capture the micro-surface topography of the milled surface. Operating on the principles of focus variation, the IFM scans surfaces at a magnification of 50x, incorporating 3x2 image stitching to obtain the morphological surface encompassing an area of 7801.02 x 3904.02 µm.

Table 3: Chemical properties of Aluminium alloy flat bar 6061

Si	Fe	Cu	Mn	Mg	Cr	Zn	Ti	Others	
								Each	Total
0.04 - 0.08	0.70	0.15 - 0.04	0.15	0.8 - 1.2	0.04 - 0.35	0.25	0.15	0.05	0.15

Table 4: Mechanical properties of Aluminium alloy flat bar 6061

Property	Value
Ultimate Tensile Strength (ksi)	42
Tensile Yield Strength (ksi)	35
Brinell Hardness (500 kg load/10 mm ball)	95
Elongation % in 2 inch (1/16 in)	10
Coefficient of linear expansion (0 – 100 $^{o}C^{-1}$ x 10^{6})	23.6
Melting range (^{o}C)	575 - 650
Thermal conductivity (0 - 100 ^{o}C) W/m ^{o}C	167
Electrical resistivity at 20 ^{o}CµΩcm	4.0

Data preprocessing and quantification

The morphological surface undergoes Gaussian bandpass filter-based data preprocessing to reduce the effect of noise in the high-frequency region and form errors in the low-frequency region. Areal surface roughness parameters are computed from the pre-processed morphological surface for quantification. The range of surface roughness parameters used is based on ISO 25178: Geometrical Product Specifications (GPS) – Surface texture: areal. The root mean square of surface amplitudes (*Sq*) and the maximum surface height (*Sz*) are amplitude parameters that measure the height standard deviation and the maximum peak-to-valley height of the surface, respectively. The developed interfacial area ratio (*Sdr*) is part of the hybrid parameters category and measures the wrinkled surface area size ratio to the flat measuring area size. The texture aspect ratio (*Str*) and the autocorrelation length (*Sal*) belong to the spatial parameter category and measure the texture pattern's symmetry and the texture dominant wavelength, respectively.

Results and Discussion

The similarity between the end milling pattern produced by the physical end milling process Figure 3 and the simulated tool edge trajectories pattern Figure 2 is evident. The obtained end mill cutting pattern is influenced by tool engagement, workpiece interaction, and feed direction during cutting operations, aligning with prior studies by Lazoglu et al. [15] and Hadad et al. [17]. Predicted and experimental patterns showcase continuous circular patterns progressing in unison. A closer examination reveals these circular shapes touching and intersecting, resulting in two distinct forms at the centre and edges. The central shape assumes a curvilinear appearance, while the patterns at the edges resemble diamonds. This overlap of cutting marks gives rise to a boundary, forming a segment where the tool edge coincides.

However, a close examination of the pattern on the experiment surface reveals missing trajectory loops, making a gap in every other loop. As shown in Figure 3, only two large blue lobes appear at the path axis (y = 2000), while in the simulation in Figure 2 (y = 6 x 104), the lobes are continuous without a gap, and the number is doubled for the same length on the feed direction. This is suspected due to dimensional differences of the cutting edge from the 2-flutes milling tool. This caused the difference in tool-work interaction, leaving prominent cutting marks from only one flute.

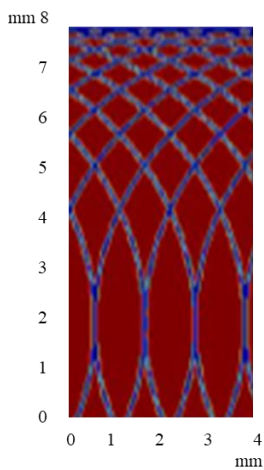

Figure 2: A representation of the tool edge trajectory pattern in the simulation

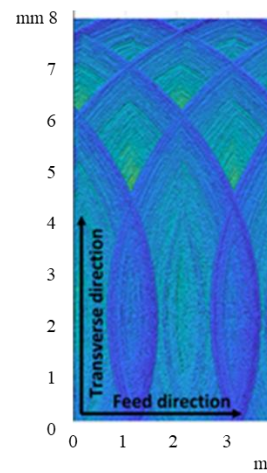

Figure 3: A depiction of the tool edge trajectory pattern through experimental optical observation

The simulation's tool edge trajectory pattern indicates that as spindle speed escalates, the segment size shrinks. The end milling pattern extracted

from practical experiments reflects a similar trend, demonstrating a decrease in segment size with increased spindle speed. This can be seen in Table 5. This is notably visible in the central zone, where the width of the curve-like pattern reduces and gives way to more curve-like shapes, known as loops.

Table 5: Segment spacing trends in cutting-edge trajectory patterns

Spindle speed (rpm)	Tool edge trajectory pattern preceding segmentation	Morphological surface by Alicona Infinite Focus Microscope (IFM)
1000	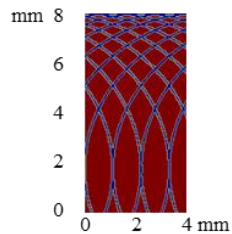	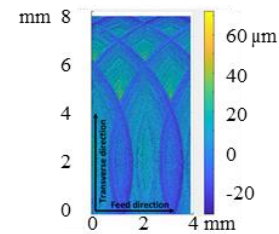
2000	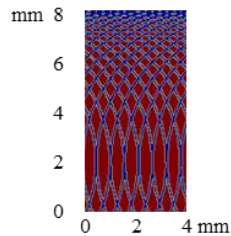	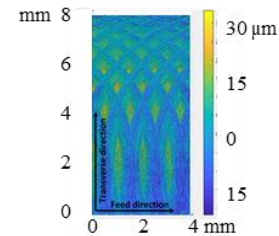
3000	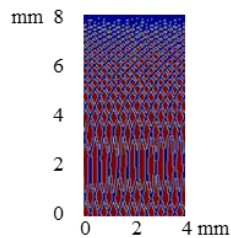	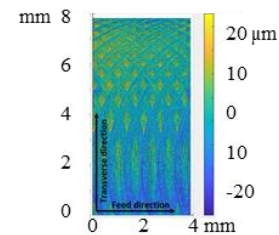
4000	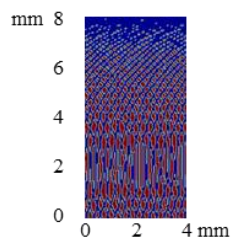	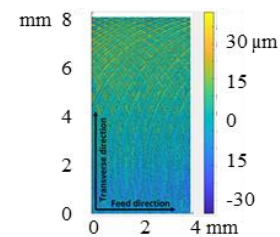

Spindle speed impacts the number of loops in both simulated tool cutting-edge trajectories and end milling patterns. Extracted feature parameters are visually presented through graphs for clarity, and their relationships are detailed in Table 6. The focus is on the feature area due to its reliability, employing statistical measures like mean and standard deviation to represent the simulated surfaces accurately.

A notable positive correlation exists between segmented area count and spindle speed, as the trend is shown in Figure 4. Higher spindle speeds correspond to the increased segmented areas. Shifting to mean values and spindle speed correlation, a distinct negative relationship emerges. Higher spindle speeds lead to lower means, while lower spindle speeds result in higher means. Figure 4 visually depicts this pattern, showcasing a nonlinear trajectory that asymptotically tends to zero at higher spindle speeds, 3000 to 4000 rpm. Similarly, standard deviation and spindle speed correlation trend negatively. Increased spindle speed corresponds to reduced standard deviation and vice versa. Figure 5 illustrates this pattern, echoing the mean correlation but with a smoother curve and an asymptote approaching zero at higher spindle speeds. A similar trend was also observed for the mean segmented area (Figure 6). This suggests that higher spindle speeds can lead to a more uniform surface pattern and less deviated surface topography, expected to lead to finer and even surface roughness. However, there is also likely to be a threshold or saturation point on the spindle speed where the surface roughness cannot be further improved.

Table 6: Correlations among spindle speed and number, mean, and standard deviation of segmented areas in trajectory analysis

	Spindle speed	Number	Mean	Standard deviation
Spindle speed	1			
Number	0.998	1		
Mean	-0.856	-0.828	1	
Standard deviation	-0.794	-0.761	0.993	1

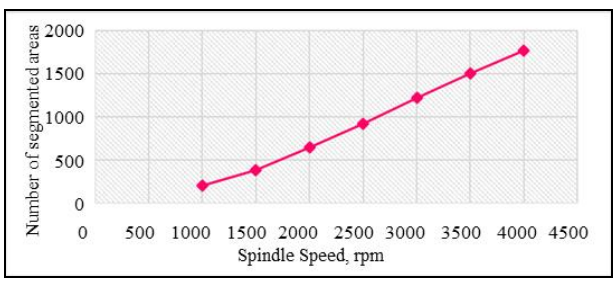

Figure 4: The influence of spindle speed on the number of segmented regions

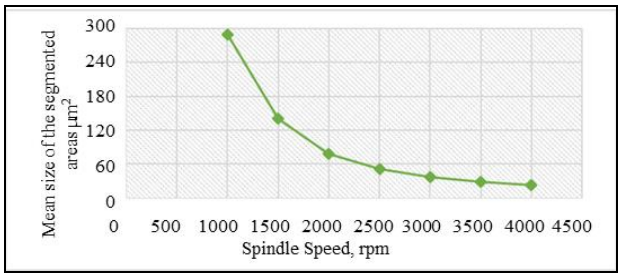

Figure 5: The influence of spindle speed on the mean of segmented areas

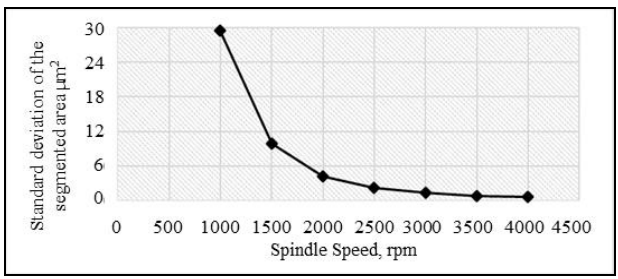

Figure 6: The influence of spindle speed on the standard deviation of segmented areas

Analysis of experimental tool edge trajectory pattern

In evaluating the experimental tool edge trajectory pattern, this section focuses on the approach employed for measuring surface roughness. The process involves conducting an actual end milling process and utilising a three-dimensional (3D) areal surface roughness measurement method to gauge the resultant surface's roughness. This applies an optical 3D metrology system for measuring three-dimensional texture and geometrical data. This enables an automated quantification of the surface's three-dimensional attributes, enhancing the accuracy and depth of analysis.

Figure 7 provides a glimpse into the surface topography of the measured dataset for the chosen area at 1000 rpm of the experimental end mill tool edge trajectory pattern. The depiction uses accurate or pseudo-colour coding based on height. Following this, a sampling process is engaged to refine the quality of the acquired surface topography, enabling more effective analysis. Figure 8 is a filtered dataset that further refines the surface topography of the selected dataset area at 1000 rpm. This step enhances the data quality by reducing noise and errors, which can significantly impact subsequent roughness measurements. However, it is noteworthy that using a low magnification lens to capture a larger measuring area during

preprocessing can inadvertently introduce noise and errors, thereby influencing roughness measurements.

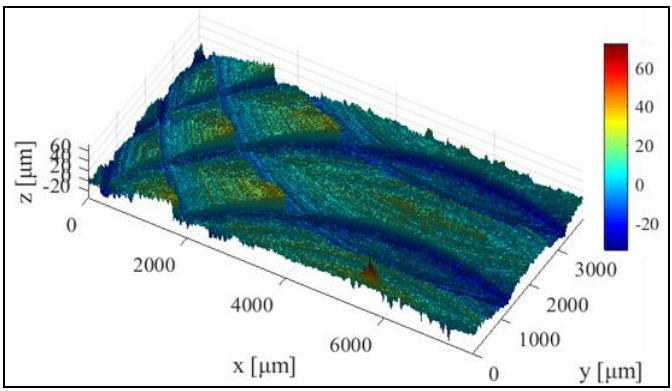

Figure 7: Pre-processed 1000 rpm area's initial surface data

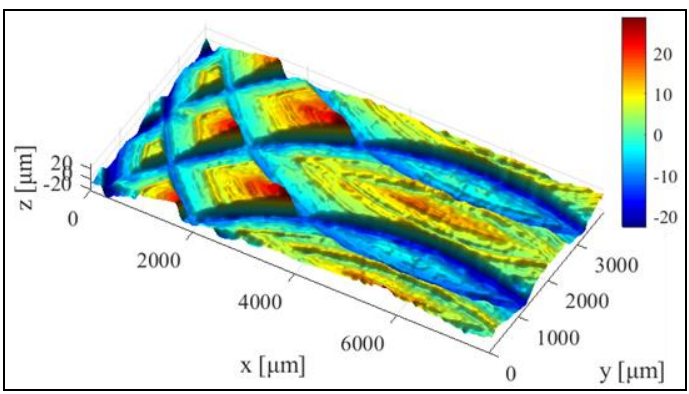

Figure 8: Preprocessing of selected 1000 rpm surface dataset area

Surface roughness analysis and graphical correlations

This section delves into the outcomes of the surface roughness measurement of the experimental tool edge trajectory pattern. These results are reflected in Table 7.

Similar negative trends with asymptotes at higher spindle speeds are observed in Figure 9 and Figure 10 for *Sq* and *Sz*, respectively, when plotted against the spindle speed. This indicates that higher spindle speed reduces the roughness amplitude, with the threshold around 3500 rpm. Figure 11 shows that the interfacial developed area ratio *Sdr* also exhibits a downward trend with increasing spindle speed, with an earlier slope reduction than *Sq* or *Sz*.

Meanwhile, in Figure 12, the texture aspect ratio (*Str*) maintains a relatively constant value for all spindle speeds, hovering around 0.2 to 0.3. This suggests the surfaces are isotropic, lacking a significant texture direction, as seen in the actual surface or the simulated trajectory pattern. The autocorrelation length (*Sal*) also experiences a similar downward trend as *Sq* and *Sz*, with the asymptote at the higher spindle speeds (refer to Figure 13).

Table 7: Measurement data for spindle speed and four machining parameters

Spindle speed, rpm	*Sq*	*Sz*, µm	*Sdr*	*Str*, µm	*Sal*
1000	8.68	51.38	0.263	0.273	328.48
1500	7.38	41.78	0.191	0.182	279.76
2000	5.10	33.48	0.130	0.174	210.29
2500	3.95	31.83	0.110	0.268	167.14
3000	2.97	23.41	0.097	0.250	147.10
3500	2.17	18.31	0.075	0.280	139.21
4000	2.12	21.79	0.080	0.286	137.89

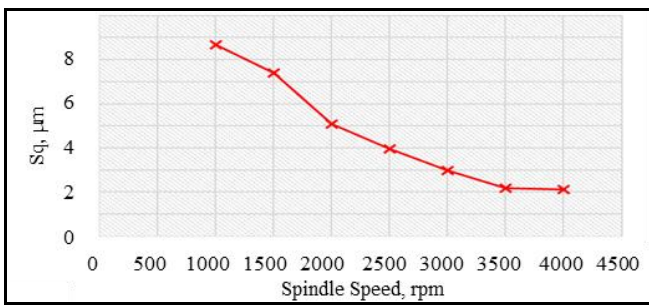

Figure 9: Influence of spindle speed on root mean square height (*Sq*)

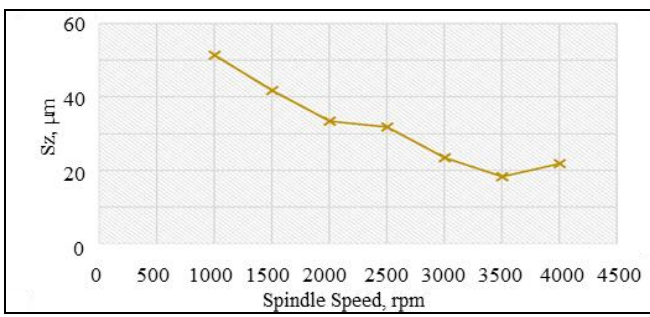

Figure 10: Influence of spindle speed on maximum surface height (*Sz*)

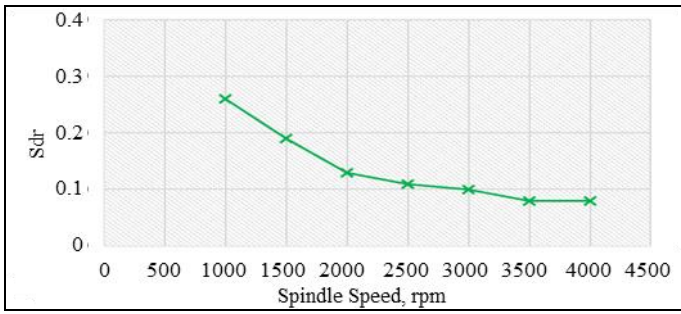

Figure 11: Influence of spindle speed on the developed interfacial area ratio (*Sdr*)

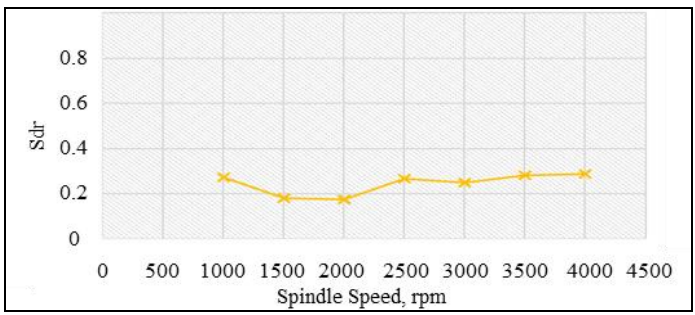

Figure 12: Influence of spindle speed on the texture aspect ratio (*Str*)

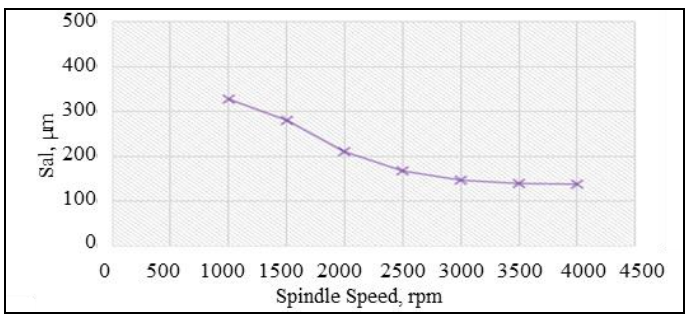

Figure 13: Influence of spindle speed on the auto-correlation length (*Sal*)

The trends in the graphs for roughness parameters are compared with the physical theory of tool geometric transcription. Figure 14 depicts the basic geometry of the 2-flute milling tool, while Figure 15 illustrates the surface geometry after transcription at both slow and high spindle speeds.

The similarity in the downward trend of *Sq* and *Sz* is expected, as they represent the same height parameters, while the surface textures in this study are repetitive and stable. The downtrend of *Sq* is similar to the trend of *Ra* (arithmetical mean of the absolute surface heights) documented in other experimental methods that use Artificial Neural Networks (ANN) [3]-[5], Design of Experiment (DoE) [6], Response Surface Method (RSM) [7]-[8], gene expression programming method [9], and linear regression analysis [10]. *Ra* (arithmetical mean of the absolute surface heights) is from the profile method. In contrast, *Sq* (root mean square value of surface amplitudes) is from the areal method. However, *Ra* and *Sq* describe very similar properties on the amplitude of surface irregularities. The downward trend of *Sq* can be explained by the geometrical transcription resulting from the tool-work interaction (see Figure 14 and Figure 15).

Assuming that the 2-flute flat-end tool has a slight relief angle, as shown in Figure 14, the geometrical transcription at lower spindle rotational speeds creates a surface profile, as depicted in Figure 15a. By increasing the spindle rotational speed alone, the surface profile transforms into the configuration shown in Figure 15b, where the smaller pattern contributes to the lower *Sq* and *Sz*. Another interesting observation is that the downward trend of *Sq* and *Sz* becomes weaker at higher spindle speeds, around 3500 to 4000 rpm, corresponding to the mean of the segmented area of the simulated trajectory pattern (Figure 5). An asymptote at higher spindle speeds indicates that further improvement in work surface roughness cannot be achieved solely by increasing spindle speed, as roughness caused by factors other than simple tool geometrical transcription becomes more prominent.

The phenomenon of *Sal* in Figure 13 can also be explained by Figure 15, where lower spindle speed produces a more extensive surface wavelength or distance between the surface features, as seen in Figure 15a, while higher spindle speed results in a shorter surface wavelength, as shown in Figure 15b. However, increasing the spindle speed beyond 3500 rpm may not further smooth the surface roughness, as other factors besides simple tool geometrical transcription become more prominent.

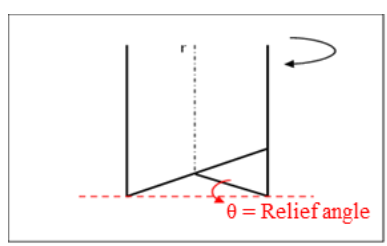

Figure 14: Tool geometry schematic diagram

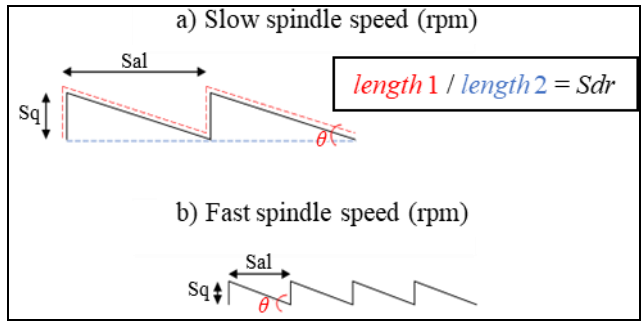

Figure 15: Surface geometry schematic diagram

On the other hand, the developed interfacial area ratio (*Sdr*), as shown in Figure 11, exhibits an unexpected trend that cannot be theoretically explained based on Figures 15a and b. According to Figure 15, the ratio, developed as the sum length of triangle sides to the length of the triangle base, similar to the *Sdr* value, should remain constant from lower spindle speed (Figure 15a) to higher spindle speed (Figure 15b). However, the experimental results show a downward trend with increasing spindle speed. The decreasing trend of *Sdr* is suspected to be due to the dataset filtering process, where a constant cutoff wavelength of a low-pass Gaussian filter is applied to all samples, smoothing the morphological surface by truncating the peaks and pits. This truncating effect is expected to be more pronounced in the higher spindle speed samples, affecting the trend of *Sdr*. Therefore, this trend should only be used as a conclusive result with further investigation.

Correlation matrix analysis of key variables

This section introduces a correlation matrix analysis encompassing spindle speed, number, and mean of segmented areas, *Sq*, *Sz*, *Str*, *Sal*, and *Sdr*, as shown in Table 8. The high coefficient values, close to one, indicate a significant correlation between the two parameters [18].

Sq and *Sz* are two parameters from the amplitude parameters explaining the two different things based on the morphological surface height. The maximum peak-to-valley height *Sz* is very sensitive to the outliers in the surface dataset that may occur due to dirt or measurement errors, while the root mean square height *Sq* is stable and less susceptible to outliers. A low-pass filter is applied to reduce the outliers' effect for the current study. However, since the geometrical transcription mainly causes the surface texture formations for the given experimental condition during tool-work interaction, the *Sz* and *Sq* are becoming interdependent, especially at the range when the spindle speed is less than 3500 rpm, and they are not suitable to be used together to describe the surface. Hence, *Sq* is selected between the two.

Table 8: Correlation matrix of segmentation area and roughness parameters

	RPM	Area-Number	Area-Mean	*Sq*	*Sz*	*Sdr*	*Str*	*Sal*
RPM	1.00	1.00	-0.86	-0.97	-0.95	-0.92	0.51	-0.93
Area-Number		1.00	-0.83	-0.96	-0.94	-0.90	0.55	-0.92
Area-Mean			1.00	0.93	0.93	0.98	-0.10	0.95
Sq				1.00	0.98	0.98	-0.42	0.99
Sz					1.00	0.97	-0.34	0.97
Sdr						1.00	-0.24	0.99
Str							1.00	-0.37
Sal								1.00

A high correlation is also observed between *Sq* and the auto-correlation length *Sal*. Unlike *Sq*, *Sal* is from spatial parameters characterising the spatial information of the surface texture, in this case, the surface prominent wavelength. As explained in Figure 15, *Sal* is highly affected by the distance between the surface features but not the surface height. In many cases, *Sq* and Sal are used concurrently to describe a surface [19]. However, in the current study, due to the simple geometrical transcription as in Figure 15, the effect of the surface height on the distance between lays is inevitable, hence explaining the high correlation value between the *Sq* and *Sal*.

The developed interfacial area ratio *Sdr*, on the other hand, despite showing a high correlation with the spindle speeds and other parameters, can only be explained by the effect of the low pass filtering of the measured data, as mentioned in the previous section. Hence, it cannot be used to describe the surface with the current setup and requires further investigation. On the other hand, *Str* shows a relatively low correlation with other roughness parameters, as explained in the previous section. Hence, *Str* can be used to describe the surface.

Area-mean in Table 8 is the average size of the segmented areas from the trajectory simulation. The area-mean highly correlates to the *Sq*, *Sz*, *Sdr*, and *Sal*. It shows that the surface roughness can be explained using the trajectory simulation.

Conclusion

The study successfully employed a mathematical model to simulate a two-flute end mill's tool edge trajectory pattern, mimicking the surface lay pattern in end milling. A visual comparison between experimental and simulated trajectories showcased continuous forward-moving spiral forms. Employing watershed segmentation, simulation outcomes revealed an increase in segmented areas with higher spindle speeds, accompanied by decreased mean

and standard deviation of these regions. Experimental results indicated that increased spindle speed reduced surface roughness metrics (*Sq*, *Sz*, *Sal*), although *Sdr* notably diverged from predictions, potentially due to measurement filters. The study's integration of simulation and experimentation underscores the connection between tool trajectories and smoother surfaces in end milling with increased spindle speed. However, this study can only explain the surface texture formation due to simple geometrical transcription during the tool-work interaction at spindle speed between 1000 to 3500 rpm combined with the other fixed machining parameters, while the finer surface roughness formation may need to include other factors such as material behaviours, friction, etc.

Contributions of Authors

The authors confirm the equal contribution in each part of this work. All authors reviewed and approved the final version of this work.

Funding

This work was supported by the Fundamental Research Grant Scheme (Grant no. FRGS/1/018/TK03/UITM/02/13) of the Ministry of Higher Education Malaysia.

Conflict of Interests

All authors declare that they have no conflicts of interest.

Acknowledgement

The authors thank the College of Engineering, Universiti Teknologi MARA, for encouraging this research.

References

[1] K. Kumar, D. Zindani, and J. P. Davim, "Introduction to Machining Processes," *Advanced Machining and Manufacturing Processes, Springer International Publishing*, Springer International Publishing, 2018, pp. 41-47.

[2] A. Sharman, D. Aspinwall, R. Dewes, and P. Bowen, "Workpiece surface integrity considerations when finish turning gamma titanium aluminide," *Wear*, vol. 249, no. 5-6, pp. 473-481, 2001. https://doi.org/10.1016/S0043-1648(01)00575-0

[3] A. M. Zain, H. Haron, and S. Sharif, "Prediction of surface roughness in the end milling machining using Artificial Neural Network," *Expert Systems with Applications*, vol. 37, no. 2, pp. 1755-1768, 2010. https://doi.org/10.1016/j.eswa.2009.07.033

[4] J. G. Parmar and A. Makwana, "Prediction of surface roughness for end milling process using Artificial Neural Network," *International Journal of Modern Engineering Research*, vol. 2, no. 3, pp. 1006-1013, 2012.

[5] R. Sanjeevi, R. Nagaraja, and B. R. Krishnan, "Vision-based surface roughness accuracy prediction in the CNC milling process (Al6061) using ANN," *Materials Science*, vol. 2214, p. 7853, 2020.

[6] P. G. Mathews, Design of Experiments with MINITAB Milwaukee, Wisconsin: ASQ Quality Press, 2004.

[7] B. S. Reddy, J. S. Kumar, and K. V. K. Reddy, "Optimization of surface roughness in CNC end milling using response surface methodology and genetic algorithm," *International Journal of Engineering, Science and Technology*, vol. 3, no. 8, pp. 102-109, 2011. https://doi.org/10.4314/ijest.v3i8.8

[8] M. Alauddin, M. El Baradie, and M. Hashmi, "Computer-aided analysis of a surface-roughness model for end milling," *Journal of Materials Processing Technology*, vol. 55, no. 2, pp. 123-127, 1995. https://doi.org/10.1016/0924-0136(95)01795-X

[9] O. Çolak, C. Kurbanoğlu, and M. C. Kayacan, "Milling surface roughness prediction using evolutionary programming methods," *Materials & Design*, vol. 28, no. 2, pp. 657-666, 2007. https://doi.org/10.1016/j.matdes.2005.07.004

[10] H. Safari, S. Sharif, S. Izman, and H. Jafari, "High speed dry end milling of Ti-6Al-4V alloy towards nano-scale surface roughness," *Journal of Applied Sciences Research*, vol. 8, no. 11, pp. 5280-5284, 2012.

[11] P. Benardos and G.-C. Vosniakos, "Predicting surface roughness in machining: a review," *International Journal of Machine Tools and Manufacture*, vol. 43, no. 8, pp. 833-844, 2003.

[12] D. K. Baek, T. J. Ko, and H. S. Kim, "Optimization of feed rate in a face milling operation using a surface roughness model," *International Journal of Machine Tools and Manufacture*, vol. 41, no. 3, pp. 451-462, 2001. https://doi.org/10.1016/S0890-6955(00)00039-0

[13] R. Wang, B. Wang, G. C. Barber, J. Gu, and J. D. Schall, "Models for prediction of surface roughness in a face milling process using triangular inserts," *Lubricants*, vol. 7, no. 1, p. 9, 2019. https://doi.org/10.3390/lubricants7010009

[14] Y. Quinsat, L. Sabourin, and C. Lartigue, "Surface topography in ball end milling process: description of a 3D surface roughness parameter," *Journal of Materials Processing Technology*, vol. 195, no. 1-3, pp. 135-143, 2008. https://doi.org/10.1016/j.jmatprotec.2007.04.129

[15] I. Lazoglu, "3D surface topography analysis in 5-axis ball-end milling," *CIRP Annals*, vol. 66, no. 1, pp. 133-136, 2017. https://doi.org/10.1016/j.cirp.2017.04.021

[16] F. Biondani and G. Bissacco, "Effect of cutting edge microgeometry on surface generation in ball end milling," *CIRP annals*, vol. 68, no. 1, pp. 571-574, 2019. https://doi.org/10.1016/j.cirp.2019.04.017

[17] M. Hadad and M. Ramezani, "Modeling and analysis of a novel approach in machining and structuring flat surfaces using face milling process," *International Journal of Machine Tools and Manufacture*, vol. 105, pp. 32-44, 2016. https://doi.org/10.1016/j.ijmachtools.2016.03.005

[18] W. Kirch (eds), "Pearson's Correlation Coefficient", Encyclopedia of Public Health, 2008, Springer, Dordrecht. https://doi.org/10.1007/978-1-4020-5614-7_2569

[19] P. Pawlus, T. Reizer, M. Wieczorowski, "Functional Importance of Surface Texture Parameters", *Materials*, vol. 14, no. 18, p. 5326, 2021. https://doi.org/10.3390/ma14185326

Effects of Printing Parameters on the Mechanical Strength of Thermoplastics 3D Printed Specimens

Mohammad Azeeb Mazlan, Muhammad Fadil Mustar,
Abdul Halim Abdullah[*], Noor Ayuni Che Zakaria
School of Mechanical Engineering, College of Engineering,
Universiti Teknologi MARA, 40450 Shah Alam, Selangor, MALAYSIA
[*]halim471@uitm.edu.my

Natiara Mohamad Hashim
Faculty of Medicine, Universiti Teknologi MARA, 40700 Sungai Buloh,
Selangor, MALAYSIA

Azizah Intan Pangesty
Department of Metallurgical and Material Engineering,
Faculty of Engineering, Universitas Indonesia, INDONESIA

ABSTRACT

3D printing is increasingly adopted in the biomedical field, particularly for developing adaptive assistive devices. Common materials for Fused Deposition Modelling (FDM) include Polylactic Acid (PLA), Acrylonitrile Butadiene Styrene (ABS), and Polyethylene Terephthalate Glycol (PETG). With the growing demand to identify the best materials and parameter settings for these applications, our project focuses on creating a 3D model of tensile test specimens with varying infill densities, wall perimeters, and layer heights for both ABS and PETG materials. Our goal is to evaluate how these parameter settings affect the tensile properties of each material. We fabricated the 3D specimen model following ASTM D638-14 Type I dimensions and conducted tensile tests using a Universal Testing Machine at a 5mm/min feed rate. Our results indicate that increasing infill density enhances Young's modulus and tensile strength for both ABS and PETG materials. Young's modulus for ABS shows marginal improvement with different wall perimeters. A similar trend is observed in Young's modulus and tensile strength for ABS

ISSN 1823-5514, eISSN 2550-164X
Received for review: 2023-09-05
Accepted for publication: 2023-10-18
Published: 2023-11-15

https://doi.org/10.24191/jmeche.v12i1.24640

and PETG at different layer heights. PETG exhibits higher tensile strength, while ABS demonstrates greater stiffness.

Keywords: *3D Printing; ABS; PETG; Young's Modulus; Tensile Test*

Introduction

Additive manufacturing, commonly known as 3D printing, has gained widespread acceptance since its inception and has become particularly popular in the DIY online community [1]. This innovative technique offers numerous advantages, including the rapid fabrication of intricate models. Among the various methods within additive manufacturing, Fused Deposition Modelling (FDM) stands out as one of the most well-known. FDM involves the precise layering of polymeric filament on a heated bed to create 3D objects [2]. The popularity of this method is attributed to the ongoing reduction in the cost of materials and equipment [3]. Filament materials and spare parts for 3D printers are readily available online, and their affordability has improved significantly over the past decade.

The widespread adoption of additive manufacturing extends to various industries, including automotive manufacturing, construction, and even everyday domestic use. However, one of its most significant contributions lies in its ability to produce customized products at a relatively low cost, particularly within the biomedical field. 3D printing has revolutionized the creation of patient-specific knee replacements that mirror the patient's anatomy [4]. With the capacity to adjust the size and shape of these parts using CAD software, it becomes easier to cater to the diverse needs of different patients. In the past, surrogate body parts were expensive for individuals with disabilities, but 3D printing has drastically reduced these costs [5]. This is largely due to the accessibility of filament materials and the simplicity of producing 3D components.

An essential consideration when using the FDM method is the selection of the appropriate material for the process. FDM 3D printers can utilize various filament materials to create 3D models, such as Acrylonitrile Butadiene Styrene (ABS) and Polyethylene Terephthalate Glycol (PETG). ABS, a polymer composed of acrylonitrile, butadiene, and styrene, is valued for its robust mechanical and physical properties [6]. On the other hand, PETG, a thermoplastic polyester, is chosen for its chemical resistance and strong mechanical performance [7]. Both materials exhibit distinct mechanical properties and behave differently when used as filaments in 3D printing. Therefore, a comprehensive study of the tensile properties of these materials is crucial for direct comparison before selecting one for 3D printing. Previous studies have shown that different materials significantly affect the performance of 3D-printed parts, as revealed through finite element analysis. Static analysis

reveals variations in mechanical properties, such as ductility, von Mises stress, and operating temperature, among different materials [8]. It's worth noting that finite element analysis (FEA) offers a cost-effective, less hazardous, and practical approach, although it may not always yield optimal results [9].

Despite all these benefits that 3D printing possesses, there are many parameters that need to be considered before a good 3D printed part can be fabricated using FDM. How precise and accurate the printed parts are dependent on the method and scale of printing used [10]. These parameters include infill density, wall perimeter, and layer height, which can be adjusted in a slicer software such as Ultimaker Cura. These three main key factors control the mechanical characteristics of the printed parts [11]. Infill density refers to the volume of material inside the 3D-printed object. Meanwhile, the wall perimeter is the thickness of the shell at the outermost layer of the 3D-printed model. Finally, layer height is the distance between each layer of plastics during the printing process. It is first assumed that as all three parameter values increase, the mechanical property of the part is also increased. Srinivasan et al. [12] reported that increasing the infill density will increase the tensile strength of PETG material. The same effect can also be seen in other materials [13]. The wall perimeter also has a great impact on the tensile strength of a printed part [14]. Meanwhile, a lower layer height is usually associated with higher tensile strength [15].

However, it's important to acknowledge that prior studies were conducted under diverse methodologies and environmental conditions, and there is a notable absence of direct comparative research on the tensile properties' response to variable infill density, layer height, and wall perimeter for ABS and PETG materials. Consequently, this research has been undertaken to fabricate 3D models for a tensile test experiment, varying infill density, wall perimeter, and layer height according to ASTM D638-Type I standards, using an Ender 3 printer. This investigation aims to identify how infill density, wall perimeter, and layer height affect the tensile properties of the model and to compare the tensile behaviour of both ABS and PETG materials.

Although numerous parameters require adjustment when preparing to 3D print a model, this study specifically centres on three key parameters: infill density, wall perimeter, and layer height, while allowing Ultimaker Cura software to automatically generate other settings. A rectilinear infill pattern is uniformly used for each specimen (as depicted in Figure 3a). The findings of this research serve as a valuable reference for manufacturers seeking to anticipate the mechanical behavior of their 3D-printed products under tensile loads. This is particularly relevant for biomedical applications in the creation of prosthetic limbs.

Methodology

Development of CAD model

3D models for both ABS and PETG materials are designed by using CATIA V5 21 software. The design dimension followed the ASTM D638 Type-I standard measurement. Figure 1 shows the ASTM D638-Type I standard dimension used to design the CAD model for both specimens. The sample is created into a dumbbell shape for the tensile test experiment [16], as shown in Figure 2. The thickness, width, and gauge length of the CAD model are 3 mm, 13 mm, and 57 mm, respectively.

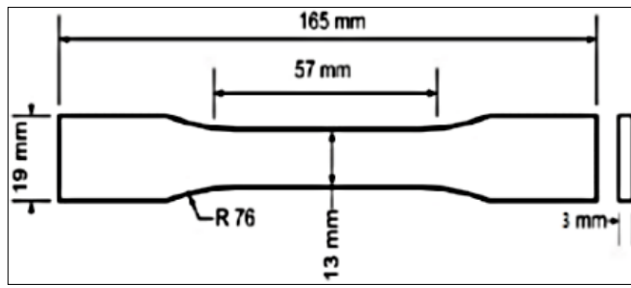

Figure 1: ASTM D638-Type I standard dimension

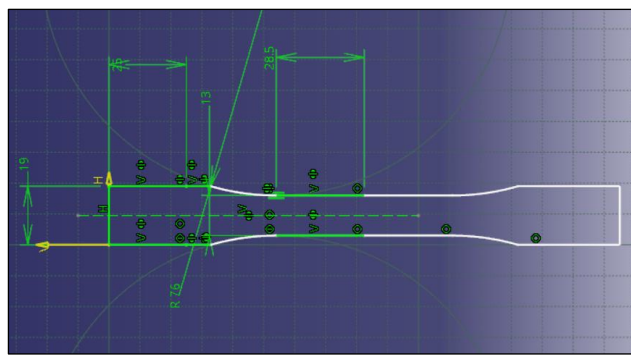

Figure 2: 3D CAD model designed using CATIA V5 21

Slicing of the 3D CAD model

Slicing stands as a pivotal step in the 3D printing process, converting a 3D model from CAD software in Stereolithography (STL) format into g-code, a language comprehensible by the 3D printer. Within this phase, the critical parameters of infill density, wall perimeter, and layer height are fine-tuned, with the entire process executed using Ultimaker Cura software. The specifics

of this control encompass three key parameters, as depicted in Figure 3b. The outcome of this slicing process is illustrated in Figure 3a. Furthermore, Table 1, Table 2, and Table 3 offer a comprehensive breakdown of the parameter settings for the infill density test, wall perimeter test, and layer height test performed during the slicing process in Ultimaker Cura.

In the infill density test, parameters were systematically adjusted in 20% increments, ranging from 0% to 100%, while maintaining a constant wall perimeter of 2 mm and a layer height of 0.20 mm. The wall perimeter test, on the other hand, involved varying the wall parameter across 1 mm, 2 mm, and 3 mm settings, with infill density and layer height consistently set at 10% and 0.20 mm, respectively. Lastly, in the layer height test, the layer height was manipulated to 0.12 mm, 0.20 mm, and 0.28 mm, with infill density and wall perimeter held constant at 10% and 2 mm, respectively. These parameter selections are based on fundamental adjustments for 3D printer slicer programs, aligning with similar settings employed by other researchers [17]-[20].

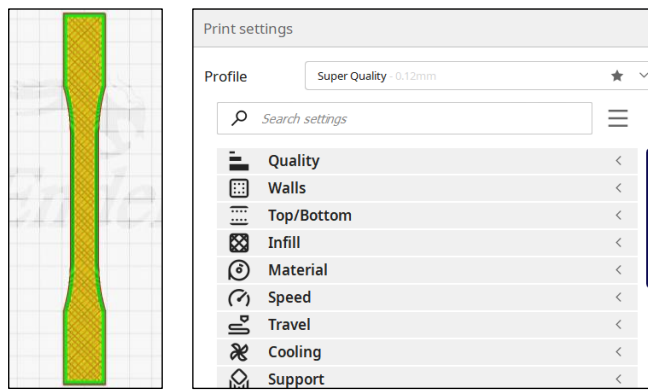

(a) (b)

Figure 3: (a) The slicing result of the ASTM D638-Type I model; and (b) print settings options in Ultimaker Cura

Table 1: Parameter settings for infill density test

Specimen no.	Infill density	Wall perimeter	Layer height
1	0	2	0.20
2	20	2	0.20
3	40	2	0.20
4	60	2	0.20
5	80	2	0.20
6	100	2	0.20

Table 2: Parameter settings for wall perimeter test

Specimen no.	Infill density	Wall perimeter	Layer height
7	10	1	0.20
8	10	2	0.20
9	10	3	0.20

Table 3: Parameter settings for layer height test

Specimen no.	Infill density	Wall perimeter	Layer height
10	10	2	0.12
11	10	2	0.20
12	10	2	0.28

3D printing of ABS and PETG specimens

The specimens for ABS and PETG materials were manufactured using Fused Deposition Modelling (FDM) technology. A total of 96 specimens were fabricated using four units of 3D printer model Ender 3 at AA3D Technology Sdn. Bhd.'s facility with 4 mm nozzle diameter. Each test or parameter setting number has four pieces of specimen. The ABS and PETG filaments were obtained from AA3D Technology Sdn. Bhd. Figure 4a and Figure 4b show the 3D printer model Ender 3 units used to print the specimen for ABS and PETG materials. Each specimen number takes around 7 hours to complete the printing process. Figure 5a and Figure 5b show the completed ABS and PETG specimens, respectively. Every finished printed specimen was stored at room temperature before the tensile test experiment.

(a) (b)

Figure 4: (a) Ender 3 printer units; and (b) specimen being printed on the heating bed

(a) (b)

Figure 5: (a) Specimen for ABS material; and (b) specimen for PETG material

Tensile test experiment

The effect of variable infill density, wall perimeter, and layer height on ABS and PETG materials 3D printed models were investigated using a tensile test experiment. The experiment is done according to the ASTM D638 standard test method for the tensile properties of plastics. The test was done using a unit of the Universal Testing Machine model Servopulser Shimadzu at the Advance Strength of Material Laboratory in UiTM Shah Alam, as shown in Figure 6a and Figure 6b. The feed rate was set to 5 mm/min, and the test was done at room temperature. The test produced a table of force and deformation. The stress and strain values were calculated using Equation (1) and Equation (2) in Excel software. A stress-strain graph is produced, and Young's Modulus is calculated by identifying the slope of the linear line of the stress-strain graph, as shown in Figure 7, using Equation (3).

$$\sigma = F/A \tag{1}$$

$$\varepsilon = \Delta L/L \tag{2}$$

$$E = \sigma/\varepsilon \tag{3}$$

where:

σ = Uniaxial stress (Pa)
ε = Strain (mm/mm)
F = Force (N)
A = Cross sectional area of specimen (m^2)
ΔL = Change in length of specimen (m)
L = Original length of the specimen (m)
E = Young's Modulus (Pa)

(a) (b)

Figure 6: (a) Tensile test was done using Universal Tensile Testing machine model Servopulser Shimadzu; and (b) each end of the specimen were attached on the testing machine machine

Results and Discussion

Effects of infill density in predicting the tensile properties of ABS and PETG materials

This experiment focused on assessing the impact of different infill percentages on the elastic modulus of ABS and PETG specimens. The initial hypothesis posited that decreasing infill density would lead to a reduction in the elastic modulus [17] for both ABS and PETG materials. Figure 7 illustrates the effect of infill density on the Young's modulus of 3D specimens for these materials, confirming the anticipated trend. The graph depicts a linear increase in the elastic modulus with higher infill density for ABS material. Specifically, specimen 1 (0% infill) exhibits the lowest Young's modulus at 995.53 MPa, while specimen 6 (100% infill) demonstrates the highest elastic modulus at 1083.45 MPa. These findings align with Ali et al.'s observations [19], which also noted that the highest infill density results in the highest elastic modulus for ABS material. This phenomenon occurs because at 100% infill density, the raster structures are closely packed, forming stronger interconnections that demand greater force to break. However, it's worth noting that there's only a marginal 8.83% improvement in the elastic modulus when infill density is increased from 0% to 100%. Additionally, there's a mere 0.3% enhancement in the elastic modulus when infill density is raised from 40% to 60% and from 60% to 80%.

For PETG material, the results mirror those observed for ABS. Young's modulus increases in PETG 3D printed material with higher infill density. A comparison between 0% infill density and 100% infill density reveals a 17% improvement in the elastic modulus for PETG material. The highest Young's modulus is recorded at 991.59 MPa with 100% infill density, while the lowest elastic modulus value stands at 841.01 MPa with 0% infill density. Lower infill densities result in more distant raster structures, leading to weaker bonds that require minimal force to break.

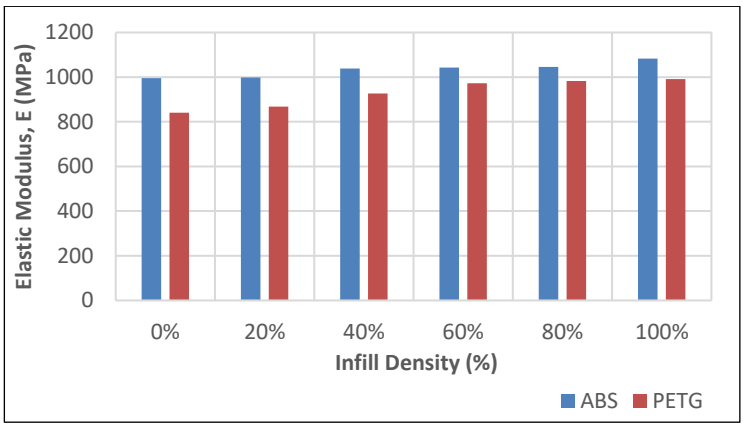

Figure 7: Comparison of Young's modulus at different ABS and PETG infill density

Figure 8 provides a comparison of the ultimate tensile strength at various infill densities for both ABS and PETG materials. In the case of ABS material, the results reveal the highest tensile strength, reaching 36.42 MPa at a 60% infill density, while the lowest tensile strength is recorded at 32.87 MPa with 0% infill density. The tensile strength of ABS increases progressively as infill density rises from 0 to 60%. However, when infill density is increased further from 60 to 80%, the tensile strength experiences a decrease of 7.7%, declining from 36.42 to 33.62 MPa. Subsequent increases in infill density, from 80 to 100%, result in a 7.3% improvement in tensile strength, reaching 36.09 MPa.

Conversely, for PETG material, the highest tensile strength recorded stands at 39.94 MPa with 100% infill density, while the lowest tensile strength is noted at 35 MPa with 20% infill density. The tensile strength of PETG material consistently improves as infill density increases from 20 to 100%. These findings align with the general observation that the tensile characteristics of 3D specimens tend to enhance as infill percentage rises [20]. Dave et al. [21] have also reported a similar pattern where, in most cases,

increasing infill density leads to an improvement in tensile strength. This improvement is attributed to stronger atomic bonds at higher infill percentages, as well as the increased density of the 3D printed specimen at greater infill ratios.

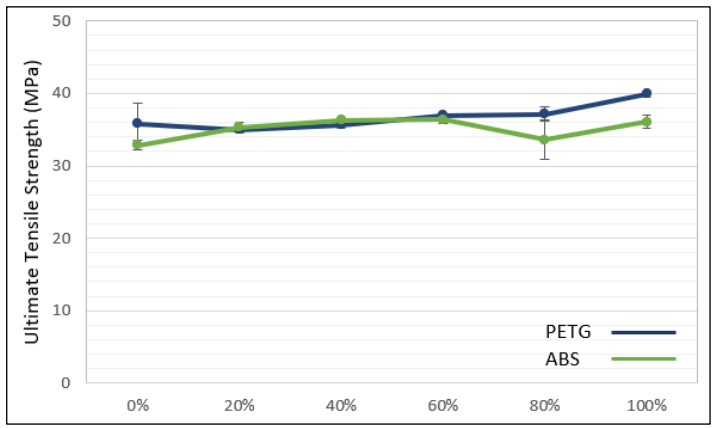

Figure 8: Comparison of ultimate tensile strength at different ABS and PETG infill density

Effects of wall perimeter in predicting the tensile properties of ABS and PETG materials

Figure 9 presents a comparison of the influence of wall perimeter on Young's Modulus for ABS and PETG materials. The results indicate that increasing the wall perimeter from 1 to 3 mm, with increments of 1 mm, has no significant impact on the elastic modulus of ABS material. For ABS, the elastic modulus experiences a slight increase, progressing from 980.09 MPa for 1 mm wall thickness to 985.05 MPa for 2 mm and further to 986.02 MPa for 3 mm wall thickness. However, a different pattern emerges for PETG material. At 1 mm wall thickness, the recorded experimental Young's modulus is 607.93 MPa. When the wall thickness is increased to 2 mm, the Young's modulus undergoes an approximate 58% increase, reaching 959.63 MPa. Further increases in wall thickness result in an approximately 2% rise in Young's modulus, reaching 979.81 MPa. The highest recorded elastic modulus for both materials is observed with the thickest wall perimeter.

Cwikla et al. [3] have suggested that increasing wall thickness is advisable when aiming for maximum strength in 3D printed models. This is because augmenting the wall thickness replaces the hollow infill of the 3D-

printed part with a solid layer of filament, thereby enhancing the overall strength of the specimen.

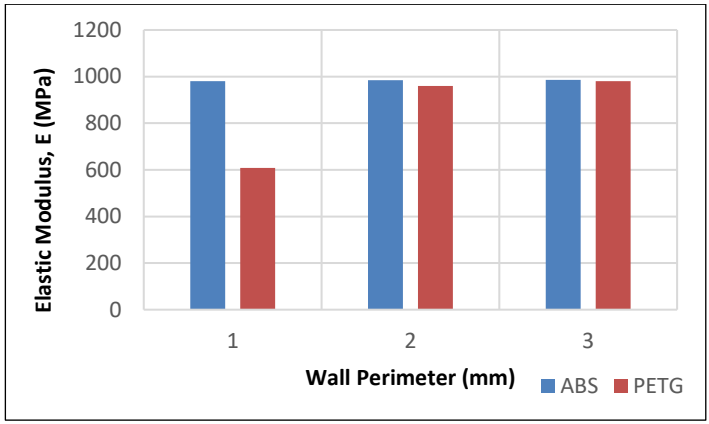

Figure 9: Comparison of wall perimeter effect on Young's modulus of ABS and PETG materials

Figure 10 provides a comparison of the tensile strength of ABS and PETG materials under varying wall perimeters. For ABS material, increasing the wall perimeter results in an improved tensile strength of the specimen. At 1 mm wall thickness, the tensile strength is recorded at 31.25 MPa. Increasing the wall thickness to 2 mm leads to an approximate 8% enhancement in the tensile strength, reaching 33.72 MPa. Further increments in the wall perimeter yield an approximately 3.6% improvement in tensile strength, reaching 34.95 MPa. Similarly, PETG material exhibits a corresponding trend. The tensile strength of PETG material improves as the wall thickness increases. At 1 mm wall thickness, the tensile strength is 22.40 MPa. Expanding the wall thickness to 2 mm results in an approximate 84% improvement in the tensile strength of PETG material, reaching 41.24 MPa. Further increases in the parameter to 3 mm only slightly raise the tensile strength to 41.27 MPa. This finding aligns with Lubombo and Huneault's observations [22], where it is acknowledged that a higher shell number enhances the specimen's strength under uniaxial tensile loading. The thicker wall replaces the hollow infill and bears most of the load applied to the specimen.

Effects of layer height in predicting the tensile properties of ABS and PETG materials

Figure 11 compares the effect of layer height on the Young's modulus of ABS and PETG materials. The graph reveals that increasing the layer height for both ABS and PETG materials enhances the elastic modulus, thereby improving the

specimen's resistance to deformation within the elastic region. For ABS material, an elastic modulus of 736.72 MPa is recorded at a 0.12 mm layer height. The elastic modulus improves by approximately 27% when the layer height is increased to 0.20 mm. A further increase in layer height to 0.28 mm results in an approximately 7% improvement in the elastic modulus, reaching 996.27 MPa. Meanwhile, for PETG material, the elastic modulus is recorded at 754.19 MPa at a 0.12 mm layer height. The result shows a 34% improvement (1010.91 MPa) when increasing the layer height to 0.20 mm. Increasing the layer height further to 0.28 mm only results in an approximately 5% improvement (1062.37 MPa) in the elastic modulus of PETG material. Overall, increasing the layer height parameters yields better mechanical properties [23]. Printing the specimen at a higher layer height results in fewer but thicker extrusions. Using a higher layer height setting when printing a specimen in a horizontal orientation increases the cross-sectional area of the filament that resists the tensile load.

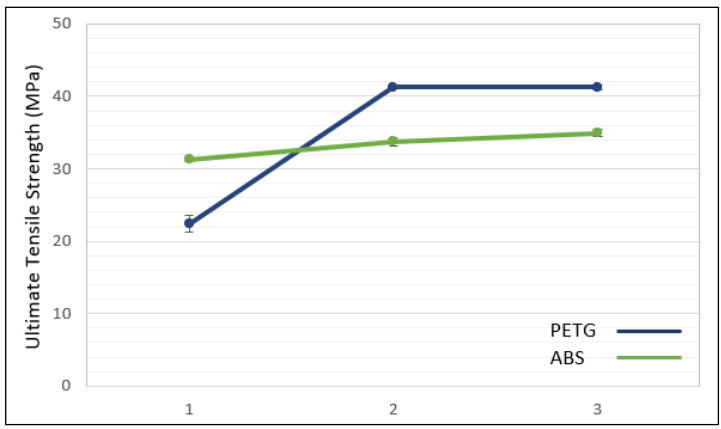

Figure 10: Comparison of wall perimeter effect on ultimate tensile strength of ABS and PETG materials

Figure 12 provides a comparison of the effect of layer height on the ultimate tensile strength of ABS and PETG materials. The results show that increasing the layer height settings improves the tensile strength of the 3D-printed specimen. For ABS material, the tensile strength is recorded at 26.65 MPa at a 0.12 mm layer height. The tensile strength increases by approximately 20% (32.02 MPa) when increasing the layer height to 0.20 mm. Further increasing the layer thickness to 0.28 mm results in approximately a 9% improvement in the tensile strength (35.06 MPa). Similarly, for PETG material, the same trend can be observed, with an improvement in tensile strength as the layer height increases. At a 0.12 mm layer height, the tensile

strength is recorded at 33.22 MPa. Increasing the layer height to 0.20 mm improves the tensile strength by approximately 28% (42.43 MPa). About an 8% improvement (45.72 MPa) in tensile strength is observed when increasing the layer height to 0.28 mm. Chokshi et al. [24] investigated the process parameters' effect on mechanical properties for FDM processing and found that the tensile strength increased with an increase in the layer height up to a certain limit. Increasing the distance between each layer allows the filament to remain hot for a longer time, providing better adhesion.

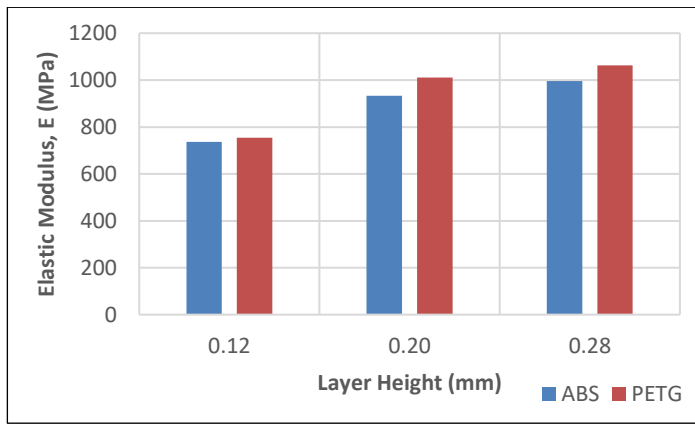

Figure 11: Comparison of layer height effect on the Young's modulus of ABS and PETG materials

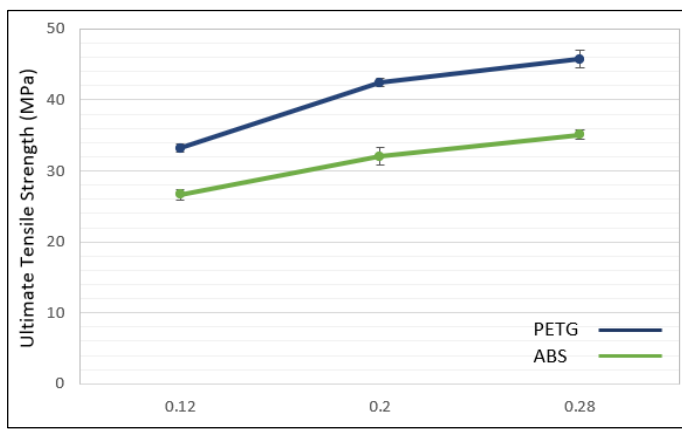

Figure 12: Comparison of layer height effect on the ultimate tensile strength of ABS and PETG materials

Conclusion

The study investigated the effects of infill density, wall perimeter, and layer height on the tensile properties of ABS and PETG materials. A total of 120 specimens were created, and the experiment was conducted using a Uniaxial tensile test machine. It was observed that increasing the values of infill density, wall perimeter, and layer height improved the tensile properties of both ABS and PETG materials. However, some parameters were found to have an insignificant impact on improving the mechanical properties of the printed parts. For example, increasing the wall thickness only slightly improved the elastic modulus for ABS material. Consequently, it's more desirable to print a 3D part with a lower wall thickness, reducing printing time without compromising the part's tensile properties. Similarly, the difference in tensile properties between printing PETG material with 2 mm and 3 mm wall thickness was found to be insignificant. Therefore, it is more rational to print a 3D part with a 2 mm wall thickness to save both printing time and filament material. The study also revealed that ABS material is stiffer compared to PETG material, while PETG material exhibits higher tensile strength than ABS material. Based on this finding, ABS material should be chosen when stiffness is a requirement for the printed part, while PETG should be preferred when high tensile strength is needed. These research findings are important for determining the tensile properties of 3D printed parts using ABS and PETG materials. They serve as a valuable reference for manufacturers and the DIY community when deciding to use ABS and PETG as filament options. Taking these parameter settings into consideration can help reduce the overall cost of filament and the time required for 3D printing.

Contributions of Authors

The authors confirm the equal contribution in each part of this work. All authors reviewed and approved the final version of this work.

Funding

This work was funded by the Ministry of Higher Education through the Fundamental Research Grant Scheme (FRGS) with reference code FRGS/1/2022/TK10/UITM/02/18.

Conflict of Interests

All authors declare that they have no conflicts of interest

Acknowledgment

We thank and acknowledge the Ministry of Higher Education Malaysia (MoHE) and Universiti Teknologi MARA for their financial and technical support. Also, to our partners from UiTM Pasir Gudang and industry partner, AA3D Technology Sdn Bhd for the technical advice and support in 3D printing procedure.

References

[1] J. Chulilla, "The Cambrian Explosion of Popular 3D Printing," *International Journal of Interactive Multimedia and Artificial Intelligence*, vol. 1, no. 4, pp. 30–32, 2011, doi: 10.9781/ijimai.2011.145.

[2] A. R. Torrado Perez, D. A. Roberson, and R. B. Wicker, "Fracture surface analysis of 3D-printed tensile specimens of novel ABS-based materials," *Journal of Failure Analysis and Prevention*, vol. 14, no. 3, pp. 343–353, 2014. doi: 10.1007/s11668-014-9803-9.

[3] G. Ćwikła, C. Grabowik, K. Kalinowski, I. Paprocka, and P. Ociepka, "The influence of printing parameters on selected mechanical properties of FDM/FFF 3D-printed parts," in *IOP Conference Series: Materials Science and Engineering*, vol. 227, no. 1, p. 012033, 2017, doi: 10.1088/1757-899X/227/1/012033.

[4] B. Berman, "3-D printing: The new industrial revolution," *Bussiness Horizons*, vol. 55, no. 2, pp. 155–162, 2012, doi: 10.1016/j.bushor.2011.11.003.

[5] C. Mawere, "The Impact and Application of 3D Printing Technology," *International Journal of Science and Research*, 2014.

[6] K. Haghsefat and L. Tingting, "FDM 3D Printing Technology and Its Fundemental Properties," in *6th International Conference on Innovation and Research in Engineering Sciences*, 2020.

[7] S. Valvez, A. Silva, and P. Reis, "Optimization of Printing Parameters to Maximize the Mechanical Properties of 3D-Printed PETG-Based Parts," *Polymers*, vol. 14, no. 13, p. 2564, 2022, doi: 10.3390/polym14132564.

[8] N. A. H. M. Nizam, M. H. Mazlan, N. S. M. Salleh, M. A. Razali, A. H. Abdullah, M. H. A. Jalil, H. Takano, and N. D. D. Nordin, "Design and analysis of interbody fusion cage materials based on finite element analysis," in *2021 IEEE National Biomedical Engineering Conference (NBEC)*, pp. 7-12, 2021, doi: 10.1109/NBEC53282.2021.9618720.

[9] M. H. Mazlan, M. Togo, I. Yonezawa, and H. Takano, "Biomechanical Alteration of Stress and Strain Distribution Associated with Vertebral Fracture," *Journal of Mechanical Engineering*, vol: SI 2, no. 2, pp 123-133, 2017.

[10] T. D. Ngo, A. Kashani, G. Imbalzano, K. T. Q. Nguyen, and D. Hui, "Additive manufacturing (3D printing): A review of materials, methods, applications and challenges," *Composites Part B: Engineering*, vol. 143, pp. 172–196, 2018. doi: 10.1016/j.compositesb.2018.02.012.

[11] H. A. Habeeb, A. Abood, and A. Mohan, "Influence of Layer Thickness and Infill Density on the Impact Strength of Carbon Particle and Polylactic Acid (CP/PLA) Composite," *Solid State Technology*, vol. 63, no. 2, pp. 1064–1076, 2020.

[12] R. Srinivasan, W. Ruban, A. Deepanraj, R. Bhuvanesh, and T. Bhuvanesh, "Effect on infill density on mechanical properties of PETG part fabricated by fused deposition modelling," in *Materials Today: Proceedings*, vol. 27, no. 2, pp. 1838–1842, 2020, doi: 10.1016/j.matpr.2020.03.797.

[13] N. S. M. Salleh, H. Mazlan, N. S. Abdullah, and I. L. Ahmad, "Design and analysis of infill density effects on interbody fusion cage construct based on finite element analysis," *IEEE National Biomedical Engineering Conference*, 2021, doi: 10.1109/NBEC53282.2021.9618756

[14] N. Wagner, D. Handayani, V. Okhuysen, K. Garibaldi, and M. Seitz, "Mechanical Testing of 3D Printed Materials," in *TMS 2020 149th Annual Meeting & Exhibition Supplement Proceedings*, pp. 153–163, 2020, doi: 10.1007/978-3-030-36296-6_14.

[15] A. Singh and M. Anas, "The Influence of Operational Settings on the Tensile Strength of an FDM-Printed Abs Component," *International Journal for Research In Applied Science and Engineering Technology*, vol. 10, no. 6, pp. 2581–2590, 2022, doi: 10.22214/ijraset.2022.42950.

[16] Y. C. Keat, Y. W. Yin, M. Z. Ramli, T. P. Leng, and S. C. Chie, "Effects of infill density on the mechanical properties of 3D printed PLA and conductive PLA," in *AIP Conference Proceedings*, vol. 2129. doi: 10.1063/1.5118021.

[17] A. Pandžić, D. Hodzic, and E. Kadric, "Experimental Investigation on Influence of Infill Density on Tensile Mechanical Properties of Different FDM 3D Printed Materials," *TEM Journal*, vol. 10, no. 3, pp. 1195–1201, 2021, doi: 10.18421/TEM103-25.

[18] M. A. Mazlan, M. A. Anas, N.A. Nor Izmin, and A. H. Abdullah, "Effects of Infill Density, Wall Perimeter and Layer Height in Fabricating 3D Printing Products," *Materials*, vol. 16, no. 695, pp. 1-12, 2023.

[19] H. Ali, J. Oleiwi, and F. Othman, "Compressive and Tensile Properties of ABS Material as a Function of 3D Printing Process Parameters," *Revue*

des Composites et des Matériaux Avancés, vol. 32, no. 3, pp. 117–123, Jul. 2022, doi: 10.18280/rcma.320302.

[20] M. Mehdi and B. Owed, "The Influence of Infill Density and Speed of Printing on the Tensile Properties of The Three Dimension Printing Polylactic Acid Parts," *Journal of Engineering and Sustainable Development*, vol. 27, no. 1, pp. 95–103, 2023, doi: 10.31272/jeasd.27.1.8.

[21] H. K. Dave, N. H. Patadiya, A. R. Prajapati, and S. R. Rajpurohit, "Effect of infill pattern and infill density at varying part orientation on tensile properties of fused deposition modelling-printed poly-lactic acid part," *Proceedings of The Institution of Mechanical Engineering, Part C: Journal of Mechanical Engineering Science*, vol. 235, no. 10, pp. 1811–1827, 2021, doi: 10.1177/0954406219856383.

[22] C. Lubombo and M. A. Huneault, "Effect of infill patterns on the mechanical performance of lightweight 3D-printed cellular PLA parts," in *Materials Today Communications*, vol. 17, pp. 214–228, 2018, doi: 10.1016/j.mtcomm.2018.09.017.

[23] A. Milovanović, Z. Golubovic, T. Babinsky, I. Šulák, and A. Mitrovic, "Tensile properties of polypropylene additively manufactured by FDM," *Structural Integrity and Life*, vol. 22, no. 3, pp. 305–308, 2022.

[24] H. Chokshi, D. B. Shah, K. M. Patel, and S. J. Joshi, "Experimental investigations of process parameters on mechanical properties for PLA during processing in FDM," *Advances in Materials and Processing Technologies*, vol. 8, no. 2, pp. 1–14, 2021, doi: 10.1080/2374068x.2021.1946756.

\

Characterization of Rubber Degradation in a Brake Wheel Cylinder under Cyclic Loading

Abdul Hakim Abdullah[*], *Muhammad Fakhruddin Abd Wahid* ,
Noorazizi Mohd Samsuddin, Zainoor Hailmee Solihin,
Nor Fazli Adull Manan
School of Mechanical Engineering, College of Engineering,
Universiti Teknologi MARA, 40450, *Shah Alam, MALAYSIA*
[*]*hakimnen@uitm.edu.my*

ABSTRACT

Rubber has been widely employed in the automotive industries in various components. One component that benefits rubber is the braking system which is essentially for stopping the vehicles safely. This investigation intends to characterize the rubber degradation by applying pre-determined cyclic loadings; 10,000, 100,000, and 500,000 cycles which implicated the deformation of this rubber in the brake wheel cylinder while in service. The residual compression properties of rubbers were determined by using a uniaxial compression test. The damage development in rubbers was characterized using X-ray crystallography (XRD), pyrolysis gas chromatography-mass Spectrometry (GC-MS), and scanning electron microscope (SEM). The result indicates the rubber degradation is clearly visualized in the compression test for which lower stiffness is associated with higher cycle specimens. There is evidence of microcracks formation in SEM images which indicates the softening effect of the 100,000 cycles sample. There is a positive correlation between the number of cycles and the peak height intensity in the programs of GC-MS. In addition, the XRD results indicate evidence of crystallization reduction on the damaged samples as samples degrade under cyclic loading.

Keywords: *Brake Wheel Cylinder; Rubber; Cyclic Loading; Damage Development*

ISSN 1823-5514, eISSN 2550-164X

https://doi.org/10.24191/jmeche.v12i1.24641

Received for review: 2023-08-28
Accepted for publication: 2023-10-23
Published: 2023-11-15

Introduction

Rubbers are versatile materials with such variety of applications in industries such as construction (earthquake resistance building), airplanes, automotive, and general consumer products [1]. Rubber can be classified into two categories: natural rubber and synthetic rubber. The former is obtained from the latex sap of rubber trees while the latter is produced by synthesizing from petroleum-based products. Rubber is a polymer material, and very elastic at room temperature. From a materials engineering perspective, rubber has both hyperelasticity and viscoelasticity characteristics. The former results from the conformational entropy change of rubber macromolecular chains while the latter is caused by the internal friction of the materials [2].

In the automotive industry, some parts use rubber in the vehicle components either in critical or non-critical applications. The brake wheel cylinder, which is the main component in the drum brake, is one of the most critical components in the braking system. The main component of the drum brake is brake wheel cylinder, brake shoes and return spring as shown in Figure 1a. When a brake pedal is applied, the brake wheel cylinders work by allowing pressurized hydraulic changes into mechanical forces that push the shoes brake against the inner surface of the drum. As illustrated in Figure 1b, the brake wheel cylinders contain rubber parts: dust boots, and a cup expander which are subjected to repetitive expansion and retraction while braking.

The repeated cyclic loads while braking may cause rubber in brake wheel cylinder to degrade over time. These repetitive stresses could initiate cracks and break in after a certain number of repeats, indicating this is a case of fatigue in rubber. Fatigue failure is caused by the local stress concentrations occurring around defects in the internal structure [3]. The rubber boots and seals in wheel cylinders may get fatigue damaged during operation. Foreign particles such as dust and other impurities may slip into the braking system and this could cause a leak and piston jam in the wheel cylinders [4]. As a result, these leaks and piston jams may compromise braking performance, leading to major fatal accidents. In addition, the failed wheel cylinders are barely noticeable due to the fact the wheel cylinders themselves are contained in the drum brake hub enclosure, and getting a direct visual inspection can be challenging.

The study of rubber degradation in automotive components has been reported in the literature such as car wiper rubber blade [5], rubber hoses for car radiators [6] and engine rubber mounting [7]. There are also many studies undertaken on fatigue damage on rubbers materials. Ruellan and co-workers [8] found that crystallization of natural rubber was reduced with the rising temperature in the uniaxial tensile fatigue tests. The influence of different filler on the fatigue resistance was studied by Dong et al. [8] on natural rubber. They found fatigue resistance on natural rubber was improved with carbon black filler but with carbon nanotube (CNT) filler, fatigue resistance was weakened.

Other authors such as Belkhira et al. [9] had proposed new model to predict fatigue life of rubber parts using cracking energy density (CED) method. The conclusion obtained by these scholars was indeed very good, but the information is still not sufficient. Based on careful literature research, there is no other research looking at the use of rubber for the brake drum cylinder.

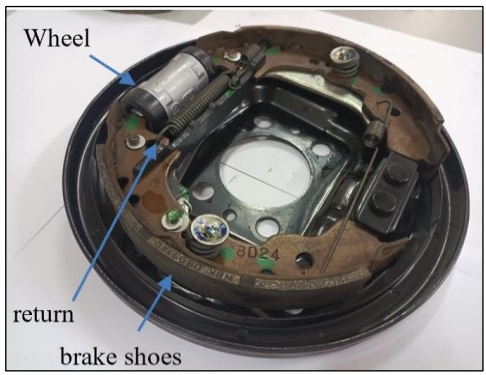

(a)

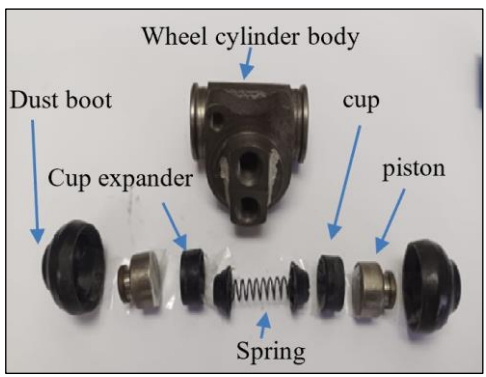

(b)

Figure 1: Schematic diagram of; (a) drum brake, and (b) its internal components

The aim of the investigation is to understand the damage progressions of rubber components of brake wheel cylinders applications subjected with a pre-determined number of cycles; 10,000, 100,000, and 500,000 cycles, respectively. The onset damage development after each cyclic test was characterized using axial compression test, X-Ray Crystallography (XRD), Scanning Electron Microscope (SEM), and Pyrolysis Gas Chromatography-Mass Spectrometry (GC-MS) between the undamaged (uncycled) and

damaged samples. This work may be of interest to both Malaysia's local automotive and rubber industries, inspiring more discovery and advancement of the knowledge in rubber materials.

Methodology

Samples preparation

In this investigation, the brake wheel cylinder designated for Proton Saga BLM (2008-2012) model was chosen for this study. The brake wheel cylinders were acquired from a local automatic spare part store. There was neither further physical information supplied by the manufacturer, nor the specification of rubber materials used in the brake wheel cylinder that came with the packaging box. The characterization route of rubber in this research is depicted in Figure 2. The ASTM and ISO standards requires the fatigue test configuration to follow dumbbell-shaped specimens [2] but in this investigation, the modification on the rubber geometry was deemed impossible. Therefore, a special jig was designed to mount and hold the brake wheel cylinder during the compression cyclic loading and uniaxial compression test as shown in Figure 3a. Comparison of damaged samples (cycled) was made with undamaged (uncycled) samples.

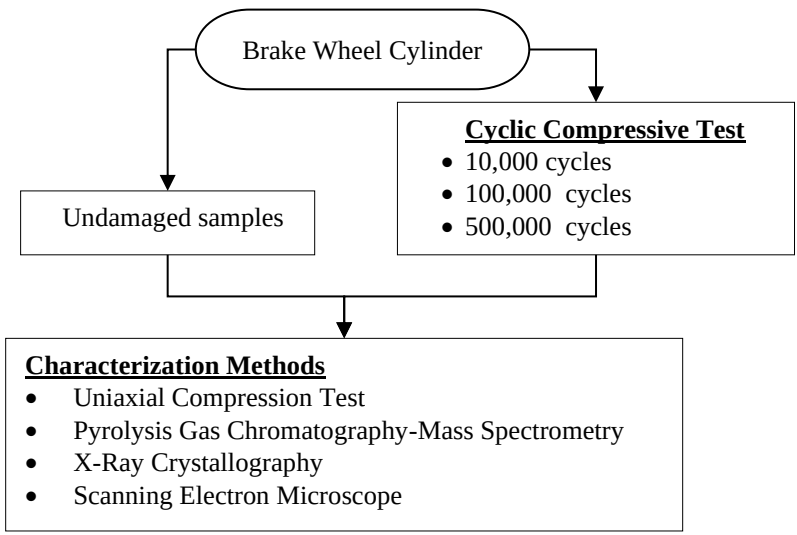

Figure 2: Process flow chart showing the applied characterization route of samples

Uniaxial compression test

Cyclic compressive test

To gain insight on the rubber's degradations due to expansion and contractions of brake wheel cylinder, uniaxial cyclic compressive tests was conducted using a Instron testing machines a 1 kN load cell. The tests were carried out at several cycles: 10,000, 100,000, and 500,000. The machine will automatically stop operating when the desired number of cycles had been completed. A constant amplitude-controlled loading method was followed throughout the cyclic test as described in Figure 3b. A low frequency of 5 Hz was selected throughout the duration of the test to replicate the movement of the rubber, assuming the brake wheel cylinder is operated during normal conditions. The amplitude refers to how much the rubber will be compressed during the period of cycles under cyclic loading.

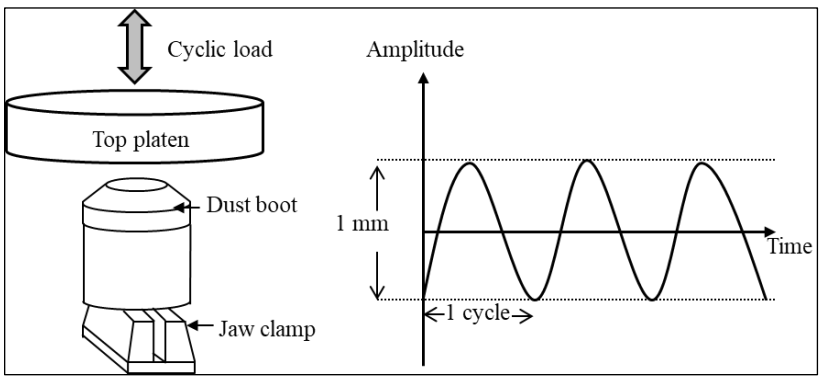

Figure 3: (a) Schematic of uniaxial cyclic compressive tests, and (b) constant amplitude-controlled loading method used in this study

Residual compressive test

The residual compression strength of rubber after pre-determined cyclic test was measured using the same Instron machine and test set-up as shown in Figure 3a. Measurement of rubber physical parameters such as inner and outer diameter, width, and height were initially taken. The samples were compressed up to the lowest predetermined height of rubber. The compressive stress, σ was calculated by simply dividing the compressive load, F with the rubber cross section area, A accordingly. The compressive strain, ε was determined by dividing the decrease in length by the initial height of the rubber. A control sample which represents the undamaged rubber had been tested to get a strength benchmark. The stiffness of the rubber, E was calculated from the linear region of the curves in the 1-2% of strain by the following equations: -

$$E = \frac{\sigma}{\varepsilon} \quad (1)$$

Scanning Electron Microscope (SEM)

The surface morphology study of rubber was done using a Gemini Scanning Electron Microscope. A small sample was cut off and placed on a metal stub with adhesive tape on it. Subsequently, it was sputter-coated before SEM imaging. The acceleration voltage was adjusted to between 2 kV and 9 kV for optimized imaging.

X-Ray Crystallography (XRD)

X-Ray Crystallography analysis of the samples was carried out using Philips Expert Pro Mr Pw3040 X-ray diffractometer in the 2θ range 20°-100° to examine the change of crystalline nature of rubber before and after compression cyclic loading.

Gas Chromatography-Mass Spectrometry (GC-MS)

A pyrolysis test was carried out at the Forensics Laboratory at the Faculty of Applied Science, UiTM Shah Alam using a Shimadzu Scientific Instruments - GCMS-QP2010 Plus model. A small amount of rubber (internal diameter 0.5 mm) was cut out from the main sample using a scalpel and it was weighted about 20 mg for GC-MS testing. The rubber was placed in the reactor and burned constantly at a temperature of 800 ºC for about 45 minutes in a nitrogen environment. The data acquisition system and parameters control were done using GCM solution software. The identification of chemical compounds was referred in the NIST 08 mass spectral library.

Results and Discussion

Compression properties

Figure 4 presents the compression stress and strain behaviour of rubber wheel cylinders after various compression cyclic loadings. The curves began with a linear trend up to 10% of compression strain which attributes to the elastic properties of the rubber materials. It is interesting to see there is a sudden increase of slopes in the curves which are seen around half of compressive strain. The curves continue to increase up to the peak of the curves which is about 0.10 MPa. The 500,000 cycles samples show the highest residual compressive deformation compared at maximum of 45% of compressive strain in comparison to the 100,000 cycles, 10,000 cycles, and undamaged samples.

A closer inspection of the curves shows there were noticeable changes in the slopes for the 100,000 cycles and 500,000 cycles, where it has lower gradients than the undamaged and 10,000 cycles. For the 100,000 cycles sample, there are slight decreases in compression stress are noticeable on the

curves. Further compression stress drop can be seen on the 500,000 cycles. The behaviour may indicate that the component exhibits Mullin's effect [10], a stress-softening effect after prolonging cyclic test caused by the bond ruptures or elastomer chain slippage [11]. Mullin's effect involves the evolution of intrinsic structures such as micrometre or submicrometric cavities or known as microcracks [10].

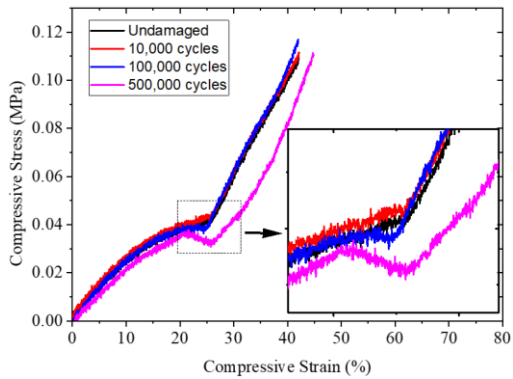

Figure 4: Typical compressive stress-strain curves of rubbers after compressive cyclic loading

The residual compression stiffness of specimens at the specific number of cyclic compressions measured at the first linear region of the curves is shown in Figure 5. The undamaged samples show a maximum value of 0.300 MPa. The rubber in brake wheel cylinder show loss in stiffness with cycling. The 10,000 cycles samples show a reduction to 0.280 MPa. The residual stiffness remains consistent at 100,000 cycles but there is a sharp decline to 0.238 MPa when the specimens were cycled at 500,000, suggesting greater damages in the samples.

The damage can be visualized in SEM micrograph where the formation and growth of multiple microcracks on the rubber surface of 100,000 cycle samples is shown in Figure 6b as compared to the undamaged samples in Figure 6a. This finding is consistent with that of Quang et al. [12] which they found cracks formation in natural rubber (NR) after cyclic loading that is associated with Mullin effects. It is believed that the alternating and long-term compression stress causes the breakage of chemical bonds, leading to the molecular break and ultimately, forming a crack. From the secondary perspective, the shear stress destroys secondary bonds, causing relative slippage of molecular chains and cracks [2].

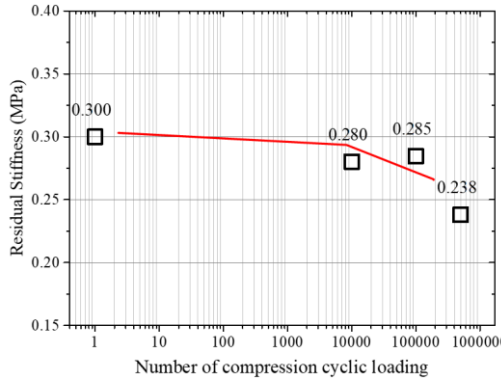

Figure 5: Residual stiffness against number of compression cyclic loading between undamaged and damaged specimens

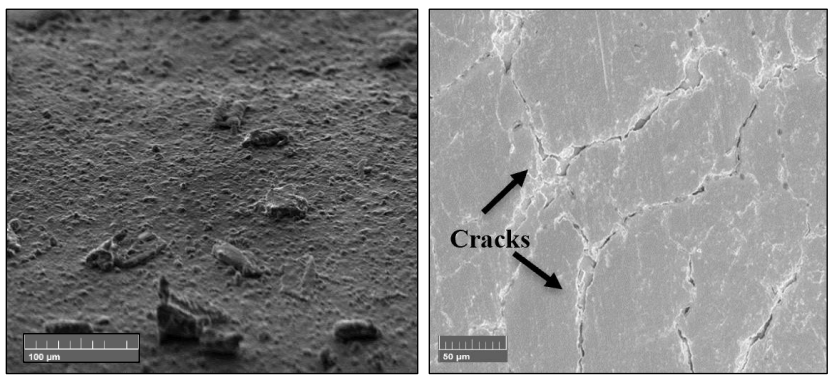

(a) (b)

Figure 6: SEM micrograph of; (a) undamaged rubber (500 X magnification), and (b)100,000 cycles rubber (1000 X magnification)

XRD analysis

The XRD technique is performed by many researchers to illustrate the crystalline nature of rubber [13]–[15]. The diffraction peak height indicates the crystallinity regions while the broadening diffraction implies the amorphous structure of a material [16]. Therefore, the position and the intensity of X-ray crystallography peaks may indirectly present damage development of rubber after cyclic loadings. By observing the rubber's XRD in Figure 7, the difference between the undamaged rubber compared to damaged rubber is clearly observed. It is rather interesting that some major peaks in the XRD have disappeared at the ~39°, ~48°, ~64°, ~81° and ~98° spectrum, respectively.

However, it appears that there is no appreciable difference between the damage samples, 10,000, 100,000, and 500,000, respectively can be seen here. The damaged samples have significantly lower intensity as compared to undamaged samples. The combination of absence and lower peak height may suggests the crystallization of rubber declines because of repetitive cyclic loadings, possibly by the oxidation of the rubber, leading to changes in molecular into loose and unpacked structures [14]. Crystallization plays an important role in the mechanical properties of polymer for which it may prevent crack growth under substantial deformation [17]. Hence, this would explain the loss of compression stiffness and higher strain in the compression test (Figure 4).

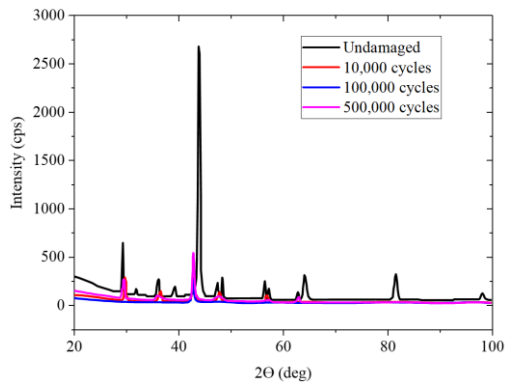

Figure 7: XRD pattern between undamaged and damaged samples under cyclic loadings

Pyrolysis GC-MS spectra analysis

Kusch et al. [18] demonstrated that the application of pyrolysis GC-MS was able to perform failure analysis in the rubber tyre for both qualitative and quantitative information. Figure 8 shows the pyrograms of the examined rubber samples pyrolyzed at 800 °C. There are many peaks available in the pyrograms across the time that made identification of the main chemical elements of the rubber not straightforward because industrial rubbers contain various additives such as plasticizers, carbon black, inorganic fillers, antioxidants, cross-linking agents, and others that essentially give particular physical and/or chemical properties [19].

With the help of the mass spectra database library NIST 08, further examination of all detected peaks suggests the identified pyrolysis rubber product as styrene-butadiene rubber (SBR) for which 2-Phenyl-1,3-butadiene monomers can be found in time = 9.8 minutes [20]. SBR is common rubber for car tyres and products for automotive. Other related pyrolysis products of SBR found in this pyrogram are toluene, benzene, pyrene, and indene [18].

The result of this study shows that pyrolysis compounds measured by peak height increase as the cyclic loading increases, suggesting some chemical compounds have been intensified.

Interestingly, the increased peak height of pyrograms corresponds to the decrease of rubber's stiffness as cyclic loading increases as shown in the compression test (Figure 4). Such increase of peak height in the pyrolysis diagram can also be noticed in the research by Yang et al. [21] where they studied the effect of before and after thermal oxidation on high-density polyethylene (HDPE) composites. Therefore, this suggests the intensified peak height of the pyrolysis product probably means is a positive indication of damage in rubber.

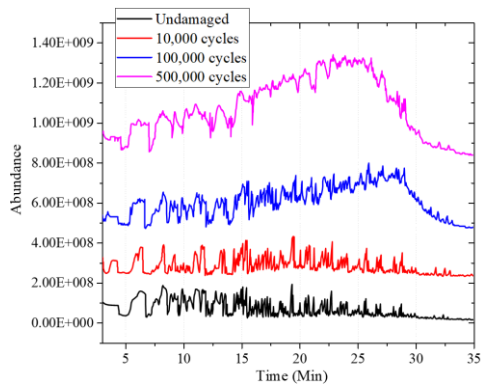

Figure 8: GC-MS comparison between undamaged and damaged rubber

Conclusions

In this investigation, the influence number of load cycles; 10,000, 10,000 and 500,000 cycles to the damage progression of rubber component in brake wheel cylinder was studied. The stress-softening effect was observed in the damaged samples in the compression test. The increasing cyclic loading of up to 500,000 cycles caused a greater stress-softening effect. The scanning electron microscopy analysis has revealed the presence of microcracks in the damaged rubber. The XRD analysis showed some major peaks disappeared between damaged and undamaged samples, showing of a decrease in crystalline region in the damaged rubbers. However, it seems there are no appreciated differences in the peak height between 10,000, 100,000, and 500,000 cycles samples. The GC-MS pyrograms could identify the type of rubber in this component, which is mainly composed of styrene-butadiene rubber. Some pyrolysis compounds

were intensified as the cyclic loading increased which corresponded to the damage experienced by the rubbers.

Contributions of Authors

The authors confirm the equal contribution in each part of this work. All authors reviewed and approved the final version of this work.

Funding

This work received no specific grant from any funding agency.

Conflict of Interests

All authors declare that they have no conflicts of interest.

Acknowledgments

The authors would like to acknowledge the financial support from the School of Mechanical Engineering, College of Engineering, Universiti Teknologi MARA.

References

[1] L. M. N. Amin, H. Ismail, and O. Nadras, "Comparative study of bentonite filled acrylonitrile butadiene rubber and carbon black filled NBR composites properties," *International Journal of Automotive and Mechanical Engineering*, vol. 15, no. 3, pp. 5468–5479, 2018. doi: 10.15282/ijame.15.3.2018.5.0420.

[2] X. Qiu, H. Yin, and Q. Xing, "Research progress on fatigue life of rubber materials," *Polymers*, vol. 14, no. 21, p. 4592, 2022. doi: 10.3390/polym14214592.

[3] B. Tan and E. Feyzullahoğlu, "The investigation of effects of environmental conditions on fatigue strength and spring stiffness of rubber materials," *Journal of Elastomers & Plastics*, vol. 53, no. 6, pp. 632–652, 2021. doi: 10.1177/0095244320988166.

[4] S. S. Gavaskar, P. K. Devan, and T. G. Loganathan, "Failure analysis of brake system in light commercial vehicles using SQC tools,"

International Journal Engineering Research Technology, vol. 3, no. 11, pp. 513–518, 2014. doi: 10.17577/IJERTV3IS110444.

[5] S. M. Mohamad, N. Othman, I. Sharif, M. Z. MD. Zain, and A. R. Abu Bakar, "Dynamic behaviour and characteristics of rubber blade car performance," *Interntional Journal of Automotive and Mechanical Engineering*, vol. 16, no. 1, pp. 6437–6452, 2019. doi: 10.15282/ijame.16.1.2019.25.0487.

[6] S.-W. Han and N.-S. Choi, "Electrochemical degradation tests on a carbon-black-filled ethylene propylene diene monomer rubber under tensile strain," *Proceedings of the Institution of Mechanical Engineering, Part D: Journal of Automobile Engineering*, vol. 232, no. 2, pp. 200–211, 2018. doi: 10.1177/0954407017694412.

[7] M. S. A. Samad, A. Ali, and M. K. A. Ariffin, "Life prediction of rubber automotive components using finite element method," *Key Engineering Materials*, vol. 462–463, pp. 535–540, 2011. doi: 10.4028/www.scientific.net/KEM.462-463.535.

[8] B. Ruellan, J. B. Le Cam, I. Jeanneau, F. Canévet, F. Mortier, and E. Robin, "Fatigue of natural rubber under different temperatures," *International Journal of Fatigue*, vol. 124, pp. 544–557, 2019. doi: 10.1016/j.ijfatigue.2018.10.009.

[9] S. Belkhiria, A. Hamdi, and R. Fathallah, "Cracking energy density for rubber materials: Computation and implementation in multiaxial fatigue design," *Polymer Engineering Science*, vol. 60, no. 9, pp. 2190–2203, 2020. doi: 10.1002/pen.25462.

[10] H. Wan, K. Gao, S. Li, L. Zhang, X. Wu, "Chemical bond scission and physical slippage in the mullins effect and fatigue behavior of elastomers," *Macromolecules*, vol. 52, no. 11, pp. 4209–4221, 2019. doi: 10.1021/acs.macromol.9b00128.

[11] S. Zakaria, L. Yu, G. Kofod, and A. L. Skov, "The influence of static pre-stretching on the mechanical ageing of filled silicone rubbers for dielectric elastomer applications," *Materials Today Community*, vol. 4, pp. 204–213, 2015. doi: 10.1016/j.mtcomm.2015.08.002.

[12] S. D. Puma-Araujo, R. Galluzzi, X. Sánchez-Sánchez, and R. A. Ramirez-Mendoza, "Study of viscoelastic rubber mounts on vehicle suspensions with in-wheel electric motors," *Materials (Basel).*, vol. 14, no. 12, p. 3356, 2021. doi: 10.3390/ma14123356.

[13] A. Z. Abidin, N. H. H. A. Bakar, and M. A. Bakar, "Studies on the properties of natural rubber/poly-3-hydroxybutyrate blends prepared by solvent casting," *Malaysian Journal of Analysis Sciences*, vol. 25, no. 1, pp. 40–52, 2021.

[14] V. I. Kasatochkin and B. V. Lukin, "X-Ray analysis of the molecular structure of rubbers. x-ray diffraction of amorphous rubber," *Rubber Chemistry and Technology*, vol. 25, no. 2, pp. 258–264, 1952. doi: 10.5254/1.3543388.

[15] S. Beurrot-Borgarino, B. Huneau, E. Verron, P. Rublon, "In situ synchrotron X-ray diffraction study of strain induced crystallisation of natural rubber during fatigue tests," *Plastics, Rubber and Composites*, vol. 41, no. 7, pp. 290–295, 2012. doi: 10.1179/1743289812Y.0000000028.

[16] K. I. Karim, N. Mohamad, L. R. Lin, H. E. A. Maulod, J. A. Razak, M. Hasan, Q. Ahsan, "Tensile properties degradation of thermally aged NR/EPDM blend and nanocomposites for engine mounting," *Malaysian Journal on Composites Sciences & Manufacturing*, vol. 2, no. 1, pp. 21–30, 2020. doi: 10.37934/mjcsm.2.1.2130.

[17] F. Noguchi, Y. Zhou, K. Kosugi, Y. Yamamoto, P. T. Nghia, M. Fukuda, S. Kawahara, "Effect of strain-induced crystallization on the tear strength of natural rubber/styrene butadiene rubber blend," *Advances in Polymer Technology*, vol. 37, no. 6, pp. 1850–1858, 2018. doi: 10.1002/adv.21843.

[18] P. Kusch, D. Schroeder-Obst, V. Obst, G. Knupp, W. Fink, and J. Steinhaus, "Application of pyrolysis-gas chromatography/mass spectrometry (Py-GC/MS) and scanning electron microscopy (SEM) in failure analysis for the identification of organic compounds in chemical, rubber, and automotive industry," in Handbook of Materials Failure Analysis with Case Studies from The Chemicals, Concrete And Power Industries, A. S. H. Makhlouf and M. Aliofkhazraei, Eds., Butterworth-Heinemann, 2016, pp. 441–469. doi: 10.1016/B978-0-08-100116-5.00017-X.

[19] P. Kusch, "Pyrolysis-gas chromatography/mass spectrometry of polymeric materials," in Advanced gas chromatography – progress in agricultural, biomedical and industrial applications, M. Mustafa Ali, Ed., IntechOpen, pp. 343–362, 2012.

[20] Y. Qi, Z. Liu, S. Liu, L. Cui, Q. Dai, J. He, W. Dong, C. Bai, "Synthesis of 1,3-butadiene and its 2-substituted monomers for synthetic rubbers," *Catalysts*, vol. 9, no. 1, p. 97, 2019. doi: 10.3390/catal9010097.

[21] R. Yang, J. Zhao, and Y. Liu, "Oxidative degradation products analysis of polymer materials by pyrolysis gas chromatography–mass spectrometry," *Polymer Degradation and Stability*, vol. 98, no. 12, pp. 2466–2472, 2013. doi: 10.1016/j.polymdegradstab.2013.05.018.

Effectiveness of RFID Smart Library Management System

Maizatul Mazni Suhaimi, Zulkifli Mohamed, Nurul Syuhadah Khusaini[*]
School of Mechanical Engineering, College of Engineering,
Universiti Teknologi MARA, Shah Alam, Selangor, MALAYSIA
[*]*nurulsyuhadah2089@uitm.edu.my*

ABSTRACT

Libraries are crucial for diverse resources, particularly for students and educators. The Library Management System (LMS) in Perpustakaan Raja Tun Uda (PRTU) still used barcode technology, which was inadequate and could increase the workload of the librarians. This study presented the development and evaluation of the Smart Portable Library Management System (SPLMS) using RFID technology. The study addressed the gap in the literature by focusing on the impact of angle adjustment on the performance of UHF RFID readers in reading RFID tags placed on book spines. The study was conducted by implementing the SPLMS and performing system testing at different angles. The scope of the study encompassed the design and implementation of the SPLMS, system testing with varying angles, and evaluation of the reader's success rate in reading RFID tags. The validation of ZK-RFID101 of the results have shown that the reader has a 100% success rate for distances between 1 and 3 meters, but the success rate drops to 80% at 5 and 6 meters due to radio frequency interference. The main findings indicated that increasing the angle from 0 to 90-degrees improved the reader's performance, although certain tags still presented challenges. The results from the five conducted trials strongly indicated that a 90-degree angle was the optimum performance. The study concluded that the angle and placement of RFID readers was crucial for optimal performance in library management systems. The SPLMS provided librarians with a user-friendly dashboard for efficient book collection management, boosting productivity and enhancing user experience.

Keywords: *Radio Frequency Identification (RFID); Library Management System; Internet of Things; Node-RED; RFID Tags; MySQL*

ISSN 1823-5514, eISSN 2550-164X

https://doi.org/10.24191/jmeche.v12i1.24642

Received for review: 2023-09-04
Accepted for publication: 2023-10-24
Published: 2023-11-15

Introduction

Efficient library resource management has long been a challenge faced by librarians and institutions globally. Various technologies have been introduced over the years to enhance library operations. Among these, Radio-Frequency Identification (RFID) technology stands out as a promising solution to revolutionize library management. This technology facilitates the seamless tracking, identification, and management of library materials. The present study delves into the development and assessment of a Smart Portable Library Management System (SPLMS) that harnesses RFID technology to optimize library operations. By adopting this innovative approach, the study aims to streamline library management, improve librarian efficiency, and enhance the overall user experience.

Figure 1 shows Perbadanan Perpustakaan Awam which known as Perpustakaan Raja Tun Uda (PRTU). This PRTU located at Seksyen 13 Shah Alam. The PRTU is the headquarters and functions to administer, maintain and coordinate libraries throughout the State of Selangor. Students, lecturers, and Selangor citizens frequently visit the PRTU. There are 6 levels with a total space of 203,600 square feet in this PRTU. This space can be occupied by 2,500 person and 400,000 books can be kept [1]. Additionally, the PRTU attracts up to 8,000 visitors each day on the weekends, public holidays, and school holidays.

Figure 1: Perpustakaan Raja Tun Uda

Due to the enormous quantity of books kept at the PRTU, the librarian frequently encounters into issues such as missing books, misplaced books, and book searching especially at peak hour on the weekends. Moreover, there are few of bookshelf need to be monitored since they contain rare books that can only be read but cannot be borrowed. Therefore, librarian have difficulty to keep track whether the book is on the shelf or not. Moreover, the existing

library management system use in PRTU is barcode. It seems to be not very convenient since the to librarian need to scan one single book at a time. Hence, this study intends to assist the PRTU staff in tracking all book movement. Advanced technology has created Smart Shelf based on RFID technology. With the aid of automated systems, this smart shelf application enables high accuracy product inventory [2]. But the cost of this Smart Shelf is expensive.

The primary objective of the study is to develop and assess the effectiveness of the SPLMS at PRTU. This project proposed to develop a SPLMS with dashboard management using dedicated software that is Node-Red which is low cost and can be used in the PRTU. By implementing the SPLMS and conducting comprehensive testing, the research aims to evaluate the system's performance in a real library setting. Specifically, the study explores how different angles and placements of UHF RFID readers impact the system's ability to read RFID tags on book spines. This research provides practical insights into the integration of RFID technology in libraries, emphasizing the importance of RFID reader placement for optimal performance and the potential challenges with specific tags.

Literature studies

Technology of library management system has grown over the years. According to the traditional of library management system, all tasks require manual support [3]. Librarians must write down every detail about each book on paper. The information on the paper needs regular checking by the librarian. Because so many papers were used to store the information, a lot of space was needed. Technology gives a lot of changes to the traditional of library system. Many libraries around the world use a variety of technology to run their process of circulation such as renewing, borrowing, checking in, and checking out of the books. According to the traditional of library management system used have been replaced by advance technology.

Barcode technology can improve library operations by enhancing transaction efficiency, reducing workloads for library employees, and enhancing services for patrons. Using a barcode, data may be quickly and precisely accessed [4]. Development of technology has introduced QR code in library management system but this technology still in primary stage. With the growing use of smartphones and their ability to read sensible data, QR codes can be widely employed in both businesses and institutions [5]. Compared to barcodes, RFID is a more recent technology. Better accuracy in managing the book collection due to RFID has led to fewer books being purchased [6]. Furthermore, time efficiency occurs because RFID tags can be read more quickly than barcodes, enabling the rapid reading of stacks of books simultaneously [7].

Table 1: Comparison between barcode, QR code and RFID

Items	Barcode	QR Code	RFID
Technology	Laser scanner	Optical scanner	Radio frequency
Range	Few inches to a foot	Few inches to a foot	30 feet or more (passive) 60 to 300 feet (active)
Cost	Low	Low	Low (passive) High (active)
Accuracy	Accurate	Accurate	Accurate
Line of sight	Required	Required	Not required
Information Collected	Fast	Fast	Extremely fast
Capability to scan	One item	One item	Multiple items
Automation	Human operator	Human operator	Only fixed reader

Table 1 above shows the comparison of various technologies used in libraries. Based on the comparison to the different kind of technology such as Barcode, QR code and RFID. The RFID technology gives a better option than others. RFID stands for Radio Frequency Identification. There are two main RFID which are active and passive. Compared to active tags, passive tags are typically less expensive, smaller, and battery-free, which has led to lower read ranges for passive tag [8]. Passive RFID will be used in this study because it only covers a small area. Moreover, it only needs a fixed reader to operate the system and the biggest advantage of using RFID technology in the library is librarian can scan multiple books at a time.

In the world of programming, efficiency and simplicity are highly sought-after qualities. One such tool that has gained popularity is Node-RED. Node-RED is an open-source programming tool that is commonly used for Internet of Things (IoT). Node-RED is a popular IoT platform that is widely used for building IoT applications using visual programming [9]. It has become a popular tool for dashboard and back-end development due to its ability to connect a broad range of hardware devices and software to web services [10]. The programming tool provides a platform for data analytics and data visualization. It can also be integrated with other software such as SQL database management tools like InfluxDB to provide a database management system [11]-[12], [13]. Node-RED is used for displaying data, monitoring, alarming, and triggering actions based on certain rules. It provides a live dashboard for monitoring and alarming purposes, and displays notification messages for different parameters such as electrical quantities or environmental conditions [14]-[15]. Node-RED can also be accessed remotely by various devices that can use web browsers to view the webpage interface

such as computers and smartphones [12]. As such, Node-RED can be utilized in a variety of applications, including library management systems, as a flexible, efficient, and easily integrated dashboard solution.

Designing a basic model in Fusion360 involves utilizing the software's features to create and optimize various designs for different applications. Fusion360 is a computer-aided design (CAD) software that offers a range of tools for modeling, simulation, and optimization. It is widely used in various fields such as robotics [1], [4], [6], additive manufacturing [1]-[2], [7], heat transfer optimization [3], vehicle design [5], and medical modeling [7], [9].

A thorough review of Library Management System research in Malaysia shows that, there is few studies focusing on developing complete system which integration of hardware and software. The paper [16] emphasized the challenges in library management efficiency and advocated the use of RFID technology while highlighting the importance of training and protection against potential attacks. However, their study primarily focused on qualitative data. The paper [17] aimed to prevent book theft through an RFID approach and proposed a filing system using four antennas. Nonetheless, the implementation faced limitations such as high costs associated with antenna placement and the absence of a database for comprehensive book tracking.

The paper [18] sought to transform the library management system in SK Jelutung using a QR approach, introducing a web-based borrowing book software design for schools. Their system lacked the capability to track book data and could only scan one book at a time. The paper [19] aimed to maintain book data tracking by employing RFID and proposed a shelf management system for libraries. However, the system was not portable and used Microsoft Visual Basic. The paper [20] focused on designing a hardware system for book location detection using RFID, with a borrowing and returning system through tag scanning at each shelf. The system used Arduino Uno and lacked a Graphical User Interface (GUI). The paper [21] concentrated on creating a user-friendly GUI but opted for the barcode approach, proposing a manual library management system to be computerized, but their solution was solely software-based.

Methodology

Figure 2 shows the flowchart illustrated the step-by-step process involved in a mechatronics project. It began with conducting a literature review to gather knowledge and identify existing solutions. This helped in designing and procuring the necessary parts for the mechatronic system. The next step involved integrating the hardware and software components to create a functional system. Afterward, the system underwent validation to ensure it met the desired specifications. Once validated, the system was installed, and its performance was continuously monitored and improved as needed. Finally, a

conclusion was drawn based on the project's outcomes, highlighting successes and potential areas for future enhancements. This comprehensive approach ensured a systematic and successful development and implementation of the mechatronics system.

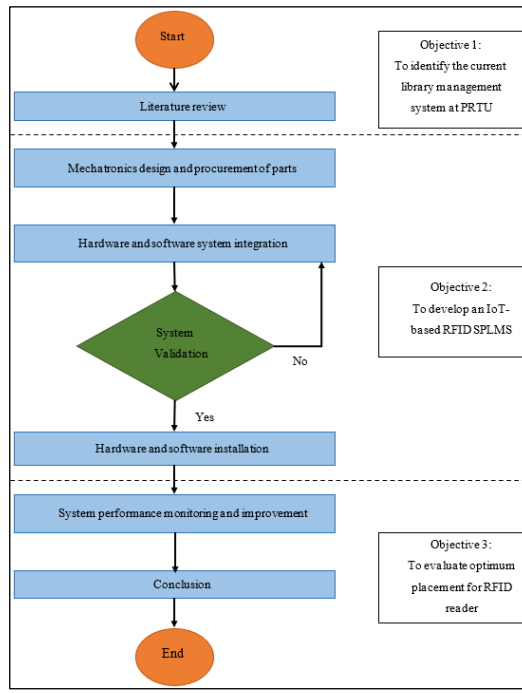

Figure 2: Methodology flow chart

Data flow

The Smart Portable Library Management System (SPLMS) prototype consisted of various components in the process layer, such as the ESP8266 and ZK-RFID101 devices, RFID tags, and push buttons as shown in Figure 3. These components were programmed using the Arduino IDE and monitored through the serial monitor. The prototype development utilized Fusion360 software. In the IoT layer, specific protocols like MQTT were used for communication and data formatting between IoT devices. The platform server comprised Node-RED and MySQL software. Data was pushed to Node-RED for dashboard visualization and also stored in MySQL as a database. The application layer was web-based, allowing librarians to access the dashboard through a laptop.

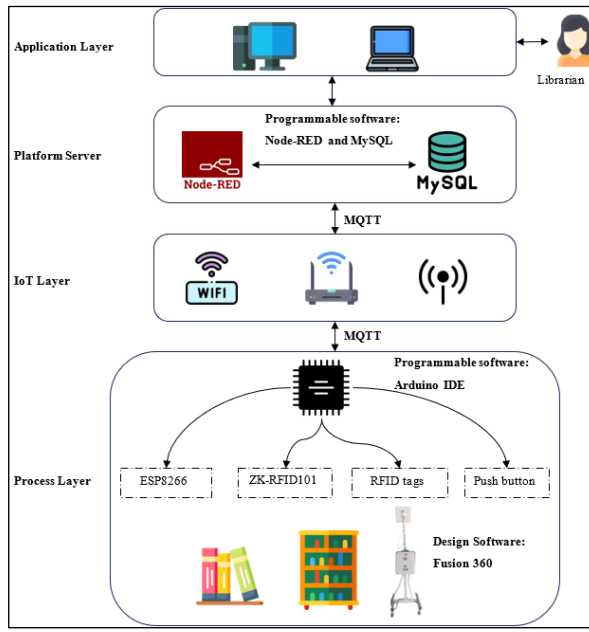

Figure 3: Overall data flow of SPLMS system

Components

The ESP 8266 is the main component that was used for coding. The components and coding were chosen precisely. Table 2 shows the list of components for the hardware used.

Table 2: List of components

Component	Function
ESP8266 NodeMCU	To read inputs and convert them into output based on user-friendly hardware and software.
UHF RFID integrated reader (ZK-RFID101)	To read and capture information stored on a tag attached to an object.
RFID tags	(RFID) tag is a device that uses radio waves to communicate wirelessly with RFID reader.
Push button switch	A mechanical device where the user manually presses a button to regulate an electrical circuit
Power supply 220V	The standard household voltage 220V
Adapter 12V 2A	The power supply for ZK-RFID101
Switching power supply 12V 5V	To convert a 12V input to a 5V output

Circuit

The ZK-RFID 101 was connected in accordance with the circuit diagram shown in Figure 4. The ZK-RFID 101 was connected to the ESP8266 NodeMCU microcontroller. The ZK-RFID 101 was powered by a 12V adapter. For data transmission, pin DATA0 was connected to pin D6 on the microcontroller, while pin DATA1 was connected to pin D5. 5V was supplied to the ESP8266 NodeMCU by a switching power supply. The switching power supply received power from the 12V 2A adapter, while the adapter received power from an external 220 V power source.

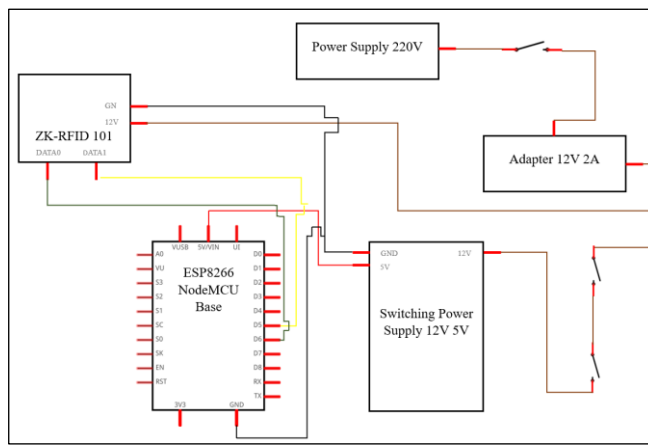

Figure 4: Circuit diagram of ZK-RFID101

Hardware design and setup

In Figure 5, the prototype of the Smart Portable Library Management System (SPLMS) was depicted. It consisted of a push button that allowed the librarian to turn the product on or off as needed. Additionally, there was an emergency button that served the purpose of quickly stopping the SPLMS in case of any unforeseen circumstances. Moving on to Figure 6, it showcased the SPLMS setup for monitoring the performance of a ZK-RFID101 at various angles. Specifically, the figure illustrated the system when the angle was set to 0 degrees.

Block diagram and flowchart of the system

The Smart Portable Library Management System (SPLMS) was a proposed system with a block diagram consisting of components like adding book details, deleting book details, and book searching, all stored in a database which was MySQL as shown in Figure 7. The system included a dashboard that demonstrated its functionality and provided an interface for the librarian to efficiently access and search for books.

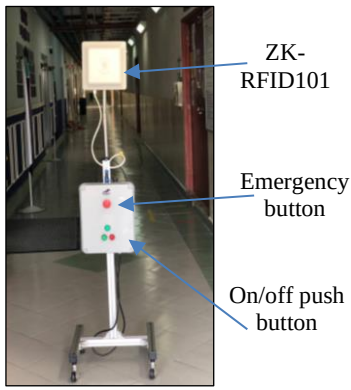

Figure 5: Prototype of SPLMS

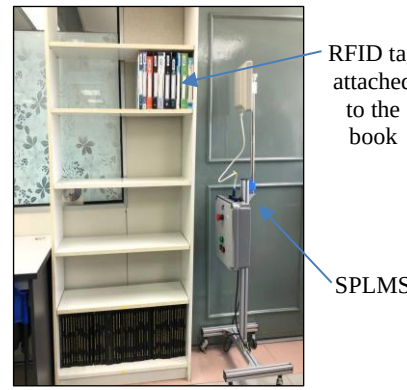

Figure 6: SPLMS setup

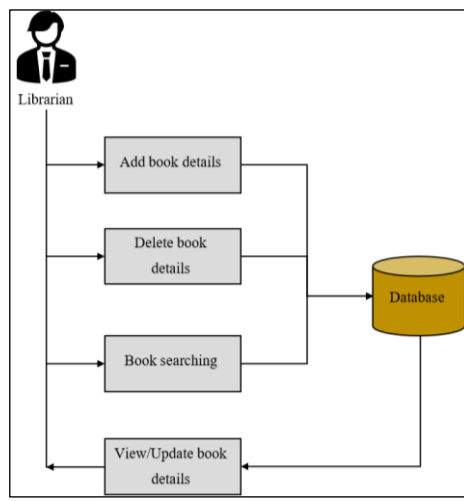

Figure 7: Block diagram of the SPLMS

The process began with the setting up of the system and the retrieval of a book with an RFID tag as shown in Figure 8. The RFID reader scanned the tag and transmitted the information it had obtained to the database. If the data was found in the database, the system displayed the return data. The process ended when the book's status was displayed through the dashboard.

Development of software

The Arduino IDE was used to program Arduino microcontrollers and interface with hardware. Data from Arduino could be sent to Node-RED for

visualization on a dashboard. MySQL was used to store the data as a database. Fusion 360 was a 3D modeling software for creating objects and prototypes. Table 3 shows the list of softwares used.

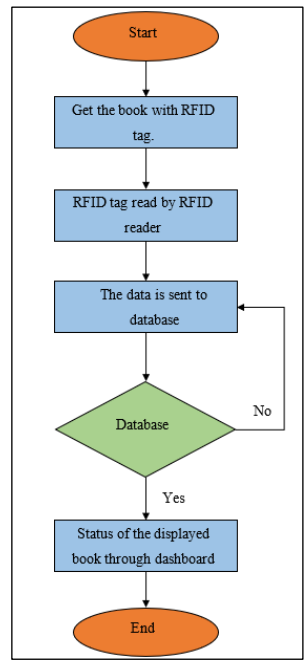

Figure 8: Flowchart of the effectiveness RFID system

Table 3: List of softwares

Software	Function
Arduino IDE	For uploading and communicating with programs, it creates a connection with the Arduino hardware.
Node-RED	An open-source programming tool for creatively and quickly linking hardware, APIs, and web services.
MySQL	An open-source database software that complies to the SQL standard.
Fusion 360	A 3D modelling program with the ability to model, simulate, and document.

Position of tags in books

Position tags play a crucial role in optimizing the effectiveness of UHD RFID technology in books. Error in multiple tag book stack detection results when

tags overlap [22]. In the case of UHF RFID, the position of the tag on the book spine can affect the read rate. According to research, tags placed right close to the spine are always read, but those placed towards the book's opening, which are farther away from the spine and inventory reader, are not always read [23]. The strategic positioning of the UHD RFID tag on the spine ensures enhanced readability, minimizes interference, and maximizes data transmission efficiency as shown in Figure 9.

Figure 9: Position of book tagging

Placement of UHF RFID reader (ZK-RFID101)

The UHF RFID reader (ZK-RFID101) was positioned at three different angles such as 0 degrees, 45 degrees, and 90 degrees as shown in Figure 10. The purpose was to find the angle that provides the best performance in reading RFID tags accurately and reliably. By comparing the results, it is possible to determine the optimal angle for achieving optimal performance. This information is valuable for industries that rely on RFID technology for tasks like inventory management and asset tracking.

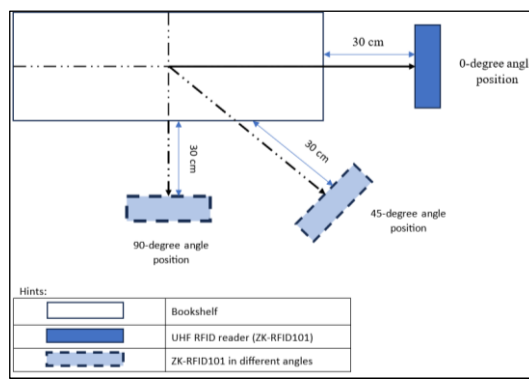

Figure 10: Top view of ZK-RFID101 placement

Results and Discussion

Dashboard

Figure 11 showed the homepage of the system provided the librarian with multiple options for managing the library's book collection. By completing a form, the librarian could add book details, delete books from the system, and view/update existing books.

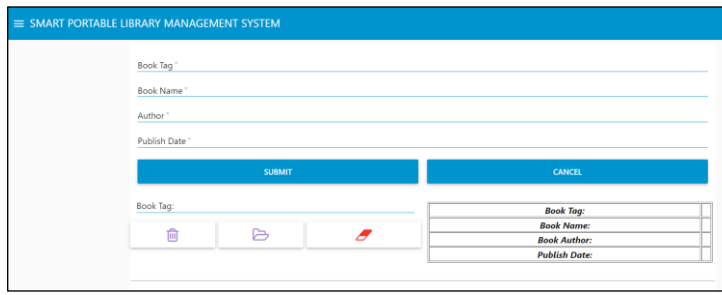

Figure 11: Dashboard of SPLMS

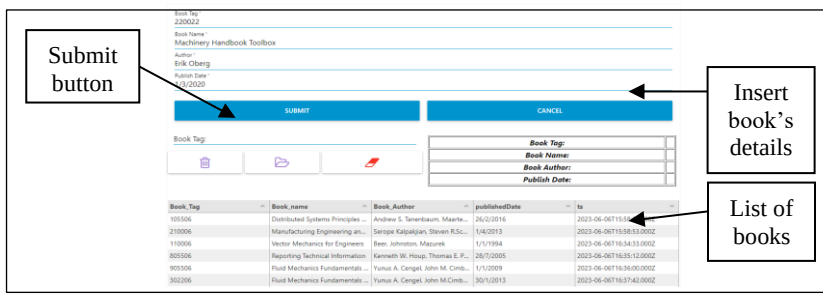

Figure 12: Add book menu

In Figure 12, the librarian was presented with a form to complete the book's information. After completing the form, the librarian could select the "Submit" button. The book's information was securely stored in the database upon submission. Additionally, the dashboard displayed a list of books' details for simple access and visibility, allowing the librarian to effectively manage the collection.

In Figure 13, the librarian has the ability to enter book tags that they wish to remove. After the librarian has inserted the book tag, librarian will be able to select the "Delete" button. The information on the tag belonging to the book will be removed from the database. The dashboard may have shown the librarian that the selected book's tag had been removed.

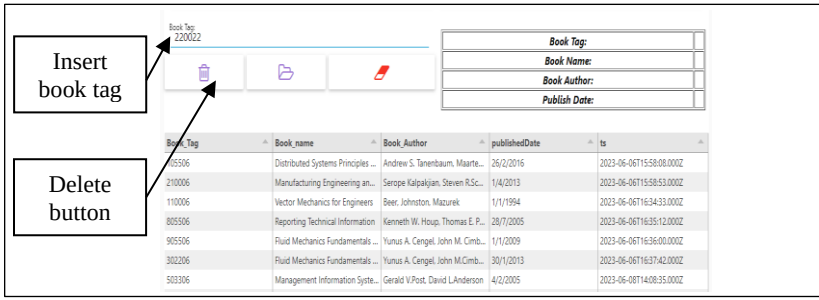

Figure 13: Delete book menu

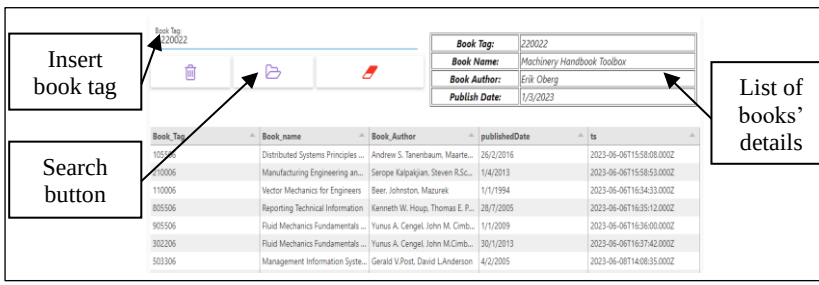

Figure 14: Book searching menu

Figure 14 showed how the librarian could conduct a search for book details by first inserting the book tag and then clicking the search button. It showed up on the dashboard for the librarian so that they were able to view it.

The homepage was built using Node Red and SQL. It enhanced library management and helped librarians work quickly. It updated all book details. This system's disadvantage disabled librarians from updating book data on the dashboard. Thus, the library progressed quickly, attracting many patrons. The librarian had to monitor and maintain the database to detect missing books.

System testing

Validation of smart portable library management system

The maximum reader range for the ZK-RFID101 was 6 metres, according to the manual [24]. The effective range of the RFID reader was shown in Table 4. The appropriate symbol indicated that the reader sent the data. The ZK-RFID101 reader's most useful range was from 3 metres to 1 metre. When the range reached 5 and 6 metres, it was almost 80%. This happened as a result of radio frequency interference, which impaired and weakened the signal received by the RFID reader [25]. In RFID networks, reader-to-reader interference could also reduce the read rates of passive RFID tags [26].

Table 4: The RFID readers's effective range

Trials	Range of the RFID reader in meters (m)					
	1	2	3	4	5	6
1	√	√	√	√	√	×
2	√	√	√	√	√	√
3	√	√	√	×	×	√
4	√	√	√	√	√	√
5	√	√	√	√	√	√
Percentage	100%	100%	100%	80%	80%	80%

Performance testing based on different angles

The system testing the effect of the angle on the reader's ability to successfully read RFID tags placed on the spine of a stack of 10 books, with a distance of 30 cm between the reader and the books.evaluated the performance of a UHF RFID reader at three different angles which were 0 degrees, 45 degrees, and 90 degrees. The aim was to determine

In the case of the 0-degree angle as shown in Table 5, where the reader was positioned in front of the book's front cover, the results showed that the reader achieved a 100% success rate for most book tags. However, tags 302206, 503306, 202206, 603306, and 402206 consistently had a 0% success rate. This suggests that at a 0-degree angle, the reader had difficulties reliably reading these specific tags.

Table 5: Reader when 0-degree angle

Trials	Book Tag									
	105506	210006	110006	805506	905506	302206	503306	202206	603306	402206
1	√	√	√	√	√	×	×	×	×	×
2	√	√	√	√	√	×	×	×	×	×
3	√	√	√	√	×	×	×	×	×	×
4	√	√	√	√	×	×	×	×	×	×
5	√	√	√	√	√	×	×	×	×	×
Percentage	100%	100%	100%	100%	60%	0%	0%	0%	0%	0%

At the 45-degree angle as shown in Table 6, where the reader was tilted slightly, there was an improvement in the success rate compared to the 0-degree angle. Most book tags achieved a 100% success rate, except for tag 302206 which still showed a 60% success rate. Additionally, tags 202206 and 402206 continued to have a 40% success rate. Meanwhile, the tag 603306 had the lowest success rate with 0%. This indicated that even with the angle adjustment, the reader faced challenges in consistently reading these particular tags.

The best performance was observed at the 90-degree angle as shown in Table 7, with the reader placed in front of the book's spine. The approach used in this testing is similar by other research [27]. At this angle, most book tags

achieved a 100% success rate. However, tag 202206 presented difficulties, resulting in a lower success rate. Tag 302206 showed a 60% success rate, indicating that the reader struggled to consistently read these tags even at the optimal 90-degree angle.

Table 6: Reader when 45-degree angle

Trials	Book Tag									
	105506	210006	110006	805506	905506	302206	503306	202206	603306	402206
1	√	√	√	√	√	×	×	×	×	√
2	√	√	√	√	√	√	×	√	×	×
3	√	√	√	√	√	√	×	×	×	×
4	√	√	√	√	√	×	√	√	×	×
5	√	√	√	√	√	√	×	×	×	√
Percentage	100%	100%	100%	100%	100%	60%	20%	40%	0%	40%

Table 7: Reader when 90-degree angle

Trials	Book Tag									
	105506	210006	110006	805506	905506	302206	503306	202206	603306	402206
1	√	√	√	√	√	√	√	×	√	√
2	√	√	√	√	√	√	√	√	√	√
3	√	√	√	√	√	√	√	×	√	√
4	√	√	√	√	√	×	√	×	√	√
5	√	√	√	√	√	×	√	√	√	√
Percentage	100%	100%	100%	100%	100%	60%	100%	40%	100%	100%

The 90-degree angle is considered an optimum angle for the placement of an RFID reader due to several factors. Firstly, at this angle, the reader is positioned directly in front of the book's spine, which provides the most direct and unobstructed path for the RFID signals to reach the tag [23]. This alignment maximizes the signal strength and minimizes signal loss or reflections, resulting in higher read rates and improved overall performance.

Moreover, at a 90-degree angle, the reader's antenna is oriented parallel to the orientation of most RFID tags, which are typically attached to or embedded within the spine or cover of the book. This alignment optimizes the coupling between the reader's antenna and the tags, enhancing the electromagnetic interaction and, consequently, improving the chances of successful tag reading [28].

Despite the advantages of the 90-degree angle, some tags may still experience reading difficulties. One possible reason is that the frequency band of the RFID system is 902 – 928 MHz. At this frequency, certain materials or environmental factors may interfere with the propagation of RFID signals [29]. For instance, metal surfaces or liquids can absorb or reflect RFID signals, leading to weaker or distorted signals reaching the tags [30]. The testing takes place in the Sports Engineering and Artificial Intelligence Centre (SEA-IC),

which consists of a metal device or machine. This encounter disrupted the RFID signal.

Furthermore, the design and construction of certain RFID tags might not be optimal for the chosen frequency band. Each RFID tag is designed with specific characteristics, and some tags may be more tuned to operate effectively at different frequencies [31]. Consequently, when operating at 902 - 928 MHz, some tags may not exhibit the same level of sensitivity or response as they would at a different frequency [32], resulting in lower success rates at the 90-degree angle.

The proposed SPLMS based on RFID technology demonstrates significant improvements in the effectiveness and efficiency of library operations when compared to the existing barcode technology system. RFID technology offers several advantages over barcoding, including faster and contactless book identification, simultaneous scanning of multiple books, and better accuracy [33]. The system's user-friendly dashboard enhances the librarian's ability to manage book details, deletions, and searches efficiently. Additionally, the performance t esting of the RFID reader at different angles revealed the optimal placement of the reader at a 90-degree angle, which further enhances its success rate in reading RFID tags on book spines.

Conclusion

The purpose of this study is to develop a fully integrated Smart Portable Library Management System (SPLMS) using RFID technology and assess its effectiveness at Perpustakaan Raja Tun Uda (PRTU). The study successfully implements the SPLMS, which provides a user-friendly dashboard for librarians to manage book details, deletion, and searching. System testing evaluates the performance of the UHF RFID reader at different angles and reveals that increasing the angle from 0 to 90 degrees improves the reader's success rate in reading RFID tags on book spines. However, certain tags exhibit lower success rates, suggesting the need for further optimization. The findings emphasize the significance of considering the angle and placement of RFID readers in achieving optimal performance. Further research is recommended to address the challenges with specific tags and explore alternative methods for tag placement, signal interference mitigation, and improvements in antenna design. The implementation of the SPLMS and the insights gained from this study contribute to the advancement of library management systems and provide valuable guidance for future research in the field.

Contributions of Authors

The authors confirm the equal contribution in each part of this work. All authors reviewed and approved the final version of this work.

Funding

This work received no specific grant from any funding agency.

Conflict of Interests

All authors declare that they have no conflicts of interest.

Acknowledgment

The authors would like to thank all members from Sports Engineering and Artificial Intelligence Centre (SEA-IC) Lab, UiTM Shah Alam for endless support and guidance.

References

[1] "Pustaka Raja Tun Uda - Perbadanan perpustakaan awam Selangor," https://www.ppas.gov.my/fasiliti/ (accessed Dec. 19, 2022).

[2] C. V. N. H. and M. K. G. U. K. Rao, V. Guru Vasista, N. K. Kumar, S. Sumanth, "Quick shelves for medical and retail industries using rfid technology," *2022 Second International Conference on Interdisciplinary Cyber Physical System, Chennai, India*, pp. 118–123, 2022, doi: 10.1109/ICPS55917.2022.00030.

[3] A. Y. Patel, D. Sharma, J. Sharma, and G. P. Goswami, "Library management system," *Journal of Xi'an University of Architecture & Technology*, vol. 12, no. 11, pp. 743-753, 2020, doi: 10.37896/JXAT12.11/29777.

[4] D. A. Chanda, "Barcode technology and its application in Libraries," *Library Philosophy and Practice*, p. 16, 2020, doi: 10.2139/ssrn.3649957.

[5] A. Dani, "QR code based library management system," *Journal of Emerging Technologies and Innovative Research*, vol. 7, no. 6, pp. 1876–1883, 2020.

[6] Y. K. Atri, "Bar codes and RFID technology use to university library

management," *International Journal of Engineering and Technical Research*, vol. 5, no. 1, pp. 8–12, 2016.

[7] A. Y. Abadi, "Application technology radio frequency identification (RFID) in digitization system document management Library University Bosowa," *Journal Research of Technology Digital Studies*, vol. 1, no. 1, pp. 1–13, 2023.

[8] M. M. Din, R. M. Anwar, and F. A. Fazal, "Asset tagging for library system-does QR relevant?," *Journal of Physics: Conference Series*, vol. 1860, no. 1, pp. 1-12, 2021, doi: 10.1088/1742-6596/1860/1/012017.

[9] S. Promput, S. Maithomklang, and C. Panya-isara, "Design and analysis performance of iot-based water quality monitoring system using lora technology," *TEM Journal*, vol. 12, no. 1, pp. 29–35, 2023, doi: 10.18421/TEM121-04.

[10] Z. Chaczko and R. Braun, "Learning data engineering: Creating IoT apps using the node-RED and the RPI technologies," *2017 16th International Conference on Information Technology Based Higher Education and Training*, pp. 1–8, 2017, doi: 10.1109/ITHET.2017.8067827.

[11] S. U. Uddin, M. J. A. Baig, and M. T. Iqbal, "Design and implementation of an open-source SCADA system for a community solar-powered reverse osmosis system," *Sensors*, vol. 22, no. 24, p. 26, 2022, doi: 10.3390/s22249631.

[12] C. Y. Lu, F. H. Chen, W. C. Hsu, Y. Q. Yang, and T. J. Su, "Constructing home monitoring system with node-red," *Sensors and Materials*, vol. 32, no. 5, pp. 1701–1710, 2020, doi: 10.18494/SAM.2020.2686.

[13] R. V. Phutane, "IoT: based weather monitoring system," *International Journal for Research in Applied Science & Engineering Technology*, vol. 10, no. 7, pp. 1695–1699, 2022, doi: 10.22214/ijraset.2022.45446.

[14] M. J. F. Arifianto and L. Prasetyani, "Sistem pemantauan dan kontrol energi listrik menggunakan platform node-red, influxdb dan grafana melalui jaringan wifi dan lora," *Jurnal Fokus Elektroda Energi Listrik, Telekomunikasi, Komputer, Elektronika dan Kendali*, vol. 7, no. 1, p. 61, 2022, doi: 10.33772/jfe.v7i1.23440.

[15] S. N. Azemi, K. W. Loon, A. Amir, and M. Kamalrudin, "An IoT-based alarm air quality monitoring system," *Journal of Physics: Conference Series*, vol. 1755, no. 1, pp. 0–17, 2021, doi: 10.1088/1742-6596/1755/1/012035.

[16] K. Suda and N. Rani, "Radio frequency identification for efficient library management", 2013. [Online]. Available: http://ijbssnet.com/journals/Vol_4_No_15_Special_Issue_November_2013/18.pdf

[17] M. S. Sclamat and B. Y. Majlis, "Challenges in implementing RFID tag in a conventional library," *IEEE International Conference on Semiconductor Electronics*, pp. 258–262, 2006, doi: 10.1109/SMELEC.2006.381060.

[18] A. Husna Madzidon and N. Ziadah Harun, "Library borrowing system using QR code for sk jelotong," *Applied Information Technology and Computer Science*, vol. 3, no. 2, pp. 225–240, 2022, doi: 10.30880/aitcs.2022.03.02.015.

[19] A. T. Bin Abdullah, I. B. Ismail, Azlina Binti Ibrahim, and Mohd Zikrul Hakim Bin Noor, "Library shelf management system using RFID technology," *2011 IEEE International Conference on System Engineering and Technology*, pp. 215–218, 2011, doi: 10.1109/ICSEngT.2011.5993453.

[20] M. Amir Zulhilmi Bin Zulkiply and F. Hanim Binti Mohd Noh, "Library book search and management system using RFID technology," *Progress in Engineering Application and Technology*, vol. 1, no. 1, pp. 303–316, 2020, doi: 10.30880/peat.2020.01.01.033.

[21] A. B. K. A, K. S. Harshith, and R. B. T. M, "A bar code based library control authentication," *International Research Journal of Engineering and Technology*, vol. 6, no. 9, pp. 1450–1453, 2019.

[22] J. H. Khor, I. R. Widad, M. N. Md Rashid, A. A. Wan Ismail, M. Q. Omar, and F. H. Mohd Zanal, "UHF RFID proof of concept (POC) with open-source ILS at Universiti Sains Malaysia (USM) libraries," *Program: Electronic Library and Information Systems*, vol. 49, no. 2, pp. 135–150, 2015, doi: 10.1108/PROG-11-2012-0060.

[23] K. Abcouwer and E. van Loon, "Library inventory using a RFID wand: contribution of tag and book specific factors on the read rate," *Library Hi Tech*, vol. 39, no. 2, pp. 368–379, 2020, doi: 10.1108/LHT-06-2019-0129.

[24] "UHF RFID ZKHY ZK_RFID101User's Manual V2.0," https://www.manualslib.com/manual/1389450/Zkhy-Zk_rfid101.html (accessed Jun. 20, 2023).

[25] J. H. Kim, J. W. Kwon, J. Y. Kim, M. G. Jeong, S. H. Bae, and W. S. Lee, "Interference analysis and experimental results of passive UHF RFID systems in Sub-1GHz wireless communications systems," *Progress in Electromagnetics Research C*, vol. 76, pp. 129–137, 2017, doi: 10.2528/PIERC17040802.

[26] S. Sohn, "Channel assignment for RFID readers in dense reader environments," *Journal of The Korea Society of Computer and Information*, vol. 18, no. 2, pp. 69–76, 2013, doi: 10.9708/jksci.2013.18.2.069.

[27] M. Dhanalakshmi and U. Mamatha, "RFID based library management system," *Proceedings of ASCNT 2009*, vol. 2, no. 1, pp. 227–234, 2009.

[28] M. Benamara, M. Grzeskowiak, M. Salhi, G. Lissorgues, A. Diet, and Y. Le Bihan, "3D HF RFID reader antenna for tag detection in different angular orientations," *2016 Loughborough Antennas & Propagation Conference (LAPC)*, pp. 1–4, 2016, doi: 10.1109/LAPC.2016.7807512.

[29] C. Li, E. Tanghe, D. Plets, P. Suanet, J. Hoebeke, E. D. Poorter, W.

Joseph, "ReLoc: Hybrid RSSI- and phase-based relative UHF-RFID tag localization with COTS devices," *IEEE Transactions on Instrumentation and Measurement*, vol. 69, no. 10, pp. 8613–8627, 2020, doi: 10.1109/TIM.2020.2991564.

[30] C.-H. Ko, "Accessibility of radio frequency identification technology in facilities maintenance," *Journal of Engineering, Project, and Production Management*, vol. 7, no. 1, pp. 45–53, 2017, doi: 10.32738/jeppm.201701.0006.

[31] I. Bulu and H. Caglayan, "Designing materials with desired electromagnetic properties," *Microwave and Optical Technology Letters*, vol. 48, no. 12, pp. 2611–2615, 2006, doi: 10.1002/mop.

[32] A. Zhigalov, J. D. Herring, J. Herpers, T. O. Bergmann, and O. Jensen, "Probing cortical excitability using rapid frequency tagging," *NeuroImage*, vol. 195, pp. 59–66, 2019, doi: 10.1016/j.neuroimage.2019.03.056.

[33] R. Y. Akbar and M. Hisjam, "Decision making analysis of Auto-Id system using analytical hierarchy process (AHP) at Pt. Akg," *Journal of Industrial Engineering Management*, vol. 6, no. 2, pp. 17–24, 2021, doi: 10.33536/jiem.v6i2.929.

Structural Performance of Ti6Al4V Tibial Tray in Total Knee Arthroplasty (TKA) by Functionally Graded Lattice Structures using Numerical Analysis

Nurasyrani Rabuan[1], Mohd Shahriman Adenan[1,2], Yupiter HP Manurung[1,2]*
Mohd Afzan Mohd Anuar[2], Solehuddin Shuib[2]

[1]Smart Manufacturing Research Institute, Universiti Teknologi MARA, Shah Alam, 40450, Selangor, MALAYSIA
[2]School of Mechanical Engineering, College of Engineering, Universiti Teknologi MARA, Shah Alam, 40450, Selangor, MALAYSIA
[*]mshahriman@uitm.edu.my

ABSTRACT

The medical industry benefits greatly from the additive manufacturing (AM) technology used on customized products. Total knee arthroplasty (TKA) has been widely used however it has drawbacks of stress shielding and loosening due to the excessive daily routine of patients. The problem could be minimized by applying lattice structures to the implant and mimicking the actual density of human bone. This study aims to investigate the optimal design of a Ti6Al4V alloy tibial tray by applying different types of lattice structure designs. A finite element analysis was used to investigate the mechanical behavior of uniform and non-uniform lattice structures in a walking position. Functional gradation structure was optimized on selected regions of the tibial tray with weight reduction and adaptation to the near actual density of the human bone without compromising its mechanical performance. The results indicated that the Voronoi structure has improved stress behavior and the capability to withstand the loads exerted, based on the Von Mises stress result of the Voronoi structure at 35.83 MPa as compared to the gyroid and diamond structures at 61.65 MPa and 49.74 MPa, respectively. The optimal design of the tibial implant was achieved by functionally graded lattice structures, replacing the solid tibial implant.

ISSN 1823-5514, eISSN 2550-164X

https://doi.org/10.24191/jmeche.v12i1.24643

Received for review: 2023-04-03
Accepted for publication: 2023-09-25
Published: 2023-11-15

Keywords: *Topology Optimization; TPMS Structures; Voronoi Structure; Finite Element Analysis; Tibial Tray*

Introduction

The rapid development of Additive Manufacturing (AM) technologies contributes towards the expansion of the industry's design and engineering approach. This technology is a process to manufacture solid parts through layer-by-layer addition of material by melting the material from a heat source [1]. Selective Laser Melting (SLM) is a process based on laser melted metal powder. This process also offers advantages in complex geometry, low manufacturing cost, and reduced fabrication time [2]. Furthermore, AM has been widely applied in biomedical industries, especially for orthopedics, implants, and human tissue.

In knee replacement surgery, artificial arthroplasty aims to relieve pain, improve function, and restore range of motion in the patients [3]. Anyhow, failures still occur after the replacement surgery such as loosening, wear, and stress shielding of the implant [4]-[5]. In a previous study, an assessment of the population was conducted to show the factors that affected the failure of tibial tray performance [6]. Another clinical study demonstrated a tibial plateau fracture caused by the patient's excessive weight [7].

To overcome the failure of implants, several studies proved that the combination of topology optimization by lattice structure and orthopedic implants has shown the enhancement of mechanical behaviour. Peto et al. [8] investigated the mechanical behaviour of Hexagonal Prism Vertex Centroid (HPVC) lattice structure which showed that lattice structures have an impact in reducing stiffness between implant and bones and minimizing stress shielding problems. Guoqing stated that due to excellent biocompatibility and good mechanical properties of the bio-fixation (solid and porous) implants, the life quality of patients has improved. The implants had been manufactured through the Selective laser melting (SLM) process [9]. Besides, this approach not only minimizes the implant weight but also facilitates tissue regeneration at the implant-bone interface. Triply Periodic Minimal Surfaces (TPMS) are common lattice structures used in the optimization of implants such as gyroid, diamond, and schwarz. There are two types of TPMS lattice structures which are solid-networks and sheet-networks types, whereas the properties for each type of lattice structure are also different [10]. Sheet-networks lattice structures show better mechanical properties compared to solid-networks lattice structures [11]. Yang et al. [12] proposed a gyroid unit cell (TPMS) made of Ti6Al4V, whose characteristic shows good strength and high manufacturability.

Yan et al. [13] developed gyroid and diamond TPMS lattices of bone implants with a percentage porosity of 80-95% for diamond and gyroid lattice

structures comparable to the porosity of trabecular bone which is 50-90%. As the value of porosity between implant and bone is almost similar, the modulus of porosity can be adjusted to the modulus of trabecular and cortical bone which may lead to reducing stress shielding problems. Lorenzo [14] compiled the reviews of AM-printed acetabular cups for total hip arthroplasty based on porous structure design, limitations of the manufacturing process, and clinical outcomes. The main highlight of the study was the comparison of conventional manufacturing such as die casting, CNC machining, and injection molding with AM printing and the enhancement of complex porous structures. Most recently, Limmahakun et al. [15] explored the optimization of orthopedic implants by functional gradation of lattice structures. The result showed that the mechanical strength gradually increased. According to Al-Ketan outcomes [16], these types of TPMS with sheet-network lattices encourage good mechanical behaviour, for example, could help improve tibial implant in structurally efficient, exhibiting better stiffness and strength to-weight ratio. In addition, the Voronoi structure showed that the irregularity of shape contributes to good mechanical behaviour which could attain stiffness comparable to bone stiffness [17]. Liang et al. [18] had proven trabecular-like porous structures with porosities between 48.83-74.28% had excellent mechanical performance in terms of elastic modulus and ultimate strength which is similar to cancellous bone mechanical behavior. Benedetti et al. [19] constructed a study of compressive behavior on nine different Ti6Al4V trabecular structures with various values of density, which displayed cross structure had the highest strength at constant stiffness compared to other structures.

The purpose of this research is to optimize the tibial tray of the TKA implant using a topology optimization approach by obtaining a suitable density compared to human bone and weight reduction. Advanced lattice structures have been proposed for optimizing the tibial component. The geometrical model of the tibial tray was first constructed, and then the Finite Element (FE) model was developed. The mechanical behaviour of the tibial tray was analysed using Finite Element Analysis (FEA). Specific regions of the tibial tray were replaced by three different lattice structures, namely, 1) gyroid, 2) diamond sheet structures, and 3) Voronoi strut structure due to stretching-dominated behavior which exhibited higher fracture strength compared to bending-dominated [21]. Their mechanical performance was analysed and evaluated by implementing similar boundary conditions and loadings. In order to improve further design and mechanical properties, functional gradation of lattice structure was applied during the optimization process.

Materials and Method

Model designs of total knee implant

Total knee replacement as shown in Figure 1 consists of three components: (a) femoral, (b) tibial insert, and (c) tibial. As for this research, it only focused on the mechanical behaviour of the tibial tray as stress shielding always occurs between the tibial tray and human bone due to a mismatch of stiffness. The tibial tray is available in a variety of complex geometric shapes and surfaces. Many factors need to be considered while designing an implant to ensure the implantation effectiveness which decreases the incidence of implant loosening. The tibial tray design for this investigation was derived from a previous study since the design has been established [20]. As indicated in Figure 2a, the tibial tray is a stem and the tibial wing to increase the stability of total knee replacement and reduce micromotion [21]. The tibial insert hole as in Figure 2b is functioning as a tibial insert holder. Figure 2c depicts the main geometric dimension of the designed tibial tray.

Lattice structure composition

This study uses the TPMS with gyroid and diamond sheet structures and Voronoi strut structures for the optimization phase due to its capability to withstand high stress loads and the most prominent structures with increased strength. The following equation shows the level-set equations of the TPMS gyroid (φ_G) and diamond (φ_D) geometries [23]-[25]:

$$\varphi_G = \sin x \cos y + \sin y \cos z + \sin z \cos x = c \quad (1)$$

$$\varphi_D = \cos x \cos y \cos z - \sin x \sin y \sin z = c \quad (2)$$

The FEA Voronoi structure is configured to resemble the bone trabecular structure, with structures created in a scattered pattern with varying shapes and geometries. The mathematical formula for Voronoi strut structures is given below [26] :

$$V(pi) = \left\{ \frac{p}{d(p,pi)}, \leq d(p,pj), j \neq i, i, j = 1,2, \dots, n \right\} \quad (3)$$

where $V(p_i)$ represents the 3D Voronoi polygon on seed p_i, $p_1 \ldots\ldots$ p_n are the definite seeds in 3D space, and $d(p$ and $p_i)$ is the usual Euclidean distance between p and pi. These structures are modelled by using nTopology (3.40.2). Figure 3 shows the workflow of tibial implant optimization with lattice structures. Firstly, Figure 3a shows a solid tibial implant and Figure 3b shows the region of lattice structure which will be applied on the tibial tray plate by topology optimization. As a result, the tibial tray plate contains gyroid lattice structures as shown in Figure 3c.

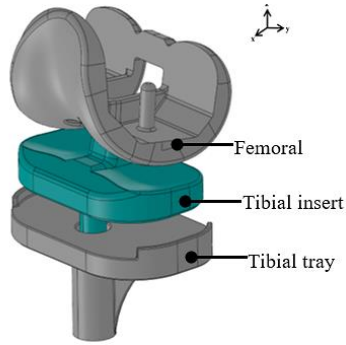

Figure 1: 3D model of total knee implant

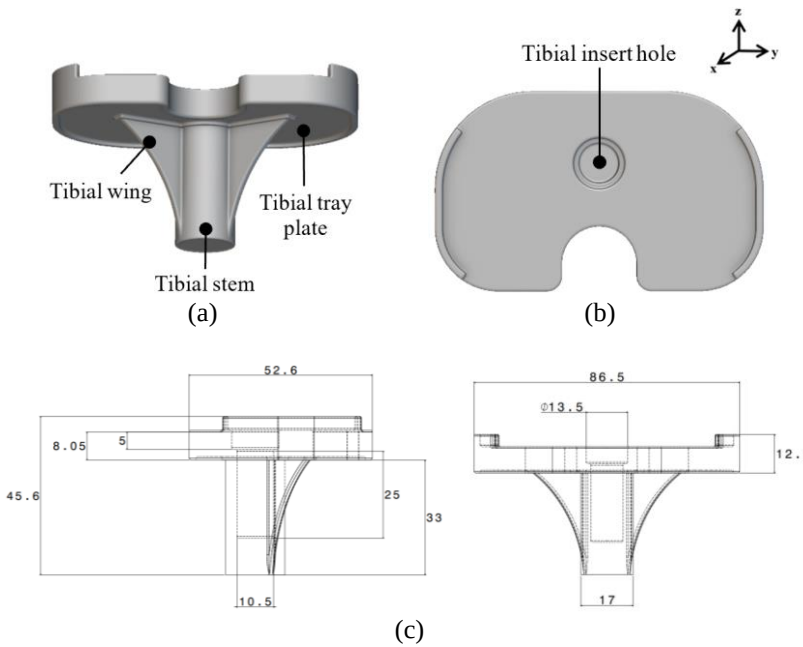

Figure 2: 3D model of tibial tray: (a) parts of tibial tray [22], (b) top view of tibial tray, and (c) geometry of tibial tray (mm)

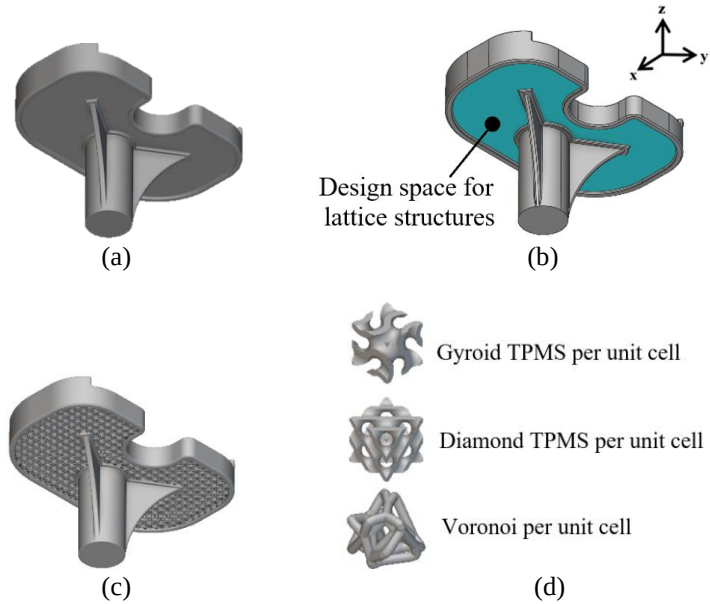

Figure 3: Workflow of tibial tray optimization: (a) solid tibial tray, (b) design region of tibial tray plate, (c) tibial tray with gyroid structures, and (d) TPMS and Voronoi structure per unit cell

For both uniform and non-uniform lattice structures, the size unit cell is 3 mm in order to maintain 50% of relative density. On the tibial tray plate, for uniform lattice structure, and diamond had a constant sheet thickness of 480 µm, meanwhile gyroid and Voronoi had a constant sheet thickness of 580 µm. As for the non-uniform lattice structure, the tibial tray plate had various ranges of sheet thickness. The non-uniform lattice for the gyroid structure had a functionally graded sheet thickness of 520-1150 µm and the diamond structure had a functionally graded sheet thickness of 440-710 µm. Moreover, for Voronoi lattice structure the functionally graded sheet thickness is between 540-850 µm. The porosity Ø of the lattice structure for both and non-uniform lattice structure is 50% determined by Equation 4. According to Arabnejad et al. [27], to ensure effective osseointegration the porosity had to be at a minimum value of 50%.

$$\text{Porosity } \emptyset = 1 - \frac{\text{Volume of scaffold}}{\text{Volume of solid structure}} \quad (4)$$

Finite Element Analysis (FEA)

The FEA is used on the tibial tray to resolve stress that occurs under various loading conditions of the optimized tibial tray. The tibial tray is meshed with

four nodes of quadratic tetrahedral elements (C3D10) of size 1.1 mm size as depicted in Figure 4. The convergence analysis is performed as shown in Figure 5 to determine the optimum number of element sizes for each design tibial tray, where the number of elements of solid tibial tray is 736, 326 and the number of nodes element is 1.12 million.

Figure 4: Mesh of solid tibial tray

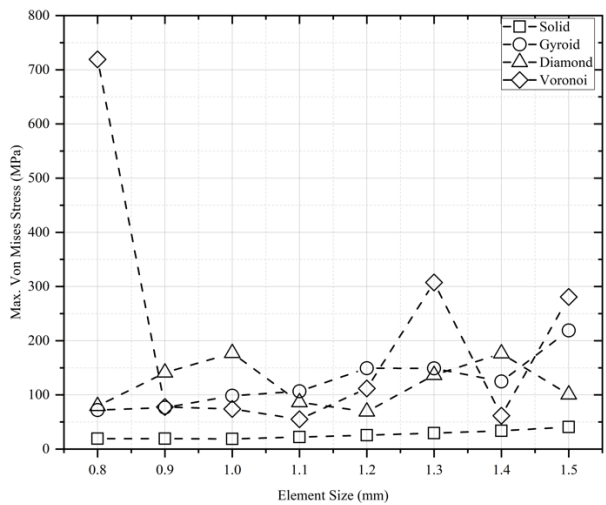

Figure 5: Convergence graph of the tibial tray for solid and variation lattice structures

The boundary conditions that mimic the actual knee joint mechanics are used for the simulation. In this case, the fixed support condition is applied at the bottom of the tibial stem to prevent any rotation and movement [28]. The axial loads of 3100 N are applied on the tibial surface which is based on walking movement due to the result of Bergmann et al. [29] who reported the knee loads are based on the percentage of weight shown in an average body

weight of 75 kg. Figure 6 illustrates the boundary condition setup of the tibial tray case.

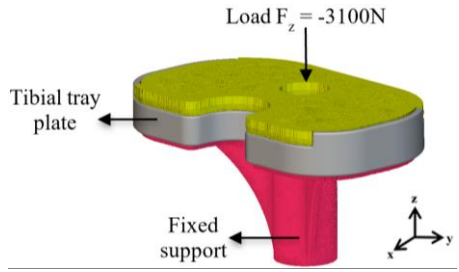

Figure 6: Boundary condition of tibial tray

The material selected for this study is titanium alloy of grade Ti6Al4V which offers good biocompatibility and corrosion resistance, besides having strength and good mechanical properties [30]. Table 1 indicates the properties of Ti6Al4V.

Table 1: Mechanical properties of Ti6Al4V [31]-[33]

Mechanical properties	Values
Density, ρ	4.43 g/cm^3
Elastic modulus, E	113.8 GPa
Poisson ratio, v	0.342
Yield strength, σ	973 MPa
Ultimate yield strength, σ_{ult}	1058 MPa

Results and Discussion

As reported in previous research, trabecular bone consists a range of 40-95% porosity [34]. For this research, the range porosity used is 50% for uniform and non-uniform lattice structures as mentioned before to enhance osseointegration [27]. Figure 7 illustrates a tibial tray with lattice structure (a, c, e) and single unit cell (b, d, f) of three different lattice structures gyroid, diamond, and Voronoi. All lattice structures are designed in 3 mm per unit cell to maintain the similarity of relative density for each structure which is 50%. In the second optimization phase, the relative density of the sheet lattice structure is controlled by the changes in wall thickness as illustrated in Figure 8. Relative density can form a huge difference even though there is the smallest change in wall thickness [35]. As an example, the unit cell for the gyroid with 3 mm has a relative density of 50% for the wall thickness of 0.58 mm, while

an increase in the wall thickness of 1.15 mm contributes to the increase in relative density of 81%. Moreover, due to the variation of lattice structures applied on the tibial tray, it shows the differences in the affected area of stress distribution as depicted in Figure 9. Meanwhile, the values of the maximum Von Mises stress of each tibial tray model are shown in Table 2. The displacement distribution of the tibial tray is shown in Figure 10 and Table 3 shows the values of the total deformation of the tibial tray.

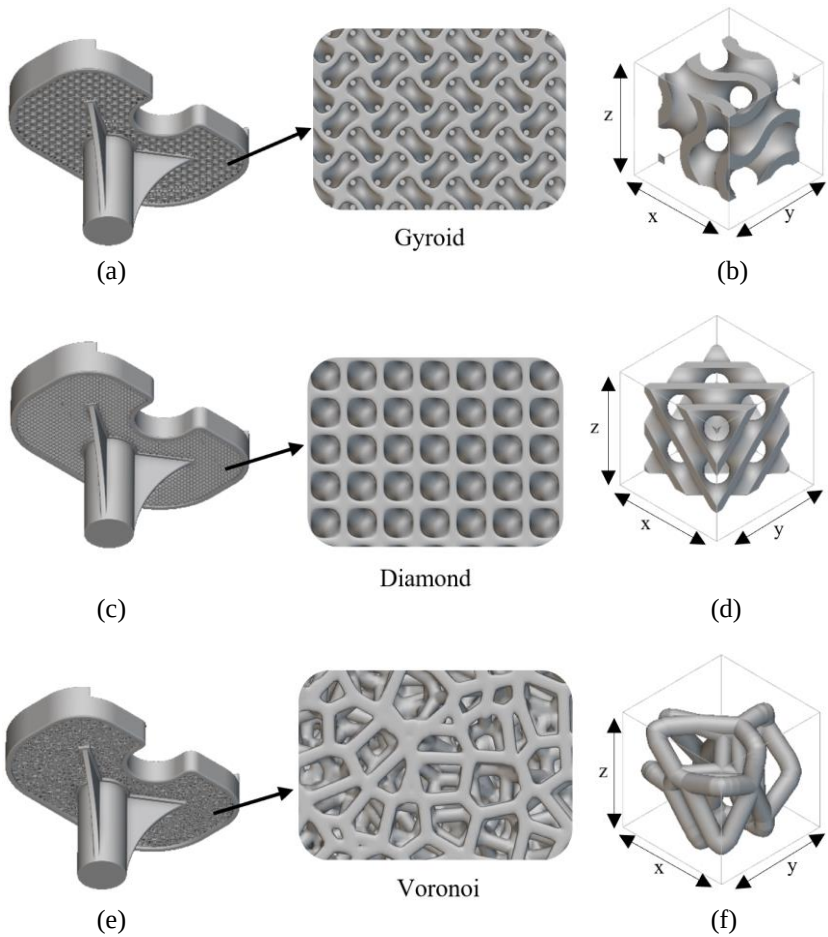

Figure 7: Gyroid structure; (a) tibial tray with lattice structure, (b) single unit cell diamond structure, (c) tibial tray with lattice structure, (d) single unit cell Voronoi structure, (e) tibial tray with lattice structure, and (f) single unit cell

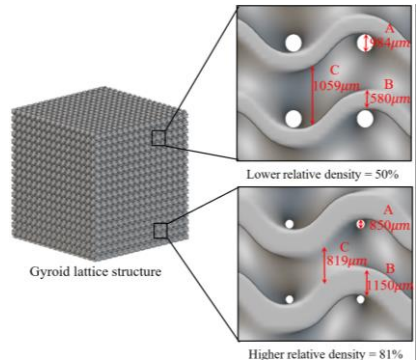

(a)

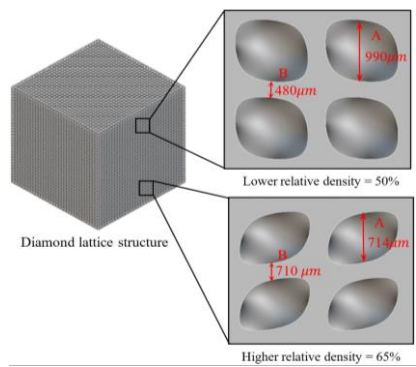

(b)

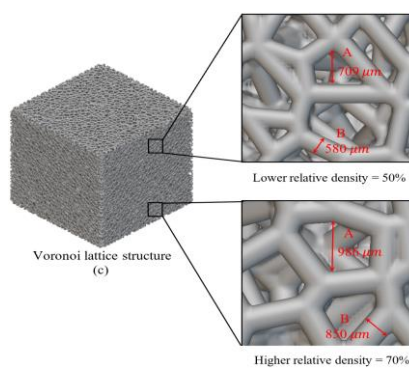

(c)

Figure 8: Relative density of various lattice structure in cube size of 50 mm; (a) pores size, (b) sheet thickness of lattice structure, and (c) length between sheet thickness

It is significant to evaluate the occurrence of solid tibial implant stress distribution area to further the topology optimization process. Since the force distribution is exerted on the tibial tray, it is shown in Figure 9a that the maximum stress distribution occurs on the edge of the tibial tray rather than the tibial stem area. Therefore, topology optimization can be reduced on the tibial tray region to reduce the stress behaviour. The maximum stress escalates up to 22.29 MPa on a specific point which does not indicate the total mechanical behaviour of the tibial implant. Furthermore, the maximum stress is in the allowable range which is below the material yield point as shown in Table 2.

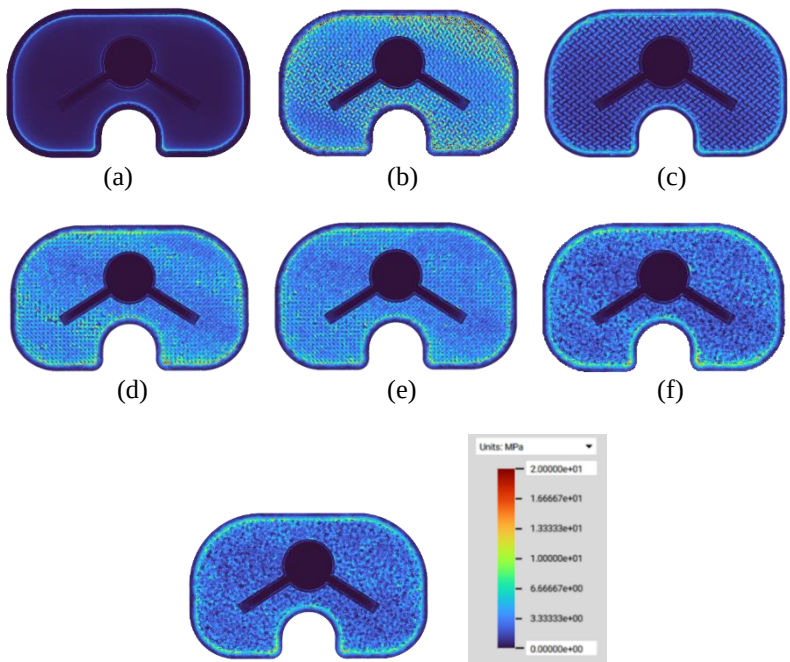

Figure 9: Stress distribution on tibial tray of solid and different lattice structures; (a) solid, (b) uniform lattice structure of gyroid, (c) non-uniform lattice structure of gyroid, (d) uniform lattice structure of diamond, (e) non-uniform lattice structure of diamond, (f) uniform lattice structure of Voronoi, and (g) non-uniform lattice structure of Voronoi

As for the Voronoi structure, high stress distribution occurs on the edge of the tibial tray. The highest strength is shown in the tibial implant which contains a Voronoi structure with a value of maximum stress of only 55 MPa due to the configuration of lattice structure being more scattered compared to

the gyroid and diamond lattice structure. In addition, the tibial implant that contains a diamond structure shows a maximum stress value of 86.36 MPa. Meanwhile, the tibial implant with a gyroid structure exhibits a maximum stress value of 161.85 MPa. The maximum stress increases in the first optimization phase because the solid area of the tibial tray is reduced through topology optimization of lattice structures which contribute to reducing the surface area of the tibial tray. Figures 9b, d, and f show the stress distribution for the first phase optimization.

Table 2: Maximum Von Mises stress of tibial tray (MPa)

Design of tibial tray	Von Mises stress (MPa)
Solid	22.29
Uniform lattice structure	
Gyroid	161.85
Diamond	86.36
Voronoi	55.0
Non-uniform lattice structure	
Gyroid	61.65
Diamond	49.74
Voronoi	35.83

All lattice structures applied on the tibial tray region are due to high stress that appears on it. In the first optimization phase, stress distribution occurs on the lattice area from the edge of the tibial implant to the center of the tibial for gyroid and diamond structures as indicated in Figure 10.

According to [36], as the lattice structures are applied to the hip implant, the value of maximum stress increases as compared to the maximum stress of the solid component. However, in order to achieve an allowable value of maximum stress, further optimization is needed to be performed by varying the range of relative density of lattice structure by a functionally graded lattice structure. It shows similarities to this research, the maximum stress of the tibial tray is increased as the lattice structures are applied on the tibial tray region. In comparison to this research, the maximum stress of the first optimization phase is still under the allowable material yield point which is 973 MPa. However, further optimization needs to be done to achieve comparable maximum stress to solid tibial implants and enhance the mechanical performance of tibial implants. Furthermore, there are studies that showed the combination of solid and lattice structures has improved the mechanical performance of tibial implants [37].

The second optimization phase continues with functionally graded lattice structures. The total relative density of the tibial tray and the relative density lattice structure region remain constant. For TPMS-based lattice, a sheet network offers good mechanical properties due to a high surface area to

volume ratio [38]. On the other hand, the Voronoi structure changes in terms of strut thickness. High stress region on the tibial tray is required to increase wall thickness compared to low stress region. The differences of stress distribution of the first optimization in Figures 9b, d, and f are compared to the second optimization in Figures 9c, e, and g which showed a reduction in the affected region of lattice structure. Figure 10 shows a close-up of stress distribution reduced from the first optimization compared to the second optimization. The percentage of maximum stress for gyroid structure reduces by about 61.91% from the first optimization to the second optimization while diamond structure reduces by 42.40% and Voronoi structure decreases by 34.85%. This demonstrates that the non-uniform lattice structure is adequate to withstand the same load exerted on the tibial tray in the first optimization with lower maximum stress. Moreover, as the wall thickness in lattice structures increases, it contributes to reducing maximum stress on each structure. This is due to the increasing surface area of lattice structures on the force exerted area of the tibial tray. According to Zineddine et al. [39], the beam thickness of lattice structures affects the amount of maximum stress by assuming the increase of cross-sectional surface of beam structures. Even though this research uses a triply periodic minimal surface (gyroid and diamond) and Voronoi lattice structure, the similar concept of force that affects the surface area is comparable.

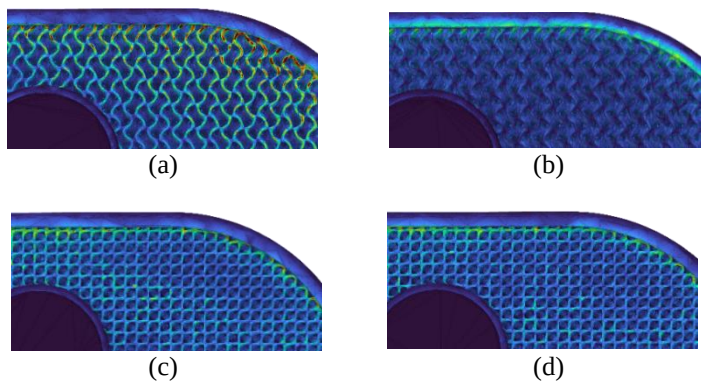

Figure 10: Stress distribution of; (a) uniform gyroid lattice structures, (b) non-uniform gyroid lattice structures, (c) uniform diamond lattice structures, and (d) non-uniform lattice structures

In addition, the deformation result shows that the highest deformation among the tibial tray model is the Voronoi structure in uniform lattice structure with the value of 0.000497 mm. Meanwhile, the lowest deformation is 0.000278 mm for non-uniform structure of the diamond. Figure 11 shows the

deformation distribution of varies types of lattice structures for uniform and non-unifrom sturctures.

Table 3: Total displacement of tibial tray (mm)

Design of tibial tray	Maximum displacement (mm)
Solid	0.000294
Uniform lattice structure	
Gyroid	0.000339
Diamond	0.000291
Voronoi	0.000497
Non-uniform structure	
Gyroid	0.000290
Diamond	0.000278
Voronoi	0.000459

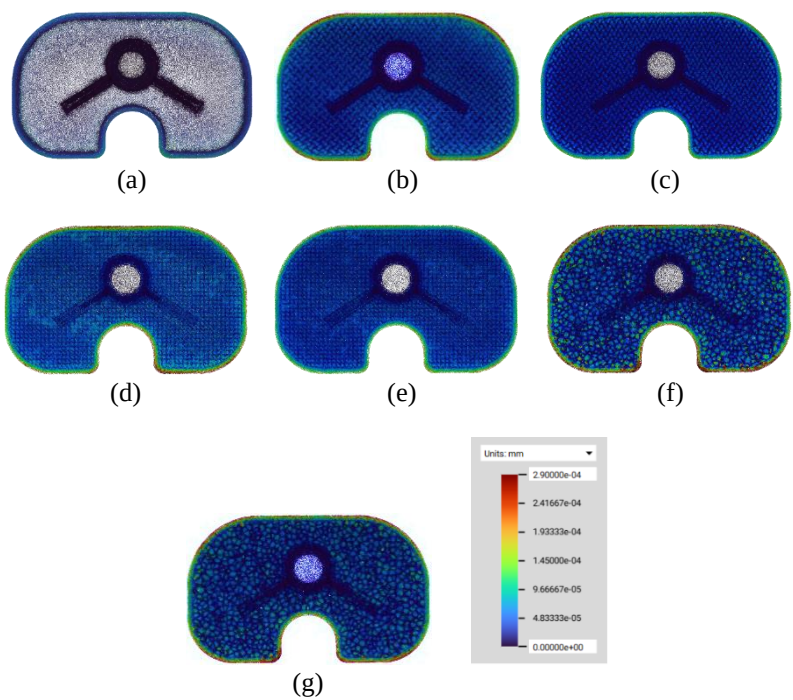

Figure 11: Displacement distribution on tibial tray of solid and different lattice structures: (a) solid, (b) uniform lattice structure of gyroid, (c) non-uniform lattice structure of gyroid, (d) uniform lattice structure of diamond, (e) non-uniform lattice structure of diamond, (f) uniform lattice structure of Voronoi, and (g) non-uniform lattice structure of Voronoi

All structures demonstrate a decrease deformation distribution for non-uniform structures as the lattice structure consists of a variation of wall thickness. Furthermore, all deformations occur at the top of the tibial tray region for all types of lattice structures and solids as demonstrated in Figure 10. The distribution of force exerted on the top of the tibial region causes maximum displacement to occur on the top of the tibial region compared to the tibial wing and stem region.

However, this research had several limitations. The tibial implant with different types of lattice structures (gyroid, diamond, and Voronoi) was simulated only by static conditions. In order to obtain acceptable data for the optimization, further studies need to be done as the walking conditions require dynamic motions. According to the literature review, the main parameters used in this research are different types of lattice structure and relative density of lattice structure which showed a significant effect on the maximum stress distribution of tibial implant. However, the effect of porosity was not mentioned in this study; thus, it should be considered as it is widely used in previous literature reviews.

Conclusion

In the present study, topology optimization of three different lattices was proposed on the tibial tray to show better mechanical performance. The topology optimization applied different lattice structures such as gyroid, diamond, and Voronoi which are considered to have superior mechanical performance. A lattice structure was applied on high-stress region to maintain the optimal mass of the tibial tray. Moreover, the optimization of the lattice structure was continued by functional gradation. By this continuity of optimization, various ranges of sheet thickness of lattice structure contributed to enhancing mechanical behaviour while the stress distribution for all lattice structures remained within the allowable range. Above all, it was examined that the tibial tray consisting of Voronoi structures showed the best mechanical behaviour compared to gyroid and diamond for both phases of lattice optimization. By topology optimization, the weight reduction of optimized tibial reached up to 40% compared to solid tibial meanwhile the density was reduced by about 48%. As for future work, the fabrication of a tibial implant by using selective laser melting and the evaluation of mechanical behaviour should be measured and compared between simulation and experimental values.

Contributions of Authors

Concept: Mohd Shahriman Adenan; Methodology: Nurasyrani Rabuan, Yupiter HP Manurung, Mohd Shahriman Adenan; Results and Discussion: Nurasyrani Rabuan, Mohd Afzan Mohd Anuar, Solehuddin Shuib, Yupiter HP Manurung, Mohd Shahriman Adenan; Review and Editing: Nurasyrani Rabuan, Mohd Shahriman Adenan. All authors have agreed to the publication of the manuscript.

Funding

This work received funding from Universiti Teknologi MARA with grant code 600-RMC/KEPU 5/3 (009/2021) Study of Design for Additive Manufacturing (DFAM) for Coated Hip Implant for the 3D printing process of the TKA implants

Conflict of Interests

One of the authors, Mohd Afzan Mohd Anuar, is an assistant managing editor of the Journal of Mechanical Engineering (JMechE). The author has no other conflict of interest to note.

Acknowledgment

The authors express the highest gratitude towards nTop. (USA) for the software license and never-ending support in the simulation section.

References

[1] M. Nematollahi, A. Jahadakbar, M. J. Mahtabi, and M. Elahinia, Additive manufacturing (AM), 2nd Ed. Elsevier Ltd., 2019. doi: 10.1016/B978-0-08-102666-3.00012-2.

[2] J. Ni, H. Ling, S. Zhang, Z. Wang, Z. Peng, C. Benyshek, R. Zan, A.K. Miri, Z. Li, X. Zhang, J. Lee, K.-J. Lee, H.-J. Kim, P. Tebon, T. Hoffman, M.R. Dokmeci, N. Ashammakhi, X.Li, and A.Khademhosseini, "Three-dimensional printing of metals for biomedical applications," *Materials Today Bio*, vol. 3, 2019. doi: 10.1016/j.mtbio.2019.100024.

[3] A. R. Balwan and V. D. Shinde, "Development of patient specific knee joint implant," *Materials Today Proceedings*, vol. 27, no. 1, pp. 288–293,

2019. doi: 10.1016/j.matpr.2019.11.032.

[4] X. Wang, S. Xu, S. Zhou, W.Xu, M.Leary, P.Choong, M.Qian, M.Brandt, Y.M.Xie, "Topological design and additive manufacturing of porous metals for bone scaffolds and orthopaedic implants: A review," *Biomaterials*, vol. 83, pp. 127–141, 2016. doi: 10.1016/j.biomaterials.2016.01.012.

[5] J. P. Luo, Y.J.Huang, J.Y.Xu, J.F.Sun, M.S. dargush, C.H.Hou, L.Ren, R.Z.Wang, T.Ebel, and M.Yan, "Additively manufactured biomedical Ti-Nb-Ta-Zr lattices with tunable Young's modulus: Mechanical property, biocompatibility, and proteomics analysis," *Materials Science and Engineering: C*, vol. 114, p. 110903, 2020.

[6] J. J. Callaghan, D. E. DeMik, N. A. Bedard, A. N. Odland, W. M. Kane, and S. M. Kurtz, "Tibial tray fracture in a modern prosthesis with retrieval analysis," *Arthroplasty Today*, vol. 4, no. 2, pp. 143–147, 2018. doi: 10.1016/j.artd.2017.12.005.

[7] F. Galloway, M. Kahnt, H. Ramm, P. Worsley, S. Zachow, P.Nair, and M.Taylor,"A large scale finite element study of a cementless osseointegrated tibial tray," *Journal of Biomechanics*, vol. 46, no. 11, pp. 1900–1906, 2013. doi: 10.1016/j.jbiomech.2013.04.021.

[8] M. Peto, "Topology and lattice-based structural design optimization for additively manufactured medical implants," Thesis, Denton, Texas, p. 55, 2019.

[9] Z. Guoqing, Y. Yongqiang, L. Hui, S. Changhui, X. Ran, and Y. Jiakuo, "Modeling and manufacturing technology for personalized biological fixed implants," *Journal of Medical and Biological Engineering*, vol. 37, no. 2, pp. 191–200, 2017. doi: 10.1007/s40846-016-0215-z.

[10] J. Zhang, Y. Shen, Y. Sun, J. Yang, Y. Gong, K. Wang, Z.Zhang, X. Chen and L. Bai, "Design and mechanical testing of porous lattice structure with independent adjustment of pore size and porosity for bone implant," *Journal of Materials Research and Technology*, vol. 18, pp. 3240–3255, 2022. doi: 10.1016/j.jmrt.2022.04.002.

[11] H. Zhou, M. Zhao, Z. Ma, D. Z. Zhang, and G. Fu, "Sheet and network based functionally graded lattice structures manufactured by selective laser melting: Design, mechanical properties, and simulation," *International Journal of Mechanical Sciences*, vol. 175, p. 105480, 2020. doi: 10.1016/j.ijmecsci.2020.105480.

[12] L. Yang, C. Yan, C. Han, P. Chen, S. Yang, and Y. Shi, "Mechanical response of a triply periodic minimal surface cellular structures manufactured by selective laser melting," *International Journal of Mechanical Sciences*, vol. 148, pp. 149–157, 2018. doi: 10.1016/j.ijmecsci.2018.08.039.

[13] C. Yan, L. Hao, A. Hussein, and P. Young, "Ti-6Al-4V triply periodic minimal surface structures for bone implants fabricated via selective laser melting," *Journal of The Mechanical Behavior of Biomedical Materials*,

vol. 51, pp. 61–73, 2015. doi: 10.1016/j.jmbbm.2015.06.024.
[14] L. Dall'Ava, H. Hothi, A. Di Laura, J. Henckel, and A. Hart, "3D printed acetabular cups for total hip arthroplasty: A review article," *Metals (Basel)*, vol. 9, no. 7, 2019. doi: 10.3390/met9070729.
[15] S. Limmahakhun, A. Oloyede, N. Chantarapanich, P. Jiamwatthanachai, K. Sitthiseripratip, Y. Xiao, and C. Yan, "Alternative designs of load−sharing cobalt chromium graded femoral stems," *Materials Today Communications*, vol. 12, pp. 1–10, 2017. doi: 10.1016/j.mtcomm.2017.05.002.
[16] O. Al-Ketan and R. K. Abu Al-Rub, "Multifunctional mechanical metamaterials based on triply periodic minimal surface lattices," *Advanced Engineering Materials*, vol. 21, no. 10, 2019. doi: 10.1002/adem.201900524.
[17] G. Wang, L. Shen, J. Zhao, H. Liang, D.Xie, Z. Tian, and C. Wang "Design and compressive behavior of controllable irregular porous scaffolds: based on voronoi-tessellation and for additive manufacturing," *ACS Biomaterials Science & Engineering*, vol. 4, no. 2, pp. 719–727, 2018. doi: 10.1021/acsbiomaterials.7b00916.
[18] H. Liang, Y. Yang, D. Xie, L. Li, N. Mao, C. Wang, Z, Tian, Q. Jiang, and L.Shen, "Trabecular-like Ti-6Al-4V scaffolds for orthopedic: fabrication by selective laser melting and in vitro biocompatibility," *Journal of Materials Science & Technology*, vol. 35, no. 7, pp. 1284–1297, 2019. doi: 10.1016/j.jmst.2019.01.012.
[19] M. Benedetti, J. Klarin, F. Johansson, V. Fontanari, V. Luchin, G.Zappini, and A. Molinari, "Study of the compression behaviour of Ti6Al4V trabecular structures produced by additive laser manufacturing," *Materials (Basel)*, vol. 12, no. 9, 2019. doi: 10.3390/ma12091471.
[20] S. Shuib, M. A. Azemi, I. Binti, M. Arrif, and N. S. Hamizan, "Design for additive manufacturing and finite element analysis for high flexion total knee replacement (TKR)," *Journal of Mechanical Engineering*, vol. 18, no. 2, pp. 97–110, 2021.
[21] N. Jindal, S. S. Sankhala, and V. Bachhal, "The role of fusion in the management of burst fractures of the thoracolumbar spine treated by short segment pedicle screw fixation: A prospective randomised trial," *The Journal of Bone and Joint Surgery British Volume*, vol. 94 B, no. 8, pp. 1101–1106, 2012. doi: 10.1302/0301-620X.94B8.
[22] G. Zhang, J. Li, X. Zhou, Y. Zhou, and A. Wang, "Optimal design and processing technology of 3D printed tibial implants," *Coatings*, vol. 12, no. 5, p. 561, 2022. doi: 10.3390/coatings12050561.
[23] C. Pan, Y. Han, and J. Lu, "Design and optimization of lattice structures: A review," *Applied Sciences*, vol. 10, no. 18, pp. 1–36, 2020. doi: 10.3390/APP10186374.
[24] T. Maconachie, M. Leary, B. Lozanovski, X. Zhang, M. Qian, O.

Faruque, and M. Brandt, "SLM lattice structures: Properties, performance, applications and challenges," *Materials and Design*, vol. 183, p. 108137, 2019. doi: 10.1016/j.matdes.2019.108137.

[25] C. Chatzigeorgiou, B. Piotrowski, Y. Chemisky, P. Laheurte, and F. Meraghni, "Numerical investigation of the effective mechanical properties and local stress distributions of TPMS-based and strut-based lattices for biomedical applications," *Journal of The Mechanical Behavior of Biomedical Materials*, vol. 126, Feb. 2022. doi: 10.1016/j.jmbbm.2021.105025.

[26] A. Dobrin, "A Review Of Properties And Variations Of Voronoi Diagrams." Oct 31, 2023. [Online]. Available: chrome-extension://efaidnbmnnnibpcajpcglclefindmkaj/https://www.whitman.edu/documents/academics/mathematics/dobrinat.pdf (Accessed Oct 31, 2023).

[27] S. Arabnejad, R. Burnett Johnston, J. A. Pura, B. Singh, M. Tanzer, and D. Pasini, "High-strength porous biomaterials for bone replacement: A strategy to assess the interplay between cell morphology, mechanical properties, bone ingrowth and manufacturing constraints," *Acta Biomateralia*, vol. 30, pp. 345–356, 2016. doi: 10.1016/j.actbio.2015.10.048.

[28] A. Z. E. A. Arab, A. Merdji, A. Benaissa, S. Roy, B. B. Bouiadjra, K. Layadi, A. Ouddane, and O. Mukdadi, "Finite-Element analysis of a lateral femoro-tibial impact on the total knee arthroplasty," *Computer Methods and Programs in Biomedicine*, vol. 192, 2020. doi: 10.1016/j.cmpb.2020.105446.

[29] G. Bergmann, A. Bender, F. Graichen, J. Dymke, A. Rohlmann, A. Trepczynski, M. Heller, and I. Kutzner, "Standardized loads acting in knee implants," *PLoS One*, vol. 9, no. 1, p.e86035, 2014. doi: 10.1371/journal.pone.0086035.

[30] A. Deing, B. Luthringer, D. Laipple, T. Ebel, and R. Willumeit, "A porous TiAl6V4 implant material for medical application," *International Journal of Biomaterials*, vol. 2014, no. 10, p. 904230, 2014. doi: 10.1155/2014/904230.

[31] T. Majumdar, N. Eisenstein, J. E. Frith, S. C. Cox, and N. Birbilis, "Additive Manufacturing of Titanium Alloys for Orthopedic Applications: A Materials Science Viewpoint," *Advanced Engineering Materials*, vol. 20, no. 9, 2018. doi: 10.1002/adem.201800172.

[32] S. Liu and Y. C. Shin, "Additive manufacturing of Ti6Al4V alloy: A review," *Materials and Design*, vol. 164, 2019, doi: 10.1016/j.matdes.2018.107552.

[33] Renishaw, "Ti6Al4V ELI-0406 powder for additive manufacturing Process specification Powder description Titanium alloy powder," 2017. [Online]. Available: www.renishaw.com/contact

[34] K. Nelson, C. N. Kelly, and K. Gall, "Effect of stress state on the

mechanical behavior of 3D printed porous Ti6Al4V scaffolds produced by laser powder bed fusion," *Materials Science and Engineering: B*, vol. 286, p. 116013, 2022. doi: 10.1016/j.mseb.2022.116013.

[35] O. Al-Ketan, D. W. Lee, R. Rowshan, and R. K. Abu Al-Rub, "Functionally graded and multi-morphology sheet TPMS lattices: Design, manufacturing, and mechanical properties," *Journal of the Mechanical Behavior of Biomedical Materials*, vol. 102, p. 103520, 2020. doi: 10.1016/j.jmbbm.2019.103520.

[36] N. Kladovasilakis, K. Tsongas, and D. Tzetzis, "Finite element analysis of orthopedic hip implant with functionally graded bioinspired lattice structures," *Biomimetics*, vol. 5, no. 3, p. 44, 2020. doi: 10.3390/BIOMIMETICS5030044.

[37] Z. Guoqing, L. Junxin, Z. Chengguang, X. Juanjuan, Z. Xiaoyu, and W. Anmin, "Design Optimization and Manufacturing of Bio-fixed tibial implants using 3D printing technology," *Journal of the Mechanical Behavior of Biomedical Material*, vol. 117, p. 104415, 2021. doi: 10.1016/j.jmbbm.2021.104415.

[38] O. Al-Ketan, R. Rezgui, R. Rowshan, H. Du, N. X. Fang, and R. K. Abu Al-Rub, "Microarchitected Stretching-Dominated Mechanical Metamaterials with Minimal Surface Topologies," *Advanced Engineering Materials*, vol. 20, no. 9, p. 1800029, 2018.

[39] Z. Izri, A. Bijanzad, S. Torabnia, and I. Lazoglu, "In silico evaluation of lattice designs for additively manufactured total hip implants," *Computers in Biology and Medicine*, vol. 144, p. 105353, 2022. doi: 10.1016/j.compbiomed.2022.105353.

Improved Mechanical Properties of Basalt and Glass Fibre Reinforced Polymer Composite by Incorporating Nano Silica

Mohamad Asrofi Muslim, Aidah Jumahat[*]*, Shahrul Azam Abdullah, Fauziah Md Yusof, M.Z. Zahari*
School of Mechanical Engineering, College of Engineering, Universiti Teknologi MARA, Shah Alam, Selangor, MALAYSIA
[*]*aidahjumahat@uitm.edu.my*

Mochamad Chalid
Department of Metallurgical and Material Engineering, Faculty of Engineering, Kampus Baru UI, Universitas Indonesia, Depok, INDONESIA

Mohd Azrul Jaafar
Centre for Instructor and Advanced Skill Training, Department of Skills Development, Ministry of Human Resources, Jalan Petani 19/1, Section 19, Shah Alam, Selangor, MALAYSIA

Raymond Siew Teng Loy
Carbon Tech Global Sdn Bhd, PT-1361, Jalan Kesidang 5, Kampung Mohd Taib, Kawasan Industri, Kampung Sungai Choh, 48000 Rawang, Selangor, MALAYSIA

ABSTRACT

Granite waste that increasingly accumulates yearly is significant with granite industry growth. This research aims to use nano silica extracted from granite dust to identify the effect of nano silica on the mechanical properties of Basalt and Glass Fibre Reinforced Polymer Composite. The approach encompassed three distinct weight percentages of nano silica, specifically 1 wt%, 3 wt%, and 5 wt%, seamlessly blended into a polyester resin matrix. The evaluation of composite mechanical attributes was conducted through compression and Izod impact tests by following ASTM D3410 and ASTM D256. Remarkably, the pinnacle of this enhancement materialises at the 1 wt% threshold,

ISSN 1823-5514, eISSN 2550-164X
Received for review: 2023-08-15
Accepted for publication: 2023-10-31
Published: 2023-11-15

https://doi.org/10.24191/jmeche.v12i1.24644

signifying the impact strength and compression strength values. Beyond this point, a decline was observed, underscoring the critical importance of judicious weight percentage selection. This novel composite configuration holds promising implications, particularly for components within container trucks, where the fusion of exceptional impact and compression strength is paramount.

Keywords: *Vacuum Silicon Mould; Nano Silica; Polyester, Basalt Fibre; Glass Fibre*

Introduction

Basalt fibre is made from natural basalt rock, which is abundant and does not require energy-intensive processing like glass or carbon fibre. The awareness and adoption of basalt fibre in various industries are still relatively low compared to more established materials like fibreglass and carbon fibre. Basalt fibre has several advantages, including high strength, durability, and resistance to high temperatures and chemicals [1]-[2]. However, its adoption may be limited by higher costs and processing challenges. Its suitability for a particular application depends on the specific requirements and budget constraints.

Granite waste is generated during the quarrying, cutting, and processing of granite stone. It comprises various types of waste, including sawdust, sludge, and leftover stone blocks. The extraction and processing of granite can have environmental consequences, such as habitat disruption, soil erosion, and water pollution [3]-[5]. Managing granite waste is critical to mitigate these impacts. However, there are opportunities to reduce its environmental footprint by recycling and reusing the waste in various applications.

Nano silica particles are microscopic, typically in the nanometer range, which results in a high surface area. This property can enhance their reactivity and effectiveness in various applications. Nano silica is used as a reinforcement filler in polymer composites, concrete, and rubber, which enhances its mechanical properties and durability. When incorporated into materials, nano silica can significantly enhance their strength, stiffness, and abrasion resistance [6]-[9]. Nano silica offers many advantages in terms of enhancing material properties and enabling various applications, but it also raises concerns related to cost, health, and environmental impact.

Nano silica, when properly dispersed and integrated into composite materials, has shown the potential to enhance impact resistance. Its high surface area and compatibility with various matrices can improve the material's ability to absorb and dissipate impact energy. Nano silica can enhance the compression strength of composites by reinforcing the matrix material, thereby reducing the risk of compressive failure. Incorporating nano silica can significantly improve composites' mechanical properties, including increased

strength, stiffness, and toughness [10]-[12]. Nano silica is lightweight, and its addition to composites can enhance its performance without adding excessive weight, making it attractive for applications where weight is critical. Achieving uniform dispersion of nano silica within the composite matrix can be challenging. Agglomeration or poor dispersion can lead to inconsistent performance [6], [13]. The optimal loading level of nano silica depends on the specific application and desired performance characteristics. Higher loading levels may improve mechanical properties but could also lead to processing difficulties.

In conclusion, nano silica can be an adequate filler in composite materials for impact and compression applications, offering improved mechanical properties and durability. However, dispersion, cost, and processing complexity challenges should be carefully considered. The success of using nano silica in composites depends on factors such as surface treatment, loading level, and thorough testing to ensure that the desired performance improvements are achieved.

Materials and Methodology

Materials

Composite materials were produced by incorporating varying amounts of nano silica, woven glass fibre, woven basalt fibre, and polyester resin as the matrix material. The polyester used, known as CRYSTIC® 272E Isophthalic Polyester Resin, is a low-viscosity organic-mineral resin, and it was supplied by Carbon Tech. Global Sdn. Bhd., located in Rawang, Selangor. The resin and Butanox M60 hardener were combined in a 100:2 ratio to create the resin mixture. The woven basalt fibres were sourced from Zhejiang GBF Basalt Fibre Co. Ltd. in Dongyang, China, while the woven glass fibres were provided by Vistec Technology in Puchong, Malaysia. The nano silica was extracted from granite fine powder and obtained from the Kelantan Branch of Jabatan Kerja Raya (JKR), Malaysia.

Methodology

The fabrication began with cutting and measuring the desired thickness for the woven glass and basalt fiber. Subsequently, these fibers were systematically stacked layer upon layer. The polyester resin was then combined with the nano silica, with the proportions determined by weight percentage. In addition, four different percentages on nano silica weight percents, 0 wt%, 1 wt%, 3 wt%, and 5 wt%, were added to determine the most effective modified resin within basalt and glass fiber-reinforced polymer composites. To achieve a homogeneous mixture, a mechanical stirrer was employed, stirring at a rate of around 400 rotations per minute for approximately 120 minutes. As the supplier recommended, the polyester resin was blended with a hardener in a

100:2 weight ratio to ensure thorough composite curing. The resulting resin, filler, and hardener mixture was poured onto the fiber layers. This resin application was conducted layer-by-layer, ensuring a comprehensive saturation of the fibers. Once the resin had been applied, the specimen was sealed within a silicon mold. A vacuum was utilized to eliminate any trapped air within the specimen, thus ensuring a complete consolidation of the composite. Following this step, the sealed FRP (Fiber Reinforced Polymer) specimen was removed from the mold and left to cure naturally at room temperature for an approximate duration of 8 hours. During this period, a chemical reaction occurred within the resin, causing it to harden and ultimately resulting in the formation of a solid composite structure.

Izod impact test

The Izod impact test is a recognised norm that quantifies the impact energy required to fracture a material. This test assists engineers and scientists in evaluating the fracture properties of a given component or element. The results were used to determine how various materials responded to impact loading. The dimensions of sample 64 x 13 x 2.5 mm were prepared. Five identical samples with the exact measurement were used for each test. The test was conducted following the ASTM D256 standard. Figure 1 shows the machine involved during the test.

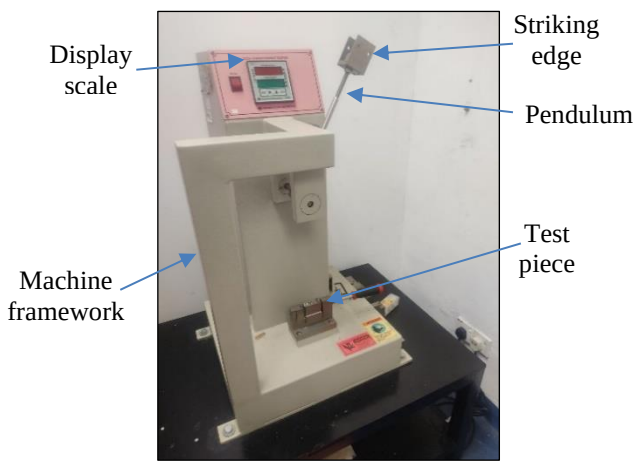

Figure 1: Izod Charpy machine used in this experiment

Compression test

The compressive test was performed according to ASTM D3410. The compressive properties were determined through compression experiments. The 110 x 10 x 2.5 mm sample was restrained in unique frames to prevent FRP

composite samples from buckling. Each test used five identical samples following the standard ASTM D3410. Figure 2 shows how the compression test is performed.

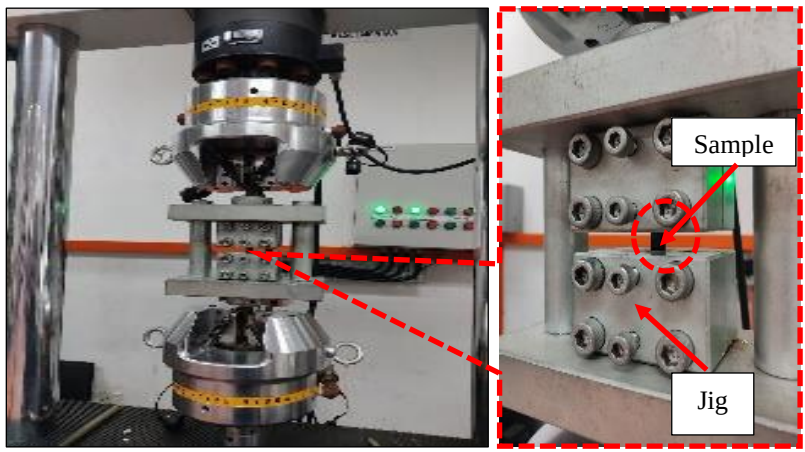

Figure 2: Compression testing

Results and Discussion

The results derived in this investigation correspond to the average values obtained by examining five distinct samples for each composite laminate category. The observed variation in the sample pertains to the weight percentage of nano silica incorporated into the resin before the pouring phase in the hand lay-up manufacturing procedure. The laminates investigated in the study consisted of basalt fibre-reinforced polymer composite (BFRPC) and glass fibre-reinforced polymer composite (GFRPC).

Effect of nano silica on impact test of BFRPC and GFRPC

Analysing Figure 3 reveals a distinct trend for BFRPC and GFRPC in impact strength, as nano silica weight percentages are varied within the composite. Commencing at 0 wt% nano silica BFRPC, we note an impact strength of 3232 Jm^{-1}. As the nano silica content increases to 1 wt%, the impact strength experiences a notable surge, ascending to 4464 Jm^{-1}. However, the subsequent transition to 3 wt% nano silica leads to a decline in impact strength to 3680 Jm^{-1}. This downward trajectory persists at 5 wt% nano silica, with impact strength further falling to 3360 Jm^{-1}.

This sequence underscores an apparent pattern: impact strength augmentation up to 1 wt% nano silica, succeeded by a diminishing trend at 3

wt% and 5 wt%. This distinctive behaviour can be attributed to the agglomeration phenomenon observed with nano silica [7]-[8]. The expansive surface area of nano silica particles makes them prone to clustering, especially at elevated concentrations. In this context, the agglomeration effect becomes discernible at 3 wt% and 5 wt%, leading to a decrease in impact strength. This outcome aligns with experimental findings wherein the optimal impact strength, evidenced by the peak at 1 wt% nano silica, reflects the delicate balance between nano silica dispersion and agglomeration effects [14]-[15].

In summary, the impact strength's interplay with nano silica weight percentages reveals a clear trend of enhancement up to 1 wt% and subsequent decline at 3 wt% and 5 wt%, attributable to nano silica's inclination to aggregate. This investigation underscores the significance of precise nano silica dispersion control in optimising composite properties [10], [16].

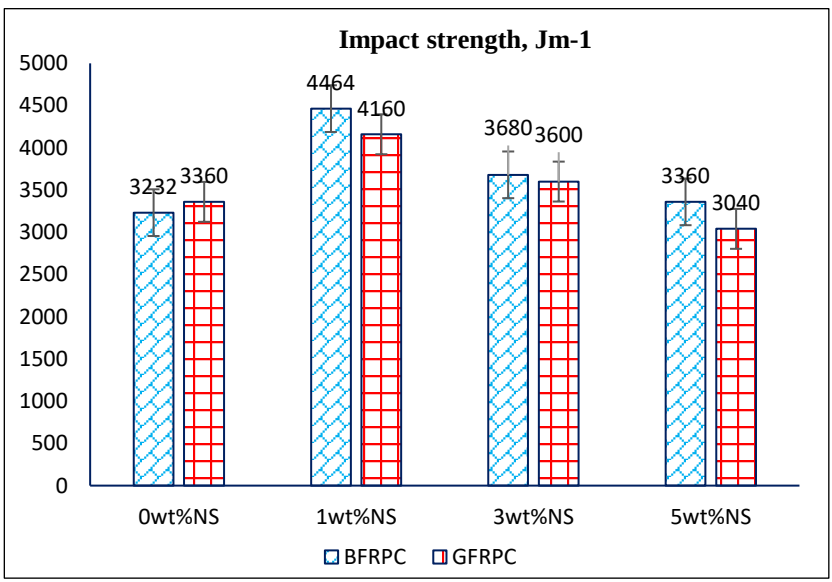

Figure 3: BFRPC and GFRPC impact strength vs. different wt% of nano silica

Meanwhile, for GFRPC, we can see from Figure 3 that a distinct trend emerges in impact strength variations across diverse nano silica weight percentages within the composite. Initiating at 0 wt% nano silica, the impact strength registers at 3360 Jm^{-1}. As the nano silica content advances to 1 wt%, a significant increase is observed, elevating the impact strength to 4160 Jm^{-1}. Subsequently, the transition to 3 wt% nano silica reduces the impact strength

to 3600 Jm^{-1}, with the descending trajectory persisting at 5 wt% nano silica, leading to a further decline of 3040 Jm^{-1}.

This progression underscores a clear pattern: an initial augmentation of impact strength up to 1 wt% nano silica, succeeded by a decrement at 3 wt% and 5 wt%. This pattern aligns with observations across both composite types. Initially, nano silica's integration positively affects impact strength, a phenomenon witnessed from 0 wt% to 1 wt%. However, a converse trend emerges as impact strength wanes at elevated nano silica concentrations (3 wt% and 5 wt%) [17]-[18].

This intriguing behaviour stems from the inherent characteristics of nano silica. As nano silica is incorporated, a propensity for agglomeration emerges, particularly prominent at 3 wt% and 5 wt% due to the expansive surface area of nano silica particles [19]-[20]. Following the outcomes, this agglomeration effect is particularly prominent in this experiment at 1 wt% nano silica.

In summary, Figure 3 unravels a consistent trend wherein impact strength ascends until it reaches 1 wt% nano silica, then tapers off at 3 wt% and 5 wt%. The underlying mechanism attributed to nano silica agglomeration underscores judicious dispersion management's importance in optimising composite characteristics [21]-[22].

Generally, at each corresponding weight percentage of nano silica, NS-BFRPC tends to have slightly higher impact strength values than NS-GFRPC. Adding nano silica might positively impact the impact strength of the Basalt Fiber-Reinforced Polymer Composite. There is an optimal nano silica percentage that yields the highest impact strength for each composite type. For NS-BFRPC, the optimal percentage might be around 1 wt%, and for NS-GFRPC, it could be around 1 wt% to 3 wt% [23]-[24].

Effect of nano silica on compression test of BFRPC and GFRPC

Based on Figure 4, the compressive strength of the BFRPC composite with 0 wt% nano silica is 125.76 MPa. For the BFRPC composite with 1 wt% nano silica, the compressive strength increases to 153.88 MPa. The compressive strength for the BFRPC composite with 3 wt% nano silica is 128.97 MPa. For the BFRPC composite with 5 wt% nano silica, the compressive strength decreases to 106.21 MPa. The data show a trend where the compressive strength initially increases from 0 wt% to 1 wt% nano silica and decreases as the nano silica content rises [25]-[26].

In summary, these results indicate that adding nano silica to the Basalt Fiber-Reinforced Polymer Composite has varying effects on its mechanical properties. Compressive strength and modulus show initial improvements at 1 wt% nano silica but decline as nano silica content increases [27]. The strain at fracture generally increases with higher nano silica content, except at 5 wt%. This complex relationship between nano silica content and mechanical

properties underscores the importance of carefully optimising composite formulations for the desired performance characteristics.

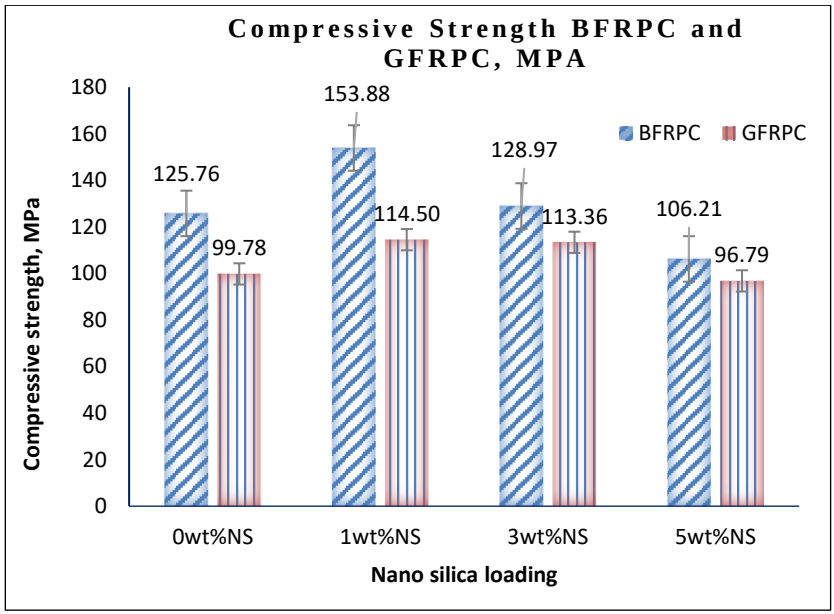

Figure 4: Compression strength of BFRPC vs. wt% of nano silica

Examining Figure 2 gives us a comprehensive grasp of the mechanical dynamics within composites, navigating the spectrum of varying nano silica weight percentages. A deeper analysis is warranted.

For the GFRPC composite with 0 wt% nano silica, the compressive strength is 99.78 MPa. Transitioning to 1 wt% nano silica introduces a remarkable surge, elevating the compressive strength to 114.50 MPa. The subsequent exploration of 3wt% nano silica content reveals a compressive strength of 113.36 MPa. As we venture further to 5 wt% nano silica, the compressive strength regresses to 96.79 MPa. This trajectory mirrors the observed pattern, affirming the correlation between nano silica content and compressive strength. The initial summit from 0 wt% to 1wt% nano silica harmonises with prior findings, while the ascent tapers fluctuate at higher nano silica proportions [18].

In synthesis, the mechanical property data for nano silica-glass Fiber-Reinforced Polymer Composite (NS-GFRPC) retraces the trends evident in prior instances. The compressive strength and modulus variances tied to nano silica content remain consistent, while strain at fracture escalates until a threshold and diminishes beyond [23], [28]. These patterns underscore the

pronounced influence of nano silica on composite performance and the indispensability of refined composite formulations in attaining the desired mechanical attributes [17].

Conclusions

Following a meticulous analysis of the mechanical test data, it is evident that among the array of eight distinct FRP composite systems distinguished by varying weight percentages of nano silica, the composite system featuring 1 wt% of both Basalt Fiber-Reinforced Polymer Composite (BFPRC) and Glass Fiber-Reinforced Polymer Composite (GFRPC) emerges as the frontrunner in terms of compression properties, outshining the remaining systems. This finding underscores a crucial principle: the influence of nano silica in enhancing mechanical properties follows an apparent pattern wherein improvements are notable until a certain threshold, beyond which these enhancements taper.

The rationale underlying this phenomenon can be attributed to the inherent characteristics of nano silica itself. With its expansively broad surface area, nano silica's propensity to enhance mechanical properties reaches an apex, beyond which it starts to exhibit signs of compression affiliated with crumpling. In this experimental context, the pivotal juncture is notably marked at the 1 wt% concentration level. Consequently, a coherent conclusion emerges - integrating nano silica can significantly elevate composites' mechanical attributes, encompassing impact strength and compression strength, up to a specific weight percentage threshold. Simultaneously, integrating nano silica presents a supplementary advantage - the reduction of granite waste, a burgeoning concern, as it is seamlessly incorporated into the composite fabrication process, thereby aiding in curbing the accumulation of daily produced waste.

Contributions of Authors

The authors confirm the equal contribution in each part of this work. All authors reviewed and approved the final version of this work.

Funding

This research work is financially supported by the KEPU Grant no: 600-RMC/KEPU 5/3 (016/2021) and the DINAMIK Grant.

Conflict of Interests

All authors declare that they have no conflicts of interest.

Acknowledgement

The authors thank Universiti Teknologi MARA (UiTM) and Carbon Tech Global Sdn.Bhd. for the research support.

References

[1] Vikas G and Sudheer M, "A review on properties of basalt fiber reinforced polymer composites," *American Journal of Materials Science*, vol. 2017, no. 5, pp. 156–165, 2017. doi: 10.5923/j.materials.20170705.07.

[2] B. Suresha, D. Sachin, and C. B. Shiddalingesha, "Morphology and physico-mechanical properties of basalt fiber reinforced composites," *Materials Today: Proceedings*, vol. 46, no. 18, pp. 9067–9072, 2021. doi: 10.1016/j.matpr.2021.05.389.

[3] S. K. Nayak, A. Satapathy, and S. Mantry, "Use of waste marble and granite dust in structural applications: A review," *Journal of Building Engineering*, vol. 46, p.103742, 2021. doi: 10.1016/j.jobe.2021.103742.

[4] L. Gautam, J. K. Jain, P. Kalla, and M. Danish, "Sustainable utilisation of granite waste in the production of green construction products: A review," *Materials Today: Proceedings*, vol. 44, no. 6, pp. 4196–4203, 2020. doi: 10.1016/j.matpr.2020.10.532.

[5] R. Chaturvedi, A.Pappu, P. Tyagi, R. Patidar, A. Khan, A. Mishra, M. K. Gupta, and V. K. Thakur, "Next-generation high-performance sustainable hybrid composite materials from silica-rich granite waste particulates and jute textile fibres in epoxy resin," *Industrial Crops and Products*, vol. 177, 2022. doi: 10.1016/j.indcrop.2022.114527.

[6] A. Fathy, A. Shaker, M. A. Hamid, and A. A. Megahed, "The effects of nano-silica/nano-alumina on fatigue behavior of glass fiber-reinforced epoxy composites," *Journal of Composite Materials*, vol. 51, no. 12, pp. 1667–1679, 2017. doi: 10.1177/0021998316661870.

[7] D. Kaka, R. A. Fatah, P. Gharib, and A. Mustafa, "Mechanical properties of polyester toughened with nano-silica," *Iraqi Journal of Industrial Research*, vol. 8, no. 3, pp.61-68, 2021. doi: 10.53523/ijoirvol8i3id67.

[8] A. Bediwy and E. F. El-Salakawy, "Mechanical properties of hybrid structures incorporating nano-silica and basalt fiber pellets," *CivilEng*, vol. 2, no. 4, pp. 909–928, 2021. doi: 10.3390/civileng2040049.

[9] Raed Hwayyin, S.K. Hussien, and A.S. Ameed, "The effect of nano-silica on the mechanical properties of composite polyester / carbon fibers," *Journal of Mechanical Engineering and Sciences*, vol. 16, no. 4, pp. 9175-9186, 2022. doi: 10.15282/jmes.16.4.2022.03.0727.

[10] R. H. Abdel-Rahim, M. S. Attallah, and R. A. Mohammed, "Investigation the effect of nano silica dioxide additives on the properties of epoxy resin for using in industrial applications," *Materials Science Forum*, vol. 1050, pp. 103–113, 2022. doi: 10.4028/www.scientific.net/MSF.1050.103.

[11] R. N. Raja Othman, D. K. Subramaniam, N. Ezani, M. F. Abdullah, and K. Z. Ku Ahmad, "The synergistic effects of hybrid micro and nano silica in influencing the mechanical properties of epoxy composites—A new model," *Polymers*, vol. 14, no. 19, p.3969, 2022. doi: 10.3390/polym14193969.

[12] P. S. Krishna Kumar and B. Navin Kumar, "Improvement of impact strength of novel intra-ply basalt/kevlar composite by addition of silica nanoparticles in comparison with basalt/kevlar composite using resin transfer mould process," *Materials Today: Proceedings*, vol. 69, no. 3, pp. 843–847, 2022. doi: 10.1016/j.matpr.2022.07.272.

[13] Y. Q. Wang, Y. Guo, R. X. Cui, Z. M. Wang, and Y. L. Wu, "Preparation and mechanical properties of nano-silica/UPR polymer composite," *Science and Engineering of Composite Materials*, vol. 21, no. 4, pp. 471–477, 2014. doi: 10.1515/secm-2013-0051.

[14] M. Tabish, M. M. Zaheer, and A. Baqi, "Effect of nano-silica on mechanical, microstructural and durability properties of cement-based materials: A review," *Journal of Building Engineering*, vol. 65, no. 4, p.105676, 2023. doi: 10.1016/j.jobe.2022.105676.

[15] T. Hao, Y. Wang, Z. Liu, J. Li, L. Shan, W. Wang, J. Liu, and J. Tang, "Emerging applications of silica nanoparticles as multifunctional modifiers for high performance polyester composites," *Nanomaterials*, vol. 11, no. 11. p.2810, 2021. doi: 10.3390/nano11112810.

[16] S. Younis, J. Oleiwi, and R. Mohammed, "Some mechanical properties of polymer matrix composites reinforced by nano silica particles and glass fibers," *Engineering and Technology Journal*, vol. 36, no. 12A, pp. 1283–1289, 2018. doi: 10.30684/etj.36.12a.10.

[17] L. d. R. S. Carneiro, M. Houmard, V. V. Rocha, and P. Ludvig, "The effect of nanosilica incorporation on the properties of cement-based materials with and without other supplementary admixtures – A literature review," *The Open Construction and Building Technology Journal*, vol. 16, no. 1, pp.1-11, 2022. doi: 10.2174/18748368-v16-e2207290.

[18] M. Ponnusamy, L. Natrayan, S. Kaliappan, G. Velmurugan, and S. Thanappan, "Effectiveness of nanosilica on enhancing the mechanical and microstructure properties of kenaf/carbon fiber-reinforced epoxy-based nanocomposites," *Adsorption Science and Technology*, vol. 2022, no. 1, pp.1-10, 2022. doi: 10.1155/2022/4268314.

[19] S. Sprenger, "Nanosilica-toughened epoxy resins," *Polymers*, vol. 12, no. 8. p.1777, 2020. doi: 10.3390/polym12081777.

[20] P. K. Oja, and A. Nanosiliko, "Nanosilica-reinforced polymer composites," *Material in Technologies*, vol. 47, no. 3, pp. 285-293, 2013. http://mail.imt.si/izvodi/mit133/conradi.pdf

[21] V. Pang, Z. J. Thompson, G. D. Joly, L. F. Francis, and F. S. Bates, "Block copolymer and nanosilica-modified epoxy nanocomposites," *ACS Applied Polymer Materials*, vol. 3, no. 8, pp. 4156–4167, 2021. doi: 10.1021/acsapm.1c00619.

[22] P. Mondal, S. P. Shah, L. D. Marks, and J. J. Gaitero, "Comparative study of the effects of microsilica and nanosilica in concrete," *Transportation Research Record: Journal of The Transportation Research Board*, vol. 2141, no. 1, pp. 6–9, 2010. doi: 10.3141/2141-02.

[23] P. K. Gopalakrishnamurthy and C. Sandur, "Investigation of dynamic mechanical behavior of nanosilica filled carbon-kevlar-epoxy polymer hybrid nanocomposite," *Annales de Chimie: Science des Materiaux*, vol. 46, no. 3, pp. 141–146, 2022. doi: 10.18280/acsm.460305.

[24] O. Y. Bozkurt, W. Kadhim Al-Azzawi, and O. Ozbek, "The effect of nanosilica on tensile and flexural behavior of glass fiber reinforced composite laminates," *International Journal of Mechanical and Production Engineering*, vol. 5, no. 9, pp. 65-68, 2017. https://www.researchgate.net/publication/335985809

[25] S. Yang, J. Choi, and M. Cho, "Elastic stiffness and filler size effect of covalently grafted nanosilica polyimide composites: Molecular dynamics study," *ACS Applied Materials & Interfaces*, vol. 4, no. 9, pp. 4792–4799, 2012. doi: 10.1021/am301144z.

[26] A. J. Salman, Z. F. Jawad, R. J. Ghayyib, F. A. Kareem, and Z. Al-khafaji, "Verification of utilizing nanowaste (glass waste and fly ash) as an alternative to nanosilica in epoxy," *Energies*, vol. 15, no. 18, p. 6808, 18, 2022. doi: 10.3390/en15186808.

[27] N. A. Bhalla, H. Chouhan, R. K. Yadav, and N. Bhatnagar, "Exploring the effect of dispersed phase on the high strain rate mechanical response of nanosilica dispersions," *IOP Conference Series: Materials Science and Engineering*, vol. 1248, no. 1, p. 012073, 2022. doi: 10.1088/1757-899x/1248/1/012073.

[28] U. R. Hashim, A. Jumahat, and M. Jawaid, "Mechanical properties of hybrid graphene nanoplatelet-nanosilica filled unidirectional basalt fibre composites," *Nanomaterials*, vol. 11, no. 6, p.1468, 2021. doi: 10.3390/nano11061468.

Numerical Analysis of Threaded Pin Fins Heat Sink by Natural Convection

Muhammad Firdaus Hamidan, Rosnadiah Bahsan[*]*, Alhassan Salami Tijani, Irnie Azlin Zakaria*
School of Mechanical Engineering, College of Engineering, Universiti Teknologi MARA, 40450 Shah Alam, Selangor, MALAYSIA
[*]*rosnadiah@uitm.edu.my*

Sajith Thottathil Abdulrahman
Department of Mechanical Engineering, KMEA Engineering College, 683560 Edathala P.O., Cochin, INDIA

ABSTRACT

Heat sinks play a crucial role in thermal management by dissipating heat away from electronic devices and reducing the device's performance. The heat sink with pin fins will enhance the rate of convective heat transfer and improve the cooling efficiency of electronic components by increasing the surface area. This study investigates the enhancement of heat transfer rate on square threaded pin fin heat sinks with or without perforation under natural convection. The fins were arranged in inline and staggered arrangement. Four different configurations were designed by using CATIA V5 and simulated by using CFD analysis with different power inputs at 5 W, 10 W and 15 W. The simulation results were validated with the experimental results from the previous study by comparing the heat transfer coefficient of the heat sink design by natural convection. The results show that the average heat transfer coefficient of square threaded pin fins with perforations in staggered arrangement is 7.365 W/m^2.^{o}C compared to the pin fins without perforations which is 7.168 W/m^2.^{o}C. Therefore, pin fin with perforation dissipates heat at the rate of 2.75% more than pin fin without perforation. In conclusion, the square threaded pin fins with perforations in staggered arrangement have higher heat transfer performance.

Keywords: *Computational Fluid Dynamics (CFD); Heat Transfer Coefficient; Natural Convection; Nusselt Number; Square Thread Pin Fins, Perforation*

ISSN 1823-5514, eISSN 2550-164X

https://doi.org/10.24191/jmeche.v12i1.24645

Received for review: 2023-10-03
Accepted for publication: 2023-10-22
Published: 2023-11-15

Introduction

Innovation in electronic device products such as smartphones, computers and electrical appliances will evolve towards miniaturization [1]. The electronic appliances are going into miniaturization in which the size of the device will be minimised to a small dimension which means the space for the cooling system is limited. The small size of the heat sink will reduce its surface area and can reduce its efficiency in a cooling system [2]. The temperature rise in electronic devices is perpendicular to the increasing chance of malfunctioning the device [3].

Effective thermal management in electronic devices is vital for maximising the performance, dependability, and lifespan, especially for high-performance devices such as gaming laptops, which consume a very high amount of electricity due to the large amount of data processed by the computer at a times causing greater heat generation. As technology progresses, the demand for innovative thermal management solutions grows. Inefficient heat transfer by the heat sink may cause a large thermal concentration within the body, which may cause the electronic devices to degrade [4]. Advancements and improvements are required in the field of cooling systems in order to meet the requirements for heat sink efficacy.

Heat sinks play a crucial role in electronic devices by dissipating excess heat generated during the operation to the surroundings as much as possible to avoid any malfunction of the system. Convection is widely used to dissipate heat through a medium in thermal management. This is the mode of heat transfer in thermal management through the movement of a fluid caused by the differences in temperature within the fluid. This movement can occur naturally (natural convection) or be induced by external means (forced convection). Natural convection known as a passive cooling system relies solely on buoyancy forces created by the variation in fluid density [5]. Natural convection is essential for designing heat sinks that can effectively dissipate heat without the need for additional power-consuming components.

In contrast, forced convection known as an active cooling system relies on the mechanical or electrical propulsion of fluid over a solid surface by mechanical or electrical devices. Enhancing the rate of cooling by using a mechanical device like a fan can increase the electrical power consumption. Although an active cooling system is more efficient in transferring heat than a passive cooling system, it consumes more energy, produces noise and is less reliable due to external devices deteriorating over time such as fans or pumps [6]. Thus, natural convection is often preferred for its simplicity, high reliability and energy efficiency [7].

To augment heat exchange efficiency, fins are employed to increase the available surface area for heat transfer processes. Numerous studies have explored various aspects of fin array and surface texture to enhance heat transfer rate. Nada et al. [8] investigated the effects of fin geometries,

arrangements, dimensions and number of fins on heat transfer due to natural convection. The author found that as the number of fins increased, the effective thermal conductivity improved. Additional perforation on the fin surfaces also demonstrated an increase in surface area which can dissipate more heat to the surrounding. In the fluid flow characteristic, the presence of perforation or hole creates a vortex along the perforation area which then allows more mixing air [9]. Reduces of the weight of the pin fin by perforation contribute to the economic design. The higher number of perforations with a smaller perforation radius is effective in enhancing the heat dissipation rate [10]. MOORA and entropy minimization methods to predict the performance of perforation fin in an inline and staggered arrangement were used by Maji et al. [11]. The result showed that lower velocities from 4 to 6 m/s elliptical perforation on linearly arranged circular fin have a higher heat dissipation against lower pressure loss. Furthermore, obstruction in fluid flow is more in staggered fin than linear fin which causes a higher pressure drop [11].

Laad et al. [12] studied the effect of pin-fin shape on the performance of the heat sink with different shapes of fins such as rectangular, trapezoidal, circular and square. The result showed that the circular pin fins have better performance than the others. An experiment to analyse the performance of fin efficiency by using different materials showed that copper material achieves 94% efficiency in thermal conductivity better than brass and aluminium with 66% and 91% efficiency, respectively [13]. The heat transfer rate in square threaded pin fin with perforations in a staggered arrangement is higher among each other arrangements in natural convection due to obstruction, more circulation, irregularity, and zigzag positions of pin fins in the array which leads to an increase in Reynolds number and Nusselt number of airflow along the pin fin array [14].

All the heat sinks with perforated solid threaded pin fins inline have a higher rate of heat transfer capacity than the other hollow pin fins [15]. The heat transfer rate of square-threaded pin fins with perforations shows the highest rate due to the obstruction in the arrangement of pin fins [16]. Despite these advancements, there exists a notable research gap when it comes to exploring alterations in surface texture such as threading and in the context of thermal management. While fin geometries have been extensively studied, there is limited research on modifying the surface with thread, perforation or additional surface coating [17]. These alterations could potentially offer innovative solutions for enhancing heat dissipation in miniaturized electronic devices. Threaded pin fins represent a specialized design variation of traditional heat sink fins. These fins are characterized by their unique geometry, featuring helical threads that spiral around the fin's central axis. The introduction of threaded pin fins disrupts the thermal boundary layer near the surface of the fin, leading to improved convective heat transfer. This disruption

enhances fluid mixing, increases heat exchange surface area, and reduces thermal resistance, resulting in more efficient heat dissipation.

Therefore, the purpose of this project is to investigate the enhancement of thermal performance through square threaded pin fins with and without perforation of the heat sink with variations of arrangement under natural convection conditions. All heat sink models were simulated using CFD Ansys to observe the flow fields and heat sink performance. Thermal characteristics of the heat sink such as Nusselt number, Rayleigh number, Prandtl number and heat transfer coefficient were analysed.

Methodology

Design specification

Threaded pin fins heat sinks were designed using SOLIDWORKS software. Figures 1 and 2 show the square threaded pin fin heat sink without perforation in inline and staggered arrangement. Figures 3 and 4 show the square threaded pin fin heat sink with perforation dimensions. The arrangements of the pin fin were in inline and staggered form. The cross-sectional area for the base plate was 250 mm in length, 125 mm in width and a thickness of 5 mm [16].

Table 1 shows the detailed specification dimensions of the geometry for each heat sink model. Figures 5 and 6 show the detailed dimensions of inline and staggered pattern heat sink. Aluminium was chosen as the material for the pin fins due to its cost effectiveness [18], ease of machining, corrosion-resistant and good thermal conductivity [19]. These characteristics make aluminium a suitable material for heat sink applications.

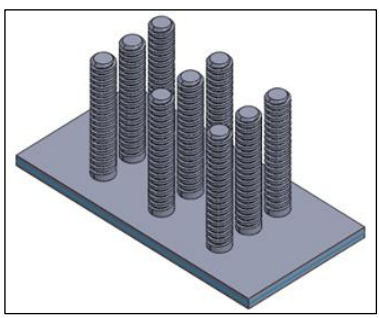

Figure 1: Square threaded pin fin without perforation in inline arrangement

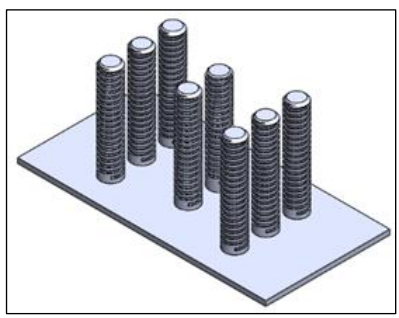

Figure 2: Square threaded pin fin without perforation in a staggered arrangement

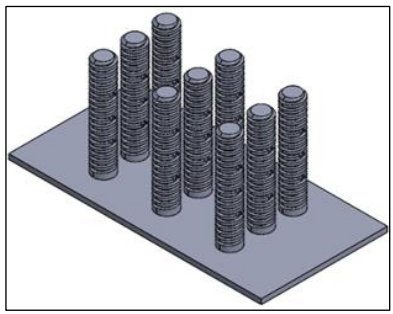

Figure 3: Square threaded pin fin with perforation in inline arrangement

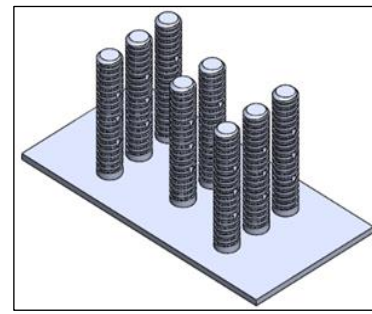

Figure 4: Square threaded pin fin with perforation in a staggered arrangement

Table 1: Dimension for the geometry of the heat sink model

Type of pin fins	Inline	Inline pattern	Staggered	Staggered
Base plate, (mm)		250 x 125 x 5		
Pin height (mm)	100	100	100	100
Pin outer	20	20	20	20
Pin inner	15	15	15	15
Pitch (mm)	5	5	5	5
Number of pins	9	9	8	8
Number of	-	27	-	27

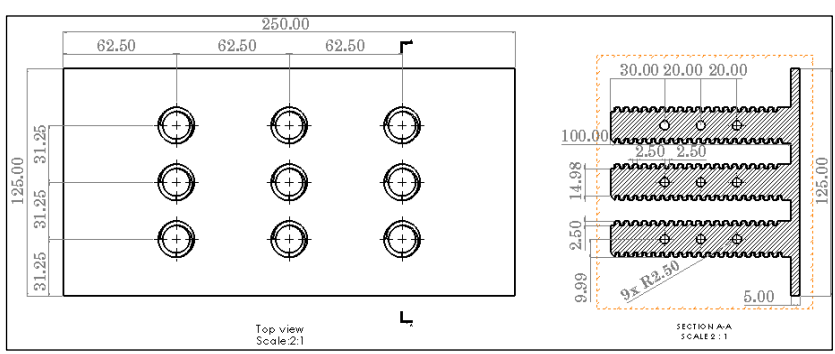

Figure 5: Dimension of pin fins in inline pattern

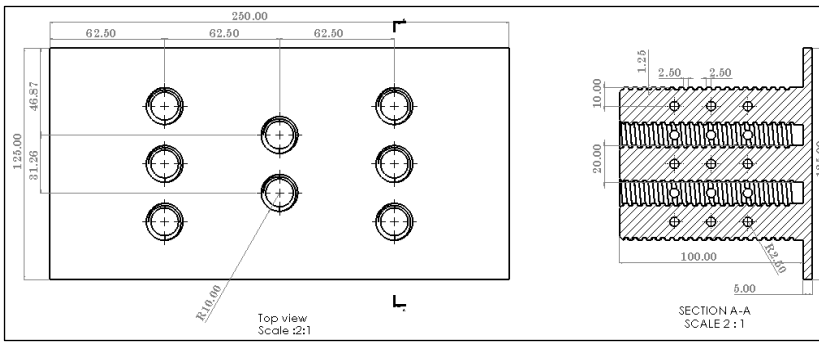

Figure 6: Dimension of pin fins heat sink in a staggered array

CFD analysis

In this project, steady-state conditions and heat transfer distribution on the heat sink were simulated using the CFD tool of Ansys CFX 2023. The computational domain of the heat sink models was simulated under natural convection conditions in which hot fluid at the bottom of the heat sink was raised and cold air came in the places of hot air. The direction of fluid flow in natural convection was raised against gravitational force. The size of the domain was 300 x 300 x 300 mm. Figure 7 shows the heat sink in the domain.

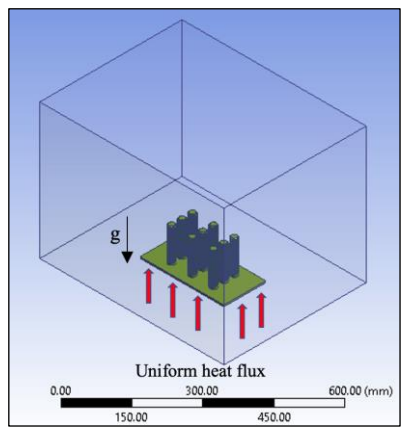

Figure 7: Heat sink in the domain

Simulation setup and boundary conditions

The modelling of CFD simulation and post-processor was carried out in the ANSYS 2023 R1 workbench using the aid of CFX. Based on a previous study on natural convection, [20] described that ANSYS CFX has the capability of

solving the convective transport of energy by fluid flow and solving thermal conduction in solids. Table 2 shows the overall boundary condition used in this project.

Table 2: Summary of boundary conditions

Physical condition	
Fluid	Steady and incompressible air
Fluid volume (L x W x H)	0.3 x 0.3 x 0.3 m
Fin and base heat sink material	Aluminium
Thermal boundary condition	
Air temperature	25 ℃
Air pressure	1 atm
Heat flux	480 W/m^2
Computational elements	
Element type	Tetrahedron
Number of elements	3 M elements
Solution model	
Turbulence models	Laminar
Analysis type	Steady state

In this analysis, the enclosure was modelled as a fluid domain and the heat sink was modelled as a solid domain with a supply of heat source from 5 W to 15 W. The analysis was conducted at an atmospheric temperature of 298 K. Boundary conditions were applied as follows:

- Domain interface - The interface between solid fin surface and fluid
- Basic setting - “fluid-solid” interface
- Activated buoyancy in Y-direction, -9.81 m/s^2
- Opening - all sides of fluid domain except bottom face
- The bottom face of the fluid domain is set for adiabatic
- The base of the heat sink is set as heat flux.

The whole geometry model was discretized into finite volumes of tetrahedral mesh using suitable mesh. Figures 8 to 11 show the details of the mesh geometry of the heat sink.

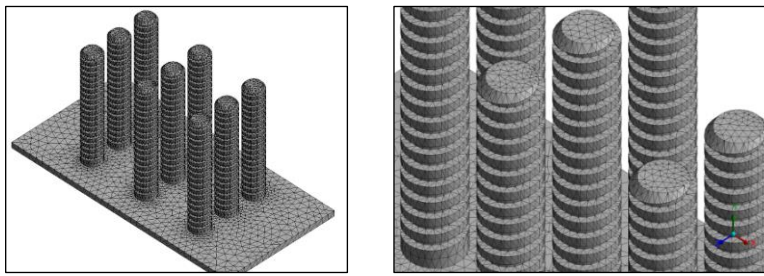

Figure 8: Meshing view of square threaded pin fin without perforation in inline arrangement

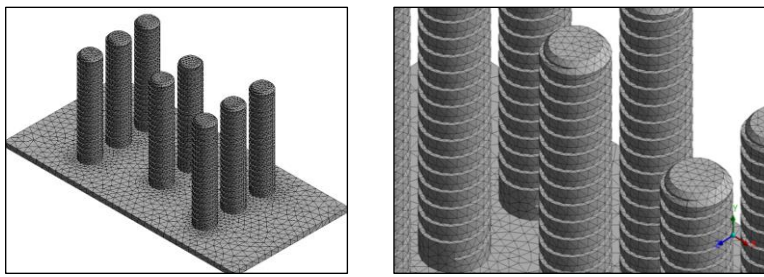

Figure 9: Meshing view of square threaded pin fin without perforation in a staggered arrangement

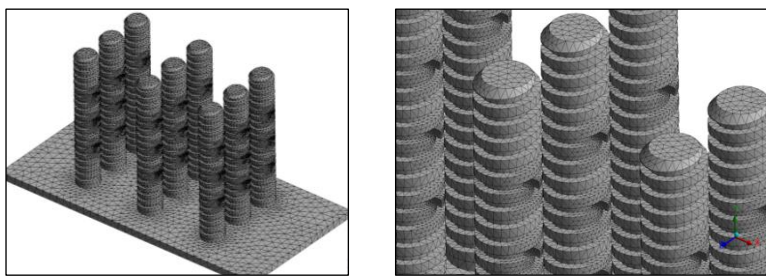

Figure 10: Meshing view of square threaded pin fin with perforation in inline arrangement

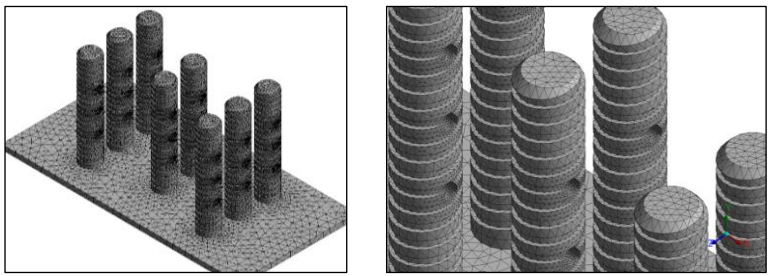

Figure 11: Meshing view of square threaded pin fin with perforation in a staggered arrangement

Grid independent test

The grid independence test was carried out to determine the appropriate number and size of the elements in the simulation of this project. In this project, the size of elements was varied by decreasing the element size while keeping other simulation parameters constant. The test was carried out on a square threaded pin fin without perforation in inline arrangement with a heat flux at 15 W. Based on Table 3, the geometry of the domain was meshed using tetrahedral mesh algorithms after selecting the targeted physical parts to investigate heat transfer phenomena. The whole computational domain was tested with a different number of mesh element sizes ranging from 10 mm to 20 mm, then the average temperature value was plotted to check the acceptable grid size used as shown in Figure 12. The element size of 10 mm gave the highest number of elements with 4 514 282 which consumed very high time of the computational process. Since the difference in base temperature was not significant between mesh elements of 18, 16 and 13, the element size chosen was 13 mm because finer element size can increase the accuracy of results with better mesh quality.

Table 3: Summary of mesh independent test

Element size (mm)	Mesh elements	Base temperature (K)	Fin temperature (K)
20	2155645	364.3123	362.6670
18	3014229	364.5981	362.9528
16	3225512	364.5688	362.9235
13	3677634	364.5597	362.9144
10	4514282	364.6497	363.0056

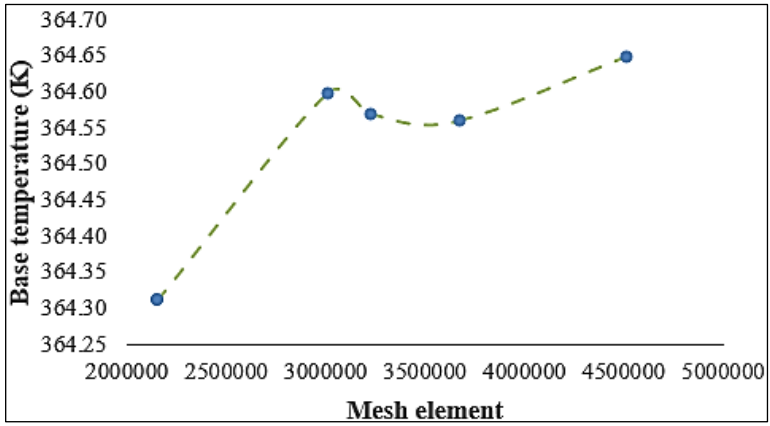

Figure 12: Mesh sensitivity analysis of grid independence test

Governing equations

The governing differential equation for steady-state condition, laminar flow, constant property, and the three-dimensional flow with the incompressible ideal gas assumption is given by [21].
Continuity equation:

$$\frac{\partial u}{\partial x}+\frac{\partial v}{\partial y}+\frac{\partial w}{\partial z}=0 \tag{1}$$

Momentum equation:

$$\rho\left(U\frac{\partial U}{\partial x}+v\frac{\partial U}{\partial y}+w\frac{\partial U}{\partial z}\right)=\frac{\partial p}{\partial x}+u(\nabla^2 U) \tag{2}$$

$$\rho\left(u\frac{\partial v}{\partial x}+v\frac{\partial v}{\partial y}+w\frac{\partial v}{\partial z}\right)=-\frac{\partial p}{\partial y}+u(\nabla^2 v)-\rho g \tag{3}$$

$$\rho\left(u\frac{\partial w}{\partial x}+v\frac{\partial w}{\partial y}+w\frac{\partial w}{\partial z}\right)=-\frac{\partial p}{\partial y}+u(\nabla^2 w) \tag{4}$$

Energy equation:

$$u\frac{\partial T}{\partial x}+v\frac{\partial T}{\partial y}+w\frac{\partial T}{\partial z}=\alpha(\nabla^2 v) \tag{5}$$

At the pressure and temperature of the surroundings $P = P_{atm}$, $T = T_{\infty}$. The energy equation for conduction in solid $\nabla^2 T = 0$.

An assumption on the working fluid is air with incompressible ideal gas and properties of the fluid are measured at film temperature $T_{film} = (T_w + T_{\infty})/2$ where the T_w is ambient temperature, and T_{∞} is the average surface temperature on the heat sink. Therefore, the result can be represented using the following non-dimensional parameters. Grashoff's Number is the ratio of buoyancy force to the viscous force acting in the fluid layer. The Grashoff number has the same importance in free convection as the Reynolds number in force convection to find the type of flow either laminar or transition turbulent in free convection [19]. The Grashoff number can be calculated as:

$$G_r = \frac{g \times \beta \times \Delta T \times z^3}{v^2} \tag{6}$$

where g is the acceleration due to the earth's gravity, z is the vertical length, β is the coefficient of thermal expansion, ΔT is the temperature difference and v is the kinematic viscosity For gases $\beta = 1/T$ where the temperature is in Kelvin. The Prandtl number is defined as the ratio of kinematic viscosity to thermal diffusivity. The Nusselt number is used to define the ratio of heat transfer by convection to the heat transfer by conduction within a fluid. Meanwhile, for natural convection, the equation for the Nusselt number can be calculated in the form of the Grashoff number and Prandtl number as,

$$Nu = 0.59(GrPr)^{0.25} \tag{7}$$

The heat transfer coefficient can be calculated as [20]:

$$h = \frac{N_u \times k}{z} \tag{8}$$

where Nu is Nusselt number, k is thermal conductivity and z is vertical height.

Results and Discussion

Validation of simulation with experimental data from literature

Validation results of simulation are vital to ensure the accuracy and reliability of the simulation model against established data published in the literature. In this project, the heat sink simulation was validated against experimental data [16], which used a similar geometrical configuration and the same operating conditions. The detailed physical geometrical configuration of this study can be found in Table 1. The same geometry was adopted for simulation and tested

with a heat source of 15 W. Heat transfer coefficient was the main parameter for testing the validity of the simulation with experimental work using Equation (8). Table 4 shows the result for the heat transfer coefficient for both simulation and experimental.

Table 4: Validation result of heat transfer coefficient for pin fins in an inline and staggered array

Heat transfer coefficient, h (W/m^2K)	Square threaded pin fin in inline pattern	Square threaded pin fin with perforation in inline pattern	Square threaded pin fin in staggered pattern	Square threaded pin fin with perforation in staggered pattern
Simulation	7.38	7.24	7.27	7.46
Experiment [16]	7.32	7.46	7.65	7.83

Based on the result, validation of the heat transfer coefficient for numerical simulation and experimental results shows a good agreement in which the value is nearly the same. The percentage difference between numerical simulation and experiment results can be calculated using Mean absolute percentage error (MAPE). The MAPE formula is expressed as below:

$$MAPE = \frac{100}{N} \times \sum_{i=1}^{N} \left| \frac{x_i - \hat{x}_i}{x_i} \right| \quad (9)$$

where n, x_i and $\hat{x}_i$ are the total numbers of value, simulation, and experimental values of the study respectively. Based on Table 5, the percentage errors are consistently less than 6%, therefore the present model is acceptable to predict the heat transfer coefficient of the heat sink.

Analysis of heat transfer distribution on the heat sinks

Effect of fin pin arrangement and perforation on temperature distribution

Figures 13 to 16 show the temperature contours over the convective surface areas for pin fin heat sinks in inline and staggered arrays. From the observations, all the design models analysed show that the temperature distribution decreases gradually from the base plate to the length of the pin fins. In Figure 13, the base plate is characterized by shades of red and yellow, indicating that the initial temperature of the base plate is around 364.5 K, which is the hottest part of the heat sink. Along the pin fins, the colour shifts to blue, this gradually decreases the temperature of the pin fin from the base

plate to approximately 362.9 K. The temperature contour plot for Figure 10 reveals a consistent temperature gradient, indicating a gradual dissipation of heat from the base plate through the pin fins. This inline arrangement facilitates heat transfer but exhibits modest temperature reduction along the fins.

Table 5: MAPE error percentages between simulation and experimental results

Heat sink	Square threaded pin fin in inline pattern	Square threaded pin fin with perforation in inline pattern	Square threaded pin fin in staggered pattern	Square threaded pin fin with perforation in staggered pattern
MAPE error %	0.79	3.1	5.3	5.0

Figure 14 shows that the base plate is slightly cooler at the temperature of 360.1 K and the temperature decreases along the pin fins until the end of the pins at 358.7 K. Along the staggered pin fins, the colour gradually shifts toward dark blue tones for all pin fins. The heat dissipation in Figure 14 is slightly more efficient compared to Figure 13. The staggered arrangement introduces irregularities in the flow pattern, which contribute to improved cooling efficiency as indicated by the lower temperature at the end of the pin fins.

Figure 15 shows that the base plate temperature is 358.9 K, with the temperature decreasing to 357.2 K at the end of perforated pin fins. Comparison between Figures 13 and 15 shows that the addition of perforations to the pin fins in inline arrangement significantly increases heat dissipation from the heat flux at the base plate. This situation is predicted because an increase in effective heat transfer area enhances the rate of heat dissipation [22].

Figure 16 shows the result of a unique temperature distribution. The base plate temperature is relatively high at 367.6 K and the temperature decreases to 366.2 K at the end of the perforated pin fins. When comparing the colour trends in the temperature contour between Figure 15 and Figure 16 along the staggered pin fins, the colour gradually shifts toward dark blue tones for all pin fins in Figure 16. It shows that the threaded fin pins with perforation in staggered arrays are cooler and highly effective in dissipating heat, even though the base plate starts at a higher temperature. The colour trends in the temperature contour plots visualize how heat is distributed across the heat sink.

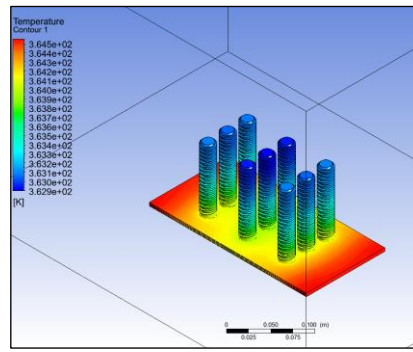

Figure 13: Temperature contour of inline pattern without perforation pin fins

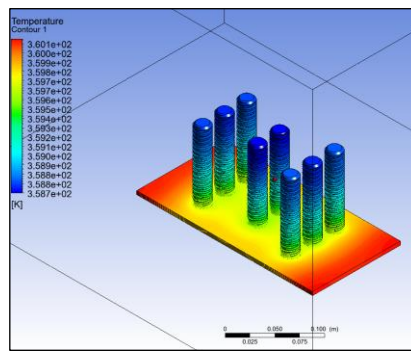

Figure 14: Temperature contour of staggered pattern without perforation pin fins

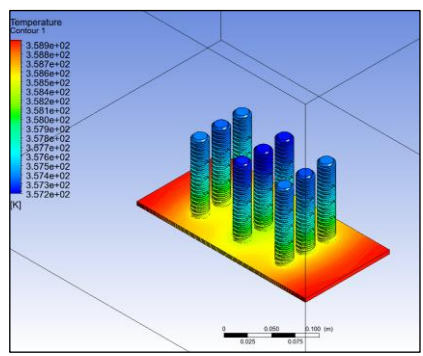

Figure 15: Temperature contour of inline pattern with perforation pin fins

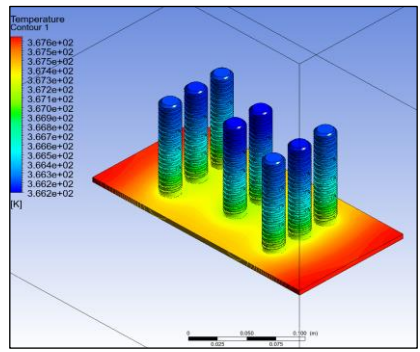

Figure 16: Temperature contour of staggered pattern with perforation pin fins

Fluid flow visualization

Effect of fin pin arrangement and perforation on fluid flow

Figures 17 to 20 show the velocity vectors of the pin fin heat sink with variations in perforation and arrangement at 15 W heat input. These velocity vector plots offer critical insights into how these design factors impact the movement of air and consequently heat dissipation.

Figure 20 shows the high-velocity profile which indicates the presence of strong airflow and fluid turbulence. Vortex formations occur within this configuration. These vortices represent areas where the fluid flow separates from the pin fins and subsequently reattaches downstream. This flow separation and reattachment contribute to enhanced heat transfer by disrupting the thermal boundary layer near the heat sink surface. This phenomenon aligns with the findings [22] which highlight the potential of improved heat dissipation.

Figure 18 exhibits a lower-velocity profile compared to Figure 20. This lower-velocity profile is indicative of reducing fluid turbulence and weaker airflow within the pin fin array. The key distinction here is that the pin fins in this configuration lack perforations. Without perforations, the airflow is more obstructed by the pin fins, leading to lower circulation and higher resistance to flow. This increased resistance results in a higher-pressure loss within the pin fin structure [23].

A noteworthy observation from these velocity vector plots is the difference between inline and staggered arrangements. Staggered pin fins tend to allow for more unimpeded fluid flow between the fins, resulting in improved circulation and reduced flow blockages compared to inline arrangements. Consequently, staggered patterns tend to exhibit more favourable fluid flow characteristics for heat dissipation.

The role of perforations in pin fins becomes apparent when comparing Figures 18 (no perforations) and 20 (with perforations). Perforations disrupt

the flow near the pin fins, creating additional turbulence and enhancing mixing. This disruption leads to increased heat dissipation from the heat sink surface, a crucial factor in optimizing cooling efficiency.

Additionally, the fluid flow patterns in the inline pattern configurations, both with and without perforations, reveal a limitation. The pin fins in the middle of the inline pattern receive insufficient airflow to dissipate heat effectively. This is attributed to the sequential arrangement of pin fins, where air struggles to rise parallel through the fins. As a result, this configuration might experience reduced heat transfer performance.

In summary, these fluid flow visualizations provide valuable insights into the impact of perforations and pin fin arrangement on heat sink performance. Perforations disrupt flow and enhance turbulence, while staggered arrangements generally promote more efficient fluid circulation. Understanding these flow patterns is critical for optimizing heat sink designs, ensuring effective heat dissipation, and maintaining safe operating temperatures for electronic devices. This analysis underscores the importance of design choices in achieving superior thermal management.

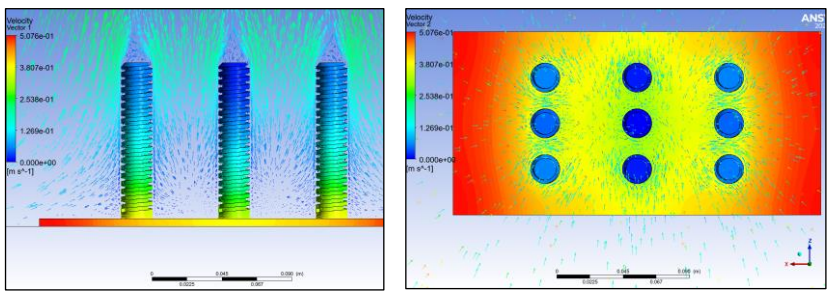

(a) xy-plane (b) yz-plane

Figure 17: Air flow velocity profile of inline pattern without perforation

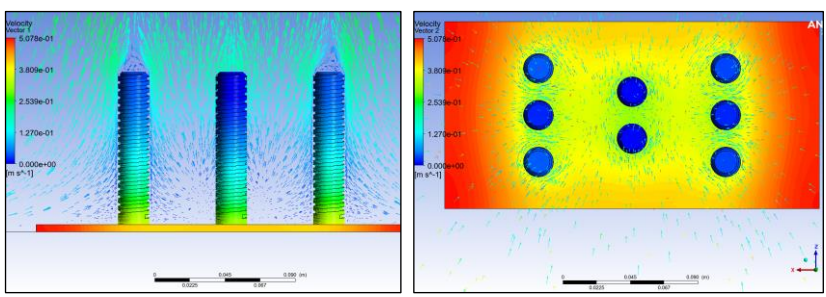

(a) xy-plane (b) yz-plane

Figure 18: Air flow velocity profile of staggered pattern without perforation

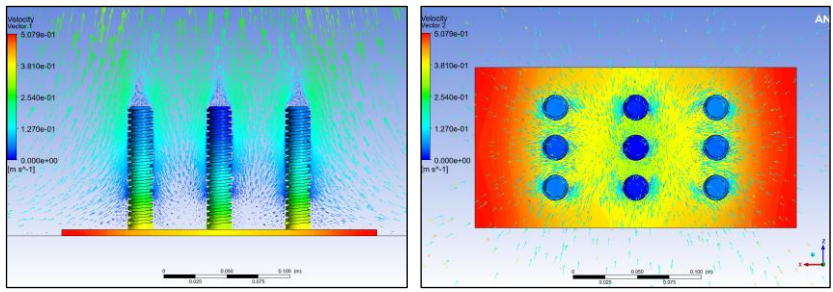

(a) xy-plane (b) yz-plane

Figure 19: Air flow velocity profile of inline pattern with perforation

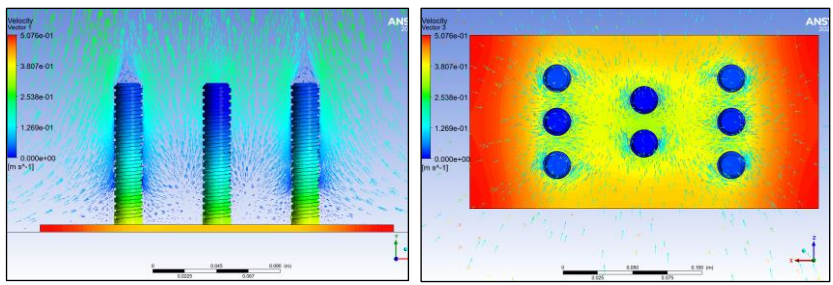

(a) xy-plane (b) yz-plane

Figure 20: Air flow velocity profile of staggered pattern with perforation

Thermal performance

In Figure 21, the graph presents a linear trend in the relationship between the resulting temperature difference *(ΔT)* and the power input applied to the base plate of the heat sink for four distinct pin fin configurations. When power input increases, the temperature difference also tends to increase. This correlation reflects the basic principle that higher heat loads lead to greater temperature differentials within the heat sink.

Pin fins with perforation in the staggered pattern have a higher temperature difference followed by pin fins in inline pattern. The higher temperature difference measured at the base plate with the temperature at atmospheric air is due to the arrangement in the staggered pattern which can reduce the obstruction for the fluid to flow through the entire pin fins. Thus, a more convective surface area actively dissipates heat to the surrounding air [24]. This configuration is the most effective in dissipating heat.

The Rayleigh number is a dimensionless number that quantifies the relative effects of buoyancy and viscous forces in fluid flow. It is a critical parameter in natural convection heat transfer. Meanwhile, the Nusselt number

represents the ratio of convective heat transfer to conductive heat transfer in a fluid. It characterizes the effectiveness of heat transfer, with higher *Nu* values indicating more efficient cooling.

For all configurations of pin fin, there is a positive correlation between *Nu* and *Ra* as shown in Figure 22. This means that as the Rayleigh number increases, the Nusselt number also tends to increase. This relationship is in line with the expectations in natural convection, where higher *Ra* values typically lead to enhanced convective heat transfer [24]. Pin fins with perforation in the staggered pattern have the highest Nusselt number while pin fins with perforation in inline pattern have the lowest Nusselt number. The difference between the highest Nusselt number of pin fins in staggered with perforation and the second highest pin fins in inline pattern is about 0.62%. The combination of staggered patterns and perforations promotes more effective convective cooling.

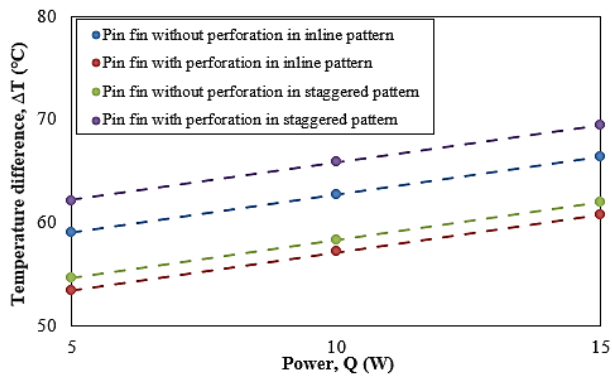

Figure 21: Temperature differences, ΔT against the power input, Q

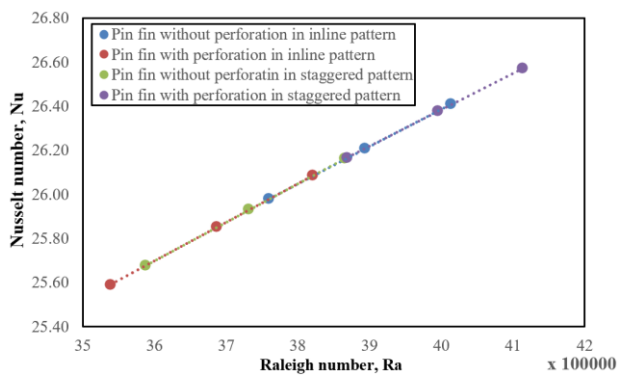

Figure 22: The relation of Nusselt number, *Nu* and Rayleigh number, *Ra*

From Figure 23, all the models showed the same trend as Figure 22 which indicates a positive correlation between Nusselt number, *Nu* and heat transfer coefficient, *h*. Higher Nusselt numbers typically indicate more efficient heat transfer, while the heat transfer coefficient quantifies the rate of heat exchange between a solid surface and a fluid. Lower Nusselt numbers reduce convective heat transfer, which is often associated with laminar flow or less effective heat dissipation. The positive correlation between *Nu* and h is essential for engineers and researchers in the field of thermal management. It implies that by optimizing the pin fin configuration and geometry to achieve higher Nusselt numbers, the heat transfer performance of a heat sink can be enhanced, resulting in more efficient cooling of electronic devices. These findings can be valuable in designing heat sinks for various applications where effective heat dissipation is crucial. From both graphs, it can be stated that pin fins with perforation in staggered patterns have better thermal performance than the other model of heat sink.

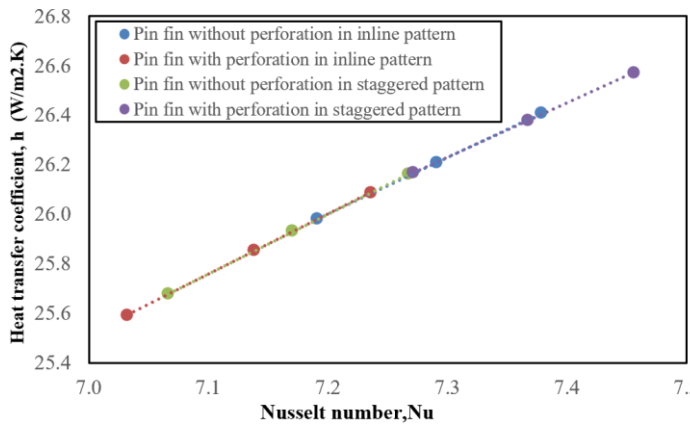

Figure 23: The relation of heat transfer coefficient, *h* and Nusselt number, *Nu*

Figure 24 shows that the heat transfer coefficient tends to increase with higher power inputs across all square threaded pin fins. This behaviour is consistent with the expected response of convective heat transfer, where higher power inputs lead to greater temperature gradients and increased heat dissipation. Pin fins with perforation in the staggered pattern have the highest heat transfer coefficient at each power supply while pin fins with perforation in inline pattern have the lowest heat transfer coefficient. For the square threaded pin fin in the staggered pattern with perforation, the result demonstrates a consistent rise in the heat transfer coefficient as power input increases. This model offers the highest heat transfer coefficients, making it a promising choice for applications with high power densities. As a comparison,

the average difference between *h* of the pin fin with perforation and the pin fin without perforation in the staggered pattern is 2.75%. Therefore, the pin fin with perforation in a staggered pattern dissipates heat at the rate of 2.75% more than the pin fin without perforation.

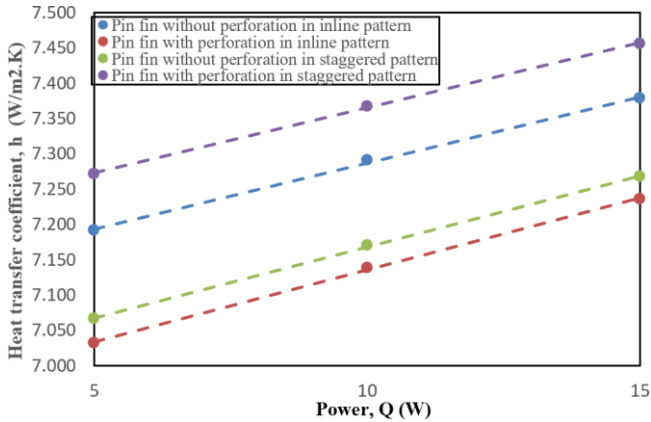

Figure 24: The relation of heat transfer coefficient, *h* and power input, Q

Conclusion

This project presents a numerical analysis for the investigation of flow patterns and quantifies the heat transfer characteristics of the square threaded pin fins integrated into the heat sink by natural convection. Four configurations were analysed based on the pin fins with or without perforations in an inline or staggered pattern. The effects of different arrangements and the presence of perforations, all under the conditions of natural convection, were analysed. The simulation was validated with previous studies to determine the heat transfer coefficient, *h*. In this project, the result for validating the Ansys CFD simulation with the experiment [16] shows about a 5% error of heat transfer coefficient for square threaded pin fins with perforation in a staggered pattern. Temperature contours reveal that all design models exhibit a gradual decrease in temperature from the base plate to the end of the pin fins. While the inline arrangements facilitate heat transfer, the staggered arrangements, especially those with perforations, demonstrate more efficient heat dissipation. This shows that the choice of pin fin arrangement plays a pivotal role in thermal performance. The additional perforations in inline arrangements significantly increase heat dissipation by expanding the effective heat transfer area. Threaded fin pins with perforations in staggered patterns prove to be highly effective in dissipating heat, despite a relatively higher base plate temperature.

The colour trends in the temperature contour plots vividly depict how heat is distributed across the heat sink. The enhancement in heat dissipation rate due to perforation is noted when having a higher contact surface with fluid in comparison with the pin fins without perforation. The extended effective surface area with the application of threaded geometry on pin fins contributes a good medium of convection heat transfer. The fluid flow visualization elucidates the relationship between pin fin patterns, perforations, and airflow patterns. Staggered pin fin pattern disrupts the flow less, resulting in improved circulation and reduced flow blockages compared to inline arrangements. Perforations introduce turbulence and enhance mixing, contributing to increased heat dissipation. For thermal performance, as power input increases, temperature differences also tend to rise. The higher heat loads lead to greater temperature differentials within the heat sink. Thus, a more convective surface area actively dissipates heat to the surrounding air. The threaded fin pins with perforations in staggered patterns are the most effective in dissipating heat. The heat transfer coefficients increase with higher power inputs. Pin fins with perforations in staggered patterns consistently offer the highest heat transfer coefficients, making them particularly attractive for applications with elevated power densities. In summary, this research project significantly contributes to the understanding of thermal management through square-threaded pin fins. By optimizing pin fin arrangements and introducing perforations, the square-threaded pin fins have higher heat transfer performance than others. These findings hold substantial implications for the design and engineering of heat sinks in a wide range of electronic applications.

Contributions of Authors

The authors confirm the equal contribution in each part of this work. All authors reviewed and approved the final version of this work.

Funding

This work was supported by the “Geran Penyelidikan Khas” from Universiti Teknologi MARA (UiTM) [600-RMC/GPK 5/3 (133/2020)].

Conflict of Interests

One of the authors, Rosnadiah Bahsan, is an assistant managing editor of the Journal of Mechanical Engineering (JMechE). The author has no other conflict of interest to note.

References

[1] M. Tejas Sonawane, M. Prafulla Patil, M. A. Chavhan, B. M. Dusane, and Nashik. Management, "A review on heat transfer enhancement by passive methods," *International Research Journal of Engineering and Technology*, vol. 3, no. 9, pp. 1567-1574, 2016.

[2] A. Al-Damook, N. Kapur, J. L. Summers, and H. M. Thompson, "An experimental and computational investigation of thermal air flows through perforated pin heat sinks," *Applied Thermal Engineering*, vol. 89, pp. 365–376, 2015. https://doi.org/ 10.1016/j.applthermaleng.2015.06.036

[3] A. S. Nathan, R. S. Silson, M. Syed Kani, G. U. Pandian, and U. Nainar, "Performance enhancement of minichannel heat sink," *International Journal of Innovative Research in Science*, vol. 8, no. 3, pp. 3201-3211, 2019. https://doi.org/ 10.15680/IJIRSET.2019.0803226

[4] H. E. Ahmed, B. H. Salman, A. S. Kherbeet, and M. I. Ahmed, "Optimization of thermal design of heat sinks: A review," *International Journal of Heat and Mass Transfer*, vol. 118, pp. 129–153, 2018. https://doi.org/10.1016/j.ijheatmasstransfer.2017.10.099.

[5] V. Choudhary, M. Kumar, and A. K. Patil, "Experimental investigation of enhanced performance of pin fin heat sink with wings," *Applied Thermal Engineering*, vol. 155, no. 9, pp. 546-562, 2019. https://doi.org/10.1016/j. applthermaleng.2019.03.139.

[6] Y. Joo, and S. J. Kim, "Comparison of thermal performance between plate-fin and pin-fin heat sinks in natural convection," *International Journal of Heat and Mass Transfer*, vol. 83, pp. 345-356, 2015. https://doi. org/10.1016/j.ijheatmasstransfer.2014.12.023

[7] X. Meng, J. Zhu, X. Wei, X., and Y. Yan, "Natural convection heat transfer of a straight-fin heat sink," *International Journal of Heat and Mass Transfer*, vol. 123, pp. 561-568, 2018. https://doi.org/10.1016/j. ijheatmasstransfer.2018.03.002

[8] S. A. Nada, and M. A. Said, "Effects of fins geometries, arrangements, dimensions and numbers on natural convection heat transfer characteristics in finned-horizontal annulus," *International Journal of Thermal Sciences*, vol. 137, pp. 121-137, 2019. https://doi.org/10.1016/j.ijthermalsci.2018.11.026

[9] M. R. Haque, T. J. Hridi, and M. M. Haque, "CFD studies on thermal performance augmentation of heat sink using perforated twisted, and grooved pin fins," *International Journal of Thermal Sciences*, vol. 182, no. 6, p. 107832, 2022. https://doi.org/10.1016/j.ijthermalsci.2022.107832

[10] G. Song, D. H. Kim, D. H. Song, J. bin Sung, and S. J. Yook, "Heat-dissipation performance of cylindrical heat sink with perforated fins,"

International Journal of Thermal Sciences, vol. 170, p. 107132, 2021. https://doi.org/10.1016/j.ijthermalsci.2021.107132

[11] A. Maji, D. Bhanja, and P. K. Patowari, "Numerical investigation on heat transfer enhancement of heat sink using perforated pin fins with inline and staggered arrangement", *Applied Thermal Engineering*, vol. 125, pp. 596–616, 2017. https://doi.org/ 10.1016/j.applthermaleng.2017.07.053

[12] P. Laad, B. Akhare, and P. Chaurasia, "Thermal analysis of heat sink with fins of different configuration using ANSYS workbench 14.0," *International Journal of Engineering Sciences & Research Technology*, vol. 5, no. 6, pp. 82-93, 2016. https://doi.org/10.5281/zenodo.54668

[13] A. Harry Richard T. L., "Experimental analysis of heat transfer enhancement using fins in pin fin apparatus," *International Journal of Core Engineering & Management*, vol. 2, no. 1, pp. 123-132, 2015.

[14] S. Bakre, A. Arya, and B. M. Rathore, "Study of thermal hydraulic performance of various pin fin heat sink by using computational fluid dynamics," *International Journal for Scientific Research & Development*, vol. 3, no. 1, pp. 499-506, 2015.

[15] S. Sharbuddin Ali, "Experimental study on heat sink using screw thread," *International Journal of Innovative Science and Research Technology*, vol. 2, no. 12, pp. 26-34, 2017.

[16] B. Olekarp and G. Tp, "Experimental and numerical analysis of cylindrical pin fins having square thread with and without perforations by natural and forced convection," *International Journal of Innovative Science, Engineering & Technology*, vol. 3, no. 7, pp. 512-516, 2016.

[17] S. T and S. K. D, "Heat transfer study on different surface textured pin fin heat sink," *International Communications in Heat and Mass Transfer*, vol. 119, p. 104902, 2020. https//doi.org/10.1016/j.icheatmasstransfer.2020.104902

[18] Perry, J, "Thermal comparison of copper and aluminum heat sinks" 28 March 2017. [Online] Available: https://www.qats.com/cms/2017/03/28/case-study-thermal comparison-copper-aluminum-heat-sinks/ (Accessed 20 April, 2022)

[19] Zagala, E. J., "Heat conductivity", in B. Bhushan (Ed.), Encyclopedia of Nanotechnology, Springer, 2016, pp. 1453-1453, https://doi.org/10.1007/978-94-017-9780-1_100385

[20] D. Hanamant, K. N. Vijaykumar, and D. Kavita, "Natural convection heat transfer flow visualization of perforated fin arrays by CFD simulation," *International Journal of Research in Engineering and Technology*, vol. 2, no. 12, pp. 483-490, 2013. https://doi.org/10.15623/ijret.2013.0212081

[21] R. Siddhardha, S. Bhatti, P. Subramanyam, and A. Professor, "Numerical investigation on heat transfer enhancement by Natural Convection with

Perforated Fins," *International Journal of Research and Analytical Reviews*, vol. 5, no. 4, pp. 693-699, 2018.

[22] A. Naufal bin Samsudin, A. Salami Tijani, S. Thottathil Abdulrahman, J. Kubenthiran, and I. Kolawole Muritala, "Thermal-hydraulic modeling of heat sink under force convection: Investigating the effect of wings on new designs," *Alexandria Engineering Journal*, vol. 65, pp. 709-730, 2023. https://doi.org/ 10.1016/j.aej.2022.10.045

[23] Y. Yan, T. Zhao, Z. He, Z. Yang, and L. Zhang, "Numerical investigation on the characteristics of flow and heat transfer enhancement by micro pin-fin array heat sink with fin-shaped strips," *Chemical Engineering and Processing - Process Intensification*, vol. 160, no. 1, p. 108273, 2021. https://doi.org/ 10.1016/j.cep.2020.108273

[24] A. S. Tijani and N. B. Jaffri, "Thermal analysis of perforated pin-fins heat sink under forced convection condition," *Procedia Manufacturing*, vol. 24, pp. 290–298, 2018. https://doi.org/ 10.1016/j.promfg.2018.06.025

Design Parameters Optimization in CNC Machining Based on Taguchi, ANOVA, and Screening Method

Armansyah[*], Lilik Zulaihah, Siti Rohana Nasution, Gary Geraldus Sinaga
Faculty of Engineering, Universitas Pembangunan Nasional Veteran,
Jl. RS. Fatmawati, Pd. Labu, 12450 Jakarta, INDONESIA
[*]armansyah@upnvj.ac.id

Juri Saedon
School of Mechanical Engineering, College of Engineering,
Universiti Teknologi MARA, Shah Alam, 40450 Selangor, MALAYSIA

Agus Sudianto
Mechanical Engineering Department, STT YBS Internasional,
Jl. Pasar Wetan, Kompleks Mayasari Plasa, 46123 Kota Tasikmalaya,
West Java, INDONESIA

ABSTRACT

Future manufacturing requires a process to achieve high productivity with high-quality products. Appropriate and optimum machining parameters during machining operation are essential to enhance the surface quality (R_a). This study investigated a design for machining parameter optimization to reduce time and cost with minimum experiments using the Taguchi method via the screening method. In this study, the machining parameters were the cut speed (v_c), fed speed (v_f), cut depth (d_{oc}), cut width (w_{oc}), and flute (z). The response analysed process was done on Aluminium alloy AA6061 via a high-speed computer numerical control machine (HSM) employing an end mill cutter in dry cutting. Analysis of Variance (ANOVA) of parameters combination applied during the process was used to analyse the results from data obtained and via the screening. Based on the result of ANOVA indicated that v_f showed a greater F-value which meant v_f had statistical significance for the terms and model. It was concluded that through the confirmation test, the optimal machining parameters v_c at 220 rpm, v_f at 150 mm/m, d_{oc} of 0.5 mm, w_{oc} at 4 mm, and z at 4 flutes, with R_a was around 0.122 - 0.127 which was achieved the requirement of standard for industries in polishing.

ISSN 1823-5514, eISSN 2550-164X
Received for review: 2023-10-09
Accepted for publication: 2023-10-26
Published: 2023-11-15

https://doi.org/10.24191/jmeche.v12i1.24646

Keywords: *CNC Machining; Surface Roughness; Taguchi; ANOVA; Screening*.

Introduction

Various machining processes in current and future manufacturing require a process with high productivity including improving the quality of products. An effective manufacturing process produces products of right dimensions and precision. One classical example is the milling operation which dispose of material quickly with excellent surface finishing results. Surface morphology is the main indicator in machining to evaluate process effectivity as well as the quality of the product [1]-[2]. Surface morphology evaluation handled by surface roughness measurement on the final product has a strong relationship to the performance of the machining and its functionality [3]-[4]. Conventionally, manufacturing processes are prepared to derive the maximum productivity with minimum cost. On the other hand, the surface quality is influenced also by the deviation of interface between tool and workpieces. Large or small deviations represent rough or smooth surface roughness respectively [5]-[6].

Materials with high strength have been manufactured as a result of numerous developments in material engineering and technology. The appropriate Computer Numerical Control (CNC) machine tool to remove the chips over the materials during machining is strongly significant [7]. Currently, aluminium alloys are widely used as main materials in various parts and products such as in the automotive industry [8]. A study by Novakowski et al. [9], focused on the influence of the milling conditions of aluminium alloy 2017A by investigating the optimum operating parameters during face milling. It was found that surface roughness (R_a) was achieved at 0.6 according to the desired $R_a > 0.2$ by optimum parameters of v_c 300 m/min and v_f 0.14 mm/tooth. Similar study can be found at [10]. Machining processes on the aluminium alloy are predominantly applied in the automotive industry such as the manufacturing of moulds and dies for producing automotive components.

In this research, the Taguchi method was chosen to analyse the machining parameters to reach the minimum R_a [11]-[12]. The Taguchi method has been widely used as a technique for process parameter optimization involving cut speed, fed speed, cut depth, and cut width, as well as the number of flutes or teeth as described in Figure 1. Several operational variables can be optimized more easily and effectively with the help of statistical design of experiments. Often used experimental design techniques include the Taguchi method, full factorial design, evolutionary operation, and response surface methodology. Taguchi's optimization technique is a distinct and potent optimization field that permits optimization with a minimal number of experiments. Robust design solutions, cost savings, and quality

improvement are all achieved with the Taguchi experimental design. The Taguchi technique has two advantages over the other methods: it can optimize many factors at once and extract more quantitative information from fewer experimental trials. Joshi and Bolar [13] discovered that end mills with additional flutes had a significantly superior surface roughness. This due to, the chip load decreases with an increase in flute number, lowering the cutting force.

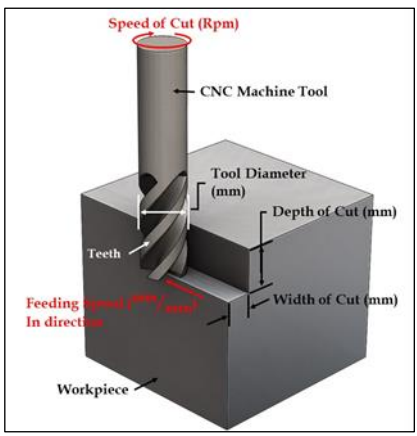

Figure 1: Illustration of the milling process in CNC machining

The Taguchi method in [14] via Orthogonal Arrays (OA) manages the experiments by reducing the number of experiments and minimizes the effects of disturbances. In addition, it reduces experiment time and costs [15]. Another study by Yang [16], and Oemar et al. [17], approved that by Taguchi method found that speed was the important parameter affecting the output of dimensional tolerance and separation force in 3D additive manufacturing, and chemical reagent concentration and activation temperature in the activated carbon production from rubber seed shell, respectively.

The average disagreement for the output response of the experimental results in each parameter context is described in the OA matrix [18]. Analysis of the response was then performed using the Signal to Noise Ratio (SNR). It can be categorized as "smaller-better", "bigger-better", and "nominal-better" in which a typical response advantage category is considered [19]. The CNC machining needs the fastest response of the swirling process of the tool on the material. Therefore, the “smaller is better” of SNR is highly recommended [20]. It is proposed using the following equation:

$$\eta = \frac{s}{n} = -10log\left(\frac{1}{n}\sum_{i=1}^{n} Y_i^2\right) \quad (1)$$

where Y_i is the data obtain from experiments and η is the experiment observation number. The Taguchi method was applied with the Minitab software for Analysis of Variants (ANOVA) that produced an unspoilt output of SNR [21]. This value was applied to measure experimental design variations. The SNR provides an increase in the control factor that is measured in terms of quality characteristics, namely the quality improvement achieved from the reduction in variability. The SNR characteristic was chosen according to the experiment response. For this reason, using the Taguchi orthogonal array can minimize the number of experiments [22]-[23]. Minitab 19.0 was applied with array L8*25 employing factors equal 5 for the screening process. The screening test and Minitab 19.0 produces small run numbers, and the variant analysis (ANOVA) output was still unspoilt. By ANOVA, the potential contribution of the CNC machining parameters based on output response from the surface roughness measurements was determined [24].

ANOVA offers tools such as the normal probability plot [25]. It can be used to describe the relationship between the roughness value and cut speed, fed speed, cut depth, cut width, and amounts of tool's teeth. The distribution of normal data was indicated by the normal probability plot, while the variables influenced the response of the process. The Pareto chart refers to the absolute values of the significant effects statistically of the selected machining parameters via plots of a reference line [26]. Another important part of ANOVA is the regression to evaluate the significant fit of the data. Through a residual plot, it can be seen how far the error between the predicted value and the observed actual value is [27].

Based on the above references it was understood that the selected value of process parameters in combination and variation among them affected significantly the end quality of the product i.e., surface finish (roughness) R_a. This can be done through investigation to process optimization of the process by analysis of the selected values of the machining parameters which was the objective of this study. Five different process parameters with their combinations were tested and analysed to find the best fit affected significantly by the R_a. Via Taguchi, ANOVA, and screening methods, the characteristics of each parameter can be analysed for their contribution to the output response R_a. Therefore, the future output response of R_a was predictable.

Material and Method

In this study, Aluminium alloy 6061 was used as sample specimens. The mechanical properties of this alloy can be seen in Table 1. The chemical composition of the specimen was obtained using Optical Emission Spectroscopy. The specimen material was identified as AA6061 based on the Designation of International Alloy and Chemical Composition for wrought aluminium and aluminium alloy with the chemical composition listed in Table

2 [29]. It was selected due to its excellent mechanical characteristics [30], with good machinability which is often used for automotive and aerospace components.

Table 1: Mechanical characteristic of aluminium alloy 6061 [28]

Properties	Metric	Imperial
Tensile strength	310 MPa	45000 psi
Yield strength	276 MPa	40000 psi
Shear strength	207 MPa	30000 psi
Fatigue strength	96.5 MPa	14000 psi
Elastic modulus	68.9 GPa	10000 ksi
Poisson's ratio	0.33	0.33
Elongation	12-17%	12-17%
Hardness, Brinell	95	95

Table 2: The chemical composition of aluminium alloy (AA6061) in the workpiece used in this study

Element	Al	Cr	Cu	Fe	Mg	Mn	Si	Ti	Ni	Pb	Zn
Wt.(%)	96	0.1	0.2	0.7	2.3	0.15	0.6	0.15	<0.005	<0.004	0.25

In the sample specimen's preparation, workpieces are set with a geometry of 50 x 38 x 20 mm and then prepared via a CNC machine. A finished sample specimen was ready for experiment shown in Figure 2.

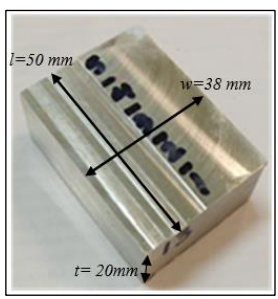

Figure 2: The geometry of workpieces made of aluminium alloy (AA6061)

In the analysis, required methods were also prepared such as the Taguchi method, ANOVA, and screening methods. As mentioned, the independent variables being selected in this study for screening were the cut speed, fed speed, cut depth, cut width, and number of flute (z). From these five independent variables, the optimum parameters are determined. These

optimum parameters form the basis for the development of the model that predicts surface roughness values in each experiment. The optimum parameters were synthesized based on the Taguchi method using analysis of table of variants in Minitab. The R_a was measured using a stylus probe type (handy surf) based on the WAS Foundry Master ASTM E 1251 standard as an output response from the CNC machining process in the experiments.

A 3-axis high-speed computer numerical control machines (HSM) of LG-1000 HARTFORD which is available in the manufacturing laboratory at Engineering Faculty, Universitas Pembangunan Nasional Veteran Jakarta was employed to conduct the experiment using end mill cutter utilized in dry cutting at 750 rpm value according to the tool geometry and workpiece. The Taguchi method was then applied to observe the significant parameters through reducing experimental works. Through this method, an efficient and systematic approach to find the optimum machining parameters can be achieved.

Table 3 lists the range of selected parameters level in this study. The five parameters were used in this study, where each parameter was set at two levels with low and high levels in Taguchi. The design of experiment (DOE) was performed using Minitab 19.0 with array $L8*2^5$ employing factors equal to 5.

Table 3: The range of selected parameters represented by two categories i.e., low- and high-level parameters used in this study

Process parameters	Status	Low level parameters	High level parameters	Unit
Cut speed (v_c)	Process input	100	220	m/min
Fed speed (v_f)	Process input	150	1681	mm/min
Cut depth (d_{oc})	Process input	0.1	0.5	mm
Cut width (w_{oc})	Process input	4	6	mm
Number of flute (z)	Process input	3	4	flute
Surface roughness (R_a)	Process output/response	The surface roughness values based on two levels of parameters could be identified.		

After laboratory preparation, the study starts with the selection of the machining parameters i.e., cut speed (v_c), fed speed (v_f), cut depth (d_{oc}), cut width (w_{oc}), and tooth amount (z). After that, the Taguchi method was employed for process parameter optimization. The machining test through experimental work on sample material (workpieces) was done to test the machining process based on the selected machining parameters. Furthermore, the surface roughness (R_a) of the finished machining product was evaluated and analysed. ANOVA was then applied in the study to determine the significant contribution of the selected machining parameters. Through

screening, the proposed machining parameters were known whether the parameters are significant or not significant.

Results and Discussion

Table 4 shows the value of surface roughness measurement (R_a) obtained for each run of experiments. The results indicated that the sixth experiment produced the lowest value of R_a of 0.108 at 220 m/min of v_c, at 150 m/min of v_f, 0.5 mm of d_{oc}, 6 mm of w_{oc}, and with 3 of z. This R_a was suited to apply for low friction or high aesthetics components based on machine component guidelines provided by industry standards (ASME B46.1). On the other hand, the highest value of surface roughness emerged in the fourth experiment when v_c, at 100 m/min, v_f at 1681 mm/min, d_{oc} at 0.5 mm, w_{oc} at 6 mm, and z at 4. From all runs of the experiment, was revealed that the lower fed speed produced a lower surface roughness value and increasing the cut speed led to reducing surface roughness value. Other parameters such as d_{oc}, w_{oc}, and z have contributed to the surface roughness value but not too significant.

Table 4: The measurement results of surface roughness (R_a) affected by selected parameters through the CNC milling process at each run

Run	v_c (m/min)	v_f (mm/min)	d_{oc} (mm)	w_{oc} (mm)	z	R_a
1	100	150	0.1	4	3	0.117
2	100	150	0.1	6	4	0.117
3	100	1681	0.5	4	3	0.753
4	100	1681	0.5	6	4	0.922
5	220	150	0.5	4	4	0.126
6	220	150	0.5	6	3	0.108
7	220	1681	0.1	4	4	0.272
8	220	1681	0.1	6	3	0.293

Furthermore, the following Tables (Table 5 and Table 6) presented the effectiveness of each condition in influencing the characteristics of the related responses within a limited range. Table 5 lists the parameter coefficients from coefficient, SE coefficient, *T*-Value, *P*-value, and VIF. It is well known that the coefficient lies in the relationship between the predictors and response variables measured by their size and direction, where the error is standardized by the SE coefficient via estimation from the sample data. Meanwhile, the ratio between the coefficient and standard error is denoted by *T*-Value. Subsequently, The *P*-value is the probability which is the lower *P*-value will lead to the null hypothesis. From Table 5 can be seen that v_c, v_f, and d_{oc}, are lower probabilities compared to other parameters, where they have a significant effect on the response R_a. Similar results of R_a can be found in [31]

and [30]. By VIF equal to 1 at all parameters indicated that they have no correlations among the predictors in the model.

Table 5: Parameter coefficients in relation to the predictor and the response variable

Term	Coef.	SE Coef.	*T*-value	*P*-value	VIF
Constant	-0.017	0.201	-0.09	0.939	
v_c	-0.002310	0.000362	-6.38	0.024	1.00
v_f	0.000289	0.000028	10.19	0.009	1.00
d_{oc}	0.695	0.109	6.39	0.024	1.00
w_{oc}	0.0215	0.0217	0.99	0.428	1.00
z	0.0415	0.0435	0.95	0.441	1.00

Table 6 presents the analysis of variance. The DF of seven determined the number of observations in the sample. Adjusted sums of squares (Adj SS) represent the variation for different parameters of the model with the error sum of squares (error Adj SS) being 0.007557. The total variation of data was then quantified through the total sum of squares (total Adj SS) which was 0.715061 [27]. Distinct from Adj SS, the adjusted mean squares (Adj MS) refer to the degrees of freedom with an error close to zero (0.003778). The *F*-value shows the significance of terms and models statistically, where v_c, v_f, and d_{oc} have greater *F*-values compared to w_{oc} and z. It shows v_f (103.86) was the greatest *F*-value compared to others. The *P*-value of v_f was 0.538211, which means a lower probability than others. The highest percentage contribution ratio (PCR) revealed that v_f had a PCR of 20%, followed by d_{oc} and v_c at PCR of 21% and 20%, respectively. The w_{oc} and z had the smallest PCR of 1%, respectively.

Table 6: The analysis of variance (ANOVA)

Source	DF	Adj SS	Adj MS	*F*-value	*P*-value	PCR
v_c	1	0.153615	0.153615	40.66	0.204259	20%
v_f	1	0.392412	0.392412	103.86	0.538211	54%
d_{oc}	1	0.154355	0.154355	40.85	0.205294	21%
w_{oc}	1	0.003682	0.003682	0.97	-0.00542	1%
z	1	0.003441	0.003441	0.91	-0.00576	1%
Error	2	0.007557	0.003778			
Total	7	0.715061	0.715061			

Figure 3 then shows the Pareto chart as a bar chart in which the bars are ordered from highest frequency of occurrence to lowest frequency of occurrence. Figure 3 shows evidence that v_f through the screening test reached the standardized effect of 10, while the others are available between 1 to 6. This means, the v_f provided the best parameter contribution to the quality of

the product via its output response (R_a), followed by v_c, d_{oc}, w_{oc}, and z, respectively.

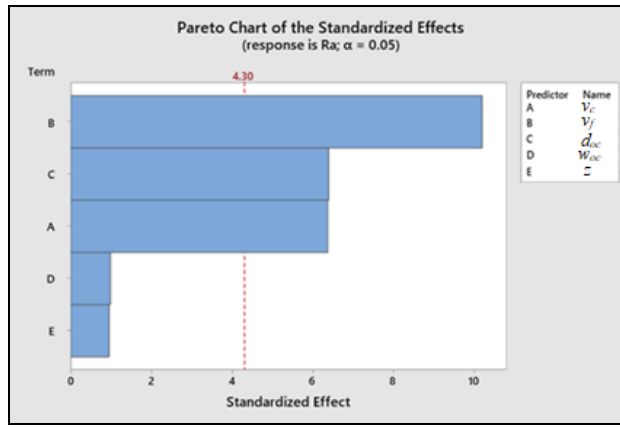

Figure 3: The five machining parameters described by the Pareto chart revealed the lowest to the highest machining parameters optimization

Figure 4 illustrates the different residual plots for R_a. The normal probability plot shows the trend of the residuals versus their predicted relatively followed a straight line which confirmed it was normally distributed. The residual versus fitted value (predicted) plot is a graphical tool to assess the assumptions and the goodness of fit of a regression model. Each data point in the plot represents a pair of predicted values and its corresponding residual. The histogram charts, which show a graphical representation of the residual versus frequency of data that emerged, represent a visualization of the distribution of a dataset [32]. It displays the frequency or count of data points falling into different intervals or bins. From histogram, it can be seen that all predicted data provided a relatively equal amount frequency of the bins. The versus order chart represents the accuracy of the fits of the predicted value of the residuals during the observation period. It is shown that the residuals fall randomly around along the centre line. A sudden shift in the points was produced, indicating that the underlying pattern of the data has changed.

Figure 5a shows a 3D contour plot of roughness value versus cut speed and cut depth. It presents roughness value (R_a) that the high R_a places in d_{oc} of 0.5 mm and v_c of 100 m/min. Figure 5b denotes the 3D plot of roughness value versus v_f and d_{oc}. It shows roughness value (R_a), where the high R_a was achieved at maximum d_{oc} of 0.5 mm and at maximum v_f of 1681 m/min. Meanwhile, low R_a was found in all ranges of d_{oc} and in minimum v_f.

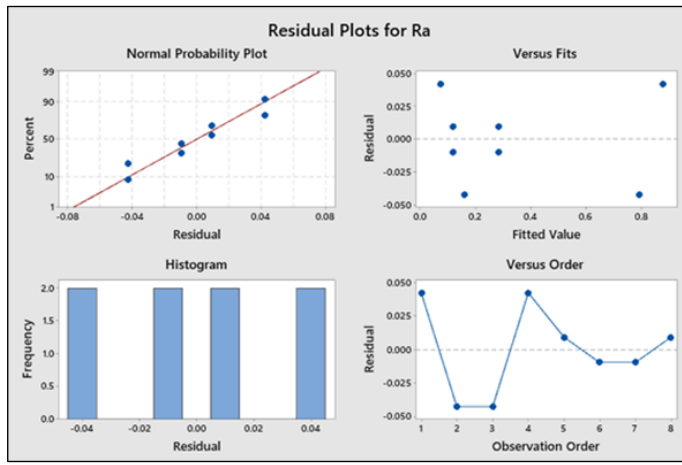

Figure 4: Different residual plots for R_a

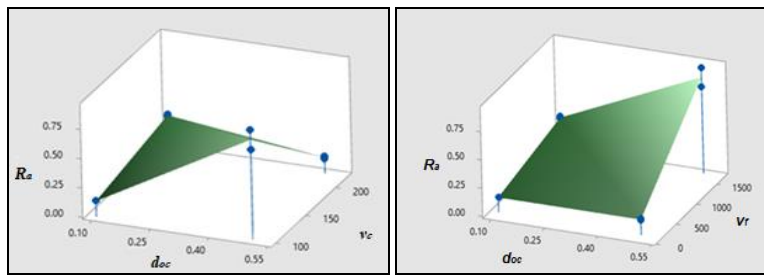

(a) (b)

Figure 5: (a) The contour plot of R_a affected by the on-cut speed (v_c) and cut depth (d_{oc}), and (b) the contour plot of R_a affected by fed speed (v_f) and cut depth (d_{oc})

Figure 6 shows the main effect plot for R_a, and explains the impact of v_c, v_f, d_{oc}, w_{oc}, and z on the final machining of R_a values. These are distinguished by the steepest slope and the longest line, which suggests that respective factors have a high effect on the R_a [33]. In addition, when the lines are similar in slant and length, the components would mostly similarly affect the R_a. Thus, no other factor has a higher impact than another. The main effect plot shows the v_f has the steepest slope and longest line compared to the others. It was confirmed that the most significant machining parameter influencing the response R_a was v_f. The lowest R_a signifies the lowest values of mean R_a for each process parameter i.e., v_f, v_c, d_{oc}, w_{oc}, and z. Based on the results faster v_c produced smaller R_a values. Meanwhile, R_a shows smaller values by using a

low v_f. On the other hand, small doc produced smaller R_a values. The main effect plot confirmed that the most suitable machining parameters for R_a were at 150 m/min of v_f, 220 mm/m of v_c, 0.1 mm of d_{oc}, 4 mm of w_{oc}, and 3 of z.

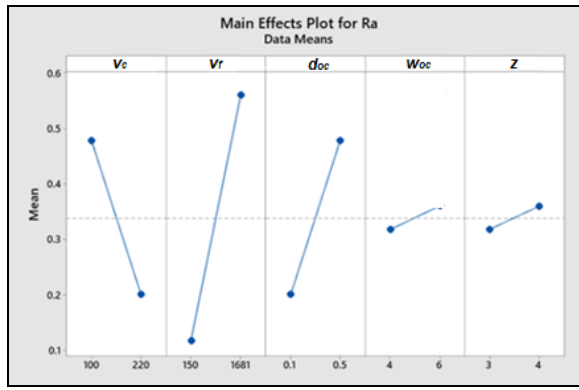

Figure 6: Main effects plot for R_a affected by v_f, v_c, d_{oc}, w_{oc}, and z

A confirmation test was performed using the above conditions of the cut speed (v_c) at 220 m/min, fed speed (v_f) at 150 mm/m, cut depth (d_{oc}) of 0.1 mm, cut width (w_{oc}) at 4 mm, and with a number of flutes (z) was 3, and with three times of repetitions, in order to validate results from the statistical analysis. The confidence interval (95%) for the R_a results of the confirmation test was calculated. Based on the calculated value, the confidence interval was ± 0.021 while the confidence limits were 0.108 ± 0.021; thus, the confidence limits were between 0.087 and 0.129 (R_a). Following the confirmation test, the surface roughness obtained was R_a = 0.122 - 0.127 µm, which was within the confidence interval calculated, indicating that the experiment was statistically acceptable, and confirmed to be used in polishing CNC machining of machine components or mechanical parts of R_a: 0.005 - 0.2 (ASME B46.1).

Conclusion

The study showed a combination of techniques to define the optimum parameters in a CNC Machining process such as v_c, v_f, d_{oc}, w_{oc}, and z. From the study, it was found that the enhancement of the quality of the product can be reached through R_a measurement with respect to the selected combination of the machining parameters. The best morphology of surface roughness was reached at 0.1088 µm with the best fit of parameters of v_c at 220 m/min, v_f at 150 mm/min, d_{oc} at 0.5 mm, w_{oc} at 6 mm, and z at 3. Furthermore, the data were analysed through ANOVA using Taguchi and Minitab based on the *F*-

value and *P*-value. The highest significant parameters to the R_a were found in the v_c, v_f, and d_{oc}, respectively. The optimum machining parameters via screening were found using v_c in the range of 100 - 220 m/min, v_f in 150 - 1681 mm/min, and d_{oc} in 0.1 - 0.5 mm by employing end mill cutter in dry cutting. Therefore, these three optimum machining parameters are recommended to be used in the CNC machining process to produce the best surface morphology on the manufacturing product which in turn increases product quality. Based on the result of ANOVA indicated that v_f showed a greater *F*-value which meant v_f had greater significance of the terms and model statistically. Via the confirmation test, the optimal machining parameters were the cut speed (v_c) at 220 m/min, fed speed (v_f) at 150 mm/m, cut depth (d_{oc}) of 0.5 mm, cut width (w_{oc}) at 4 mm, and a number of flutes (z) at 4, with the surface finish quality (R_a) were around 0.122 - 0.127, which was achieved the requirement of standard for industries in polishing.

Contributions of Authors

The authors confirm the equal contribution in each part of this work. All authors reviewed and approved the final version of this work.

Funding

This work was supported by the “HIBAH INTERNAL PENELITIAN UPN VETERAN JAKARTA RISCOP 2022” [719/UN61.0/HK.02/2022].

Conflict of Interests

All authors declare that they have no conflicts of interest

Acknowledgment

The authors especially would like to thank the Engineering Faculty and LPPM of the Universitas Pembangunan Nasional “Veteran”, Jakarta, Indonesia, for the internal research grant scheme of RISCOP 2022 awarded, College of Engineering, Universiti Teknologi MARA, Shah Alam, Selangor, Malaysia, and STT YBS Internasional Tasikmalaya, West Java Indonesia, for the support given in the collaboration.

References

[1] S. Prakashrao Patil, G. Leela Prasad, C. Sai Kiran, S. Kumar, V. Ramasamy, and H. Mohammed Ali, "Surface roughness and topography of EDM machining of Inconel 718," *Materials Today Proceedings*, In Press, 2023, doi: 10.1016/j.matpr.2023.02.444.

[2] A. B. Bonţiu Pop, "Application of Taguchi's Method for Study of Machining Parameters on Surface Roughness of 7136 Aluminum Alloy in End Milling," *Applied Mechanics and Materials*, vol. 809–810, pp. 123–128, 2015. doi: 10.4028/www.scientific.net/AMM.809-810.123.

[3] M. A. Ali, K. Ishfaq, and M. Jawad, "Evaluation of surface quality and mechanical properties of squeeze casted AA2026 aluminum alloy using response surface methodology," *The International Journal of Advanced Manufacturing Technology*, vol. 103, no. 9–12, pp. 4041–4054, 2019. doi: 10.1007/s00170-019-03836-6.

[4] M. Yahul and R. Saravanan, "An analysis on CNC machined surface roughness between AA7475 and AA7475/fly ash composite," *Journal of Physics: Conference Series*, vol. 2484, no. 1, p. 012026, 2023. doi: 10.1088/1742-6596/2484/1/012026.

[5] N. H. Alharthi, S. Bingol, A. T. Abbas, A. E. Ragab, E. A. El-Danaf, and H. F. Alharbi, "Optimizing Cutting Conditions and Prediction of Surface Roughness in Face Milling of AZ61 Using Regression Analysis and Artificial Neural Network," *Advances in Materials Science and Engineering*, vol. 2017, pp. 1–8, 2017. doi: 10.1155/2017/7560468.

[6] S. Sulaiman, M. S. Alajmi, W. N. Wan Isahak, M. Yusuf, and M. Sayuti, "Dry Milling Machining: Optimization of Cutting Parameters Affecting Surface Roughness of Aluminum 6061 using the Taguchi Method," *International Journal of Technology*, vol. 13, no. 1, p. 58, 2022. doi: 10.14716/ijtech.v13i1.4208.

[7] S. Khatai, R. Kumar, A. Kumar Sahoo, and A. Panda, "Investigation on tool wear and chip morphology in hard turning of EN 31 steel using AlTiN-PVD coated carbide cutting tool," *Materials Today Proceedings*, vol. 59, pp. 1810–1816, 2022. doi: 10.1016/j.matpr.2022.04.387.

[8] S. Abban, O. M. Ikumapayi, T. S. Ogedengbe, S. A. Afolalu, C. Ananaba, and A. T. Ogundipe, "Development of aluminium-tin alloy for high strength application," *Materials Today Proceedings*, pp. 1-5, 2023. doi: 10.1016/j.matpr.2023.06.377.

[9] L. Nowakowski, M. Bartoszuk, M. Skrzyniarz, S. Blasiak, and D. Vasileva, "Influence of the Milling Conditions of Aluminium Alloy 2017A on the Surface Roughness," *Materials*, vol. 15, no. 10, p. 3626, 2022. doi: 10.3390/ma15103626.

[10] Y. Sun, Y. Liu, M. Zheng, J. Xu, and Q. Guo, "A review on theories/methods to obtain surface topography and analysis of corresponding affecting factors in the milling process," *The International*

Journal of Advanced Manufacturing Technology, vol. 127, no. 7–8, pp. 3097–3131, 2023. doi: 10.1007/s00170-023-11723-4.

[11] M. Boy and M. Avci, "The Effect of Machining Conditions on Surface Roughness and Burr Formation in Milling of AISI 304 Cast Stainless Steel," *Gazi Journal of Engineering Sciences*, vol. 8, no. 1, pp. 49–59, 2022. doi: 10.30855/gmbd.2022.01.06.

[12] E. Setyo Pradana and W. Sulistiyowati, "Literature Review: Use of the Taguchi Method for Quality Improvement," *PROZIMA (Productivity, Optimization and Manufacturing System Engineering)*, vol. 6, no. 2, pp. 85–96, 2022. doi: 10.21070/prozima.v6i2.1575.

[13] S. N. Joshi and G. Bolar, "Influence of End Mill Geometry on Milling Force and Surface Integrity While Machining Low Rigidity Parts," *Journal of The Institution of Engineers (India): Series C*, vol. 102, no. 6, pp. 1503–1511, 2021. doi: 10.1007/s40032-020-00608-0.

[14] W.D. Lestari, Rifky Ismail, Jamari Jamari, Athanasius Bayuseno, and Paulus Anggoro, "Optimization of CNC milling parameters through the Taguchi and RSM methods for surface roughness of UHMWPE acetabular cup," *International Journal of Mechanical Engineering and Technology*, vol. 10, pp. 1762–1775, 2019. http://www.iaeme.com/ijmet/issues.asp?JType=IJMET&VType=10&IType=2.

[15] N. K. Sahu, M. K. Singh, A. K. Sahu, and A. K. Sahu, "Employment of cylindrical electrolytic copper grade electrode under EDMed Inconel 825 super alloy: emphasis on machining behavior accompanied with surface topography for sustainability," *The International Journal of Advanced Manufacturing Technology*, vol. 154, pp. 1-27, 2023. doi: 10.1007/s00170-023-10967-4.

[16] C.-J. Yang, "Optimizing Manufacturing Parameters of DLP Machine by Taguchi Method and Desirability Approach," *Machines*, vol. 10, no. 10, p. 901, 2022. doi: 10.3390/machines10100901.

[17] B. Oemar and W.-C. Chang, "Taguchi method for optimizing process parameters in the production of activated carbon from rubber seed shell," *The International Journal of Advanced Manufacturing Technology*, vol. 107, no. 11–12, pp. 4609–4620, 2020. doi: 10.1007/s00170-020-05344-4.

[18] M. Fan, X. Zhou, S. Chen, S. Jiang, and J. Song, "Study of the surface roughness and optimization of machining parameters during laser-assisted fast tool servo machining of glass-ceramic," *Surface Topography: Metrology and Properties*, vol. 11, no. 2, p. 025017, 2023. doi: 10.1088/2051-672X/acd5ec.

[19] D. Brahmeswara Rao, K. Venkata Rao, and A. Gopala Krishna, "A hybrid approach to multi response optimization of micro milling process parameters using Taguchi method-based graph theory and matrix

approach (GTMA) and utility concept," *Measurement*, vol. 120, pp. 43–51, 2018. doi: 10.1016/j.measurement.2018.02.005.

[20] M. Mia and N. R. Dhar, "Optimization of surface roughness and cutting temperature in high-pressure coolant-assisted hard turning using Taguchi method," *The International Journal of Advanced Manufacturing Technology*, vol. 88, no. 1–4, pp. 739–753, 2017. doi: 10.1007/s00170-016-8810-2.

[21] P. Kumar J, A. Raj, R. K, and I. S. Rout, "Design and Optimization of Friction Stir Welding of Al-Cu BUTT Joint Configuration using Taguchi Method," *Journal of Mines, Metals and Fuels*, vol. 70, no. 8A, pp. 471–479, 2022. doi: 10.18311/jmmf/2022/32029.

[22] I. Maher, M. E. H. Eltaib, A. A. D. Sarhan, and R. M. El-Zahry, "Investigation of the effect of machining parameters on the surface quality of machined brass (60/40) in CNC end milling—ANFIS modeling," *The International Journal of Advanced Manufacturing Technology*, vol. 74, no. 1–4, pp. 531–537, 2014. doi: 10.1007/s00170-014-6016-z.

[23] S. Debnath, M. M. Reddy, and Q. S. Yi, "Influence of cutting fluid conditions and cutting parameters on surface roughness and tool wear in turning process using Taguchi method," *Measurement*, vol. 78, pp. 111–119, 2016. doi: 10.1016/j.measurement.2015.09.011.

[24] Nur Hudha Wijaya, Zanella Oktavihandani, Kunal Kunal, Elsayed T. Helmy, and Phong Thanh Nguyen, "Tympani Thermometer Design Using Passive Infrared Sensor," *Journal of Robotics and Control*, vol. 1, no. 1, pp. 27–30, 2020. https://journal.umy.ac.id/index.php/jrc/article/download/7475/4777.

[25] V. Y. Bhise and B. F. Jogi, "Investigations on the Machining of Inconel X-750: Effect of Cutting Speed, Feed, Forces, Energy Consumption and MRR," *Advances in Multidisciplinary Analysis and Optimization*, vol. 269, pp. 377-389, 2022. doi: 10.1007/978-981-19-3938-9_39.

[26] S. Chauhan and K. Dass, "Optimization of Machining Parameters in Turning of Titanium (Grade-5) Alloy Using Response Surface Methodology," *Materials and Manufacturing Processes*, vol. 27, no. 5, pp. 531–537, 2012, doi: 10.1080/10426914.2011.593236.

[27] G. S. Prihandana, T. Sriani, M. F. Jamaludin, F. Yusof, B. Arifvianto, and M. Mahardika, "Parameters Optimization for Electropolishing Titanium by Using Taguchi-Based Pareto ANOVA," *Metals*, vol. 13, no. 2, p. 392, 2023. doi: 10.3390/met13020392.

[28] T. Hong, F. Ding, F. Chen, H. Zhang, Q. Zeng, and J. Wang, "Mechanical Properties of 6061 Aluminum Alloy under Cyclic Tensile Loading," *Crystals*, vol. 13, no. 8, p. 1171, 2023. doi: 10.3390/cryst13081171.

[29] The Aluminum Association, International Alloy Designations and Chemical Composition Limits for Wrought Aluminum and Wrought

Aluminum Alloys. The Aluminum Association, Inc., ISSN: 2377-6692, pp. 12, Aug 2018.

[30] Suhas Prakashrao Patil, Kishor Laxman Ghadage, and Sahil Vishnu Bhave, "Machinability Studies of Aluminium-based Hybrid Metal Matrix Composites – A Critical Review," *International Journal of Advanced Research in Science, Communication and Technology*, vol. 3, no. 1, pp. 94–99, 2023. doi: 10.48175/IJARSCT-9014.

[31] A. Ercetin, K. Aslantaş, Ö. Özgün, M. Perçin, and M. P. G. Chandrashekarappa, "Optimization of Machining Parameters to Minimize Cutting Forces and Surface Roughness in Micro-Milling of Mg13Sn Alloy," *Micromachines*, vol. 14, no. 8, p. 1590, 2023. doi: 10.3390/mi14081590.

[32] U. K. Sanivada, F. P. Brito, I. P. Moreira, and R. Fangueiro, "Optimization of Processing Parameters of Compression Molding Process by Application of Taguchi and Minitab," *Materials proceeding*, vol. 8, no. 31, pp. 1-2, 2022. doi: 10.3390/materproc2022008031.

[33] K. Othman, J. Abdul Ghani, A. Juri, M. S. R. Mohd, S. Kassim, and C. H. Che Haron, "Optimization of Tool Life and Surface Roughness for Hypereutectic Al – Si Alloys in Face Milling," *Journal of Mechanical Engineering*, vol. 17, no. 2, pp. 27–44, 2020. doi: 10.24191/jmeche.v17i2.15299.

Physical Properties of Graphene

Mohd Rafal Sahudin[1, 2], Muhammed Zourob[3], Muhammad Haziq Noor Akashah[2], Rozina Abdul Rani[2], Siti Rabizah Makhsin[,2]*

[1]Mechanical Engineering Branch, Public Works Department Malaysia, 50480, Kuala Lumpur, MALAYSIA
[2]School of Mechanical Engineering, College of Engineering, Universiti Teknologi MARA, 40450 Shah Alam, Selangor, MALAYSIA
[3]Department of Chemistry, Alfaisal University, Al Zahrawi Street, Al Maather, Al Takhassusi Rd, Riyadh, 11533, SAUDI ARABIA
[*]sitirabizah@uitm.edu.my

ABSTRACT

In the realm of engineering materials, a profound understanding of structural and physical characteristics holds paramount importance due to their ubiquitous presence and diverse applications. This comprehensive review delves deeply into the intricate physical attributes, commonly referred to as "physical properties," of materials based on graphene. It encompasses a wide range of aspects, including magnetic properties, optical behaviours, electrical and thermal conductivities, thickness and layer arrangements, size and shape variations, colour properties, melting points, and hardness traits. This review also explores the intriguing correlation between graphene's thickness and layering and their respective effects on its properties. Special emphasis is placed on the characterization techniques used to unveil these properties, with detailed examples from recent literature illustrating their significance. Advanced instrumentation, such as Atomic Force Microscopy (AFM), Surface Plasmon Resonance spectroscopy (SPR), Raman spectroscopy, Transmission Electron Microscopy (TEM), and X-ray Diffraction (XRD), is harnessed to provide comprehensive insights into the physical characteristics of graphene-based materials. In essence, this concise yet comprehensive review illuminates the exceptional physical properties of graphene-based materials and their potential to revolutionize various industrial sectors.

Keywords: *Physical Properties; Graphene; Mechanical Properties; Single-Layer Graphene; Multi-Layer Graphene*

ISSN 1823-5514, eISSN 2550-164X

https://doi.org/10.24191/jmeche.v12i1.24649

Received for review: 2023-09-25
Accepted for publication: 2023-10-30
Published: 2023-11-15

Introduction to Graphene

Graphene is pure carbon in one atom thick of a single layer of graphite, a very thin and nearly transparent sheet. It conducts heat and electricity with excellent efficiency, and it is extreme for its very low weight. Graphene with complex physical properties and a unique combination of bonded carbon atom structures with its myriad poised to significantly impact the future advancement of nanotechnology, electronics, material sciences, *etc* [1]. The term "physical properties of graphene" refers to the characteristics, attributes, and behaviours of graphene that can be observed and measured without altering the chemical composition of the material. These properties are primarily related to graphene's structure and how it interacts with various physical phenomena.

In general, graphene typically has great physical properties for high mobility of electrons, thermal conductivity, mechanical strength, optical transparency, and electric conductivity [2]-[3]. For instance, the demand for lightweight magnets to open new ways for flexible information storage systems design, adaptable and wearable further highlights the importance of magnetic graphene. Besides, the unbelievable potential use of graphene-based magnets in spintronics is promising, as graphene has exceptional carrier mobility and can easily integrate spin and molecular electronics [4]. Since the first graphene study was published in October 2004, over a hundred articles on graphene have appeared in prestigious journals like Science and Nature [3].

This comprehensive review article addresses a critical need in the realm of graphene research by shedding light on its multifaceted physical properties as illustrated in Figure 1. By delving deep into the intricacies of graphene-based materials, including magnetic behaviours, optical attributes, electrical and thermal conductivities, and more, it significantly contributes to our understanding of this remarkable material. The novelty of this review lies in its ability to bridge the gap between theoretical studies and experimental research, offering valuable insights that are essential for the advancement of graphene science. This comprehensive exploration of graphene's physical characteristics is particularly relevant today, as experimental researchers increasingly focus on these properties, recognizing their pivotal role in various industrial applications and cutting-edge materials research. In an era where graphene is poised to catalyse transformations in nanotechnology and materials engineering, this review article provides a clear aim and underscores its significant importance in guiding future research and applications of this extraordinary material.

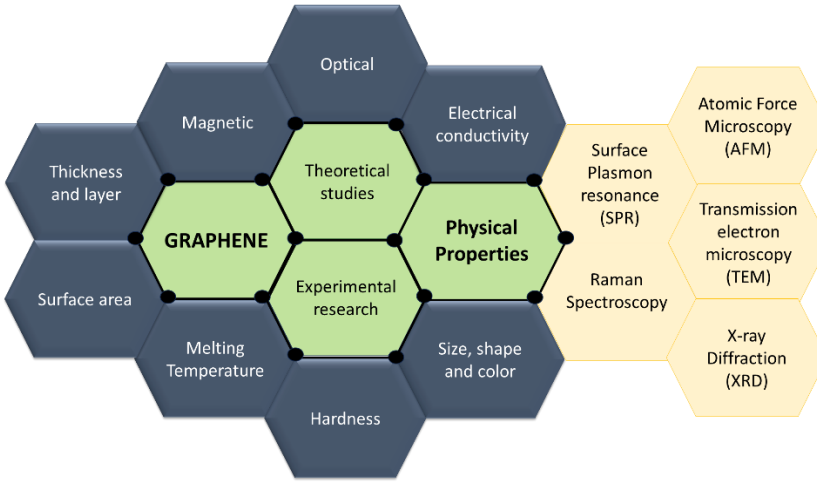

Figure 1: Overview of the content covered in the review

Thickness and Layer of Graphene

Graphene presents diverse stacking configurations, leading to various types, including monolayer or single-layer graphene (SLG), few-layer graphene (FLG), and multilayer graphene (MLG), as depicted in Figure 2. SLG comprises a lone layer of carbon atoms arranged in a hexagonal lattice, where each carbon atom forms sp^2 covalent bonds with its neighbouring atoms. This monolayer graphene is incredibly thin, consisting of just one atom's thickness.

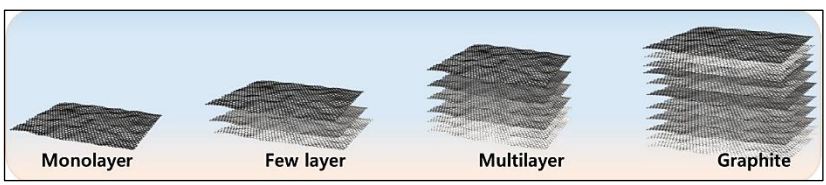

Figure 2: Schematic representation of monolayer (SLG), FLG (with ≤ 5 layers), and MLG (with ≤ 10 layers) versus graphite structure. Reproduced from [5]

The number of stacked layers plays a pivotal role in shaping the properties of graphene. For instance, SLG often exhibits superior properties when compared to both FLG and MLG [5]. SLG showcases extraordinary properties, including exceptional electrical conductivity and impressive

mechanical strength, as summarized in Table 1. SLG has an estimated 1 TPa of modulus of elasticity, a thickness range of about 1−2 nm, 2600 m^2/gr of surface area, 2.25 g/cm^3 an actual density and 4840−5300 W/mK of thermal conductivity [6]-[7].

On the contrary, FLG and MLG refer to graphene structures consisting of multiple layers of carbon atoms stacked atop each other. These layers can adopt various stacking configurations, leading to variations in MLG's properties, which depend on the number of layers and their stacking arrangement. Some types of SLG may retain some of its unique characteristics, while others may exhibit properties more akin to bulk graphite. Thicker MLG can still possess distinct attributes, although they may differ from those of SLG due to interlayer interactions. These changes encompass modifications in electronic behaviour, mechanical strength, optical transparency, and thermal conductivity, as well as the emergence of interlayer interactions and quantum effects. Each variant of graphene finds suitability for different applications [5].

Several techniques are proposed to measure the graphene thickness including one technique based on the image contrast of the graphene layers. Examples of this image contrast method include narrow-band illumination, selecting a suitable substrate, and reflection and contrast spectroscopy.

Table 1: Selected important physical and mechanical properties of single-layer graphene. Adapted with permission from [6]-[7]

Properties	Value
Bond types	sp^2
Layer number	Single layer
Crystal structure	Hexagonal
Dimension	2-D
Purity degree (%)	99
Mass (bulk) density (g/cm^3)	~0.3
Real density(g/cm^3)	2.25
Thickness (nm)	~1 – 2
Surface area (m^2/g)	2600 – 2630
High-temperature resistivity	−75 + 200 °C between not changing
Thermal conductivity (W/mK)	4840 – 5300
Electron mobility cm^2/ (V. s)	$\sim 0.015\times10^5 – 2.5\times10^5$
Elasticity module (TPa)	~0.5 – 1
Resistivity (Ω-cm)	10^{-6}
Transmittance	>95% for 2 nm thick film >70% for 10 nm thick film
Coefficient of thermal expansion	$–6\times10^{-4}$/K
Tensile strength (GPa)	130

The total colour difference (TCD) approach is a method that combines the International Commission on Illumination colour space with the reflection spectrum for accurate and rapid identification of graphene images. By restricting the light source's wavelength range, the TCD between graphene and a substrate can be improved when viewed by a regular light source [8]-[9]. Figure 3 shows an example of a TCD contour plot as a function of the number of graphene layers for different preferential dielectric films such as silicon nitride (Si_3N_4), silicon dioxide (SiO_2) and aluminium dioxide (Al_2O_3) thicknesses. Work reported by [8] improved the TCD contour of the graphene layer and substrate by narrowing the wavelength range of the light source. The outcomes of this measurement deliver a useful analysis of the graphene layer simply by measuring the different colour bands, thus showing that this technique is a non-destructive method for physical property graphene identification.

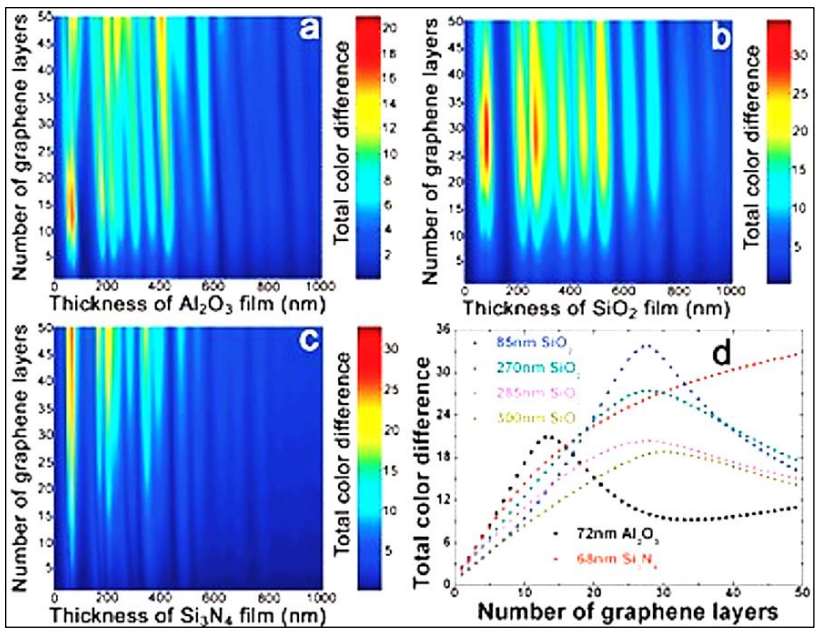

Figure 3: TCD contour plot using a different substrate with; (a) Al_2O_3 film, (b) SiO_2 film and (c) Si_3N_4 film, and (d) summary of TCD versus the number of graphene layers. Reprint with permission from [8]

[8] reported the graphene layer measurements were performed using contrast spectra for a SLG, a bi-layer and MLG on silicon (Si) substrate using SiO_2 as a capping layer and white light source. To compare the result, the calculations were made using Fresnel's reflection law and the true analysis was

obtained with a 2% standard deviation, thus showing that this contrast spectrum gives huge benefits including a straightforward, swift method for measuring graphene layers' morphology and efficiency. Later, an analytical method and a graphical method were used to calculate the number of graphene layers based on contrast spectra [9]-[11].

Furthermore, the precise determination of the number of layers and lateral dimensions of graphene film thickness can be achieved through Atomic Force Microscopy (AFM) [5], [12]. AFM is a high-resolution microscopy technique renowned for its atomic-scale resolution. It empowers the characterization of diverse material properties, including thickness, grain height, topographic features, phase diagrams, and surface roughness. Figure 4 presents topographical AFM images obtained during the measurement of SLG, two-layer graphene (2LG), and four-layer graphene (4LG). Notably, numerous adsorbed contaminants are observable on the surface of SLG (refer to Figure 4a). However, as the graphene layer count increases, these contaminants diminish, as evidenced by the topographical images from AFM (Figure 4b and 4c). This phenomenon arises from the heightened thermodynamic stability of graphene with an increasing number of layers. Specifically, the adjustment of C-C bond lengths results in the formation of wrinkles or the adsorption of molecules, which becomes notably reduced for 2LG and disappears as the graphene films become thicker [12].

[12] conducted a study utilizing AFM to determine the thickness of a graphene flake. The corresponding histogram revealed that the flake's thickness ranged from 1.1 to 1.6 nm. Considering an interlayer distance of 0.33 nm, it can be estimated that the graphene flake consists of approximately 4 to 5 layers. Consequently, it falls within the category of FLG.

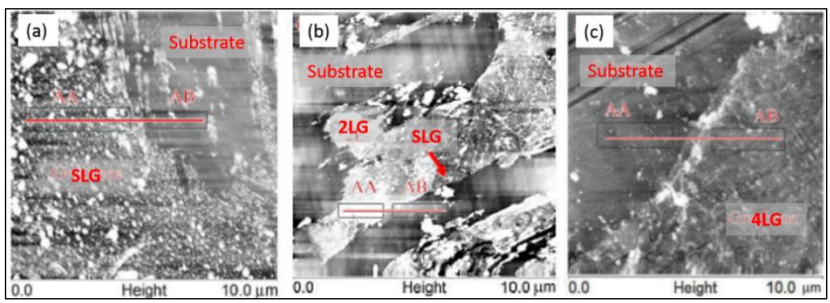

Figure 4: AFM results of topographical images for; (a) SLG, (b) 2LG, and 4LG. Reproduce with permission from [13]

The thickness of graphene film can also be measured using Surface Plasmon Resonance (SPR) as reported by [13]. SPR method is simple and well-suited for measuring thin films made from nanomaterial, although the

thickness is less than 10 nm. Their work demonstrated that the obtained SPR measurements are greatly decreased compared to AFM. The graphene film thickness was linearly increasing with an increasing number of printing cycles. Furthermore, the complex refractive index (RI) of the printed graphene flake films based on SPR provides more rigorous information on the optical absorption than that previously available using a combination of AFM and the extinction coefficient of mechanically exfoliated graphene flakes [14].

Raman spectroscopy is the foremost method for precisely assessing the average layer thickness of graphene, thanks to its exceptional sensitivity to molecular geometric structures and bonding [5], [15]-[16]. Its primary application lies in determining the number of graphene layers, as exemplified in Figure 5. The Raman spectra of graphene reveal essential insights through three key bands: the G-band (around 1587 cm^{-1}), originating from in-plane vibrational modes of sp^2 hybridized carbon atoms within the graphene sheet and highly sensitive to layer count; the D-band, which signifies defects or disorder and intensifies with increased defects, displaying resonant behaviour; and the 2D-band, consistently strong in graphene and used for layer thickness determination, relying on both its position and shape.

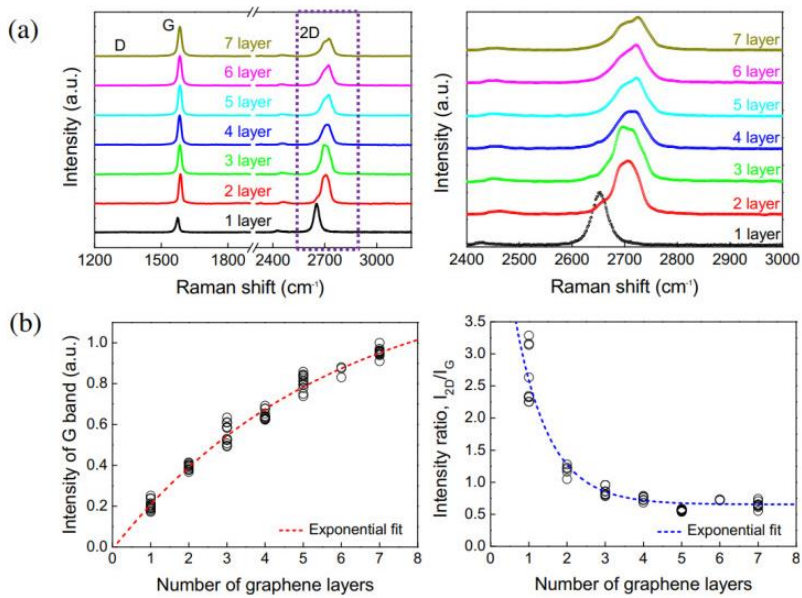

Figure 5: Example of Raman spectra of 1 to 7 layered graphenes; (a) spectral evolution of G and 2D bands, and (b) intensities of G-bands and intensity ratios of 2D vs. G bands. Reproduced with permission from [16]

Additionally, the peak intensity ratio of the 2D and G-bands aids in the identification of SLG, where a ratio of I_{2D}/I_G equalling two indicates defect-free SLG. Raman spectroscopy not only distinguishes SLG from graphite but also precisely determines layer thickness, even at atomic layer resolution. This exceptional capability establishes Raman techniques as indispensable tools in contemporary graphene research [14].

Magnetic Properties of Graphene

Magnetic materials are very useful in today's technology. It is used in data storage, power generation, and many other areas. Typical magnetic materials are metal-based including iron, cobalt, nickel, *etc*. These metals can show heavy magnetism because of their *d* and *f* electrons and can coordinate their spins to generate magnetic moments, which align along the direction of the applied magnetic fields. Almost all magnetic materials today contain elements of *3d*- or *4f*- transition metals, and they are usually ferromagnets at room temperature [4], [17]-[18].

Graphene, initially non-magnetic, has been transformed into a magnetic material through innovative techniques. Magnetic properties in graphene are closely tied to the formation of magnetic domains. Typically, ferromagnetic materials possess a single magnetic domain, where all magnetic dipoles align due to exchange energy. This energy encourages simultaneous alignment of electron spins and magnetic dipole moments. Magnetic domain formation minimizes exchange energy, enhancing material stability. Creating these magnetic domains in graphene during magnetization holds immense technological potential.

Various methods, including functionalization, doping, and atom addition, can introduce magnetism by breaking the electronic structure's symmetry locally, resulting in magnetic moments. Vacancy and edge defects offer another route to magnetization. By removing one carbon atom and rearranging others in a vacancy defect, a magnetic moment arises due to a remaining dangling bond. Experimentally, vacancy defects are created through processes like ionic bombardment and graphene oxide reduction. Among these methods, the highest magnetization occurs with sulphur and nitrogen doping, albeit at extremely low temperatures [17].

In graphene, the coexistence of π- and σ-bonding permits the carrier spin to change as well, as this change produces the magnetic property because of the lawful magnetic order. The existence of *s* and *p* electrons alone makes anticipating magnetism counterintuitive. Graphene also becomes an interesting candidate for novel spintronic devices as it has a long spin diffusion length, thus triggering a quest to incorporate the electrical and magnetic spin degrees of freedom [4]. Spintronics is considered an emerging technology based on the spin of the electron and molecular electronics associated with

magnetic moment principles, in which carbon-based magnetism could theoretically be of value [19].

However, the long-range ordering in graphene can cause complications for magnetism in 2D systems due to the lack of *d* and *f* electrons, as commonly found in conventional magnetic materials. The magnetism phenomenon can be described based on localized electronic states dependent on spin polarisation. These properties are highly affected by the state of the edge [20]. Furthermore, the graphene sheet provides a versatile medium for surface adjustments for tuning the electronic and magnetic characteristics. From *G* to *F-G-H* to *G-H* to *F-G-F* and to *H-G-H* (*G* is a graphene atom, *H* is a hydrogen atom and *F* is a fluorine atom), the properties can be tuned from nonmagnetic to magnetic, from direct gap to indirect gap or metallic to semiconducting, depending on the coverage of atoms used for the surface modification and species [21].

[22] reported on the investigation of magnetic properties, electronic properties and surface structure of the graphene layer on the lattice-matched surface of a ferromagnetic material (nickel; 111). The induced magnetic moment of the carbon atoms is evident from both spin-resolved photoemission and x-ray magnetic circular dichroism analyses. Investigations of graphene's magnetic properties are prepared by two different methods: thermal exfoliation of graphitic oxide (EG) and reducing single-layer graphene oxide (SLGO) with hydrazine hydrate. The result discloses that dominant ferromagnetic interactions coexist along with antiferromagnetic interactions in all the samples, which can be observed in phase-separated systems. The experiment concluded the magnetic properties of graphene samples depend on the area of the sample and the number of layers. As such, small values of all these variables contribute to the magnetization of the sample being greater. The magnetic properties of graphene are influenced by the molecular charge transfer that interacts with an electron donor and, thus has a greater influence than with electron-withdrawing groups like tetracyanoethylene [23].

In a study by [18], it was found that magnetism could be induced in graphene by evaporating graphene droplets under high temperatures and an external magnetic field. This innovative approach applied temperature, magnetic field, and strain simultaneously to graphene flakes, resulting in magnetization. As a consequence, all these methods led to the creation of ferromagnetic graphene powders (FGPs). The magnetization of FGPs was confirmed through measurements using a vibrating-sample magnetometer (VSM), as shown in Figure 6. This magnetic transformation can be attributed to changes in the electronic system and lattice structure of graphene. A summary of the magnetic properties of graphene is tabulated in Table 2.

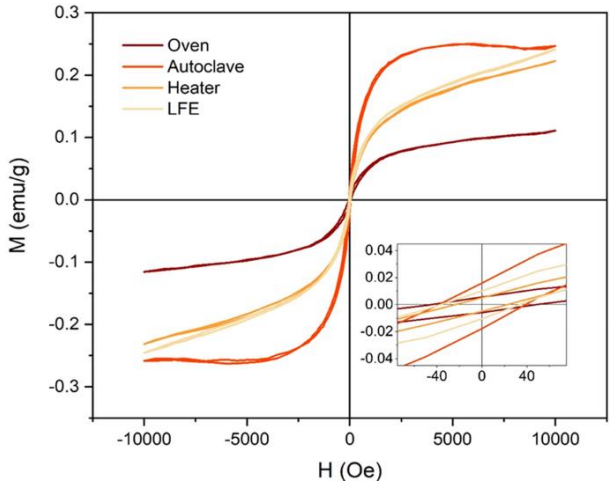

Figure 6: VSM Diagram of FGPs, illustrating the influence of temperature, pressure, and magnetic field on magnetism. The diagram includes hysteresis loops for all samples, with a zoomed-in section showing the range $-90 < H < 90$ (Oe) and $-0.045 < M < 0.045$ (emu/g) in the inset. Reproduced with permission from [18]

Table 2: Summary of graphene magnetic properties

Magnetic Property behaviour	Summary	Ref.
Methods for inducing magnetism	Functionalization, doping, and atom addition can introduce magnetism by breaking electronic symmetry.	[24]
	Vacancy and edge defects result in magnetism due to dangling bonds.	[25]
	Sulphur and nitrogen doping are effective at low temperatures.	[26]
Synthesis of Ferromagnetic Graphene Powders (FGPs)	High-temperature processes with magnetic field and strain can lead to magnetization Require high-temperature evaporation and external magnetic fields. VSM can be used to measure the magnetization of FGPs.	[27]

Optical Properties of Graphene

Graphene is composed of a monolayer of carbon atoms arranged in a honeycomb grid, where hybridized sp^2 carbon atoms form robust σ-bonds within the plane, and unhybridized p-orbitals overlap with adjacent atoms to create π-bonds. While σ-bonds primarily contribute to graphene's structural integrity, it is the π-bonds that define its optical and electronic properties. The interaction of graphene with electromagnetic radiation is especially fascinating due to the confinement of electrons in two dimensions. Graphene boasts a relatively simple band structure characterized by zero band gaps, but its optical properties are far from straightforward [22]. Unfortunately, the absence of bandgaps in graphene poses a significant challenge to its application in modern electronic components.

A simulation work reported by [28] showed that the stacking of SLG with one molybdenite monolayer formed hetero-structures generated a small bandgap around 2.5 meV showing that value can modulate for low temperature and electronic applications. In addition, this heterojunction showed some significant changes in complex dielectric function and its associated properties in the visible-light spectrum, which could be useful for future technologies and applications.

The massless Dirac fermion nature favours graphene with a universal optical response, as presented by the fine-structure constant (α) as shown in Equation 1.

$$\alpha = e^2/hc \approx 1/137.036 \quad (1)$$

where e is the electron charge, h is Planck's constant, and c is the speed of light. Experimental measurements will possibly be used to determine a fundamental constant of the universe. The graphene absorption coefficient: $\pi\alpha$ is ≈ 2.3% in the infrared region, making graphene visible without the need to observe under a microscope. The amount of light absorption may reach 10 % or even more at higher frequencies, due to van Hove singularities at the edge of the region. For graphene multilayers, the energy of visible light; $h\omega$ is around 1 to 2 eV, which is considerably higher than the Fermi energy in graphene and the electron hopping energy between graphene layers; thus, the N-layer of graphene's light absorption is Nπα [29].

Dirac Fermions in graphene are among the strongest light-matter interactions known to any system, with an optical transmission that is regulated by a constant fine structure. The pristine graphene system is a valuable testbed for table-top physics studies. On the other hand, graphene's optical properties are often commonly tuneable, either using electrical gate modulation or by the presence of defects, the effects of quantum confinement and the presence of interfacial water layers [30].

The optical properties of the electron-hole distribution of the optical excitation for the SLG have been revealed by the charge different density (CDD) method. The van der Waals interaction by edge atoms is found as a primary binding in the ground state between graphene and boron nitride as shown in Figure 7. In addition, the result of CDD shows that through optical excitation in the visual spectral region, there is no charge transfer between boron nitride and graphene. Theoretical studies reveal that for graphene-based nano-photonic applications, boron nitride is an excellent substrate for it. The findings can provide a thoughtful understanding of future optical and electrical applications of graphene/boron nitride [31]. A summary of graphene's optical properties is shown in Table 3.

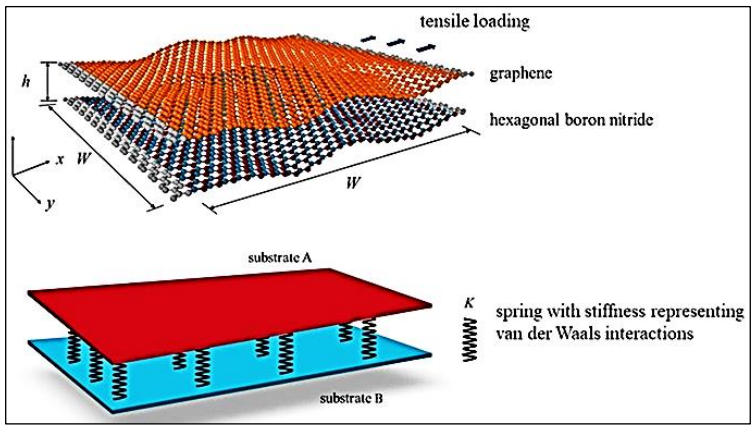

Figure 7: Van der Waals heterostructure of graphene and hexagonal boron nitride. Reprint with permission from [32]

Electrical Conductivity of Graphene

MLG has higher electrical, thermal conductivity and current-carrying potential than copper (Cu). High electrical conductivity can be generated by controlling the thickness of the MLG on an insulator formed by diffusion-controlling interlayer (IL) as first reported by [41]. This process caused the enlargement of MLG grain as the nucleation of the MLG was restrained, thus significantly affecting the crystallinity of the forming semiconductor layer. The reported electrical conductivity (2700 S/cm) was the highest measured value among other works on MLG layers and even exceeded the value of a highly oriented pyrolytic graphite (HOPG) synthesized at 3000 °C or higher.

Table 3: Summary of optical properties of graphene

Optical properties behaviour	Summary	Ref.
Generating small bandgap	Simulation work by stacking of SLG with one molybdenite monolayer formed hetero-structures generated ~2.5 meV revealing that value can modulate for low temperature and electronic applications.	[28]
Optical response	Graphene exhibits a universal optical response due to its massless Dirac fermion nature, described by the fine-structure constant (α).	[33]
Fine-structure constant (α)	$\alpha = e^2/hc \approx 1/137.036$, where e is the electron charge, h is Planck's constant, and c is the speed of light.	
Infrared absorption	The graphene absorption coefficient, $\pi\alpha$, is $\approx 2.3\%$ in the infrared region, making graphene visible without the need for microscopic observation.	[34]
Enhanced absorption at higher frequencies	Graphene can absorb over 10% of light at higher frequencies due to van Hove singularities at the edge of the region.	[35]
Graphene multilayers	For N-layer graphene, light absorption is $N\pi\alpha$, with energy levels in the visible light range (~ 1 to 2 eV).	[36]
Tuneability	Tuneable through electrical gate modulation, defects, quantum confinement, and interfacial water layers.	[37]
Charge distribution and interaction	The charge distribution reveals the primary van der Waals interaction at the ground state between graphene and boron nitride.	[38]
Charge transfer	Optical excitation in the visible spectral region shows no charge transfer between boron nitride and graphene, making boron nitride an excellent substrate for graphene-based nano-photonic applications.	[39]
Future applications	These findings provide insights into potential optical and electrical applications of graphene, particularly in combination with boron nitride.	[40]

[42] reported graphene with metal nanowires (Graphene/NW) substantially decreases the resistance of the graphene films. Graphene/NW films with a sheet resistance compared to that of the graphene's intrinsic resistance have been formed and verified as a transparent electrode substituting

one of the Indium Tin Oxides (ITO) films in ElectroChromic (EC) devices as shown in Figure 8. The result shows that the optical modulation and repeatable cycling were stable and homogenous, resulting from an integration of Graphene/NW films as a transparent electrode in EC devices, thus demonstrating their excellent potential for global optoelectronic device applications.

Conductive composites are considered for any composite that has substantial electrical conductivity, whereby the electrical conductivity can be increased by the addition of conductive fillers such as carbon-based materials including graphene into the matrix phase. The conductive filler particles begin to come into contact with each other as their content increases forming a continuous path that makes the free electrons travel easily and thus allows the composites to conduct electricity [43]-[44].

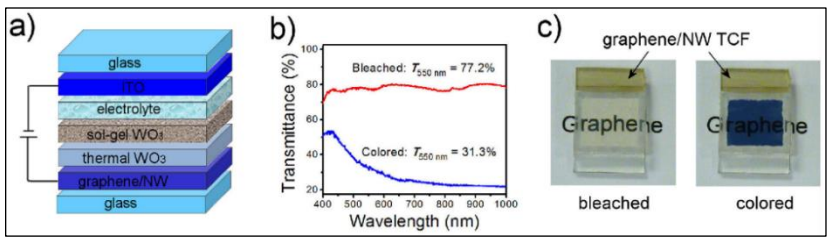

Figure 8: (a) EC device structure with one of the transparent electrodes using graphene/NW, (b) measurement of optical transmittance spectra of the EC device, and (c) the photograph of the transparent electrode of the EC device with a yellow area is a conductive silver paste consisting of Graphene/NW. Reprinted with permission from [42]

For instance, silicon nitride based (Si_3N_4) ceramics have quite notable thermal properties and mechanical properties. However, silicon nitride (Si_3N_4) also possesses electric insulators, hence the addition of 25% volume of graphene nanoplatelets (GNPs) changes the properties of these composites with the highest electrical conductivity (40 S/cm) recorded for these ceramics with added conductive particles. A desired orientation of GNPs occurs by applying plasma spark sintering by compaction and pressure-assisted densification process. As a result, the electrical conductivity measured along the direction perpendicular to the plasma spark sintering pressing axis is more than one order of magnitude higher than that measured along the parallel direction [45].

Moreover, embedding graphene into polymer matrices to form advanced multifunctional composites will dramatically enhance the electrical conductivity, elastic modulus, tensile strength and thermal conductivity to take full benefit of its application properties. Therefore, aerospace firms sought to

make conductive composites rather than metals as conductive composites are lightweight, have high strength, and have a high electrical conductivity that can protect aircraft systems from lightning strikes and electromagnetic interference [46]. A summary of graphene's electrical conductivity can be found in Table 4.

Table 4: Summary of electrical conductivity of graphene

Electrical conductivity behavior	Summary	Ref.
High electrical conductivity	MLG exhibits significantly high electrical conductivity, even surpassing highly oriented pyrolytic graphite (HOPG) synthesized at very high temperatures.	[41]
Thickness-dependence	Careful thickness control of MLG on an insulator can lead to high electrical conductivity.	[47]
Graphene with metal nanowires (Graphene/NW)	Combining graphene with metal nanowires in films results in materials with significantly reduced resistance, making them suitable as transparent electrodes in optoelectronic devices.	[48]
Conductive composites	Adding graphene to composite materials increases their electrical conductivity.	[49]
Conductive ceramics with GNPs	Incorporating GNPs into ceramics significantly enhances electrical conductivity. *E.g.* Addition of 25% volume of GNPs into Si_3N_4 changes the properties of these composites with the highest electrical conductivity of 40 S/cm.	[50]
Composite applications	Embedding graphene into polymer matrices for aerospace applications dramatically improves electrical conductivity, making them ideal for lightning strike protection and electromagnetic interference shielding.	[46, 51]

Thermal Conductivity of Graphene

The thermal conductivity, K, of a material, is defined as its capability to conduct heat. Equation 2 shows the relationship of local heat flux, q with the K with respect to the local temperature gradient, ∇T described by Fourier's law for heat conduction.

$$q = -K\nabla T \tag{2}$$

Over a wide temperature range, K is a function of T and in anisotropic materials, it relies on crystal orientation and this multi-dimensional array of numerical values can be measured by a tensor [52].

The thermal conductivity of SLG is measured in the range of 3000 – 5000 W/mK, making the value higher than the thermal conductivity of graphite (2000 W/mK). This is due to SLG being considered the basic structural component of graphite, the thermal conductivity of bulk materials comprising graphene nanoflakes is considerably supposed to be anisotropic, depending on the number of layers stacked in the sheet, the size of graphene flakes and the agglomeration state of the flakes. Thus, the thermal conductivity of graphene can be said to strongly depend on the stacking number [53].

The anisotropic bonding, and strong and low mass of the carbon atoms, make graphene and related materials unique. For example, sp^2 bonds between the carbon atoms are considered the strongest. In contrast, the adjacent graphene sheets are bonded to each other by weak van der Waals forces. This result is in agreement with [54], which also reports graphene to be highly conductive, containing a K value around 4000 W/mK.

The first simulation work performed by [56], predicted the graphene's thermal conductivity simulated at 6000 W/mK (at room temperature). Later, another experiment [55] was carried out to find the graphene's true thermal conductivity and graphene thermal conductivity to be 2000 – 4000 W/mK. Furthermore, an optical method was used to measure graphene's thermal conductivity and the reported value of thermal conductivity is about 5000 W/mK [56]-[57].

The method for measuring the thermal conductivity of graphene using confocal micro-Raman spectroscopy. Here, laser light based on the centre of the suspended graphene sheet generates heat in the graphene. Laser excitation spreads laterally through the graphene-produced heat due to the air's negligible thermal conductivity. Hence, although a small amount of heat propagated from the centre of the graphene will result in a noticeable temperature variant. Two components may describe the heat distributed from the graphene sheets' top layer: the radial heatwave and the plane-wave heat front [58].

The thermal characteristics of graphene have previously been investigated through Raman spectroscopy [38]-[40]. In these investigations, the focus was on calculating the Raman temperature shift coefficient for the G peak in graphene spectra, with an emphasis on single-layer, bi-layer, and multi-layer mechanically exfoliated graphene. The detected shift in the peak was attributed to the elongation of C-C bonds, leading to elevated stress levels, which were particularly pronounced in the case of graphene on SiO_2/Si substrates, as illustrated in Figure 9. For instance, the reactive ion etching (RIE) method was used to produce trenches on silica-based (Si/SiO_2) substrates and later, graphene was suspended over the trenches with a width of 2 – 5 μm and a depth of 300 nm [59]. Additionally, it was established that annealing graphene leads to shifts in the G, D, and 2D peaks, along with an

increase in compressive stress. Another factor contributing to the G peak shift involves lattice thermal expansion and phonon-phonon interactions [60].

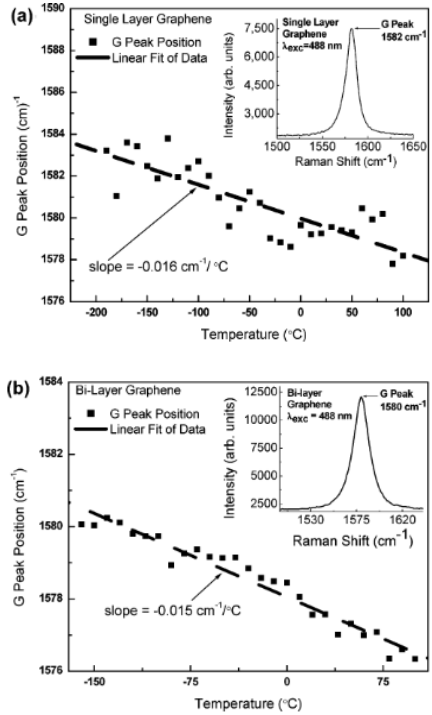

Figure 9: Temperature-dependent G-peak frequency in; (a) SLG, and (b) BLG with G-peak shape insets, and determination of the G-peak temperature coefficient. Reprint with permission from [60]

In a recent study by [61], Raman spectroscopy was employed to unveil intriguing insights about single-layered graphene's resilience at high temperatures, particularly at 600 °C. Surprisingly, it was found that the decomposition temperature of SLG exhibits a linear dependency on the coefficient of thermal expansion (CTE) of the underlying substrate. Furthermore, the study revealed distinct mechanisms governing the decomposition of graphene in different environments: air and vacuum. In both air and vacuum environments, the initiation of decomposition was linked to the extension of C-C bonds. However, a crucial distinction emerged: in the presence of oxygen in the air, the heightened strain amplified graphene's reactivity with oxygen, leading to its degradation. Conversely, in a vacuum environment, the strain alone was sufficient to induce decomposition.

The thermal conductivity (K) from the plane-wave heat front can be demonstrated in Equation 3 while for the case of the radial heatwave, Equation 4 can be used to calculate the thermal conductivity.

$$K = (L/2S)(\Delta P/\Delta T) \quad (3)$$

$$K = \chi_G(1/2h\pi)(\delta\omega/\delta P)^{-1} \quad (4)$$

Whereby L is the distance from the center of the graphene to the heat sink, $\Delta P/\Delta T$ is the changes of the heating power with respect to the temperature change and cross-sectional area, $S = h$ x W; where h is SLG thickness and W is layer width. For the temperature coefficient, χ_G is $-1.6 \times 10^{-}$ and $\delta\omega/\delta P$ designates for the slope of the G peak position shift as reflecting the heating power change.

As shown in Figure 10, the G peak excitation of Raman spectroscopy is power dependence measured for the suspended graphene layers. The increment in laser power induced an increment in the intensity of the spectra and redshift the position of the G peak. The slope from the graph in Figure 10 is represented by $\delta\omega/\delta P_D$ which is measured to be around -1.29 $cm^{-1}mW^{-1}$, where P_D is the total dissipated power [61]-[62]. When these data values are substituted into Equation 4, the thermal conductivity of freely suspended graphene is calculated at approximately 2000 ~ 4000 W/mK, which is the highest K value reported of any known material [54].

Graphene has an extraordinary thermal conductivity of up to $(5.30 \pm 0.48) \times 10^3$ W/mK measured at room temperature using a non-contact optical-based technique [59]. Measurements can be made for a SLG suspended over a large trench in the Si/SiO_2 substrate [63]-[64]. The measurements were conducted using a non-contact technique of micro-Raman spectroscopy. The quantity of power dissipated in the graphene and the subsequent temperature rise was measured from the position of the spectra and the G peak of graphene integrated intensity. The extremely high thermal conductivity in the range of 3080 – 5150 W/mK and the mean phonon-free path of around 775 nm near room temperature were determined for a set of graphene flakes [64]. This data shows that graphene as an excellent thermal management material can be applied to future nanoelectronics circuits [59].

For graphene multilayers, the weak coupling between graphene layers decreases the in-plane thermal conductivity and scatters the propagating phonons. The measurement of thermal conductivity for thicker multilayers (1 to 10 graphene layers) can approach the value of graphite in the range of 600 – 2000 W/mk. As the number of graphene layers increases from 2 to 4, the in-plane thermal conductivity drops from 2800 to 1300 W/mK [29].

The high thermal conductivity of graphene can be applied as thermal interface materials created within the composites for electronics devices which are efficient and faster in transferring the heat away from the circuits compared

to the traditional materials. For instance, [65] reported Cu/graphene nanosheet composites fabricated at 800 °C by the hot-pressing method using graphene and Cu as initial materials. Graphene content was varied from 1 %wt to 5 %wt. From the investigation of the physical properties of these composites, the relative density was found to increase by increasing the graphene content which reached the highest value at 96.78% for 5 %wt of graphene content. In addition, the composites show anisotropic properties as the pressure in the vertical direction is higher than the pressure in the parallel direction. Moreover, as the graphene content increases, the activities of thermal conductivity and electronic conductivity of the composites were decreased with the minimum of thermal conductivity and electric conductivity was measured at ~3 %wt - 4 %wt of graphene contents.

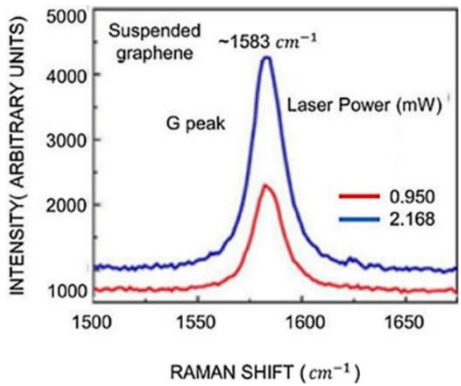

Figure 10: G-peak region counts at two different levels of power measured using Raman spectroscopy [59]

In a recent study by [71], they looked into how adding graphene nanoplatelets (GNP) to recycled polycarbonate (PC) affects thermal properties. The results showed that GNP had little impact on thermal stability and glass transition temperature (T_g) for both virgin and recycled PC when compared to PC without GNP. Recycled PC was weaker and less heat-resistant than virgin PC, but it improved when mixed with GNP. The best thermal stability for virgin PC/GNP composites came with 1 %wt GNP (a 2.74% increase), while recycled PC/GNP composites achieved their highest thermal stability at 10 %wt GNP (a 2.42% increase). However, recycled PC-based composites were less thermally stable than virgin PC-based composites under the same GNP loading. T_g for virgin PC/GNP initially increased with 1 wt.-% GNP and then decreased with more GNP. For recycled PC/GNP, T_g showed irregular changes with GNP loading. A comprehensive summary of graphene's thermal conductivity is presented in Table 5.

Table 5: Summary of thermal conductivity of graphene

Thermal conductivity behaviour	Summary	Ref.
Single layer of graphene (SLG)	SLG exhibits high thermal conductivity in the range of 3000 - 5000 W/mK, surpassing that of graphite (2000 W/mK).	[65]
Anisotropic thermal conductivity	The thermal conductivity of graphene depends on crystal orientation, making it anisotropic. This anisotropy is contingent on several factors, including the number of layers stacked in the sheet, the size of graphene flakes, and the agglomeration state of the flakes.	[59], [64]-[66]
Multilayer of graphene (MLG)	It is evident that the thermal conductivity of graphene is influenced by the stacking number of layers. The weak coupling between graphene layers decreases the in-plane thermal conductivity and scatters the propagating phonons. E.g. the measurement of K for thicker multilayers (1 to 10 graphene layers) can approach the value of graphite in the range of 600 – 2000 W/mk.	[29]
Strong carbon bonds	Graphene's strong sp^2 carbon bonds contribute to its high thermal conductivity.	[59]
Variability in reported values	Experimental measurements of graphene's thermal conductivity have reported values ranging from 2000 to 6000 W/mK.	[67]
Measurement techniques	Often measured using techniques such as confocal micro-Raman spectroscopy.	[68]
Composite applications	The high thermal conductivity of graphene makes it suitable for thermal management materials in electronic devices.	[69]
Graphene Nanoplatelets (GNP) in Polycarbonate Composites (PC)	The addition of GNP to recycled PC enhances thermal stability and glass transition temperature, offering the potential for composite applications.	[70]

Size, Shape, and Colour of Graphene

There are many ways to characterize graphene and find its properties, such as using spectroscopy techniques including Raman spectroscopy, X-ray

diffraction [71], TEM [72], *etc*. [73] reported that by examining using TEM, graphene was observed as a transparent figure and stable under high energy electrons in contrast to GO was observed as semi-transparent which is not stable under high energy beam. Here, the morphology of GO was demonstrated as a thick, rough surface with flat flake layers, irregular in-shape with non-uniform particle size and not crumpled. However, a graphene sheet film was observed with a thin flat flake with crumpled morphology and composed of a wrinkled flake structure.

In Figure 11, a low-magnification TEM image provides a glimpse of graphene nanosheets. These nanosheets, some spanning hundreds of square nanometers, appear perched atop the copper grid, resembling the delicate, undulating waves of crumpled silk veils. The graphene nanosheets exhibit a rippled and interwoven structure, creating a mesh-like appearance. Remarkably, they maintain their transparency and structural stability when exposed to the electron beam. In Figure 11a, the most transparent and unremarkable regions, indicated by arrows, are likely monolayer graphene nanosheets. Additionally, Figure 11b reveals the presence of scrolled graphene nanosheets in the sample [48].

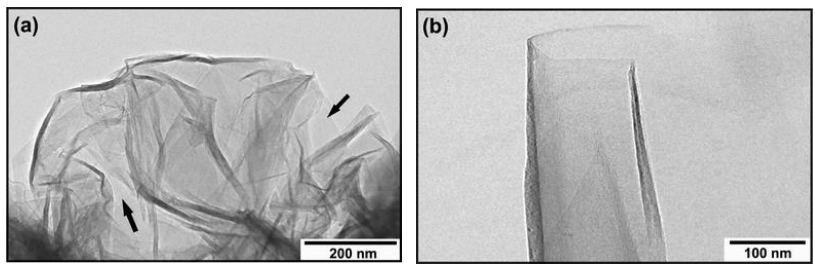

Figure 11: (a) TEM characterization of graphene nanosheets – low magnification overview resembling crumpled silk with arrows showing mono-layer (SLG), and (b) a close-up of scrolled nanosheet structures. Reproduced with permission from [48]

Dynamic dispersion of light is a simple and fast method of characterizing the size of the graphene nanosheets and the exfoliated graphene oxide [73]. This method is more reliable for spherical particles [74] and the dynamic dispersion of light would not measure the particle size of graphene nanomaterial if the sample is polydisperse [75].

Furthermore, two methods have started emerging in recent years to characterize nanoparticles: nanoparticle tracking analysis and asymmetric flow field-flow fractionation. Nanoparticle tracking analysis has given an average size of ca. 150 nm and higher resolution than dynamic dispersion of light and approximate concentrations. It has been indicated that the dynamic dispersion of light given the average particle size of graphene which the intensity was a

bias towards larger particles. Asymmetric flow field-flow fractionation separated different populations of graphene nanosheets with different gyration radii (centered at approximately 360 nm) and provided information on the graphene structure and shape of the particles [76]-[77].

Other characterization such as XRD can be used to determine the number of graphene layers. For instance, the average number of graphene layers decreased from 15 to 3 as the average sp^2 crystallite size decreased from 17.33 nm to 14.75 nm. Moreover, the increased ID/IG ratio from Raman spectroscopy measurement demonstrated an increase in the quantity of sp^2 domains with the defect density increment after reduction [78].

The graphene color deposited on the substrates can be found using an imaging microscope and AFM measurements [79]-[81]. The TCD method (as described in detail in the previous section: Thickness and Layer of Graphene) of assessment assesses the color difference between the graphene layer and the underlying substrate. With this technique, one can figure out the most viable thickness of the dielectric layer (the single layer of metals and insulators or the layered structure) to ensure the optimum optical transparency of a graphene-based multilayer.

Colour is a useful technique for visual analysis. It can be beneficial when detecting and judging the thickness of graphene and multilayer approaches [81]. The data on the colors of graphene and GO were confirmed by the method of an optical microscope and profilometer. Here, GO has a lower extinction coefficient than graphene, which causes the reflectance of GO to fluctuate more clearly over a range of material thicknesses. Consequently, the resulting colors of GO changed continually as a function of the material thickness. However, the colors of the graphene multilayer became saturated without periodic change.

In summary, manipulating and visualizing the optical contrast of SLG and other 2D materials will lead to new knowledge about the various aspects of light and matter interactions with atomic thickness. The optical properties of SLG can be tuned by gating, and it can be demonstrated and manipulated in color contrast. Another important potential application is in ultra-thin, versatile color displays. Under white light using broadband photon management, scalable large-area color displays the novel chromatic color contrast optical visibility of SLG. The optical absorption of SLG on fused quartz (SiO_2) substrate is drastically enlarged to more than 10 % from ∼1.4 at wavelength, λ of the scan range between 560 − 990 nm (from yellow to near-infrared spectral regimes). The current process is much more appealing without the excessive artificial color utilized with SLG [82]. The characterization methods employed to determine the size, shape, and color of graphene are summarized in Table 6.

Table 6: Summary of characterization method in determining size, shape and colour of graphene

Characterization method	Summary	Ref.
Size measurement (dynamic dispersion of light)	Methods like nanoparticle tracking analysis and flow field fractionation provide size and shape details	[83]
Number of layers (XRD and Raman)	Determines layer count based on crystallite size of XRD spectrum. Thicker graphene layers exhibit a higher ID/IG ratio in Raman spectroscopy, indicating a greater number of defects or discontinuities in their structure compared to single-layer graphene (SLG) measurements.	[84]-[85]
Color-thickness correlation (Microscopy and AFM)	TCD method assesses the color difference between the graphene layer and the substrate.	[9]

Hardness of Graphene

The hardness-displacement and elastic module-displacement curves in various graphene layers can be measured using nano-indentation as shown in Figure 12. A large dip is found to be below 10 nm in the depth range and the curves are increasing progressively to stability. An additional continuous rigidity calculation (CSM) demonstrates an inflected depth of 10 nm. The load-displacement curve also shows that the load decreases with an increment of layers at the same indentation depth. Figure 12 also illustrates that both graph hardness and the graphene elastic modulus decrease as the number of graphene layers increases. The layers of graphene were further confirmed through AFM images, as depicted in Figure 12d, which show a range from a single layer at spot A to more than four layers at spot E, respectively.

Because of its superior mechanical properties, graphene can be considered an ideal reinforcement to produce composites so that the hardness can be improved. These features provide an increased opportunity to study metal matrix composites. [87] reported that they made mechanical alloys to study the composites. The time used for milling was 1 hour, 3 hours, and 5 hours. In an aluminium (Al) powder matrix, graphene nanoplatelets (GNPs) were added at concentrations of 0.25, 0.50, and 1.0 %wt. The Al coating on graphene delayed the formation of amorphous graphene structures as the milling time increased. Milling time and the presence of GNPs have a beneficial effect on hardness values. The mechanical behaviour of the

hardness-assessed GNP/Al composites shows that increased milling time leads to harder compounds being produced at a sintering time of 2 hours.

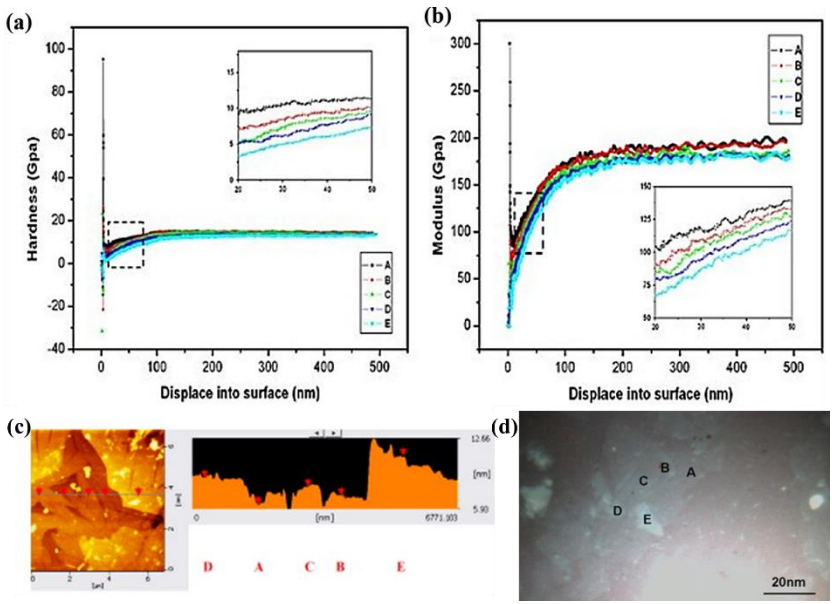

Figure 12: (a) Hardness–displacement, (b) elastic modulus–displacement graph, and (c) AFM of graphene measured on various spots as in (d) optical microscope image of graphene on the Si substrate [86]

Graphene reinforced with Al-based metal matrix composites has also been developed successfully using stir casting technology which retains the graphene loading rate of 0.5, 1, 1.5, and 2 %wt. The hardness number of the rocks well is found by testing all prepared specimens. The conclusion was that the sample filled with 0.5 %wt graphene shows the maximum indentation resistance because the graphene is uniformly dispersed into the aluminium matrix. Graphene particles enhance the hardness of the soft matrix and record 78 Rockwell hardness numbers (RHN) in relation to the parental composition. The minimum hardness figure is also found in the sample that has 2 %wt graphene because graphene particles are overloaded as the parental atoms have difficulty replacing them when cooled down, and the graphene particle saturation limit that fills the aluminium matrix is emphasized. Consequently, the material cannot bear more load to find its response to indentation[87].

[89] also reported on developing different graphene-enhanced (GNP) reinforced titanium (Ti) composites using the powder metallurgy (PM) process. As a result, GNPs GNP-reinforced Ti composites have improved hardness, microstructure, and density properties for optimal process

parameters. The highest hardness (566 HV) and density (4.39 g/cm^3) were achieved for the right amount of GNP at 1100 ºC for 120 min (0.15 %wt). Meanwhile, Ti composites reduced their density and hardness when GNPs content was above 0.15 %wt because of the GNPs agglomeration trend. Better atomic motion and diffusion at optimal time and temperature are positive for Ti composite characteristics. However, density, hardness, and structure deteriorated due to the damage to GNP structure and titanium carbide (TiC) formation at high-content GNPs. Over 0.30 %wt of the undesired TiC was detected. In comparison to pure Ti, the hardness of the Ti–GNPs composite increased from 304 HV to 566 HV because of fine-grain strengthening mechanisms and dislocation. A summary of graphene`s hardness is tabulated in Table 7.

The Melting Temperature of Graphene

For a first phase transition from 2D solid to 3D liquid, the melting of graphene is based on the nucleation theory. Because these two phases have different dimensions, it is difficult to determine the free energy difference between them, and thus it is unclear how to describe the melting temperature (T_m). T_m is a well-defined temperature as the point at which the liquid and solid phases of Gibb's free energy curves intersect. Here, a 2D nucleation theory shows how this difficulty can be overcome and gives T_m a reliable quantitative value. Spontaneous melting of graphene occurs at a temperature known as T^*_m of 4900 K, providing an upper limit of T_m for graphene. Nucleation theory can explain the melting of bulk graphene, allowing for an unambiguous definition of the T_m, which is 4510 K, approximately 250 K higher than that of graphite and currently the highest of all materials [93].

Furthermore, atomic simulations are used to study high-temperature graphene behaviour based on an exact atomic carbon potential. As a result, the aggregation of Stone–Wales defects and the formation of octagons are the initial stages of the melting process, which is carried out via the formation of carbon chains. Rather than being a simple liquid, the molten state is a 3D network of entangled chains. The melting temperature is approximately 4900 K, as determined by the extrapolation of simulation and 2D Lindemann criterion and results for various heating rates [94].

Table 7: Summary of the hardness properties of graphene with respect to various compositions added to the graphene

Graphene-composite	Hardness properties	Ref.
Graphene layers	Hardness and elastic modulus were measured using nano-indentation. A large dip is observed at depths below 10 nm. The load-displacement curve shows a decrease in load with increased layers at the same indentation depth. Graph hardness and elastic modulus decrease with increasing graphene layers.	[89]
Copper coated graphene reinforced aluminium composites (Cu-GNP-Al)	With the introduction of 0.5 %vol graphene, the composite material displays a tensile strength of 242 MPa and demonstrates a conductivity of 34.5 MS/m. This signifies a noteworthy improvement, with an increase of 102% in tensile strength and approximately 8.15% in conductivity compared to the characteristics of pure aluminium manufactured under the same conditions.	[90]
Graphen Aluminium Composites (GNP-Al)	Graphene was added to the aluminium powder matrix to form composites. Milling time and the presence of GNPs positively affect hardness values. Increased milling time results in harder compounds, especially with 2 hours of sintering. Stir casting technology was used to create composites with different graphene loadings. Uniform graphene dispersion enhances hardness. A sample with 0.5 %wt graphene shows maximum indentation resistance, achieving a hardness of 78 RHN. Samples with 2 %wt graphene exhibit reduced hardness due to graphene particle overload and agglomeration.	[90] [91]
Graphene-Ti Composites (Ti-GNP)	GNP-reinforced Ti composites developed using the powder metallurgy process. The right amount of GNP at 0.15 %wt achieves the highest hardness (566 HV) and density (4.39 g/cm^3) at 1100 ºC for 120 min. Higher GNP content results in reduced density and hardness due to agglomeration and TiC formation. The hardness of Ti-GNPs composite increases from 304 HV to 566 HV compared to pure Ti.	[92]

[96] reported the dynamic properties and structure of bulk materials consisting of graphene nanosheets using simulations of coarse-grain molecular dynamics. Results demonstrate convincing evidence of fluid-like melts of linear polymers at elevated temperatures in bulk graphene. In addition, at temperatures below the glass transfer temperature (T_g), the materials transform into a glassy "foam" condition. Due to the high T_g (≈ 1600 K) of bulk graphene materials in their glassy foam state, they have high thermal stability and an enormous free volume compared to standard polymer materials. This shows that the lubricating properties and attractive plastic flow at high temperatures are in graphene melting. Additionally, graphene foams show great promise as high-surface-area fire suppression additives and filtration materials for mechanical reinforcement and increasing the thermal conductivities of polymer materials.

Atomic simulations were used to investigate the melting behaviour of graphene-supported pure platinum (Pt), pure palladium (Pd), Pt-core/Pd-shell (Pt@Pd), and Pdcore/Pt-shell (Pd@Pt) nanoparticles (NPs) of the same size. The melting point of supported NPs is approximately 120 K lower than the free melting point. This can be attributed to restrictions of NPs by raising the temperature and distortions at the interface between metal and carbon on the graphene support. The analysis shows that the graphene support does not significantly impact melting modes because of the low distortion in the structure of the nanoparticles [97].

In addition, computer simulation has been used to study the dynamics of graphene disordering upon heating. Seeds in the 3D liquid stage form with heating graphene due to a complex disruption sequence and the formation of many interatomic bonds. Because of the 5-7 defects, groups of adjacent rings, and big rings and carbon chains perpendicular to the monolayer floor appear in the final stage. Although Stone–Wale (SW) defects occur, they do not accumulate, soon become rinsed, and have no significant impact on the melting mechanism. During the melting process, disordered and crystalline regions coexist. From the above, the melting point is estimated at 5100 K. To conclude, high graphene thermal stability is essential in real-world applications, for instance, visible light emitters based on thermal radiation resulting from solid sample heating [98]. The melting temperature behaviours of graphene are summarized in Table 8.

The Surface Area of Graphene

Graphene is supposed to have outstanding properties, such as a high specific surface area, and excellent electrical and thermal conductivity [101]. Graphene nanoplates are ideal nanomaterial compared to other nanoparticles of metal oxide or conventional metal because they have a very high specific surface area. It is recognized as the world's thinnest material and has significant

application potential in various technologies, including liquid crystal devices. [102] reported graphene has an extremely high specific surface area, and it is a highly effective additive for promoting the heterogeneous nucleation of water. A minimal amount of graphene can eliminate the degree of water subcooling. With a surface area concentration of about 0.070 ± 0.003 m^2/ml and a meagre mass fraction of about 0.020 ± 0.001 wt% of graphene, the need for subcooling to freeze water was eliminated as shown in Figure 13. Surfactants can be used to decrease the degree of subcooling, increase suspension stability, and slightly increase the total freezing time.

Table 8: Summary of graphene's melting temperatures in relation to defects and mixing with other materials

Material	Melting Temperature (K)	Ref.
Graphene (2D Nucleation Theory)	4510 K, about 250 K higher than that of graphite based on nucleation theory for a first order phase transition from the 2D solid to the 3D liquid via an intermediate quasi-2D liquid.	[94]
High-temperature graphene (atomistic simulations)	Stone-Wales (SW) defects are pivotal in governing graphene's melting temperature, with the aggregation of these defects triggering the formation of octagons. These octagons act as precursors for the spontaneous melting process, which occurs at approximately Tm ≈ 4900 K.	[95]
Graphene nanosheets (simulations of coarse-grain molecular dynamics)	Approx. 1600 K (T_g), graphene foams show great promise as high-surface-area fire suppression additives and filtration materials	[96]
Graphene-supported nanoparticles (simulation)	Approx. 120 K lower than the free melting point	[97], [99]
Graphene disorder upon heating (simulation)	5100 K	[98], [100]

Graphene composites, more specifically polymer matrix composites, are among the most profitable industrial products in various applications. The current state of the study of surface characteristics of graphene is predominant in graphene composite applications. The influence factors of surface characteristics of graphene, such as surface energy, microstructure, surface chemistry and composition, surface area, surface chemistry, and the techniques used for determining the graphene surface characteristics [103].

The properties of composites are mainly determined by the synergistic combination of concrete graphene surface, high interface adhesion of filler matrix, and exceptional characteristics of graphene and the main features of the matrix [104]. The conclusions showed that graphene surface characteristics could be adapted to better compatibility by altering graphene surface chemistry and improving interfacial interaction by increasing the surface area and wrinkling by mechanically interlocking. Furthermore, the chemical bonds on the graphene surface by functional groups like van der Waals and hydrogen bonding, result in a decrease in graphene dispersive surface energy while improving graphene wettability for the matrix. Modified graphene with unique surface properties would result in better composites considering the desired lifespan of high-performance reinforced materials [103].

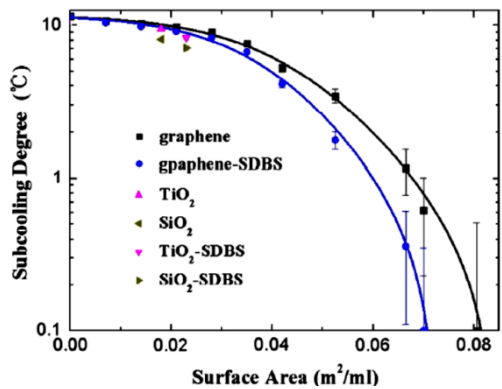

Figure 13: Relationship between graphene–H_2O nanofluids subcooling degree and the surface area per volume of samples [102]

The porous graphene materials have been given significant attention in recent years and rapidly developing because of their excellent electrochemical performances, larger surface areas, and unique pore structures in conversion and storage devices. Due to these extraordinary properties, porous graphene materials can be used as critical components in high-performance conversion devices and electrochemical energy storage such as fuel cells, lithium-ion batteries, and supercapacitors. Although the application and synthesis of porous materials have significantly progressed, a few significant points are left to be addressed. There is also an exciting challenge in developing porous graphene materials because it is necessary to precisely control pore morphology, including wall thickness. In addition, the interaction of various pores, such as mesopores, macropores, and micropores, is necessary for utilizing the synergistic effects of multiple pores [105].

The surface porosity of graphene-based aerogels plays a critical role in their performance in applications involving mass transfer. Many applications

of graphene-based aerogels, including but not limited to energy storage, gas sensing, chemical adsorption, and catalysis, crucially rely on efficient mass transfer processes. However, understanding the factors that determine surface porosities has been a challenge, impeding their optimization for specific applications. [106] have introduced an innovative approach to control surface porosity, which is essential for enhancing the performance of 3D-printed aerogels. They highlight the significance of ink properties, typically adjusted through additives in graphene oxide (GO) suspensions, and print parameters in shaping the surface porosity of graphene-based aerogels. Through a combination of experiments and hydrodynamic simulations, they demonstrate that the high shear stress experienced during the 3D printing process leads to a non-porous surface, whereas crosslinking of the sheets inhibits flake alignment induced by shearing, resulting in a porous surface (see Figure 14). These findings provide valuable insights for precise control of the surface porosity in printed graphene-oxide aerogels (GOA) by regulating crosslinking agents and shear stress.

Conclusions

In conclusion, graphene stands as a formidable force poised to exert a transformative influence across multiple scientific disciplines and technological domains. Its unparalleled amalgamation of bonded carbon structures, underpinned by a plethora of intricate physical attributes, positions it as a cornerstone of innovation. These remarkable properties span its thickness, layering, magnetic and optical characteristics, electrical and thermal conductivity, supercapacitance, hardness, and more. The inherent potential in these properties extends to diverse applications, ranging from cutting-edge sensor devices to integrated circuit components and beyond. Particularly captivating is the optical absorption behaviour of single-layer graphene (SLG), which is exclusively governed by a fundamental constant of nature, rendering it truly distinctive. This peculiarity signifies a noteworthy departure from frequency-dependent materials, solidifying its significance in the scientific landscape.

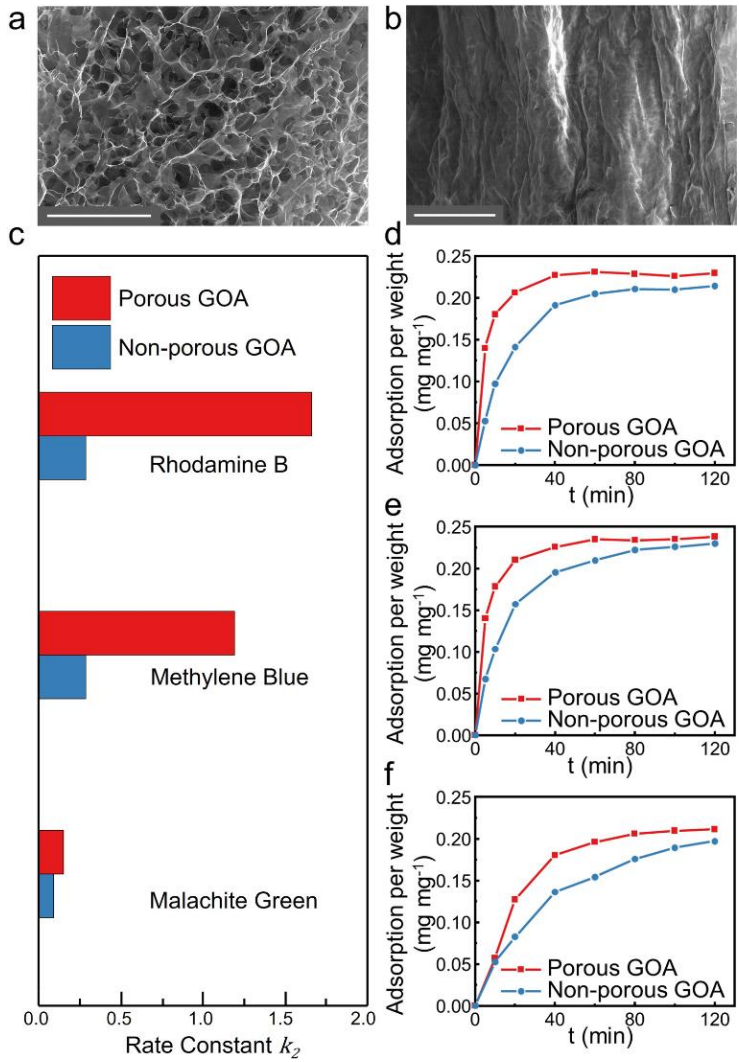

Figure 14: Comparative examination of surface structures and dye adsorption performance in porous and non-porous graphene oxide aerogels (GOA). SEM images of the surface of; (a) porous GOA, (b) non-porous GOA with scale bars of 100 μm, (c) rate constants derived from adsorption kinetics fitting. (d)–(f) Dye adsorption curves of porous GOA and non-porous GOA for; (d) rhodamine B, (e) methylene blue, and (f) malachite green. Reprinted with permission from [106]

Moreover, the development of graphene films unveils a suite of exceptional physical properties that underpin its promise in advanced applications. These include its potential as a high-power system component and an efficient heat-spreading material, offering novel avenues for thermal management within form factor-driven electronics. In essence, the exceptional attributes of graphene and its far-reaching implications underscore its pivotal role in shaping the future of various scientific disciplines and driving technological advancements. Its unique blend of structural and physical characteristics not only fuels curiosity in research but also holds the promise of revolutionizing industries and enhancing our understanding of the fundamental properties of matter.

Future Outlooks

To unlock the full potential of graphene in today's research and development landscape, fostering collaboration among researchers from diverse scientific fields is essential. These collaborations serve as a catalyst for innovative solutions, addressing complex challenges and contributing to our evolving understanding of graphene's physical properties. They underscore graphene's pivotal role in shaping the present and future of science and technology across a range of domains.

Given the growing importance of graphene in both scientific and industrial contexts, a pressing need exists for comprehensive assessments of the environmental impact of graphene-based materials and technologies. These assessments are crucial not only for sustainability but also for managing potential risks associated with the expanding production and application of graphene. To enhance awareness and appreciation of graphene's significance, it's highly advisable to establish educational initiatives and outreach programs targeting both the scientific community and the general public. These efforts have the potential to broaden understanding and recognition of graphene's extraordinary properties and its transformative impact across various industries.

Moreover, when designing applications, understanding graphene's physical properties is a crucial initial step. However, the effects of heterogeneity and defects on chemical interactions and graphene's properties require further investigation. For instance, the complexity of transport in multilayer graphene, influenced by multiple conducting layers, and the challenges of achieving precise atom-by-atom functionalization of graphene on large-area graphene wafers warrant in-depth research. Further exploration of graphene's integration into existing materials and engineering processes is vital, aligning with current trends in material science and engineering.

Efforts to explore comprehensive, reliable, and large-scale graphene production should be undertaken. A key challenge is scaling up the production

of high-quality graphene, which significantly impacts material properties. The production parameters should align with the chosen method or route. Moreover, characterizing graphene products at an industrial scale is crucial. Techniques such as XRD, Raman spectroscopy, X-ray photoelectron spectroscopy (XPS), and additional specialized characterizations for parameters like surface area and electrical conductivity should be considered.

Lastly, the establishment of standardized protocols and stringent quality control measures for graphene production and characterization is essential in today's rigorous research and industrial environments. These measures are critical for ensuring consistency and reliability in graphene-related studies, fostering confidence and uniformity in the field. Graphene's exceptional properties continue to offer ongoing opportunities for researchers to explore its potential, driving advancements across various fields in alignment with the current state of research and development in graphene and materials science.

Contributions of Authors

The authors confirm the equal contribution in each part of this work. All authors reviewed and approved the final version of this work. Mohd Rafal: Data curation, Writing – original draft. Mohamed Zourob; Review Muhammad Haziq Noor Akashah: Writing – original draft and correction, Rozina Abdul Rani: Writing – review & Siti Rabizah Makhsin: Validation, Supervision, Writing – review & editing, formatting, submission.

Funding

This work is financially supported by the GIP grant UiTM (600-RMCGIP5/3(106/2022)).

Conflict of Interests

All authors declare that they have no conflicts of interest.

Acknowledgment

The authors would like to acknowledge all the support from the School of Mechanical Engineering, UiTM Shah Alam, Malaysia.

References

[1] T. M. Radadiya, E. Journal, M. S. Vol, E. Centre, and D. Uk, "A properties of graphene," European Journal of Material Sciences, vol. 2, no. 1, pp. 6–18, 2015. [Online]. Available: https://www.eajournals.org/wp-content/uploads/A-Properties-of-Graphene.pdf (Accessed May 14, 2022).

[2] I. Jung, J.-S. Rhyee, J. Y. Son, R. S. Ruoff, and K.-Y. Rhee, "Colors of graphene and graphene-oxide multilayers on various substrates," *Nanotechnology*, vol. 23, no. 2, p. 025708, 2011. https://doi.org/10.1088/0957-4484/23/2/025708.

[3] M. H. Noor Akashah, M. R. Sahudin, R. A. Rani, P. J. Scully, and S. R. Makhsin, "Chemical properties of graphene," in Woodhead Publishing Series in Electric and Optical Materials, 2022, pp. 43-67. https://doi.org/10.1016/B978-0-323-85457-3.00023-2

[4] N. Tang, T. Tang, H. Pan, Y. Sun, J. Chen, and Y. Du, "Chapter 6 - Magnetic properties of graphene," in Spintronic 2D Materials, W. Liu and Y. Xu, Eds., Elsevier, 2020, pp. 137–161. https://doi.org/10.1016/B978-0-08-102154-5.00005-9

[5] N. Parvin, V. Kumar, S. W. Joo, S.-S. Park, and T. K. Mandal, "Recent advances in the characterized identification of mono-to-multi-layer graphene and its biomedical applications: A Review," *Electronics*, vol. 11, no. 20, p. 3345, 2022. https://doi.org/10.3390/electronics11203345

[6] O. Guler and N. Bagci, "A short review on mechanical properties of graphene reinforced metal matrix composites," *Journal of Materials Research and Technology*, vol. 9, no. 3, pp. 6808–6833, 2020. https://doi.org/10.1016/j.jmrt.2020.01.077

[7] H. G. P. Kumar and M. A. Xavior, "Graphene reinforced metal matrix composite (GRMMC): A Review," *Procedia Engineering*, vol. 97, pp. 1033–1040, 2014. https://doi.org/10.1016/j.proeng.2014.12.381

[8] L. Gao, W. Ren, F. Li, and H. M. Cheng, "Total color difference for rapid and accurate identification of graphene," *ACS Nano*, vol. 2, no. 8, pp. 1625–1633, 2008. https://doi.org/10.1021/nn800307s

[9] S. Reshmi, R. Sundheep, and D. J. Late, "Optical Based Techniques for 2D Layered Materials," in Advanced Analytical Techniques for Characterization of 2D Materials, AIP Publishing, 2022. https://doi.org/10.1063/9780735425422_002

[10] Z. H. Ni, H. M. Wang, J. Kasim, H. M. Fan, T. Yu, Y. H. Wu, Y. P. Feng, and Z. X. Shen, "Graphene thickness determination using reflection and contrast spectroscopy," *Nano Letters*, vol. 7, no. 9, pp. 2758–2763, 2007. https://doi.org/10.1021/nl071254m

[11] M. Tahriri, M. D. Monico, A. Moghanian, N. T. Yaraki, R. Torres, A. Yadegari, and L. Tayebi, "Graphene and its derivatives: Opportunities

and challenges in dentistry," *Materials Science and Engineering: C*, vol. 102, pp. 171–185, 2019. https://doi.org/10.1016/j.msec.2019.04.051

[12] X. Xu, S. Sun, J. Luo, R. Ma, J. Lin, L. Fang, P. Zhang, and Y. Chen, "Few-layer graphene prepared via microwave irradiation of black sesame for supercapacitor applications," *Chemical Engineering Journal*, vol. 425, p. 130664, 2021. https://doi.org/10.1016/j.cej.2021.130664

[13] Y. Yao, L. Ren, S. Gao, and S. Li, "Histogram method for reliable thickness measurements of graphene films using atomic force microscopy (AFM)," *Journal of Materials Science & Technology*, vol. 33, no. 8, pp. 815–820, 2017. https://doi.org/10.1016/j.jmst.2016.07.020

[14] H. Jussila, T. A. Owen, H. Yang, G. Hu, S. Aksimsek, N. Granqvist, H. Lipsanen, R. C. T. Howe, Z. Sun, and T. Hasan, "New approach for thickness determination of solution-deposited graphene thin films," *ACS Omega*, vol. 2, no. 6, pp. 2630–2638, 2017. https://doi.org/10.1021/acsomega.7b00336

[15] M. Wall, "The raman spectroscopy of graphene and the determination of layer thickness," Semantic Scholar, 2011. Available: https://api.semanticscholar.org/CorpusID:13670837 (Accessed Oct. 31, 2023).

[16] Y. Hwangbo, C. K. Lee, A. E. M. Isa, J. W. Jang, H. J. Lee, S. B. Lee, S. S. Kim, and J. H. Kim, "Interlayer non-coupled optical properties for determining the number of layers in arbitrarily stacked multilayer graphenes," *Carbon*, vol. 77, pp. 454–461, 2014. https://doi.org/10.1016/j.carbon.2014.05.050

[17] S. Trivedi, K. Lobo, and H. S. S. R. Matte, "Synthesis, Properties, and Applications of Graphene," in Woodhead Publishing Series in Electronic and Optical Materials, Fundamentals and Sensing Applications of 2D Materials, Woodhead Publishing, pp. 25–90, 2019. https://doi.org/10.1016/B978-0-08-102577-2.00003-8

[18] M. Alimohammadian and B. Sohrabi, "Observation of magnetic domains in graphene magnetized by controlling temperature, strain and magnetic field," *Scientific Reports*, vol. 10, no. 1, p. 21325, 2020. https://doi.org/10.1038/s41598-020-78262-w

[19] O. Hod, V. Barone, and G. E. Scuseria, "Half-metallic graphene nanodots: A comprehensive first-principles theoretical study," *Physical Review B*, vol. 77, no. 3, p. 035411, 2008. https://doi.org/10.1103/physrevb.77.035411

[20] T. Enoki and K. Takai, "The edge state of nanographene and the magnetism of the edge-state spins," *Solid State Communications*, vol. 149, no. 27–28, p. 1144–1150, 2009. https://doi.org/10.1016/j.ssc.2009.02.054

[21] J. Zhou, M. M. Wu, X. Zhou, and Q. Sun, "Tuning electronic and magnetic properties of graphene by surface modification," *Applied*

Physicals Letters, vol. 95, no. 10, 2009. https://doi.org/10.1063/1.3225154

[22] Y. S. Dedkov and M. Fonin, "Electronic and magnetic properties of the graphene-ferromagnet interface," *New Journal of Physics*, vol. 12, no. 12, 2010. https://doi.org/10.1088/1367-2630/12/12/125004

[23] H. S. S. Ramakrishna Matte, K. S. Subrahmanyam, and C. N. R. Rao, "Novel magnetic properties of graphene: Presence of both ferromagnetic and antiferromagnetic features and other aspects," *Journal of Physical Chemistry C*, vol. 113, no. 23, p. 9982–9985, 2009. https://doi.org/10.1021/jp903397u

[24] Z. Li, S. Li, Y. Xu, and N. Tang, "Recent advances in magnetism of graphene from 0D to 2D," *Chemical Communications*, vol. 59, no. 42, pp. 6286–6300, 2023. https://doi.org/10.1039/D3CC01311A

[25] O. V. Yazyev and L. Helm, "Defect-induced magnetism in graphene," *Physical Review B*, vol. 75, no. 12, p. 125408, 2007. https://doi.org/10.1103/physrevb.75.125408

[26] G. Vignesh, P. Devendran, N. Nallamuthu, S. Sudhahar, P. S. Kumar, and M. K. Kumar, "Effects of nitrogen, sulphur, and temperature treatments on the spectral, structural, and electrochemical characteristics of graphene oxide for energy storage applications," *Carbon Trends*, vol. 11, p. 100262, 2023. https://doi.org/10.1016/j.cartre.2023.100262

[27] A. Saren, V. Laitinen, M. Vinogradova, and K. Ullakko, "Twin boundary mobility in additive manufactured magnetic shape memory alloy 10M Ni-Mn-Ga," *Acta Materialia*, vol. 246, p. 118666, 2023. https://doi.org/10.1016/j.actamat.2022.118666

[28] G. Ulian, D. Moro, and G. Valdrè, "Electronic and optical properties of graphene/molybdenite bilayer composite," *Composite Structures*, vol. 255, p. 112978, 2021. https://doi.org/10.1016/j.compstruct.2020.112978

[29] Z. Xu, Fundamental properties of graphene. Elsevier Inc., 2017. https://doi.org/10.1016/B978-0-12-812651-6.00004-5

[30] M. Kavitha and M. Jaiswal, "Graphene: A review of optical properties and photonic applications", *Asian Journal of Physics*, vol. 25, no. 7, p. 809–831, 2016, Available: https://home.iitm.ac.in/manu.jaiswal/AJP%20Optical%20Prop%20Graphene.pdf (Acessed Oct 31, 2023).

[31] J. Wang, S. Cao, P. Sun, Y. Ding, Y. Li, and F. Ma, "Optical advantages of graphene on the boron nitride in visible and SW-NIR regions," *RSC Advances*, vol. 6, no. 112, p. 111345–111349, 2016. https://doi.org/10.1039/c6ra24588a

[32] H. Qin, Y. Liang, and J. Huang, "Size and temperature effect on the mechanical properties of graphene/hexagonal boron nitride van der Waals heterostructure*," Materials Science Engineering: B*, vol. 265, p. 115006, 2021. https://doi.org/10.1016/j.mseb.2020.115006

[33] R. Shimano, G. Yumoto, J. Y. Yoo, R. Matsunaga, S. Tanabe, H. Hibino, T. Morimoto, and H. Aoki, "Quantum faraday and kerr rotations in graphene," *Nature Communications*, vol. 4, no. 1, p. 1841, 2013. https://doi.org/10.1038/ncomms2866

[34] Q. Li, J. Lu, P. Gupta, and M. Qiu, "Engineering Optical Absorption in Graphene and Other 2D Materials: Advances and Applications," *Advanced Optical Materials*, vol. 7, no. 20, p. 1900595, 2019. https://doi.org/10.1002/adom.201900595

[35] R. Debbarma, S. K. Behura, Y. Wen, S. Che, and V. Berry, "WS2-induced enhanced optical absorption and efficiency in graphene/silicon heterojunction photovoltaic cells," *Nanoscale*, vol. 10, no. 43, pp. 20218–20225, 2018. https://doi.org/10.1039/c8nr03194k

[36] W. Li, G. Cheng, Y. Liang, B. Tian, X. Liang, L. Peng, A. R. H. Walker, D. J. Gundlach, N. V. Nguyen, "Broadband optical properties of graphene by spectroscopic ellipsometry," *Carbon*, vol. 99, pp. 348–353, 2016. https://doi.org/10.1016/j.carbon.2015.12.007

[37] M. H. Tsai, Y. X. Lu, C. Y. Lin, C. H. Lin, C. C. Wang, C. M. Chu, W. Y. Woon, and C. T. Lin, "The first-water-layer evolution at the graphene/water interface under different electro-modulated hydrophilic conditions observed by suspended/supported field-effect-device architectures," *ACS Applied Materials & Interfaces*, vol. 15, no. 13, pp. 17019–17028, 2023. https://doi.org/10.1021/acsami.3c00037

[38] W. Aggoune, C. Cocchi, D. Nabok, K. Rezouali, M. Akli Belkhir, and C. Draxl, "Enhanced light–matter interaction in graphene/h-bn van der waals heterostructures," *The Journal of Physical Chemistry Letters*, vol. 8, no. 7, pp. 1464–1471, 2017. https://doi.org/10.1021/acs.jpclett.7b00357.

[39] A. Kuzmina, M. Parzefall, P. Back, T. Taniguchi, K. Watanabe, A. Jain, and L. Novotny, "Resonant light emission from graphene/hexagonal boron nitride/graphene tunnel junctions," *Nano Letters*, vol. 21, no. 19, pp. 8332–8339, 2021. https://doi.org/10.1021/acs.nanolett.1c02913

[40] J. Wang, F. Ma, W. Liang, and M. Sun, "Electrical properties and applications of graphene, hexagonal boron nitride (h-BN), and graphene/h-BN heterostructures," *Materials Today Physics*, vol. 2, pp. 6–34, 2017, https://doi.org/10.1016/j.mtphys.2017.07.001

[41] H. Murata, Y. Nakajima, N. Saitoh, N. Yoshizawa, T. Suemasu, and K. Toko, "High-electrical-conductivity multilayer graphene formed by layer exchange with controlled thickness and interlayer," *Scientific Reports*, vol. 9, no. 1, pp. 1–5, 2019, https://doi.org/10.1038/s41598-019-40547-0

[42] I. N. Kholmanov, C. W. Magnuson, A. E. Aliev, H. Li, B. Zhang, J. W. Suk, L. L. Zhang, E. Peng, S. H. Mousavi, A. B. Khanikaev, R. Piner, G. Shvets, and R. S. Ruoff, "Improved electrical conductivity of graphene films integrated with metal nanowires," *Nano Letters*, vol. 12, no. 11, pp. 5679–5683, 2012, https://doi.org/10.1021/nl302870x

[43] B. Alemour, M. H. Yaacob, H. N. Lim, and M. R. Hassan, "Review of electrical properties of graphene conductive composites," *International Journal of Nanoelectronics and Materials*, vol. 11, no. 4, pp. 371–398, 2018.

[44] V. B. Mohan, K. Lau, D. Hui, and D. Bhattacharyya, "Graphene-based materials and their composites: A review on production, applications and product limitations," *Composites Part B: Engineering*, vol. 142, pp. 200–220, 2018.https://doi.org/10.1016/j.compositesb.2018.01.013

[45] C. Ramirez, F. M. Figueiredo, P. Miranzo, P. Poza, and M. I. Osendi, "Graphene nanoplatelet/silicon nitride composites with high electrical conductivity," *Carbon*, vol. 50, no. 10, pp. 3607–3615, 2012. https://doi.org/10.1016/j.carbon.2012.03.031

[46] B. Alemour, O. Badran, and M. R. Hassan, "A Review of Using Conductive Composite Materials in Solving Lightening Strike and Ice Accumulation Problems in Aviation," *Journal of Aerospace Technology and Management*, vol. 11, pp. 1–23, 2019. https://doi.org/10.5028/jatm.v11.1022

[47] I. Torres, S. M. Aghaei, N. Pala, and A. Gaitas, "Selective area multilayer graphene synthesis using resistive nanoheater probe*," Scientific Reports*, vol. 13, no. 1, 2023. https://doi.org/10.1038/s41598-023-34202-y

[48] G. Wang, J. Yang, J. Park, X. Gou, B. Wang, h. Liu, and J. Yao, "Facile synthesis and characterization of graphene nanosheets," *The Journal of Physical Chemistry C*, vol. 112, no. 22, pp. 8192–8195, 2008. https://doi.org/10.1021/jp710931h

[49] F. A. Chyada, A. R. Jabur, and H. A. Alwan, "Effect addition of graphene on electrical conductivity and tensile strength for Recycled electric power transmission wires," *Energy Procedia*, vol. 119, pp. 121–130, 2017. https://doi.org/10.1016/j.egypro.2017.07.055

[50] Y. Tan, H. Luo, H. Zhang, and S. Peng, "Graphene nanoplatelet reinforced boron carbide composites with high electrical and thermal conductivity," *Journal of The European Ceramic Society*, vol. 36, no. 11, pp. 2679–2687, 2016. https://doi.org/10.1016/j.jeurceramsoc.2016.04.036

[51] B. Zhang, S. A. Soltani, L. N. Le, and Ramazan Asmatulu, "Fabrication and assessment of a thin flexible surface coating made of pristine graphene for lightning strike protection," *Materials Science and Engineering: B*, vol. 216, pp. 31–40, 2017. https://doi.org/10.1016/j.mseb.2017.02.008

[52] J. H. Warner, F. Schäffel, A. Bachmatiuk, and M. H. Rümmeli, "Chapter 3 - Properties of Graphene," in Graphene, Elsevier, 2013, pp. 61–127. https://doi.org/10.1016/B978-0-12-394593-8.00003-5

[53] K. Takai, S. Tsujimura, F. Kang, and M. Inagaki, "Chapter 6 - Thermal properties and applications," in Graphene, Elsevier, 2020, pp. 415–447. https://doi.org/10.1016/B978-0-12-819576-5.00006-2

[54] M. Sang, J. Shin, K. Kim, and K. J. Yu, "Electronic and thermal properties of graphene and recent advances in graphene based electronics applications," *Nanomaterials*, vol. 9, no. 3, pp. 1–33, 2019. https://doi.org/10.3390/nano9030374

[55] Q. F. Cheng, J. P. Wang, J. J. Wen, C. H. Liu, K. L. Jiang, Q. Q. Li, S. and S. Fan, "Carbon nanotube/epoxy composites fabricated by resin transfer molding," *Carbon*, vol. 48, no. 1, pp. 260–266, 2010. https://doi.org/10.1016/j.carbon.2009.09.014

[56] J. K. W. Sandler, J. E. Kirk, I. A. Kinloch, M. S. P. Shaffer, and A. H. Windle, "Ultra-low electrical percolation threshold in carbon-nanotube-epoxy composites," *Polymer*, vol. 44, no. 19, pp. 5893–5899, 2003. https://doi.org/10.1016/S0032-3861(03)00539-1

[57] M. D. Siti Hajar, A. Ghani. Supri, and J. A. Jalil, "Effect of carbon black loading on tensile properties, electrical conductivity and swelling behavior of poly(vinyl) chloride/polyethylene oxide conductive films," *Applied Mechanics and Materials*, vol. 679, pp. 128–131, 2014. https://doi.org/10.4028/www.scientific.net/amm.679.128

[58] J. Shiomi and S. Maruyama, "Non-fourier heat conduction in a single-walled carbon nanotube: classical molecular dynamics simulations," *Physical Review B*, vol. 73, no. 20, pp. 1–7, 2006. https://doi.org/10.1103/PhysRevB.73.205420

[59] A. A. Balandin, S. Ghosh, W. Bao, I. Calizo, D. Teweldebrhan, F. Miao, and C. N. Lau, "Superior thermal conductivity of single-layer graphene," *Nano Letters*, vol. 8, no. 3, pp. 902–907, 2008. https://doi.org/10.1021/nl0731872

[60] I. Calizo, A. A. Balandin, W. Bao, F. Miao, and C. N. Lau, "Temperature dependence of the raman spectra of graphene and graphene multilayers," *Nano Letters*, vol. 7, no. 9, pp. 2645–2649, 2007, https://doi.org/10.1021/nl071033g

[61] L. Průcha, M. Lejeune, M. Kizovský, and E. Materna-Mikmeková, "In-situ thermal Raman spectroscopy of single-layer graphene on different substrates," *Materials Today Communications*, vol. 35, p. 105921, 2023. https://doi.org/10.1016/j.mtcomm.2023.105921

[62] A. A. Balandin, S. Ghosh, W. Bao, I. Calizo, D. Teweldebrhan, F. Miao, and C. N. Lau, "Extremely High Thermal Conductivity of Graphene: Experimental Study," *Nano Letters*, vol. 8, no. 3, pp. 902-907, 2008. https://doi.org/10.1109/SNW.2008.5418404

[63] H. Malekpour and A. A. Balandin, "Raman-based technique for measuring thermal conductivity of graphene and related materials," *Journal of Raman Spectroscopy*, vol. 49, no. 1, pp. 106–120, 2017. https://doi.org/10.1002/jrs.5230

[64] A. A. Balandin, S. Ghosh, W. Bao, I. Calizo, D. Teweldebrhan, F. Miao, and C. N. Lau, "Extremely high thermal conductivity of graphene: Prospects for thermal management applications in nanoelectronic

circuits," *Applied Physics Letters*, vol. 92, no. 15, pp. 1–4, 2008. https://doi.org/10.1063/1.2907977

[65] B. W. Wei, D. Qu, C. F. Hu, F. Z. Li, T. L. Zhou, R. Jun Xie, Z. M. Zhou, "Synthesis and physical properties of graphene nanosheets reinforced copper composites," *Advanced Materials Research*, vol. 833, pp. 310–314, 2014. https://doi.org/10.4028/www.scientific.net/AMR.833.310

[66] A. Li, C. Zhang, Y. F. Zhang, "Thermal conductivity of graphene-polymer composites: mechanisms, properties, and applications," Polymers, vol. 9, no. 12, p. 437, 2017. https://doi.org/10.3390/polym9090437

[67] S. Norouzi and M. M. Seyyed Fakhrabadi, "Anisotropic nature of thermal conductivity in graphene spirals revealed by molecular dynamics simulations," *Journal of Physics and Chemistry of Solids*, vol. 137, p. 109228, 2020. https://doi.org/10.1016/j.jpcs.2019.109228

[68] J. Renteria, D. Nika, and A. Balandin, "Graphene thermal properties: applications in thermal management and energy storage," *Applied Sciences*, vol. 4, no. 4, pp. 525–547, 2014. https://doi.org/10.3390/app4040525

[69] K. Bera, D. Chugh, Aditya Bandopadhyay, Hark Hoe Tan, A. Roy, and Chennupati Jagadish, "Decoupling the roles of defects/impurities and wrinkles in thermal conductivity of wafer-scale hBN films," *Journal of Applied Physics*, vol. 134, no. 15, 2023. https://doi.org/10.1063/5.0168186

[70] Y. Fu, J. Hansson, Y. Liu, S. Chen, A. Zehri, M. K. Samani, N. Wang, Y. Ni, Y. Zhang, and Z. B. Zhang, "Graphene related materials for thermal management," *2D Materials*, vol. 7, no. 1, p. 012001, 2019. https://doi.org/10.1088/2053-1583/ab48d9

[71] D. Wijerathne, Y. Gong, S. Afroj, N. Karim, and C. Abeykoon, "Mechanical and thermal properties of graphene nanoplatelets-reinforced recycled polycarbonate composites," *International Journal of Lightweight Materials and Manufacture*, vol. 6, no. 1, pp. 117–128, 2023. https://doi.org/10.1016/j.ijlmm.2022.09.001

[72] D. F. Báez, H. Pardo, I. Laborda, J. F. Marco, C. Yáñez, and S. Bollo, "Reduced graphene oxides: Influence of the reduction method on the electrocatalytic effect towards nucleic acid oxidation," *Nanomaterials*, vol. 7, no. 7, 2017. https://doi.org/10.3390/nano7070168

[73] M. Aziz, F. S. A. Halim, and J. Jaafar, "Preparation and characterization of graphene membrane electrode assembly," *Jurnal Teknologi*, vol. 69, no. 9, pp. 11–14, 2014. https://doi.org/10.11113/jt.v69.3388

[74] M. Lotya, A. Rakovich, J. F. Donegan, and J. N. Coleman, "Measuring the lateral size of liquid-exfoliated nanosheets with dynamic light scattering," *Nanotechnology*, vol. 24, no. 26, 2013. https://doi.org/10.1088/0957-4484/24/26/265703

[75] S. Badaire, P. Poulin, M. Maugey, and C. Zakri, "In situ measurements of nanotube dimensions in suspensions by depolarized dynamic light scattering," *Langmuir*, vol. 20, no. 24, pp. 10367–10370, 2004. https://doi.org/10.1021/la049096r

[76] H. Kato, A. Nakamura, and S. Kinugasa, "Effects of angular dependency of particulate light scattering intensity on determination of samples with bimodal size distributions using dynamic light scattering methods," *Nanomaterials*, vol. 8, no. 9, 2018. https://doi.org/10.3390/nano8090708

[77] J. Amaro-gahete, A. Ben, and D. Esquivel, "A comparative study of particle size distribution of graphene nanosheets synthesized by an ultrasound-assisted method," *Nanomaterials*, vol. 9, no. 2, p. 152, 2019. https://doi.org/10.3390/nano9020152

[78] Y. G. Andreev and P. G. Bruce, "Size and shape of graphene layers in commercial carbon blacks established by Debye refinement," *Journal of Applied Crystallography*, vol. 49, no. 1, pp. 24–30, 2016. https://doi.org/10.1107/s1600576715021378

[79] A. Kaushal, S. K. Dhawan, and V. Singh, "Determination of crystallite size, number of graphene layers and defect density of graphene oxide (GO) and reduced graphene oxide (RGO)," *Nucleation and Atmospheric Aerosols*, vol. 2115, pp. 1–5, 2019. https://doi.org/10.1063/1.5112945

[80] J. Kim, F. Kim, and J. Huang, "Seeing graphene-based sheets," *Materials Today*, vol. 13, no. 3, pp. 28–38, 2010. https://doi.org/10.1016/s1369-7021(10)70031-6.

[81] S. Roddaro, P. Pingue, V. Piazza, V. Pellegrini, and F. Beltram, "The optical visibility of graphene: interference colors of ultrathin graphite on SiO_2," *Nano Letters*, vol. 7, no. 9, pp. 2707–2710, 2007. https://doi.org/10.1021/nl071158l

[82] I. Jung, J. S. Rhyee, J. Y. Son, R. S. Ruoff, and K. Y. Rhee, "Colors of graphene and graphene-oxide multilayers on various substrates," *Nanotechnology*, vol. 23, no. 2, 2012. https://doi.org/10.1088/0957-4484/23/2/025708

[83] X. Yu, S. Fu, Y. Song, H. Wang, X. Wang, J. Kong, and J. Liu, "Color contrast of single-layer graphene under white light illumination induced by broadband photon management," *ACS Applied Materials & Interfaces*, vol. 12, no. 3, pp. 3827–3835, 2019. https://doi.org/10.1021/acsami.9b16149

[84] L. E. Crica, T. J. Dennison, E. A. Guerini, and K. Kostarelos, "A method for the measurement of mass and number of graphene oxide sheets in suspension based on non-spherical approximations," *2D Materials*, vol. 8, no. 3, pp. 035044–035044, 2021. https://doi.org/10.1088/2053-1583/abfe01

[85] S. H. Huh, "X-ray diffraction of multi-layer graphenes: Instant measurement and determination of the number of layers," *Carbon*, vol. 78, pp. 617–621, 2014. https://doi.org/10.1016/j.carbon.2014.07.034

[86] Y. Zhang and C. Pan, "Measurements of mechanical properties and number of layers of graphene from nano-indentation," *Diamond and Related Materials*, vol. 24, pp. 1–5, 2012. https://doi.org/10.1016/j.diamond.2012.01.033

[87] R. Pérez-Bustamante, D. Bolaños-Morales, J. Bonilla-Martínez, I. Estrada-Guel, and R. Martínez-Sánchez, "Microstructural and hardness behavior of graphene-nanoplatelets/aluminum composites synthesized by mechanical alloying," *Journal of Alloys and Compounds*, vol. 615, pp. S578–S582, 2014. https://doi.org/10.1016/j.jallcom.2014.01.225

[88] T. Pinto and Umesh, "Influence of graphene on hardness number of Aluminium-7075 based metal matrix composites," *International Journal of Innovative Science and Research Technology*, vol. 2, no. 12, pp. 285–289, 2017.

[89] M. Gürbüz and T. Mutuk, "Effect of process parameters on hardness and microstructure of graphene reinforced titanium composites," *Journal of Composite Materials*, vol. 52, no. 4, pp. 543–551, 2017. https://doi.org/10.1177/0021998317745143

[90] Y. Luo, Y. Huang, J. Liu, and Q. Chen, "Copper coated graphene reinforced aluminum composites with enhanced mechanical strength and conductivity," *Vacuum*, vol. 218, p. 112610, 2023. https://doi.org/10.1016/j.vacuum.2023.112610

[91] P. Lava Kumar, A. Lombardi, G. Byczynski, S. V. S. Narayana Murty, B. S. Murty, and L. Bichler, "Recent advances in aluminium matrix composites reinforced with graphene-based nanomaterial: A critical review," *Progress in Materials Science*, vol. 128, p. 100948, 2022. https://doi.org/10.1016/j.pm atsci.2022.100948

[92] R. Ranjan, N. Kumar Singh, A. Prakash Jaiswal, and V. Bajpai, "Metal matrix nano composites using graphene nano platelets indented on copper particles in aluminium matrix," *Advanced Materials Letters*, vol. 9, no. 09, pp. 652–655, 2018. https://doi.org/10.5185/amlett.2018.2078

[93] W. Zhang, S. Zhou, W. Ren, Y. Yang, L. Shi, Q. Zhou, and M. Liu, "Uniformly dispersing GNPs for fabricating graphene-reinforced pure Ti matrix composites with enhanced strength and ductility," *Journal of Alloys and Compounds*, vol. 888, p. 161527, 2021. https://doi.org/10.1016/j.jallcom.2021.161527

[94] J. H. Los, K. V. Zakharchenko, M. I. Katsnelson, and A. Fasolino, "Melting temperature of graphene," *Physical Review B*, vol. 91, no. 4, pp. 1–6, 2015. https://doi.org/10.1103/PhysRevB.91.045415

[95] K. V. Zakharchenko, A. Fasolino, J. H. Los, and M. I. Katsnelson, "Melting of graphene: from two to one dimension," *Journal of Physics: Condensed Matter*, vol. 23, no. 20, pp. 202202–202202, 2011. https://doi.org/10.1088/0953-8984/23/20/202202

[96] W. Xia, F. Vargas-Lara, S. Keten, and J. F. Douglas, "Structure and dynamics of a graphene Melt," *ACS Nano*, vol. 12, no. 6, pp. 5427–5435, 2018. https://doi.org/10.1021/acsnano.8b00524

[97] B. Mobedpour, S. Rajabdoust, and R. Roumina, "Melting of graphene supported Pd-Pt core-shell nanoparticles: A molecular dynamics study," *Computational Materials Science*, vol. 151, pp. 132–143, 2018. https://doi.org/10.1016/j.commatsci.2018.05.010

[98] L. A. Openov and A. I. Podlivaev, "On graphene melting," *Physics of The Solid State*, vol. 58, no. 4, pp. 847–852, 2016. https://doi.org/10.1134/S1063783416040168

[99] Q. Zheng, Z. Tian, T. Gao, Y. Liang, Q. Chen, and Q. Xie, "Effect of graphene on solid–liquid coexistence in Cu nanodroplets," *Applied Surface Science*, vol. 637, p. 157952, 2023. https://doi.org/10.1016/j.apsusc.2023.157952

[100] S. Subrina and D. Kotchetkov, "Simulation of heat conduction in suspended graphene flakes of variable shapes," *Journal of Nanoelectronics and Optoelectronics*, vol. 3, no. 3. pp. 249–269, 2008. doi: 10.1166/jno.2008.303.

[101] L. Li, X. Zhang, J. Qiu, B. L. Weeks, and S. Wang, "Reduced graphene oxide-linked stacked polymer forests for high energy-density supercapacitor," *Nano Energy*, vol. 2, no. 5, pp. 628–635, 2013, https://doi.org/10.1016/j.nanoen.2013.07.011

[102] L. Xing, Y. Chen, Z. Cheng, L. Jia, S. Mo, and Z. Liu, "Ultrahigh specific surface area of graphene for eliminating subcooling of water," *Applied Energy*, vol. 130, pp. 824–829, 2014. https://doi.org/10.1016/j.apenergy.2014.02.032

[103] J. F. Dai, G. J. Wang, L. Ma, and C. K. Wu, "Surface properties of graphene: Relationship to graphene-polymer composites," *Reviews on Advanced Materials Science*, vol. 40, no. 1, pp. 60–71, 2015.

[104] J. Longun, G. Walker, and J. O. Iroh, "Surface and mechanical properties of graphene-clay/polyimide composites and thin films," *Carbon*, vol. 63, pp. 9–22, 2013. https://doi.org/10.1016/j.carbon.2013.06.024

[105] S. Han, D. Wu, S. Li, F. Zhang, and X. Feng, "Porous graphene materials for advanced electrochemical energy storage and conversion devices," *Advanced Materials*, vol. 26, no. 6, pp. 849–864, 2014. https://doi.org/10.1002/adma.201303115

[106] B. Zhou, Z. Chen, Q. Cheng, M. Xiao, G. Bae, D. Liang, and T. Hasan, "Controlling surface porosity of graphene-based printed aerogels," *2D Materials and Applications*, vol. 6, no. 1, pp. 1–8, 2022. https://doi.org/10.1038/s41699-022-00312-w

The Densification of Hydroxyapatite from Eggshell Waste at Different Sintering Temperature

Natasha Ahmad Nawawi[*1, 2], *Nur Natrah Auni Ahmad*[1], *Nurul Hidayah Imaniah Noor Hamdan*[1], *Le Thi Bang*[3]

[1]*School of Mechanical Engineering, College of Engineering, Universiti Teknologi MARA, 40450 Shah Alam, Selangor, MALAYSIA*
[2]*Fracture Mechanics and Materials Integrity (FMMI) Research Group, College of Engineering, Universiti Teknologi MARA, 40450 Shah Alam, Selangor, MALAYSIA*
[3]*School of Materials Science and Engineering, Hanoi University of Science and Technology, No. 1 Dai Co Viet, Hai Ba Trung, Hanoi, VIETNAM*
[*]*natashanawawi@uitm.edu.my*

ABSTRACT

The outstanding biocompatibility and bioactivity properties of hydroxyapatite (HA) as a bio-implant material have garnered significant attention in prompting its extensive study. However, due to its brittleness and lower strength, its usage as a bone implant in load-bearing regions of biomedical applications is limited. The mechanical performance of the HA bodies is decreased by transformation-induced cracking as well as uncontrolled grain development. However, sintered HA ceramics with superior mechanical characteristics may be created if the prepared powder has better powder attributes including stoichiometry, crystallinity, agglomeration, and morphology from the start. Thus, this research explored the preparation of HA from discarded eggshells as a source of calcium via the dry reaction method and the correlation between its sinterability, densification, and mechanical properties at various sintering temperatures. In this work, the calcined eggshell powder was mixed with Calcium Hydrogen Phosphate Dihydrate (CHPD) via ball milling at 400 rpm speed for 4 hours and subsequently heat treated at 800 °C. The synthesized HA powder was compacted via hydraulic press and then sintered at temperatures of 1100 °C, 1150 °C, 1200 °C, and 1250 °C. The XRD analysis of the sintered HA samples revealed that the phase stability of the HA phase remained unaffected up to 1250 °C. Similar trends of

ISSN 1823-5514, eISSN 2550-164X
Received for review: 2023-07-17
Accepted for publication: 2023-11-03
Published: 2023-11-15

https://doi.org/10.24191/jmeche.v12i1.24650

average grain size, relative density, and hardness to sintering temperature were observed. HA samples sintered at 1250 °C exhibited the optimum mechanical properties with a relative density of 90.72% and a hardness of 4.34 GPa. It is believed that the grain boundary diffusion through the densification mechanism does not reach a densification level that is conducive to grain growth. Hence, the hardness still increased although the densification was relatively low. It can be concluded that HA densification significantly influences the grain coarsening and mechanical properties of the eggshell-derived HA.

Keywords: *HA; Eggshell; Densification; Mechanical Properties*

Introduction

Calcium Phosphate (CaP) is a compound that contains calcium and phosphorus which can be found naturally in inorganic waste among others such as eggshells, corals, cow bones, chicken bones, and fish bones [1]. One of the many variations of CaP mineral, HA (HA) has gained much interest in the medical and health-related fields as a bone graft alternative due to its mineral composition, which is comparable to teeth and bone besides its excellent bioactivity and biocompatibility. To date, it has been applied in drug delivery systems and bone tissue engineering implants in the form of powders, porous blocks, and hybrid composites. For example, it has been used when extensive bone removal is required or when bone augmentations are necessary (e.g., dental applications) [2].

However, due to its brittleness and lower strength, its application as bone implants in load-bearing regions of biomedical applications is limited [3]. It was reported that grain growth affects its density and hardness which contribute to its strength [4]. Besides that, poor mechanical properties and porosity can affect the biocompatibility of HA whereby the presence of voids or defects can hinder cell attachment, proliferation, and impede the formation of strong bonds between the implant and the surrounding tissue [5]. However, sintered HA ceramics with superior mechanical characteristics may be produced if the prepared powder has better powder attributes from the start including stoichiometry, crystallinity, agglomeration, and morphology. As a consequence, the employment of a suitable processing regimen enables the production of well-crystallized, high-density sintered HA that exhibits enhanced mechanical properties.

Hence, various synthesis methods have been employed to produce synthetic HA powder with significant purity and good mechanical properties [6]. Among the available methods are the hydrothermal method, solid-state reactions, the sol-gel process, emulsion, micro-emulsion, and predominantly chemical precipitation [7]. In addition, the synthesis of HA has also been

conducted using waste materials such as fish bone, eggshell, and coral as calcium precursors [1]. Typically, the eggshell constitutes around 11% of the total weight of an egg and is commonly regarded as a food waste with little commercial value. However, its abundant calcium content can be utilized as a viable source of calcium precursor. Besides that, by deriving HA from a natural source, it becomes feasible to obtain a material that closely matches the stoichiometry of human bone [8]. On another note, this practice not only offers economic advantages but also aligns with a sustainable approach to solid waste management, fostering economic growth and environmentally friendly practices.

Among the conventional techniques employed for the synthesis of eggshell-derived HA are wet precipitation, hydrothermal processes, low-temperature synthesis, solid-state reactions, and sol-gel methods [9]. Among these different techniques, wet chemistry methods, such as precipitation and sol-gel, are widely preferred due to their ability to provide precise control over particle morphology and size. However, these methods can be laborious and need more reproducibility. On the other hand, dry methods, such as mechanochemical and solid-state methods, offer a straightforward and highly reproducible synthesis process, as they do not require stringent control conditions [10].

One of the methods, mechanical milling, has been used to produce HA derived from eggshells. However, this dry-state reaction method has been claimed to increase the possibility of contamination in the final HA powder. In previous research, the solid-state reaction was used to study the eggshell-derived HA powders through the attrition milling method [11]. In that research, with a proper processing regime, it has been proven that it did not produce any contaminations which resulted in good mechanical properties [11]. Ball milling is a widely utilized technique that involves the use of ceramic balls placed in a milling jar with the material to be milled. By rotating the jar, the balls collide with the material, resulting in size reduction through impact and abrasion. This process effectively breaks down particles and achieves the desired particle size distribution, making ball milling a popular method for producing fine powders with precise sizing [12]-[13]. To date, no work has been reported on the production of HA using calcium carbonate from eggshells through the ball milling method.

Hence, this study aims to produce HA using eggshell as the source of calcium precursor in the form of calcium carbonate through the solid-state reaction method and to determine its sinterability at various sintering temperatures. Subsequently, the influence of different sintering temperatures will be examined to ascertain the correlation of densification on the mechanical properties of eggshell-derived HA.

Methodology

In this work, the waste eggshells were cleaned with distilled water to remove the protein membrane layer. Then, they were dried in the oven before being crushed using a mortar and pestle into a fine powder. Afterward, the eggshell powder was calcined at 700 ℃ for two hours to obtain pure calcium carbonate ($CaCO_3$) (Figure 1a). This pure $CaCO_3$ was then used as the source of calcium (Ca) in the synthesis and mixed with a phosphate (P) precursor, Calcium Hydrogen Phosphate Dihydrate (CHPD), at a Ca/P molar ratio of 1.67 via ball milling for 4 hours milling time at 400 rpm speed (Figure 1b). Following that, the powder mixture was sieved with a 212 µm mesh sieve and then heat treated at 800 °C (Figure 1c) to obtain pure HA powder.

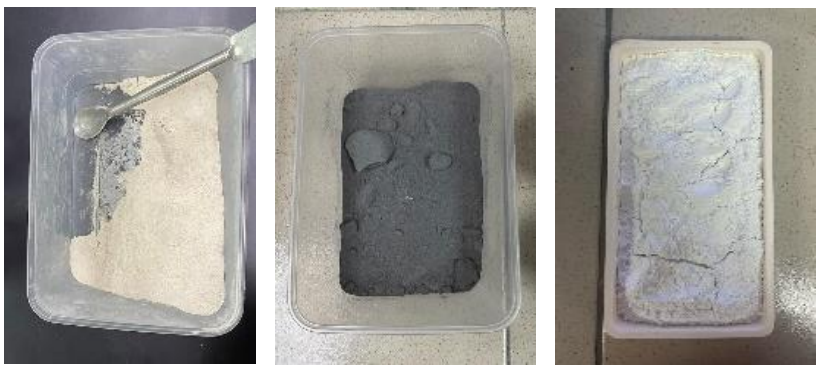

(a) (b) (c)

Figure 1: The HA powder preparation: (a) crushed eggshell, (b) eggshell calcined at 700 °C, and (c) ball-milled mixture calcined at 800 °C

Subsequently, the synthesized eggshell-derived HA powder was pressed into disc samples (26 mm diameter) (Figure 2) via uniaxial pressing and followed by a sintering regime in an air atmosphere at temperatures varying from 1100 to 1250 °C for 2 hours in a box furnace at a rate of 5 °C/min which will induce densification to the prepared eggshell-derived HA powder. The physical change due to densification was shown clearly in Figure 2 by the shrinkage in the sample dimension after sintering. These sintered samples were later addressed as ES-1100, ES-1150, ES-1200, and ES-1250, concerning its sintering temperature.

Phase stability evaluation of the sintered HA dense ceramics was determined using X-ray diffraction (XRD) (Rigaku Ultima IV) to observe any phase transformation corresponding to sintering temperature with standard reference to the International Centre for Diffraction Data (ICDD). Meanwhile, the morphological characterization was evaluated using a Field Emission

Scanning Electron Micrograph (FESEM). Subsequently, the grain size of the sintered sample was determined from the FESEM image based on the line intercept method [11]. Archimedes' principle was used in the bulk density measurement for the sintered samples with distilled water as an immersion medium. The relative density of the sintered sample was calculated by taking the theoretical density of HA as 3.156 g cm^{-3}. Meanwhile, the hardness of all the green compacted samples was measured via the Vickers indentation) using an applied load of 100–200 grams with a dwell time of 10 seconds and repetitive indentation to get an accurate reading.

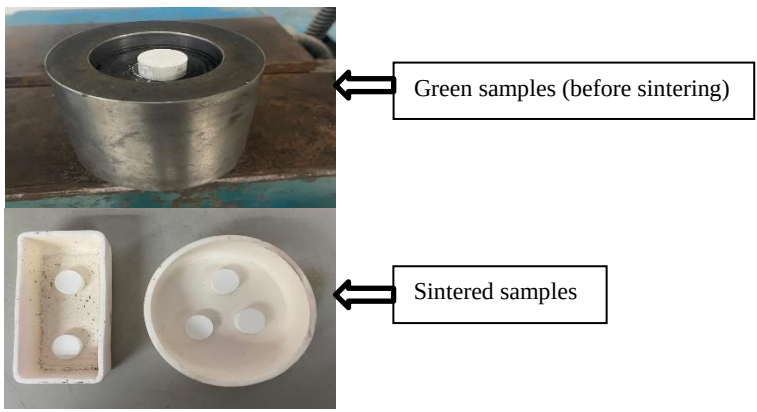

Figure 2: As-prepared dense and sintered eggshell-derived HA samples

Results and Discussion

Figure 3 presented the XRD pattern of the powder mixture (eggshell powder and CHPD) after heat treatment at 800 °C. It could be observed that all the XRD peaks matched those in the ICDD 01-076-8436 for HA; thus, indicating that a pure HA phase was successfully obtained. Besides that, sharper peaks that are visible in the XRD pattern denote the high crystallinity of the synthesized powder.

Meanwhile, Figure 4 depicts the phase stability of the sintered HA samples at various temperatures. All XRD peaks in Figure 4a to Figure 4d perfectly matched those found in the ICDD 01-076-8436 for HA; thus, demonstrating that the stability of the HA phase was not compromised when sintered between 1100 °C and 1250 °C. Nonetheless, HA phase decomposition may happen due to further sintering at 1300 °C and 1350 °C, forming minute amounts of α-tricalcium phosphate (α-TCP) and tetracalcium phosphate (TTCP) [11]. In addition, it was observed that the intensity of the highest peak for HA corresponding to the (211) lattice plane (~2θ = 31.96°- 32.07°)

increased as the sintering temperature increased from 1100 °C to 1250 °C. This indirectly reveals that a highly crystalline HA structure has been formed. A similar XRD pattern of HA at different sintering temperatures has been reported in previous studies [14]-[15].

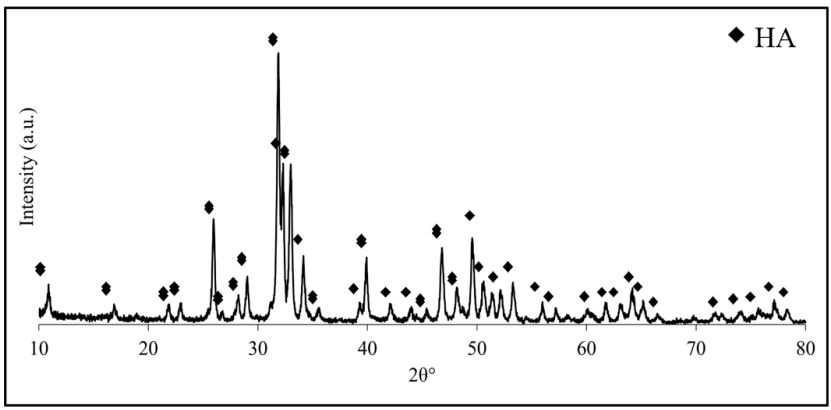

Figure 3: XRD pattern of eggshell-derived HA powder heat treated at 800 °C

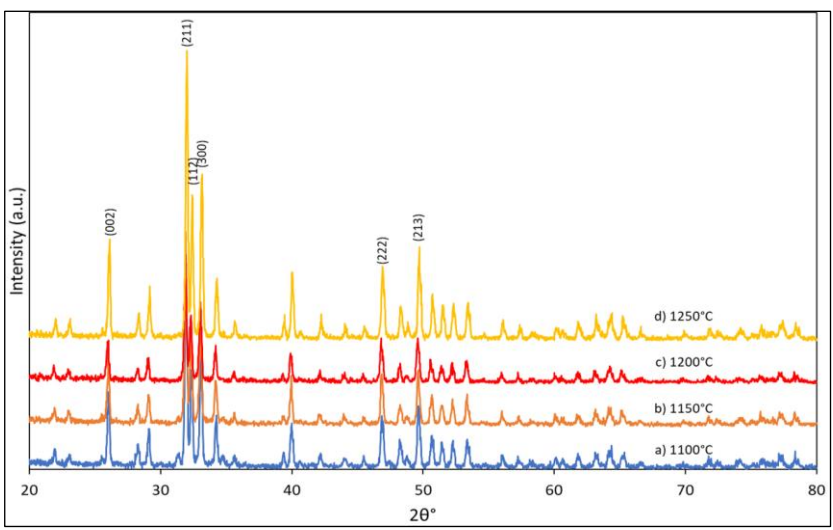

Figure 4: XRD patterns of eggshell-derived HA samples sintered at temperatures ranging from 1100 °C to 1250 °C

The FESEM images showing the microstructural evolution of the samples sintered at various temperatures are presented in Figure 5. Generally,

globular particles are visible in all sintered samples. It was observed that at 1100 °C (Figure 5a), necking formation between the grains has taken place. These phenomena correspond to the first stage of sintering [11]. Besides, with increasing sintering temperature beyond 1100 °C, densification started to occur and formed agglomerated particles. It was found that samples sintered at 1200 °C (Figure 5c) and 1250 °C (Figure 5d) exhibited a more densely packed microstructure with less amount of porosity. The smaller pore sizes exhibit a higher strength and better mechanical properties [15].

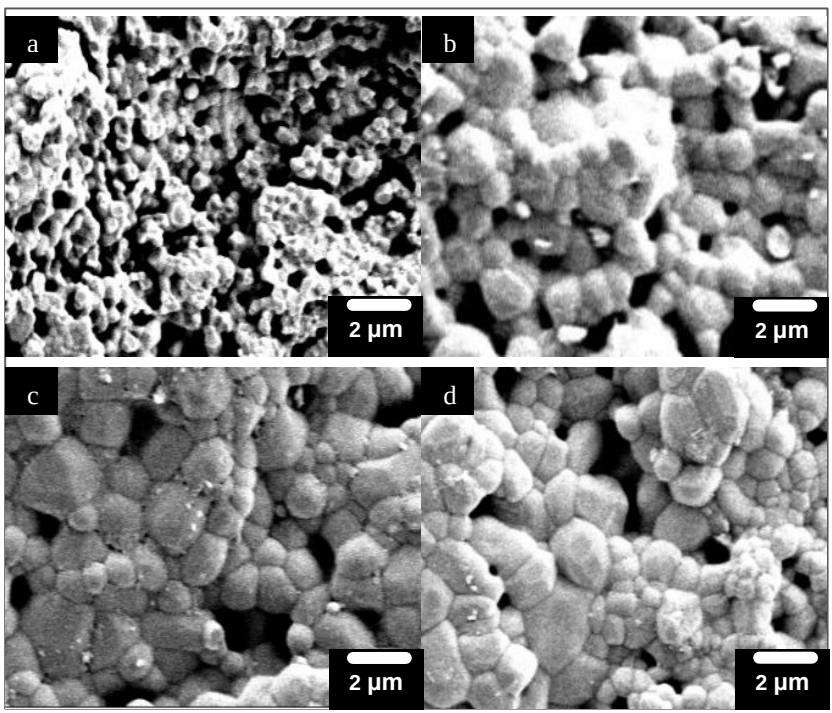

Figure 5: FESEM images of eggshell-derived HA samples sintered at; (a) 1100 °C, (b) 1150 °C, (c) 1200 °C, and (d) 1250 °C

Although this densification was accompanied by grain coarsening, it can be seen that the rate of grain coarsening was not primary when compared to that reported in other works where the grain size of HA increased from approximately 2 to 8 mm as the sintering temperature increased from 1200 °C to 1250 °C [16]. An increase in grain size was not favoured as induced strength deterioration of the sintered samples. Moreover, accelerated grain growth at high sintering temperatures is a typical result of conventional pressureless sintering due to the uncontrollable presence of moisture in the sintering

atmosphere [17] but this was not observed in this work. Thus, it is believed that the grain boundary diffusion through the densification mechanism does not reach a densification level that is conducive to grain growth [18].

The influence of sintering temperature on the average grain sizes of HA is presented in Figure 6a. The graph illustrates a linear relationship between average grain size and sintering temperature. The smallest average grain size of the sintered HA was 0.83 ± 0.02 µm, which was obtained at 1100 °C as shown in Figure 6a, while the largest average grain size of the sintered HA was 2.29 ± 0.02 µm, which was obtained at 1250 °C.

In studying mechanical properties, the ability of the material to densify is used to evaluate the material's structure as well as porosity predictions [19]. Figure 6b and Figure 6c depict the relative density and Vickers hardness of HA as a function of sintering temperatures, respectively. A steady increase in density is observed with an increase in sintering temperature up to 1250 °C. These findings align with the compacted arrangement of the sintered HA microstructure, which becomes denser as the sintering temperature increases, as demonstrated in Figure 6a. The relative density exhibited an increase, starting at 89.42% at 1100 °C and reaching a peak of 90.72% at 1250 °C. Nevertheless, based on the previous study, higher relative density values were obtained ranging from 96% - 97% [6], [11], [15]. The lower relative density values obtained in the current work could also possibly be due to insufficient pressing pressure applied during the compaction of the green samples. This is shown in Figure 5 whereby the presence of porosity between the grains was still observed at 1250 °C. Hence, it can be generalized that pressing pressure applied during the preparation of green samples also plays a vital role in their densification. Nevertheless, a study by Ramesh et al. [11] acquired a similar trend for the result of sintered HA samples from 1100 °C to 1250 °C although a different processing method (attrition milling) was used.

It is noteworthy that in Figure 6b, the Vickers hardness also exhibited a similar trend to that observed for relative density. It was also observed that grain size imparted a significant impact on the sintered sample hardness. The Vickers hardness values ranged from 1.59 GPa at 1100 °C to a maximum of 4.34 GPa at a sintering temperature of 1250 °C. It was reported in a previous study that the value of hardness for 1100 °C to 1250 °C temperature ranged from 1 GPa to 5 GPa but via a two-step sintering method [11], [14]. Besides that, the significant increase in hardness up to 1250 °C can be attributed to the concurrent increase in relative density, as depicted in Figure 6a. It is widely acknowledged that the hardness of HA tends to increase with relative density. In addition, hardness is also governed by grain growth [6], [11]. In this work, although the grain growth was observed to gradually increase with sintering temperature, the comparative value of hardness to the previous study that worked on eggshell-derived HA via the different source of Ca and method was obtained. This could be attributed to the hardness of the material which will increase if the indentation is smaller [20] as observed on the indented sintered

sample. Overall, it was observed that sample ES-1250 demonstrated the best mechanical properties compared to all other samples in this study.

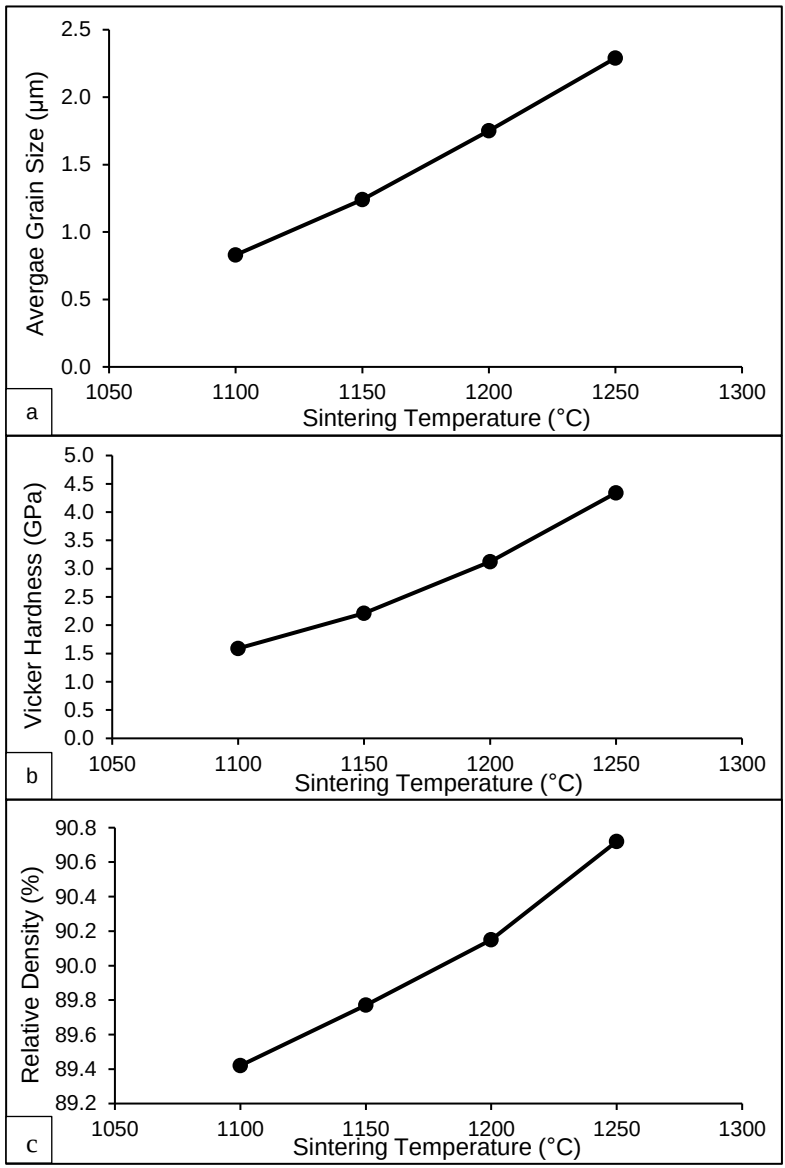

Figure 6: The effect of sintering temperature on; (a) average grain size, (b) Vickers hardness, and (c) relative density of eggshell-derived HA samples

Conclusion

Ultimately, highly crystalline and phase-pure HA from bio-waste eggshells were successfully produced via a combination of mechanical alloying and sintering methods. The HA powder was obtained after pre-heat treatment of calcined eggshell and CHPD at 800 °C. Throughout the sintering regime, the phase stability of the HA samples was not disrupted at all sintering temperatures as shown in the XRD analysis. The resulting sintered HA samples, which have globular agglomerated particles as their microstructure, were found to increase in grain size with sintering temperature as the first stage of sintering took place at 1100 °C. However, in this work, it is believed that the grain boundary diffusion through the densification mechanism did not reach a densification level which is conducive to grain growth as the presence of porosity between the grains was still observed at 1250 °C. A similar trend was also observed for both densification and hardness of the sintered HA samples with increased sintering temperature. Similarly, it can be concluded that lower grain growth by these samples indicates the lower-level densification obtained. Although the densification was comparatively low, the measured hardness of these sintered samples still increased as the resulting diamond indentation on the sample was smaller. Overall, it was observed that sample ES-1250 demonstrated the best mechanical properties compared to all other samples from this study with the highest relative density of 90.72% and a hardness of 4.34 GPa. On top of that, the usage of this natural waste as a precursor in synthesizing HA is not only sustainable and cost-effective but would also be beneficial to environmental waste recovery.

Contributions of Authors

The authors confirm the equal contribution in each part of this work. All authors reviewed and approved the final version of this work.

Funding

The authors acknowledge the Ministry of Higher Education (MOHE) for funding under the Fundamental Research Grant Scheme (FRGS) (FRGS/1/2022/TK10/UITM/02/20).

Conflict of Interests

One of the authors, Natasha Ahmad Nawawi, is a Section Editor of the Journal of Mechanical Engineering (JMechE). The author has no other conflict of interest to note.

Acknowledgement

The authors would like to thank the School of Mechanical Engineering, College of Engineering, Universiti Teknologi MARA (UiTM), Shah Alam for the support and providing research facilities.

References

[1] M. Z. A. Khiri *et al.*, "Crystallization behaviour of low-cost biphasic HA/β-tricalcium phosphate ceramic at high sintering temperatures derived from high potential calcium waste sources," *Results Phys*, vol. 12, pp. 638–644, Mar. 2019. doi: 10.1016/j.rinp.2018.12.025.

[2] G. Gergely *et al.*, "Preparation and characterization of HA from eggshell," *Ceram Int*, vol. 36, no. 2, pp. 803–806, Mar. 2010. doi: 10.1016/j.ceramint.2009.09.020.

[3] C. Paredes, J. Roleček, L. Pejchalová, T. Spusta, D. Salamon, and P. Miranda, "Evaluating the suitability of fast sintering techniques for the consolidation of calcium phosphate scaffolds produced by DLP," *Journal of the European Ceramic Society*, vol. 43, no. 14, pp. 6493–6503, Nov. 2023. doi: https://doi.org/10.1016/j.jeurceramsoc.2023.05.052.

[4] C. M. Mardziah, S. Ramesh, H. Chandran, A. Sidhu, and S. Krishnasamy, "Properties of sintered zinc HA bioceramic prepared using waste chicken eggshells as calcium precursor," *Ceram Int*, Dec. 2022. doi: 10.1016/j.ceramint.2022.12.098.

[5] R. Choudhary *et al.*, "In-vitro bioactivity, biocompatibility and dissolution studies of diopside prepared from biowaste by using sol-gel combustion method," *Materials Science and Engineering C*, vol. 68, pp. 89–100, Nov. 2016. doi: 10.1016/j.msec.2016.04.110.

[6] P. Kamalanathan *et al.*, "Synthesis and sintering of HA derived from eggshells as a calcium precursor," *Ceram Int*, vol. 40, no. PB, pp. 16349–16359, Dec. 2014. doi: 10.1016/j.ceramint.2014.07.074.

[7] M. S. Firdaus Hussin, H. Z. Abdullah, M. I. Idris, and M. A. Abdul Wahap, "Extraction of natural HA for biomedical applications—A review," *Heliyon*, vol. 8, no. 8. Elsevier Ltd, Aug. 01, 2022. doi: 10.1016/j.heliyon.2022.e10356.

[8] E. R. Muñoz-Sanchez, C. D. Arrieta-Gonzalez, A. Quinto-Hernandez, E. Garcia-Hernandez, and J. Porcayo-Calderon, "Synthesis of HA from eggshell and its electrochemical characterization as a coating on Titanium," *Int J Electrochem Sci*, p. 100204, May 2023. doi: 10.1016/j.ijoes.2023.100204.

[9] H. Khandelwal and S. Prakash, "Synthesis and Characterization of HA Powder by Eggshell," *Journal of Minerals and Materials Characterization and Engineering*, vol. 04, no. 02, pp. 119–126, 2016. doi: 10.4236/jmmce.2016.42011.

[10] A. N. Natasha, S. Ramesh, L. T. Bang, and M. H. Koay, "Influence of calcination temperature in synthesizing eggshell-derived calcium phosphate," in *Materials Today: Proceedings*, Elsevier Ltd, 2021, pp. 1915–1919. doi: 10.1016/j.matpr.2021.09.388.

[11] S. Ramesh *et al.*, "Direct conversion of eggshell to HA ceramic by a sintering method," *Ceram Int*, vol. 42, no. 6, pp. 7824–7829, May 2016. doi: 10.1016/j.ceramint.2016.02.015.

[12] M. Baláž, "Ball milling of eggshell waste as a green and sustainable approach: A review," *Advances in Colloid and Interface Science*, vol. 256. Elsevier B.V., pp. 256–275, Jun. 01, 2018. doi: 10.1016/j.cis.2018.04.001.

[13] A. C. Ferro and M. Guedes, "Mechanochemical synthesis of HA using cuttlefish bone and chicken eggshell as calcium precursors," *Materials Science and Engineering C*, vol. 97, pp. 124–140, Apr. 2019. doi: 10.1016/j.msec.2018.11.083.

[14] R. Singh, Y. H. Wong, and M. Akhtari-Zavareh, "Thermal phase stability and properties of HA derived from biowaste eggshells," *Journal of Ceramic Processing Research*, vol. 18, no. 1, pp. 69-72, 2017. [Online]. Available: https://www.researchgate.net/publication/316062556

[15] N. Monmaturapoj and C. Yatongchai, "Effect of Sintering on Microstructure and Properties of HA Produced by Different Synthesizing Methods," *Journal of Metals, Materials and Minerals*, vol. 21, no. 2, 2010. [Online]. Available: https://jmmm.material.chula.ac.th/index.php/jmmm/article/view/210

[16] P. Gnanamoorthy, V. Karthikeyan, and V. A. Prabu, "Field Emission Scanning Electron Microscopy (FESEM) characterisation of the porous silica nanoparticulate structure of marine diatoms," *Journal of Porous Materials*, vol. 21, no. 2, pp. 225–233, 2013. doi: https://doi.org/10.1007/s10934-013-9767-2.

[17] W. Suchanek and M. Yoshimura, "Processing and properties of hydroxyapatite-based biomaterials for use as hard tissue replacement implants," *Journal of Materials Research*, vol. 13, no. 1, pp. 94–117, 1998. doi: https://doi.org/10.1557/jmr.1998.0015.

[18] D. J. Curran, T. J. Fleming, M. R. Towler, and S. Hampshire, "Mechanical parameters of strontium doped hydroxyapatite sintered

using microwave and conventional methods," *Journal of the Mechanical Behavior of Biomedical Materials*, vol. 4, no. 8, pp. 2063–2073, 2011. doi: https://doi.org/10.1016/j.jmbbm.2011.07.005.

[19] S. A. Agrawal, "Simplified Measurement of Density of Irregular Shaped Composites Material using Archimedes Principle by Mixing Two Fluids Having Different Densities," *International Research Journal of Engineering and Technology*, vol. 8, no. 3, pp. 1005-1009, 2021. [Online]. Available: www.irjet.net

[20] A. R. Noviyanti, I. Rahayu, R. P. Fauzia, and Risdiana, "The effect of Mg concentration to mechanical strength of HA derived from eggshell," *Arabian Journal of Chemistry*, vol. 14, no. 4, Apr. 2021. doi: 10.1016/j.arabjc.2021.103032.